

**A Thesis Submitted for the Degree of PhD at the University of Warwick**

**Permanent WRAP URL:**

<http://wrap.warwick.ac.uk/136766>

**Copyright and reuse:**

This thesis is made available online and is protected by original copyright.

Please scroll down to view the document itself.

Please refer to the repository record for this item for information to help you to cite it.

Our policy information is available from the repository home page.

For more information, please contact the WRAP Team at: [wrap@warwick.ac.uk](mailto:wrap@warwick.ac.uk)

# High-Performance Electric Vehicle Duty Cycles and their Impact on Lithium Ion Battery Performance and Degradation

by

Quirin Kellner

A thesis submitted in partial fulfilment of the requirements for  
the degree of  
Doctor of Philosophy in Engineering

University of Warwick, WMG  
February 2019

# Table of Contents

Table of Contents.....	i
Table of Figures.....	vii
Table of Tables .....	xi
Acknowledgements.....	xiii
Declaration.....	xiv
List of Publications .....	xv
Journal Publications .....	xv
Conference Proceedings .....	xv
Abstract.....	xvi
Abbreviations.....	xvii
Nomenclature .....	xix
1    Introduction .....	1
1.1    Context.....	1
1.2    Problem statement .....	3
1.3    Introduction to the sponsoring companies and motivation for the direction of research .....	3
1.4    Scope of the Thesis .....	4
1.5    Thesis outline .....	5
2    A Review of Lithium ion battery cells and testing methodologies .....	6
2.1    Introduction .....	6
2.1.1    Research Question 1: Do existing LIB testing methodologies adequately represent HP-BEV racing applications?.....	6
2.2    Basic components and operational principles.....	7
2.2.1    Open circuit potential and capacity .....	10

2.2.2	Operating potential.....	11
2.2.3	Temperature dependency .....	14
2.3	Electrode materials .....	14
2.3.1	Anode materials.....	15
2.3.2	Cathode Materials.....	16
2.4	LIB Degradation mechanisms.....	18
2.4.1	Surface film effects .....	20
2.4.2	Structural changes .....	20
2.4.3	Mechanical changes.....	21
2.4.4	Parasitic reactions .....	21
2.4.5	Influencing environmental factors and operating parameters.....	22
2.5	Characterisation Testing .....	24
2.5.1	Galvanostatic energy capacity .....	24
2.5.2	Pseudo-OCV testing and dQ/dV analysis .....	26
2.5.3	Hybrid Pulse Power Characterisation (HPPC) .....	30
2.5.4	Pulse-Multisine Characterisation .....	31
2.5.5	Electrochemical Impedance Spectroscopy .....	34
2.5.6	Ultrasonic testing .....	36
2.6	Degradation Testing / Ageing .....	37
2.6.1	Storage Testing – Calendar Ageing .....	38
2.6.2	Cycle Testing .....	39
2.7	Performance Testing.....	45
2.8	Conclusion & Definition of the Knowledge Gap .....	46
2.8.1	Definition of the Knowledge Gap.....	47
3	A Review of Duty Cycle Construction Methods .....	48
3.1	Introduction .....	48



3.1.1	Research Question 2: How can a duty cycle representative of HP-BEV racing applications be defined? .....	48
3.2	Driving Cycle Methods .....	49
3.3	Data Collection .....	49
3.4	Data Segmentation, Processing & Cycle Construction .....	50
3.4.1	Random Microtrip Cycles .....	50
3.4.2	ARTEMIS Cycles .....	53
3.4.3	Markov Chain Cycles .....	55
3.4.4	Best-fit Cycles .....	58
3.5	Frequency Domain Methods .....	59
3.6	Conclusion & Definition of the knowledge gap .....	62
3.6.1	Definition of the knowledge gap .....	62
3.6.2	<b>Research Task 1:</b> Collate a database of battery duty cycles representative of HP-BEV racing applications. ....	64
3.6.3	<b>Research Task 2:</b> Define a methodology, from which a duty cycle that is suitable for LIB performance and degradation testing may be derived. ....	64
3.6.4	<b>Research Task 3:</b> Devise an experiment to conduct LIB performance and degradation testing to investigate differences between HP-BEV applications and standard testing procedures. ....	65
3.6.5	<b>Research Task 4:</b> Analyse the experimental results and determine any use-case specific behaviour between HP-BEV applications and standard testing procedures. ....	65
4	Development of a High-Performance Duty Cycle Database .....	67
4.1	Introduction .....	67
4.2	Vehicle model .....	67
4.2.1	Target vehicle .....	67
4.2.2	Chassis and handling .....	68
4.2.3	Powertrain .....	69

4.3	Circuit Models .....	73
4.4	Driver Model .....	75
4.5	Simulation & Data processing .....	78
4.5.1	Normalised duty cycles .....	82
4.6	Results .....	83
4.6.1	Recorded profiles .....	83
4.6.2	Effect of road inclination .....	85
4.6.3	Normalised profiles .....	86
4.7	Duty cycle selection .....	86
4.8	Limitations of the database .....	87
4.9	Conclusion .....	88
5	Development of a generic HP duty cycle .....	89
5.1	Introduction .....	89
5.2	Method One: HP Random Pulse Cycle (HP-RPC) .....	89
5.2.1	HP-RPC Data Processing and Target Criteria .....	90
5.2.2	HP-RPC Construction .....	94
5.3	Method Two: HP Multisine Cycle (HP-MS) .....	96
5.3.1	HP-MS Data Processing and Target criteria .....	96
5.3.2	HP-MS Construction .....	100
5.4	Results .....	104
5.4.1	Validation of HP-MS and HP-RPC .....	105
5.4.2	Comparison between HP cycles and the IEC Test standard .....	107
5.4.3	Thermal simulation study .....	110
5.5	Discussion .....	112
5.5.1	Validation of the HP duty cycles for the Bahrain International Circuit .....	112

5.5.2	Comparison of the HP Duty cycles against Standard Test and Characterisation Cycles	113
5.6	Conclusion.....	114
6	Experimental Assessment of Cell Performance and Degradation .....	116
6.1	Introduction .....	116
6.2	Experimental set-up.....	117
6.2.1	Cell selection .....	117
6.2.2	Test equipment .....	117
6.3	Cell characterisation testing .....	121
6.3.1	Galvanostatic energy capacity .....	122
6.3.2	Pulse-Multisine Characterisation.....	123
6.3.3	Electrochemical Impedance Spectroscopy .....	126
6.4	Performance testing .....	126
6.5	Duty cycle degradation study .....	129
6.5.1	Hardware malfunctions.....	131
6.6	Conclusion.....	134
7	Experimental Results & Discussion .....	135
7.1	Introduction .....	135
7.2	Cell characterisation testing .....	135
7.2.1	Galvanostatic energy capacity .....	135
7.2.2	Pulse Multisine Characterisation .....	137
7.2.3	EIS tests .....	143
7.2.4	Initial characterisation summary .....	147
7.3	Performance testing .....	148
7.4	Duty Cycle Degradation Study .....	154
7.5	Further Discussion on the Results of the duty cycle degradation Study .....	163

7.6	Limitations of the experimental study.....	165
7.7	Conclusion.....	166
8	Conclusions and future direction.....	168
8.1	Contributions to knowledge .....	168
8.2	Future direction and further work.....	171
9	References .....	173

# Table of Figures

FIGURE 2-1 - SCHEMATIC DRAWING OF A LI-ION BATTERY CELL.....	9
FIGURE 2-2 – CELL POLARISATION, AND SOURCES OF POTENTIAL DROPS ADAPTED FROM [65].....	12
FIGURE 2-3 - SCHEMATIC DRAWING OF THE SEI LAYER.....	16
FIGURE 2-4 – COMMON DEGRADATION MECHANISMS OF A LIB .....	19
FIGURE 2-5 – CURRENT AND VOLTAGE PROFILE OF A 53 AH G-NMC CELL DURING CC-CV PROCEDURE. ....	25
FIGURE 2-6 - GALVANOSTATIC CHARGE/DISCHARGE POTENTIAL PROFILES MEASURED AT VARIOUS C- RATES FOR A CARBON-LFP CELL AT 25°C. FROM [130]. INCREASES IN CURRENT REDUCE THE OVERALL ENERGY CAPACITY THAT MAY BE EXTRACTED FROM THE CELL, CAUSED BY INCREASED POLARISATION AND THERMAL LOSSES.....	26
FIGURE 2-7 – CURRENT AND VOLTAGE PROFILE OF A 53 AH G-NMC CELL DURING PSEUDO-OCV MEASUREMENTS .....	27
FIGURE 2-8 – CAPACITY VS CELL POTENTIAL CORRESPONDING TO THE P-OCV CHARGE IN FIGURE 2-7.....	28
FIGURE 2-9 – dQ/dV CURVE DERIVED FROM FIGURE 2-8, RED ARROWS INDICATE PEAKS ASSOCIATED WITH PHASE CHANGES IN THE ACTIVE ELECTRODE MATERIALS DURING CHARGING .....	28
FIGURE 2-10 – OCV AND PHASES OF GRAPHITE AS A FUNCTION OF LITHIATION, ADAPTED FROM [135] .....	29
FIGURE 2-11 – VOLTAGE RESPONSE OF A CELL TO A DISCHARGING CURRENT INPUT .....	30
FIGURE 2-12 – RANGLES ECM WITH 2 RC PAIRS, R1 REPRESENTS THE CHARGE TRANSFER RESISTANCE, C1 IS USED TO MODEL THE EFFECT OF THE DOUBLE LAYER CAPACITANCE. THE 2ND RC PAIR CAN BE USED TO MODEL THE EFFECTS OF THE SEI .....	31
FIGURE 2-13 – PULSE MULTISINE CHARACTERISATION PROFILE FROM [141]. THE DYNAMIC MULTISINE SIGNAL IS SUPERIMPOSED ON THE MODAL BASE SIGNAL TO CREATE A MORE DYNAMIC PROFILE.....	32
FIGURE 2-14 – NON-LINEAR ECM CONSISTING OF A LINEAR ECM, OCV BLOCK, AND NON-LINEAR OVER-POTENTIAL FUNCTION, ADAPTED FROM [142].....	32
FIGURE 2-15 - TYPICAL NYQUIST PLOT FOR A LIB, SEPARATED INTO THREE DISTINCT FREQUENCY REGIONS.....	35
FIGURE 2-16 – SCHEMATIC OF ULTRASONIC TESTING SET UP.....	36
FIGURE 2-17 – TYPICAL PROCESS OF DEGRADATION TESTING. ....	37
FIGURE 2-18 – CYCLE LIFE TESTING PROFILES .....	43
FIGURE 3-1 - THE PROCESS OF DETERMINING A RANDOM DRIVING CYCLE, AS DESCRIBED WITHIN [178,179,184,189]	51
FIGURE 3-2 - MICROTRIPS FOR THE FIRST 220S OF THE LA92 CYCLE [188] .....	51
FIGURE 3-3 - ILLUSTRATION OF SPEED ACCELERATION CROSS DISTRIBUTIONS OF TWO URBAN DRIVING SCENARIOS FROM [175].....	52
FIGURE 3-4 - HEV DUTY CYCLE RECORDING AND FILTERED VERSION. MANY OF THE DYNAMIC CHANGES ARE NOT PRESERVED WITHIN THE FILTERED PROFILE. FROM [169]. ....	56
FIGURE 3-5 - TABLE CONTAINING THE CODE FOR A JOURNEY ANALYSED BY TRAFIX METHOD, FROM [194] .....	59
FIGURE 3-6 – PROPOSED ADDITION TO THE EXISTING TESTING FRAMEWORK .....	64

FIGURE 4-1 – POWERTRAIN SCHEMATIC OF THE HP-BEV WITHIN CARMAKER COMPRISING TWO DRIVE SOURCES COMPOSED OF AN EM-INVERTER ASSEMBLY, A 2 SPEED GEARBOX, AND A DIFFERENTIAL FOR EACH, A POWER SUPPLY REPRESENTING THE BATTERY, AND A POWERTRAIN CONTROL SYSTEM, COMPRISING A BATTERY CONTROL UNIT (BCU), MOTOR CONTROL UNIT (MCU), AND TRACTION CONTROL UNIT (TCU).....	70
FIGURE 4-2 – TYPICAL TORQUE-SPEED CHARACTERISTICS OF ELECTRIC MACHINES .....	71
FIGURE 4-3 – EM-INVERTER EFFICIENCY MAPS FOR FRONT AND REAR DRIVE SOURCES; THE DATA WAS PROVIDED BY AN INDUSTRIAL PARTNER. ....	71
FIGURE 4-4 - LEFT TO RIGHT, NÜRBURGRING GP AND NORDSCHLEIFE TRACKS TRACED IN BING MAPS, BIRDS' EYE VIEW OF NÜRBURGRING GP TRACK IN IPG ROAD, NÜRBURGRING NORDSCHLEIFE IN IPGROAD .....	74
FIGURE 4-5 – IPGDRIVER PARAMETERISATION. EACH PARAMETER IS TUNEABLE TO INCREASE OR DECREASE DRIVER AGGRESSIVENESS WITH RESPECT TO LONGITUDINAL AND LATER VEHICLE DYNAMICS. ....	76
FIGURE 4-6 – SUMMARY OF THE DATA PROCESSING STEPS. FOLLOWING SIMULATION WORK, THE SIGNALS FOR VELOCITY AND POWER DEMAND ARE RECORDED. AN INITIAL PART OF THE SIGNAL IS DELETED TO AVOID THE STANDSTILL PORTION OF EACH SIMULATION. THE PERIOD, I.E. LAP LENGTH OF EACH CIRCUIT IS DETERMINED THROUGH AN UNBIASED AUTO-CORRELATION. THE COLLECTED SIGNAL IS SPLIT INTO INDIVIDUAL LAPS, FROM WHICH A MEAN LAP IS CALCULATED. ....	78
FIGURE 4-7 – A) VEHICLE SPEED RECORDED FROM THE SILVERSTONE SIMULATION; B) ASSOCIATED BATTERY DUTY CYCLE PROFILE FROM THE SILVERSTONE SIMULATION .....	79
FIGURE 4-8 – NORMALISED UNBIASED AUTOCORRELATION VS SAMPLE SHIFT. THE RED CROSSES MARK THE LOCATION OF THE HIGHEST PEAKS, INDICATING COMPLETION OF A FULL LAP. THE NUMBER OF SAMPLE POINTS BETWEEN PEAKS IS EQUAL TO THE SAMPLES CONTAINED WITHIN EACH LAP. ....	81
FIGURE 4-9 – A) LAP PROFILES EXTRACTED FROM ORIGINAL RECORDING FOR THE SILVERSTONE SIMULATION; B) MEAN LAP CALCULATED FROM THE LAPS SHOWN IN SUBFIGURE A).....	82
FIGURE 4-10 – MEAN VALUES FOR THE MEASURES LISTED IN TABLE 4-7. ERROR BARS REPRESENT ONE STANDARD DEVIATION FROM THE MEAN. ERROR BARS REPRESENT ONE STANDARD DEVIATION FROM THE MEAN .....	85
FIGURE 4-11 – A) NORMALISED PROFILE OF THE MEAN LAP FROM THE SILVERSTONE CIRCUIT SIMULATION, B) IEC 62660-1 CYCLE LIFE PROFILE A.....	86
FIGURE 5-1 – DUTY CYCLE CONSTRUCTION PROCESS AS SUGGESTED FOR THE HP-RPC.....	90
FIGURE 5-2 – ILLUSTRATION OF DUTY PULSES AND ASSOCIATED DRIVING MANOEUVRES.....	92
FIGURE 5-3 – RANDOM PULSE CYCLE (HP-RPC) CONSTRUCTION METHODOLOGY.....	94
FIGURE 5-4 – AMPLITUDE SPECTRA FOR $PNorm, zm(t)$ FOR 12 CIRCUITS OF THE DATABASE; MEAN AMPLITUDE SPECTRUM; FUNCTION APPROXIMATING THE MEAN AMPLITUDE SPECTRUM .....	98
FIGURE 5-5 – ICDF FOR $PNorm, zm(t)$ FOR 12 CIRCUITS OF THE DATABASE; MEAN AMPLITUDE SPECTRUM; FUNCTION APPROXIMATING THE MEAN AMPLITUDE SPECTRUM .....	99
FIGURE 5-6 – HP-MSC CONSTRUCTION PROCESS .....	100

FIGURE 5-7 - OVERVIEW OF ALGORITHM OUTCOME A) A SINGLE PERIOD OF THE ZERO-MEAN MULTISINE CYCLE; B) THE AMPLITUDE SPECTRUM UP TO 0.3 Hz; C) DESIRED, INITIAL AND OPTIMISED INVERSE CUMULATIVE DISTRIBUTION FUNCTION; D) PROGRESSION OF POWER ROOT MEAN SQUARED ERROR (RMSE) .....	103
FIGURE 5-8 - A) MULTISINE CYCLE; B) RANDOM PULSE CYCLE; C) BAHRAIN RACING-CIRCUIT SIMULATION DUTY CYCLE; D) IEC 62660-1 CYCLE LIFE TEST PROFILE A.....	104
FIGURE 5-9 – VALIDATION OF HP-MSC AND HP-RPC AGAINST THE BAHRAIN CYCLE BASED ON HP-RPC AND HP-MSC DESIGN CRITERIA. A) FRACTION BASED CRITERIA; B) TIME BASED CRITERIA; C) DEVIATION OF HP-MSC & HP-RPC FROM BAHRAIN CYCLE BASED ON HP-RPC CRITERIA; D) AMPLITUDE SPECTRA FOR HP-RPC, HP-MSC AND BAHRAIN; E) ICDF FOR HP-RPC,HP-MSC AND BAHRAIN. ....	107
FIGURE 5-10 - DIRECT COMPARISON BETWEEN HP-RPC, HP-MSC AND IECC IN TERMS OF A) FRACTION BASED CRITERIA; B) TIME BASED CRITERIA; C) DEVIATION OF HP-RPC, HP-MSC AND IECC FROM HP-RPC TARGETS CRITERIA; D) AMPLITUDE SPECTRA FOR HP-RPC, HP-MSC AND IECC; E) ICDF FOR HP-RPC,HP-MSC AND IECC .....	109
FIGURE 5-11 – A) AVERAGE CELL TEMPERATURE IN DEG C DURING CYCLING FROM 100% - 10% SOC FOR A 20 AH LFP CELL; B) CELL HEAT GENERATION FOR HP-RPC; C) CELL HEAT GENERATION FOR HP-MSC; D) CELL HEAT GENERATION FOR BAHRAIN; E) CELL HEAT GENERATION FOR IECC.....	112
FIGURE 6-1 - TEST RIG DESIGN PROCESS ILLUSTRATION; A) TEST RIG CAD MODEL B) TOP VIEW OF THE ASSEMBLED EXPERIMENTAL RIG; C) FRONT VIEW OF HALF RIG WITH BENT COOLING PLATES; D) FOAMGLAS® AND POLYSTYRENE PACKING OF GAPS BETWEEN CELLS; E) POSITIONS OF THERMOCOUPLES; F) INSTRUMENTED COOLING FINS. ....	119
FIGURE 6-2 – BRASS BLOCK DESIGN AND DIMENSIONS; TAPPED HOLES IN BLOCK 2 ALLOW FOR IN SITU EIS TESTING....	120
FIGURE 6-3 – PULSE MULTISINE PROFILE COMPOSITION: (A) BASE SIGNAL WITH PULSES OF 357.6 A DISCHARGING AND 67.6 A CHARGING CURRENT AMPLITUDE; (B) ZERO-MEAN MULTISINE SIGNAL WITH A PEAK AMPLITUDE OF 43.4 A; (C) COMBINED PULSE MULTISINE SIGNAL USED FOR PMC CHARACTERISATION TESTS.....	125
FIGURE 6-4 – A SINGLE PERIOD OF THE THREE DUTY CYCLES SELECTED FOR TESTING: A – HP-MSC; B – IECC; C – BAHRAIN .....	127
FIGURE 6-5 – ANNOTATED IECC TEST CYCLE: RED – CC-CV PERIOD, GREEN – EQUILIBRATION PERIODS .....	128
FIGURE 6-6 – NYQUIST PLOTS OF EIS MEASUREMENTS AT 50% SOC PRE STORAGE, POST STORAGE AND 13 GALVANOSTATIC 1C DISCHARGES POST-STORAGE .....	131
FIGURE 6-7 – CELL SURFACE TEMPERATURE ON THERMOCOUPLE POSITIONS 1, 4, AND 6 ON CELL 3 DURING BITRODE MALFUNCTION. TEMPERATURE DIFFERENCE AT HOTTEST POINT OF 4.2 °C FOR TC4 AND 0.3°C FOR TC6.....	133
FIGURE 7-1 - CAPACITY TEST RESULTS. (A) DISSIPATED ENERGY CAPACITY DURING A 1C DISCHARGE, (B) TOTAL ENERGY DURING CHARGE .....	136
FIGURE 7-2 – VOLTAGE AND TEMPERATURE RESPONSE OF CELL No 1 AT 50% SOC, INITIAL CHARACTERISATION TEST (A) MEASURED VOLTAGE RESPONSE TO THE PMC SIGNAL. (B) BITRODE SAFETY THERMOCOUPLE MEASUREMENT ...	137
FIGURE 7-3 – ESTIMATED CELL IMPEDANCE AND 1 <sup>ST</sup> ORDER TRANSFER FUNCTION FIT. ....	138
FIGURE 7-4 – 1 <sup>ST</sup> ORDER EQUIVALENT CIRCUIT MODEL COMPRISING A SERIES RESISTOR WITH ONE RC PAIR USED TO MODEL THE OVER-VOLTAGE RESPONSE.....	139

FIGURE 7-5 – MEASURED OVER-VOLTAGE VS MODELLED OVER-VOLTAGE MODELLED FROM ECM. A LINEAR RELATIONSHIP BETWEEN MODELLED AND MEASURED OVER-VOLTAGE CAN BE OBSERVED; SOME NON-LINEAR TENDENCY FOR 10% SOC.....	140
FIGURE 7-6 – PMC VOLTAGE RESPONSE FOR CELL 3 AT 10% SOC DURING INITIAL CHARACTERISATION. RED CIRCLES INDICATE OCCURRENCES, WHERE THE CELL VOLTAGE SAFETY LIMIT WAS REACHED, RESULTING IN CURRENT DE-RATING. ....	141
FIGURE 7-7 – PMC MEAN ECM PARAMETERS AND STANDARD DEVIATION. (A) DC RESISTANCE $R_0$ . (B) CHARGE TRANSFER AND DIFFUSION RESISTANCE $R_1$ . (C) TIME CONSTANT $\tau_1$ . ....	142
FIGURE 7-8 – SECOND ORDER ECM USED TO MODEL THE IMPEDANCE RESPONSE OF A CELL UNDER EIS WITHIN SCRIBNER® ZVIEW. ....	144
FIGURE 7-9 – NYQUIST PLOTS FOR EIS MEASUREMENTS AT 95%, 80%, 50%, 20% AND 10% SOC. ....	145
FIGURE 7-10 – RESISTANCE PARAMETERS DETERMINED FROM EIS MEASUREMENTS. (A) PURE OHMIC RESISTANCE( $R_0$ ). (B) CHARGE TRANSFER RESISTANCE $R_{ct}$ – $EIS$ . (C) COMBINED RESISTANCE.....	146
FIGURE 7-11 – NYQUIST PLOT FOR CELL 3 AT 50% SOC. THE 1HZ IMPEDANCE HAS A RESISTIVE VALUE OF $1.469\text{ m}\Omega$ . THIS CORRESPONDS WELL WITH THE $R_0$ – $PMC$ MEASUREMENTS .....	147
FIGURE 7-12 – PERFORMANCE TEST RESULTS FOR THE HP-MSC FOR CELL 4 FOR A DYNAMIC DISCHARGE FROM 95-10% SOC. (A) POWER PROFILE. (B) MEASURED VOLTAGE RESPONSE. (C) MEASURED CELL SURFACE TEMPERATURE .	151
FIGURE 7-13 – PERFORMANCE TEST RESULTS FOR THE BAHRAIN CYCLE FOR CELL 4 FOR A DYNAMIC DISCHARGE FROM 95-10% SOC. (A) POWER PROFILE. (B) MEASURED VOLTAGE RESPONSE. (C) MEASURED CELL SURFACE TEMPERATURE .....	152
FIGURE 7-14 – PERFORMANCE TEST RESULTS FOR THE IECC FOR CELL 4 FOR A DYNAMIC DISCHARGE FROM 95-10% SOC. (A) POWER PROFILE. (B) MEASURED VOLTAGE RESPONSE. (C) MEASURED CELL SURFACE TEMPERATURE. ....	153
FIGURE 7-15 - CELL CAPACITY THROUGHOUT TESTING AT CHARACTERISATIONS. ....	156
FIGURE 7-16 - INCREMENTAL CAPACITY ANALYSIS - TOP LEFT: INITIAL CHARACTERISATION; TOP RIGHT: FINAL CHARACTERISATION; BOTTOM LEFT: HP-MSC CELL PROGRESSION; BOTTOM RIGHT: IECC CELL PROGRESSION ...	159
FIGURE 7-17 – PROGRESSION OF ECM PARAMETERS AS DERIVED FROM PMC TESTS FOR A – $R_0$ ; B – $R_1$ ; C – $\tau_1$ . ...	160
FIGURE 7-18 – NYQUITS PLOTS: A – NYQUIST PLOTS FOR CELL 1 AT BEGINNING OF TESTING; B – NYQUIST PLOT FOR CELL 1 AFTER 200 CYCLES; C – NYQUIST PLOTS FOR CELL 4 AT BEGINNING OF TESTING; D – NYQUIST PLOT FOR CELL 4 AFTER 200 CYCLES .....	161
FIGURE 7-19 – A – MEAN OHMIC RESISTANCE OF TEST GROUPS DERIVED FROM NYQUIST PLOTS, B – MEAN CHARGE-TRANSFER RESISTANCE OF TEST GROUPS DERIVED FROM NYQUIST PLOTS. ....	162
FIGURE 8-1 – PROPOSED FRAMEWORK FOR PERFORMANCE AND DEGRADATION TESTING .....	168



# Table of Tables

TABLE 2-1 – PROPERTIES OF SELECTED ANODE MATERIALS .....	15
TABLE 2-2 – PROPERTIES OF SELECTED CATHODE MATERIALS .....	17
TABLE 2-3 – LIB OPERATING CONDITIONS AND RESULTING DEGRADATION MECHANISMS FOR LIBS.....	23
TABLE 2-4 – OVERVIEW AND COMPARISON OF CYCLE LIFE TESTS IN IEC-62660, ISO-12405, AND DoE BATTERY TEST MANUAL.....	44
TABLE 2-5 – KNOWLEDGE GAP IN EXISTING TESTING PROCEDURES .....	47
TABLE 3-1 – KNOWLEDGE GAPS IN THE EXISTING TESTING FRAMEWORK.....	63
TABLE 3-2 – RESEARCH TASKS COMPLETED WITHIN THIS THESIS.....	66
TABLE 4-1 – COMPARISON OF SELECTED PERFORMANCE CHARACTERISTICS OF DIFFERENT COMMERCIALLY AVAILABLE AND CONCEPT EVs, DATA FROM [94,207–210].....	68
TABLE 4-2 – ESTIMATED MASS SAVING POTENTIALS TO ACHIEVE TARGET VEHICLE MASS .....	69
TABLE 4-3 – VEHICLE MODEL PARAMETERS USED WITHIN THE IPG SOFTWARE .....	72
TABLE 4-4 – RACING-CIRCUIT MODEL OVERVIEW – NOMENCLATURE: TRACK DAY (TD), DEUTSCHE TOURING MASTERS (DTM), FORMULA 3 (F3), FORMULA 1 (F1) ENDURANCE (END.) .....	74
TABLE 4-5 – MODEL PARAMETERS AND EXPLANATIONS FOR THE PARAMETERISATION FOR IPG DRIVER.....	77
TABLE 4-6 – G-G DIAGRAM EXPONENTS DESCRIBING THE SPEED DEPENDENT DRIVER BEHAVIOUR WITH RESPECT TO LONGITUDINAL AND LATERAL ACCELERATION DURING CORNERING.....	77
TABLE 4-7 – RACING CIRCUIT MODEL AND SIMULATION RESULT OVERVIEW.....	84
TABLE 5-1 - RANDOM PULSE CYCLE TARGET PARAMETERS .....	93
TABLE 5-2 - THERMAL SIMULATION RESULTS FOR 20AH POUCH CELLS .....	110
TABLE 6-1 – CELL CHARACTERISTICS.....	117
TABLE 6-2 - TEST RIG COMPONENTS DIMENSIONS.....	121
TABLE 6-3 – TESTING HARDWARE OPERATING RANGES .....	121
TABLE 6-4 – CHARACTERISATION TESTS. TESTS IN BOLD CONSTITUTE PARTIAL CHARACTERISATION TESTS DURING DUTY CYCLE DEGRADATION STUDY. ....	122
TABLE 6-5 - TEST PROGRAM FOR SHORT TERM CYCLING STUDY, * INDICATES OCCURRENCES WHERE HARDWARE MALFUNCTIONS WERE ENCOUNTERED .....	130
TABLE 6-6 – LIST OF BITRODE MALFUNCTIONS DURING LONG TERM TESTING FOR THE HP-MSC TEST GROUP. ....	132
TABLE 7-1 – ENERGY CAPACITY TEST RESULTS FROM INITIAL CHARACTERISATION TESTS.....	136
TABLE 7-2 – MEAN AND STANDARD DEVIATION OF THE ESTIMATED ECM PARAMETERS FOR THE DC INTERNAL RESISTANCE AND CHARGE TRANSFER PHENOMENA FROM SIX G-NMC 53AH CELLS.....	141
TABLE 7-3 – MEAN DURATION OF THE DISCHARGE FOR EACH DUTY CYCLE, MEAN ENERGY THROUGHPUT AND THE ASSOCIATED STANDARD DEVIATION FOR EACH MEASURE FOR THE SET OF CELLS.....	148
TABLE 7-4 – MEAN PEAK TEMPERATURES OF THE HOTSPOT, COLDSPOT, AND GRADIENTS FOR THE SET OF CELLS. ....	150

---

TABLE 7-5 - CHARGE AND DISCHARGE CAPACITY FOR THE HP-MSC AND IECC TEST GROUPS .....	154
TABLE 7-6 – PERCENTAGE CHANGE FOR MEAN VALUES OF PMC-ECM PARAMETERS FROM INITIAL TO FINAL CHARACTERISATION. ....	160
TABLE 7-7 - PERCENTAGE CHANGE OF MEAN VALUES OF EIS-ECM PARAMETERS FROM INITIAL TO FINAL CHARACTERISATION .....	163
TABLE 8-1 – KNOWLEDGE GAPS IN THE EXISTING FRAMEWORK FOR LIB PERFORMANCE AND DEGRADATION TESTING; <input checked="" type="checkbox"/> - ADDRESSED, <input checked="" type="checkbox"/> - NOT ADDRESSED, <input type="checkbox"/> - INCONCLUSIVE .....	169

# Acknowledgements

---

I would like to extend thanks to all the people whose contributions have made these past four years the adventure it was. First and foremost, I would like to express sincere gratitude to Dr James Marco and Dr Dhammika Widanalage for their great support, guidance, excellent technical knowledge, and encouragement when things did not go to plan. I could not have wished for better supervisors. I would also like to thank Paul Haney and Nigel Taylor from Jaguar Land Rover, and Nick Carpenter from Delta Motorsport for their industrial supervision and mentorship.

I would like to thank Dr Anup Barai, Dr Gael Chouchelamane, Dr Limhi Somerville and Ronny Genieser for invigorating discussions and the guidance and support they provided for writing journal and conference publications. I express my thanks to Daniel Worwood and Dr Elham Hosseinzadeh for collaborative research. I would also like to thank John Palmer for his expert knowledge during testing, especially when hardware faults occurred. Further thanks go to Dr Yue Gao, who ensured I had a test chamber available for the duration of my experiments, and Jason Page for valuable feedback on my work. I would like to thank everyone else I have had the pleasure and opportunity to work with within the Energy Storage Group at WMG, and at Jaguar Land Rover.

I would like to acknowledge that the research presented within this thesis is supported by the Engineering and Physical Science Research Council through the award EPSRC- EP/M507593/1. The research was undertaken in collaboration with the WMG Centre High Value Manufacturing Catapult (funded by Innovate UK) in collaboration with Jaguar Land Rover and Delta Motorsport.

I thank all my wonderful friends, especially Markus Dittmann and Murray Mitchell for good banter, plenty of laughter, and many climbing and hiking adventures in the mountains.

Finally, I would like to express my deepest gratefulness to my family. To my mother Petra Kellner and father Dr Maximilian Kellner, thank you for always supporting me and encouraging me to follow my dreams. You are the best parents anyone can wish for. To my sister Dr Maximiliane Kellner, thank you for your encouragement and for always knowing when I need a pick-me-up. To my fiancée Dr Rachel Reed, thank you for your never-ending support, patience, and love. I could not have done this without you!

## Declaration

---

This thesis is submitted to the University of Warwick in support of my application for the degree of Doctor of Philosophy in Engineering. It has been composed by myself and has not been submitted in any previous application for any degree. The work presented was carried out by myself except where otherwise stated.

Signed:

Date:

Quirin Kellner

## List of Publications

---

### Journal Publications

First author:

**Q. Kellner**, E. Hosseinzadeh, G. Chouchelamane, W.D. Widanage, J. Marco, “Battery cycle life test development for high-performance electric vehicle applications”, *Journal of Energy Storage*. 15 (2018): p. 228–244. [1]

**Q. Kellner**, D. Worwood, A. Barai, W.D. Widanage, J. Marco, “Duty-cycle characterisation of large-format automotive lithium ion pouch cells for high performance vehicle applications”, *Journal of Energy Storage*. 19 (2018): p.170–184. [2]

Co-author:

D. Worwood, **Q. Kellner**, M. Wojtala, W.D. Widanage, R. McGlen, D. Greenwood, J. Marco, A new approach to the internal thermal management of cylindrical battery cells for automotive applications, *J. Power Sources*. 346 (2017) 151–166. [3]

### Conference Proceedings

First author:

**Q. Kellner**, W. Dhammika Widanage, J. Marco, “Battery power requirements in high-performance electric vehicles”, 2016 IEEE Transportation Electrification Conference and Expo, IEEE, Dearborn, MI, USA. [4]

**Q. Kellner**, D. Worwood, W.D. Widanage, J. Marco, “Electrical and thermal behavior of pouch-format lithium ion battery cells under high-performance and standard automotive duty-cycles”, 2017 IEEE Vehicle Power and Propulsion Conference, IEEE, Belfort, France. [5]

Co-author:

D. Worwood, E. Hosseinzadeh, **Q. Kellner**, J. Marco, D. Greenwood, W. McGlen, R., W. Dhammika, A. Barai, P.A. Jennings, “Thermal analysis of a lithium-ion pouch cell under aggressive automotive duty cycles with minimal cooling”, *IET Hybrid Electr. Veh. Conf.* (2016) 2–3. [6]

D. Worwood, **Q. Kellner**, E. Hosseinzadeh, D. Mullen, D. Greenwood, J. Marco, R. McGlen, K. Lynn, Thermal Analysis of Fin Cooling Large Format Automotive Lithium-Ion Pouch Cells, 2017 IEEE Vehicle Power and Propulsion Conference, IEEE, Belfort, France.[7]

---

# Abstract

---

High performance (HP) battery electric vehicle (BEV) and racing applications represent significantly different use cases than those associated with conventional consumer vehicles and road driving. The differences between HP-BEV use cases and the duty cycles embodied within established lithium ion battery cell (LIB) test standards will lead to unrepresentative estimates for battery life and performance within HP-BEV applications. Furthermore, the behaviour of LIBs in these applications is not well understood due to a lack of suitable testing cycles and experimental data. The research presented within this thesis addresses this knowledge gap through the definition and implementation of a new framework for LIB performance and degradation testing.

The new framework encompasses the definition of a methodology through which a suitable duty cycle may be derived, and subsequent definition of the experimental procedures required to conduct LIB performance and degradation testing. To underpin the development of a suitable duty cycle, a method is presented to simulate race circuits, a HP-BEV and a driver model to generate a database that defines a range of HP duty cycles that are deemed representative of the real-world use of a HP-BEV. Subsequently, two methods to design a HP duty cycle are evaluated and validated. One of the methods studied (HP Random Pulse Cycle) extends an established driving-cycle construction technique, based on the derivation of micro-trips. The second method (HP Multisine Cycle) utilises a time-frequency domain-swapping algorithm to develop a duty cycle with a target amplitude spectrum and histogram. The design criteria for both construction techniques are carefully selected based on their potential impact on battery degradation. The new HP duty cycles provide a more representative duty cycle compared to a traditional battery test standard and facilitate experimental work, which will more accurately describe the performance and degradation rate of cells within HP-BEV use.

Utilising the newly developed HP-Multisine Cycle, an experimental procedure for LIB performance and degradation testing is presented. Six lithium ion cells are characterised, followed by a performance and degradation study. The performance study investigates the thermal behaviour of the cells when subjected to HP-BEV scenarios and a standard testing cycle (IECC). Results show an increase in excess of 200% in surface temperature gradients for the HP use case compared to the standard testing cycle. The degradation study compares the degradation progression between the HP-BEV environment and conventional testing standards. Two test groups of cells are subject to an experimental evaluation using the HP Multisine Cycle and the IECC. After 200 cycles, both test groups display, counter to expectations, an increased energy capacity, increased pure Ohmic resistance, lower charge transfer resistance and an extended OCV operating window. The changes are more pronounced for the cells subjected to the HP Multisine Cycle. It is hypothesised that the 'improved' changes in cell characteristics are caused by cracking of the electrode material caused by high electrical current pulses. With continued cycling, the cells cycled with the HP Multisine Cycle are expected to show degradation at an increased rate.

The results from the experimental studies provide new insights into the thermal management requirements and evolution of cell characteristics during use within HP-BEVs, and highlight the limitations in the understanding of the complex cell degradation in this area. The new framework addresses the lack of suitable testing cycles and experimental investigations for the HP-BEV environment. The methodologies presented are not limited to the automotive sector but may be used in all areas, where existing testing standards are unrepresentative of the typical usage profile, and LIB degradation and performance are a concern.

# Abbreviations

Abbreviation	Meaning
AI	Artificial Intelligence
AWD	All Wheel Drive
BCU	Battery Control Unit
BEV	Battery Electric Vehicle
BMS	Battery Management System
BOL	Beginning of Life
BTMS	Battery Thermal Management System
CC-CV	Constant Current – Constant Voltage Schedule
CDF	Cumulative Distribution Function
C-rate	Current Rate
DOD	Depth of Discharge
DOE	Department of Energy
DST	Dynamic Stress Test
DTM	Deutsche Touring masters
eCDF	Empirical Cumulative distribution function
ECM	Equivalent Circuit Model
EIS	Electrochemical Impedance Spectroscopy
EM	Electric Machine
End.	Endurance
EOL	End of Life
EU	European Union
EV	Electric Vehicle
F1	Formula 1
F3	Formula 3
FFT	Fast Fourier Transform
FTP-75	Federal Testing Procedure
FUDS	Federal Urban Driving Schedule
G	Graphite
HP	High-Performance
HP-BEV	High-Performance Battery Electric Vehicle
HP-MSC	High-Performance Multisine Cycle

HPPC	Hybrid Pulse Power Characterisation
HP-RPC	High-performance random pulse cycle
iCDF	Inverse cumulative distribution function
ICE	Internal combustion engine
JLR	Jaguar Land Rover
KPI	Key performance indicator
LA92	California Unified Cycle
LCO	Lithium Cobalt Oxide ( $LiCoO_2$ )
LFP	Lithium Iron Phosphate ( $LiFePO_4$ )
LIB	Lithium Ion Battery Cell
LMO	Spinel Lithium Manganese Oxide ( $LiMn_2O_4$ )
LTO	Spinel Lithium Titanium Oxide ( $Li_4Ti_5O_{12}$ )
MCU	Motor Control Unit
NEDC	New European Driving Cycle
NL-ECM	Non-Linear Equivalent Circuit Model
NMC	Lithium Nickel Manganese Cobalt Oxide ( $LiNi_xMn_yCo_zO_2$ )
OCV	Open Circuit Potential
OEM	Original Equipment Manufacturer
pHEV	Plug-in Hybrid Electric Vehicle
PMC	Pulse Multisine Characterisation
R&D	Research and Development
RMS	Root Mean Square
RWD	Rear Wheel Drive
SAFD	Speed Acceleration Frequency Distribution
SC03	Supplemental Federal Test Procedure with Air Conditioning
SEI	Solid-Electrolyte-Interphase
SEM	Scanning Electron Microscopy
SOC	State of charge
SUV	Sports Utility Vehicle
TCU	Traction control unit
TD	Track day
XRD	X-ray Diffraction

---



# Nomenclature

Symbol	Meaning	Value/Units
$\Delta G$	Gibbs Free Energy	$\text{kJ} \cdot \text{mol}^{-1}$
$F$	Faraday constant	$96485 \text{ C} \cdot \text{mol}^{-1}$
$U_{cell}^e$	Cell Equilibrium potential /Open circuit potential	$V$
$U_{cathode}^e$	Cathode Equilibrium Potential	$V$
$U_{anode}^e$	Anode Equilibrium Potential	$V$
$U_e^e$	Electrode Equilibrium Potential	$V$
$U_e^0$	Formal Electrode Equilibrium potential	$V$
$R$	Universal gas constant	$8.314 \text{ J} \cdot \text{mol}^{-1} \cdot \text{K}$
$c_0$	Concentration of oxidant	$[-]$
$c_R$	Concentration of reductant	$[-]$
$Q$	Coulombic capacity	$A \cdot h$
$\eta_{IR}$	Potential drop arising from internal resistance	$V$
$\eta_{ct}$	Charge-transfer overpotential	$V$
$\eta_{ct_{electrode}}$	Electrode Charge-transfer overpotential	$V$
$I$	Current	$A$
$R_{bulk}$	Bulk Ohmic Impedance	$\Omega$
$\phi_S$	Potential of the Solid electrode	$V$
$\phi_E$	Potential of the Electrolyte	$V$
$j_{cd}$	Current density	$A \cdot \text{cm}^{-2}$
$j_0$	Exchange current density	$A \cdot \text{cm}^{-2}$
$T$	Temperature	$K$
$\alpha_A$	Anodic exchange coefficient	$[-]$
$\alpha_C$	Cathodic exchange coefficient	$[-]$
$R_{ct_{electrode}}$	Electrode charge transfer resistance	$\Omega$
$C_{dl}$	Double layer capacitance	$F$
$j_{dl}$	Double layer current density	$A \cdot \text{cm}^{-2}$
$\eta_c$	Concentration overpotential	$V$
$C_B$	Concentration of active species in the electrode bulk	$[-]$
$C_E$	Concentration of active species on the electrode surface	$[-]$
$\Psi$	Temperature dependent parameter	$[-]$
$\Psi_{ref}$	Parameter $\Psi$ at the reference temperature	$[-]$

$T_{ref}$	Reference temperature (25 °C)	$K$
$E_{act}^{\Psi}$	Activation energy of parameter $\Psi$	$J.mol^{-1}$
$C$	Current rate	$[-]$
$R_0$	ECM – Bulk Ohmic resistance	$\Omega$
$R_1$	ECM – Charge transfer resistance	$\Omega$
$C_1$	ECM – Double layer capacitance	$F$
$R_2$	ECM – SEI resistance	$\Omega$
$C_2$	ECM – SEI capacitance	$F$
$Z$	Impedance	$\Omega$
$P_{CLT}$	Peak Power	$W$
$S$	Set of states	$[-]$
$Q_{ij}$	Transition probability matrix	$[-]$
$P_{trans}$	Transition probability	$[-]$
$s_n$	State within the set $S$	$[-]$
$p_{ij}$	Probability to change from state $s_i$ to $s_j$	$[-]$
$A_0$	DC component of the Fourier Series	$[-]$
$A_k$	Amplitude at $k^{th}$ harmonic	$[-]$
$\phi_k$	Phase of the $k^{th}$ harmonic	$rad$
$f_s$	Sampling frequency	$Hz$
$k_{rr}$	Tyre rolling resistance coefficient	$[-]$
$\mu_{rr}$	Tyre friction coefficient	$[-]$
$r$	Tyre radius	$m$
$R_{x,x,unbiasse}$	Unbiased auto correlation of signal $x(n)$	$[-]$
$R_{Norm}$	Normalised Unbiased auto correlation of signal $x(n)$	$[-]$
$P_{system}$	System output power	$W$
$\mathbb{P}$	Set of duty pulses	$[-]$
$\mathbb{D}$	Set of discharging pulses	$[-]$
$\mathbb{C}$	Set of charging pulses	$[-]$
$\zeta_{Cycle}$	HP-RPC Assessment Parameter targets	$[-]$
$P_{DC}$	Normalised mean duty cycle discharge power	$[-]$
$P_C$	Normalised mean duty cycle charging power	$[-]$
$P_{net}$	Normalised net duty cycle discharge power	$[-]$
$P_{abs}$	Normalised mean duty cycle absolute power	$[-]$
$\kappa_{DC}$	% of time on discharge	$[-]$
$\kappa_C$	% of time on discharge	$[-]$

---

$\tau_{AvgDC}$	Mean discharge pulse duration	$s$
$\tau_{maxDC}$	Maximum discharge pulse duration	$s$
$\tau_{AvgC}$	Mean charge pulse duration	$s$
$\tau_{maxC}$	Maximum charge pulse duration	$s$
$t_{Cycle}$	Duration of a duty cycle	$s$
$P_{Candidate}$	Candidate Cycle	$[-]$
$\zeta_{Candidate}$	Assessment Parameters for candidate cycles	$[-]$
$\delta_{\zeta}^{Candidate}$	Error between Candidate cycle parameter and HP-RPC target	$[-]$
$\varepsilon_{Candidate}$	Cumulative error from all $\delta_{\zeta}^{Candidate}$	$[-]$
$P_{Norm,zm}$	Zero-mean signal of $P_{Norm}$	$[-]$

---

# 1 Introduction

---

## 1.1 Context

Tailpipe emissions from internal combustion engine (ICE) vehicles have an adverse effect on human health [8] and contribute significantly to the greenhouse gasses responsible for global climate change [9,10]. Consequently, state governments and intergovernmental institutions such as the European Union (EU) have introduced legislation aiming to reduce the overall emissions of road vehicles [11]. Additionally, in 2018 the government of the United Kingdom announced their “Road to Zero” policy, detailing their ambition to end the sale of new conventional powered petrol and diesel cars and vans by 2040, stating that by then all new cars will have “*significant zero-emission capability*” [12]. Electric vehicles (EVs) and battery electric vehicles (BEVs) provide a potential pathway to reduce these emissions. If the power for charging is sourced from renewables, BEVs offer a route toward eliminating all mobile emissions [13].

EVs for the mainstream mass market have been explored over several years. Examples include the Detroit Electric (in production 1907-1939) [14] and the General Motors EV1 (1997-2003). The latter received wide criticism as it was expensive to produce and the batteries lacked the capacity and durability to supply the range demanded by customers [15], [16]. Over the past decade, the improvement of lithium ion batteries (LIBs) has underpinned the electrification of the transport sector [17]. As of 2018, many major automotive original equipment manufacturers (OEMs) offer at least one hybrid electric vehicle (HEV), plug-in hybrid electric vehicle (pHEV) and/or BEV in their product line-up. Examples include the Nissan Leaf, Renault ZOE, Mitsubishi Outlander pHEV, Volkswagen e-Golf and BMW i3 and i8 and Mercedes C-Class pHEV. Although BEVs are reported to have lower cost of ownership compared to ICE vehicles and pHEVs [18], prominent barriers to the commercial success of these vehicles are the high initial vehicle cost, range anxiety [19], safety and reliability [20]. These are functions of key battery characteristics, such as cell cycle life, degradation, energy capacity, power capability, safety, reliability and cost, as well as all system integration requirements, such as packaging and thermal management [21].

With ongoing developments, battery energy capacity and power capability are steadily increasing whilst costs are decreasing [22]. This in turn has opened up the strategically important high-performance (HP) vehicle segment, which has become a target for many new start-up organisations and more established OEMs [23]. Initially pioneered by Tesla Motors with the Tesla Roadster in 2008, currently an increasing number of automotive OEMs are developing BEVs for

this segment. Specific examples include the Jaguar I-PACE, launched in 2018, and the Aston Martin Rapide-E, with customer deliveries planned for Quarter 4 in 2019 [24], in addition to more established vehicles such as the Tesla Model S. A prominent use case for these HP-BEVs are track applications; specifically Formula E [25], which launched in 2014 and is the FIAs first fully electric racing championship, and the Jaguar I-PACE eTrophy [26], a Formula E support racing series.

In order to decide upon the most appropriate battery type and their management strategies for automotive use cases, researchers and industry conduct a wide range of research regarding characterisation, performance and degradation of battery cells [27,28]. One limitation of this research is that often, several studies use relatively simplistic constant current charge and discharge tests, often at different current rates and environmental temperatures as a means to estimate cycle life over a broad spectrum of operating conditions [28–30]. These tests are known to be largely unrepresentative of the day-to-day LIB operation within an EV. Research published by Barre et al. [31] has indicated that complex electrical loading profiles result in different ageing characteristics than conventional galvanostatic profiles.

As such, more complex testing profiles are required to predict the behaviour and cycle ageing progression of cells in HP automotive use cases. A further study by Barre et al. [32] investigated battery system data, which was collected from a passenger EV following a predetermined driving cycle, to determine the causality between vehicle use and battery ageing. This study identified that capacity fade increases at elevated temperatures and over time, is primarily related to temperature and test duration, and impedance rise is primarily related to the current profile and the maximum current delivered by the battery. Omar et al. [33] used the cycle life tests defined within the International Standard IEC 62660-1 [34] and ISO 12405-2 [35] to determine the cycle life of a cell intended for passenger vehicle use. Further, Dubarry et al. utilised a dynamic stress test, described within [36], in a cycle life evaluation to determine the rate of change and nature of battery degradation within passenger vehicles [37,38], providing further evidence that battery degradation is a function of usage profiles.

As such, the testing methodologies employed to evaluate the suitability of LIBs for a given automotive use case should encompass the thermal conditions and electrical loading profiles that the battery cell will experience.

## 1.2 Problem statement

HP-BEV and EV racing applications represent significantly different use cases than those associated with conventional consumer EVs and road driving. Such HP-BEVs are typically driven to the performance limits of the vehicle or the capabilities of the driver. Asus et al. [39,40] conducted extensive tests on a series hybrid racing car to develop a detailed mathematical model of the vehicle that characterised its dynamic behaviour and could underpin drive-cycle prediction. The authors present experimental data, including driver pedal input and system power demands, for the vehicle being driven on the Magny-Cours racing circuit in France. Their analyses highlight significant proportions of time spent at peak demand, in addition to rapid transitions from vehicle acceleration and braking. For a HP-BEV, such a usage profile would translate to extended periods of time when the battery system is under full electrical load for charging or discharging.

By comparing the data presented within [39,40] with that found in studies into urban driving, e.g. [41,42] one of the unique measures of HP driving is not just the high amplitude power demands placed on the vehicle's powertrain, but also the relative time that the vehicle spends at peak-power. In contrast, peak power demand in urban driving is rare, of short duration and interspaced with extended periods of low demand. For HP applications, a complete energy discharge of the battery pack may occur within less than a single hour. Conversely, with a conventional EV it may take many hours or even days to deplete the energy content of the battery pack [43].

These differences between HP-BEV use cases and existing LIB research are likely to influence requirements for battery thermal management and the rate of degradation that may occur within the cells that comprise the HP vehicle battery system. The author asserts that, consequently, existing testing methodologies and their findings are unlikely to capture the performance and degradation of LIBs in HP-BEV applications.

## 1.3 Introduction to the sponsoring companies and motivation for the direction of research

The research presented within this thesis was conducted in collaboration with the two companies Jaguar Land Rover and Delta Motorsport. Jaguar Land Rover (JLR) are the UK's largest premium automobile manufacturer comprising the two brands Jaguar and Land Rover, known for luxury saloon and high-performance sports cars, and premium all-wheel drive vehicles, respectively. JLR are actively involved in research and development (R&D) of powertrains and energy storage [44]. The company is the first European premium manufacturer with a fully electric battery powered

sports utility vehicle (SUV) and aims to become the European brand leader for BEVs. Furthermore, JLR competes within the FIA Formula E racing series, a championship for all electric vehicles. For the 2018/2019 season JLR is also sponsoring the “*I-PACE eTROPHY*”, a support racing series in which 20 Jaguar I-PACE vehicles compete over 10 races [26].

As a manufacturer whose brands are associated with premium and HP vehicles, JLR needs to ensure that their vehicles are competitive and reliable. This requires maximising the vehicle power output, concurrently with component weight reduction, whilst guaranteeing safe operation. Specific examples for LIBs are the design and sizing of the battery pack and battery management system (BMS) and battery thermal management system (BTMS), which account for a large portion of the overall pack weight. Furthermore, warranty issues may be avoided by developing mitigation strategies to address the degradation and failure modes of the battery pack. For these purposes, the company requires extensive knowledge of the thermal performance and degradation behaviour of LIBs.

Delta Motorsport was founded in 2005 with background in HP vehicle engineering and since then has established itself as a consultancy in motorsport, road vehicle, and low carbon vehicle engineering. The company has its office at Silverstone race circuit and offers consultancy services ranging from single component design and development through to complete programmes. Their low carbon projects include amongst others the “E-4”, a high-performance electric vehicle, the “Microcab”, a hydrogen-hybrid vehicle, and a lightweight high power electric motor [45]. Delta Motorsport have been working with JLR as a development and consulting partner for a range of projects with a high-performance focus, an example of which is the battery system of Jaguar C-X75 prototype.

## 1.4 Scope of the Thesis

The scope of this thesis is to investigate the instantaneous performance and long-term degradation of LIBs within HP-BEV and racing applications from an engineering perspective. As such, a non-invasive testing methodology, through which LIB characteristics, performance and degradation can be evaluated, requires definition. Non-invasive in this context refers to testing methods that do not require the disassembly of batteries. This, in turn, demands the evaluation of the fundamentals of LIB operation and degradation, and a review of existing testing methods and determination of their applicability to HP driving and racing applications. Where no suitable methodologies can be found, new testing procedures are defined. Once a testing procedure has been devised, an experimental investigation into the short and long-term behaviour of cells

subject to HP-BEV specific use cases and standardised testing is undertaken on a commercial battery cell. The author asserts that the outcomes of this research will provide a suitable testing methodology to evaluate the performance of LIBs and to identify the onset and progression of degradation specifically encountered within HP applications.

## 1.5 Thesis outline

This thesis is structured as follows. Chapter 2 presents a critical literature review of LIB operation, degradation and current best practice procedures for battery characterisation, performance testing, and degradation testing. The applicability of these methods to HP use cases is examined and a knowledge gap within the existing literature pertaining to degradation and performance testing of LIBs in HP-BEV applications is identified. Chapter 3 critically reviews testing-profile design methodologies to devise an electrical loading profile representative of HP applications. A further knowledge gap regarding a systematic approach to the generation of LIB testing profiles is identified. Subsequently, four distinct research tasks are defined to address these two knowledge gaps. Chapter 4 describes the development of a driving and duty cycle database for track driving applications. Chapter 5 describes a systematic approach to the development of testing profile for LIB performance and degradation testing, that is representative of the database derived in Chapter 4. Chapter 6 details the experimental work conducted to perform characterisation, performance and degradation testing to investigating the short and long-term performance of a commercial LIB pouch cell. Chapter 7 presents and discusses the results from the experiments, and offers a hypothesis to explain the findings. Chapter 8 provides conclusions of this thesis and recommendations for future work.



## 2 A Review of Lithium ion battery cells and testing methodologies

---

### 2.1 Introduction

HP-BEV applications such as racing represent significantly different use cases than those associated with standard consumer BEVs. It is believed that this will influence the performance and degradation of LIBs employed within the energy storage systems of the vehicles. The operation, performance and degradation of LIBs is dependent on several intrinsic factors such as the battery's cell chemistry, manufacturing processes and form factor [46], and extrinsic factors such as environmental conditions and operational parameters [47]. Furthermore, battery degradation is difficult to forecast as the dominating mechanisms and resulting impedance augmentation and capacity fade are heavily influenced by the operating conditions and electrical [48], mechanical [49] and thermal [50] loading profiles. To better understand the relationship between these parameters and battery degradation, researchers have developed extensive test methodologies to investigate the degradation related to storage [51–56] and operation [30,54,55]. Consequently, this leads to a key research question:

#### 2.1.1 Research Question 1: Do existing LIB testing methodologies adequately represent HP-BEV racing applications?

To answer this question, it is first necessary to understand the operational principles and degradation mechanisms of LIBs as well as the influence of external factors and operational parameters. Further, through a critical review of the existing body of literature regarding LIB testing methodologies, it can be determined whether these procedures adequately capture those operating conditions likely to be encountered during HP-BEV use.

As such, sections 2.2 and 2.3 describe the basic components of LIBs, and their operational principles. Section 2.4 reviews the different degradation mechanisms, and identifies those environmental conditions and operating parameters, which affect LIB degradation most.

Sections 2.5 – 2.7 provide a critical review of testing methodologies to assess the operation and degradation in LIBs. These are characterisation testing (section 2.5), degradation testing (section 2.6), and performance testing (section 2.7). Characterisation testing enables the identification of

key cell attributes, which often underpin the parameterisation of electrical and thermal models. Furthermore, regular characterisation throughout a battery cell's useful life allows for the identification and tracking of degradation. Degradation testing or ageing are umbrella terms for tests intended to investigate the causes and progression of LIB degradation. Degradation testing can often be categorised into mechanical testing, storage testing, and cycling degradation testing. Cycle testing is conducted by subjecting cells to galvanostatic profiles or transient duty cycles over time.

Performance testing within this work describes cycling testing with the aim to determine the instantaneous behaviour of cells. This primarily comprises electrical loading of cells under galvanostatic and transient duty cycles. Outcomes of these tests include the determination of cell self-heating during electrical loading, useful energy capacity in realistic operation, and datasets underpinning the validation of electrical and thermal models derived from characterisation testing. As such, overlaps exist between characterisation testing, performance testing, and degradation testing.

To provide a standardised set of methodologies for charge and discharge, performance, reliability, abusive, and cycle life testing within the automotive context, a number of international testing standards and guidelines have been conceptualised. Each standard, parts of which are reviewed within this chapter, addresses different requirements for performance, robustness and safety and how testing should be undertaken at either a cell (i.e. IEC 62660-1 [34]), module (i.e. ISO 12405-2 [35]) or system level (i.e. Department of Energy (DoE) battery test manual for electric vehicles [36]).

Following this review, key findings are summarised in section 2.8, and a knowledge gap is identified.

## 2.2 Basic components and operational principles

A schematic diagram of a commercial LIB under discharge is shown in Figure 2-1. The principal components of a LIB are two electrodes, an electrolyte, current collectors, and a separator. For a cell under discharge, the negative and positive electrodes are referred to as anode and cathode, respectively. For simplicity and consistency, in this work, anode always refers to the negative electrode under discharge. In modern LIBs, the active electrode materials in powder form are mixed with binders and additives and attached to metal current collectors, and saturated with electrolyte to create porous electrodes.

For many commercially available LIBs, the anode active material is carbon based ( $Li_xC$ ), and the cathode active material is a metal oxide ( $Li_{1-x}MO_2$ ), where the M represents a transition metal. The active materials are discussed in more detail in section 2.3. The electrolyte enables ion transfer between the electrodes and is often a non-aqueous liquid or gel containing a lithium salt such as  $LiPF_6$  [57],  $LiClO_4$  or  $LiAsF_6$  [58], acting as the ion conducting medium. The current collectors serve as terminals for the electrodes and are not actively involved in the chemical redox-reactions under operation. For anodes, the material of choice is copper, for cathodes, the current collector is usually an aluminium alloy. The separator provides a physical barrier between the anode and the cathode to prevent internal short circuits. As such, the material needs to be electrically insulating and block the flow of electrons. For ion transfer between the electrodes to occur, the separator requires a porous structure. The material of choice for this is usually a microporous polyethylene or polypropylene film [59–61].

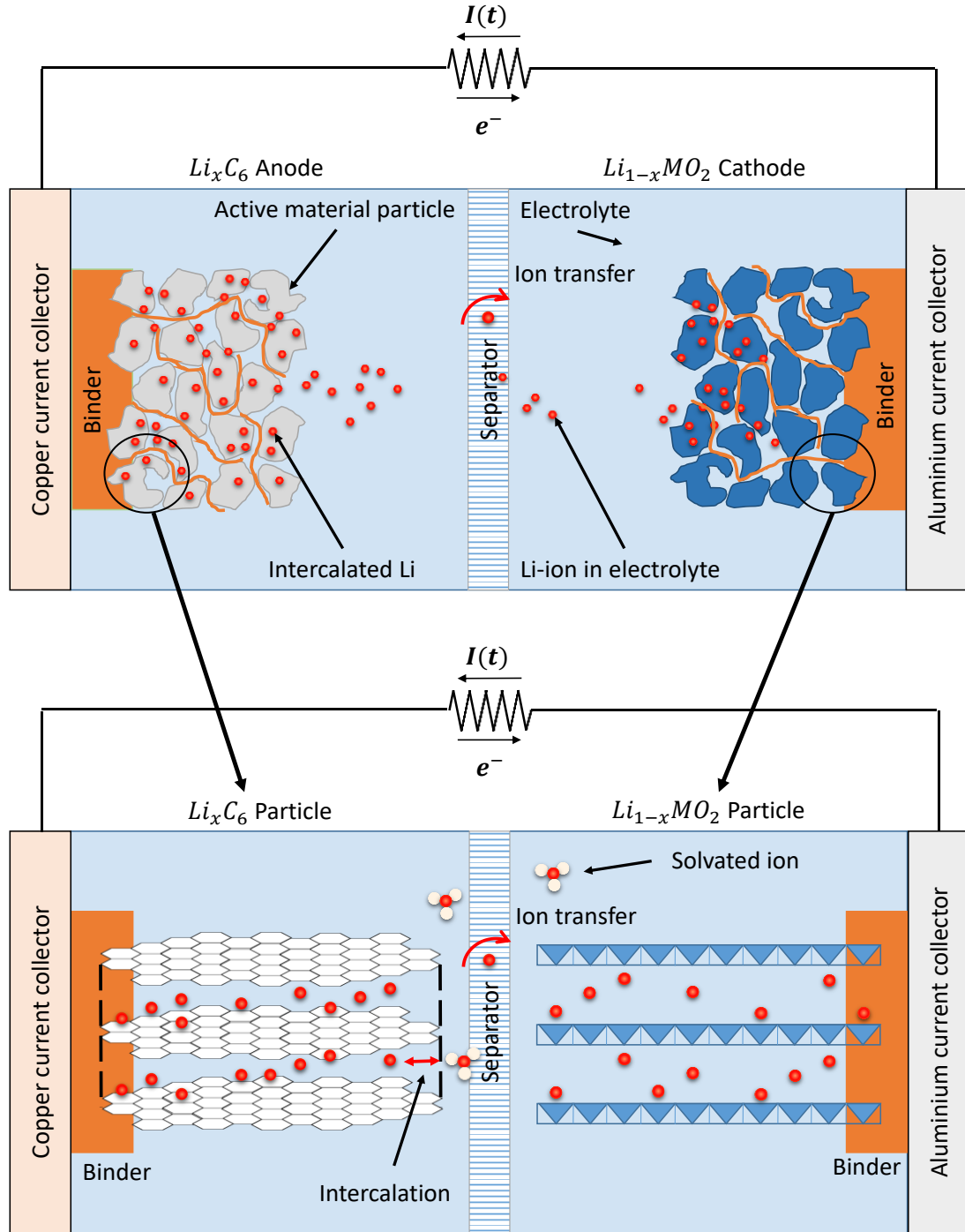
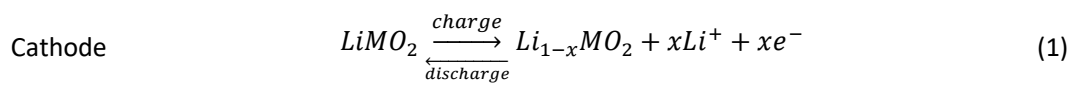
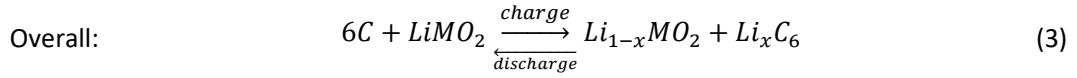
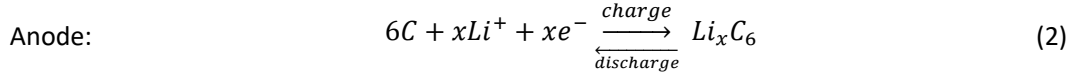


FIGURE 2-1 - SCHEMATIC DRAWING OF A LI-ION BATTERY CELL

Using the example illustrated in Figure 2-1 the chemical equations for the charge/discharge cycles can be written as [62,63]:





During discharge, lithium stored in metal form in the anode, gives up an electron and becomes a lithium ion. The electron travels through the external circuit which results in an electrical current in the opposite direction to electron flow. As current is defined as the rate of charge flow, the current which can be supplied by the cell is dependent on the rate at which the redox reactions can occur. For every electron travelling through the external circuit, an ion needs to transfer from the anode to the cathode to maintain charge balance. The lithium ions de-intercalate from the anode, travel through the electrolyte and separator, and intercalate into the cathode, accepting an electron.

### 2.2.1 Open circuit potential and capacity

The electrode reactions (1) and (2) are accompanied by either a release or absorption of energy. The energy change for the reaction is the change in Gibbs free energy ( $\Delta G$ ) as described in equation (4), where  $n$  is the number of moles of electrons transferred in the reaction,  $F$  is the Faraday constant ( $9.649 \times 10^4 \text{ C mol}^{-1}$ ), and  $U_{cell}^e$  is the cell potential required for the reaction.

$$\Delta G = -nFU_{cell}^e \quad (4)$$

In the absence of a current, each of the two electrodes are at equilibrium, i.e. for each electrode, the backward and forward reactions occur at the same rate. In this case, the open circuit potential (OCV,  $U_{cell}^e$ ) of the cell can be measured and is defined as the difference between the cathode equilibrium potential ( $U_{cathode}^e$ ) and the anode equilibrium potential ( $U_{anode}^e$ ), as described in equation (5).

$$U_{cell}^e = U_{cathode}^e - U_{anode}^e \quad (5)$$

In this case, the equilibrium potential for individual electrodes ( $U_e^e$ ) against lithium ions in the solution can be measured using a reference electrode and potentiostat, and calculated from the Nernst equation shown (6).

$$U_e^e = U_e^0 + \frac{2.3RT}{nF} \log\left(\frac{c_O}{c_R}\right) \quad (6)$$

$U_e^0$  is the formal equilibrium potential,  $R$  is the universal gas constant ( $8.314 \text{ J K}^{-1} \text{ mol}^{-1}$ ),  $T$  is the absolute temperature in Kelvin, and  $c_O$  and  $c_R$  are the concentrations of oxidant and reductant, respectively [64]. As such, the open circuit potential is dependent on the concentration of reactive species at the chemical reaction sites on the surface of the electrode.

The coulombic capacity of a cell ( $Q$ ), measured in Ah, is a representation of the total amount of charge which can be stored within, or be extracted from a cell. This depends on the amount of lithium ions, which can transfer between anode and cathode, also referred to as cyclable lithium. This relates to the amount of active material used in the electrodes. When all cyclable lithium is present within the anode, the state of charge (SOC) of the cell is at 100%. Similarly, when no cyclable lithium, which is the amount of lithium inventory that can shuttle between electrodes, is present within the anode, the state of charge of the cell is 0%. A change in cyclable lithium in the electrodes is synonymous with a change in concentration at the electrodes and as such, the OCV of a cell changes with SOC.

### 2.2.2 Operating potential

When a discharge current is flowing, the operating potential of a cell is smaller than the OCV due to internal impedance losses and polarisation owing to the electrochemical and physical properties of the cell. Polarisation refers to the deviation of the electrode potential from its equilibrium values. The relationship between these potential drops and the discharge current is illustrated in Figure 2-2.

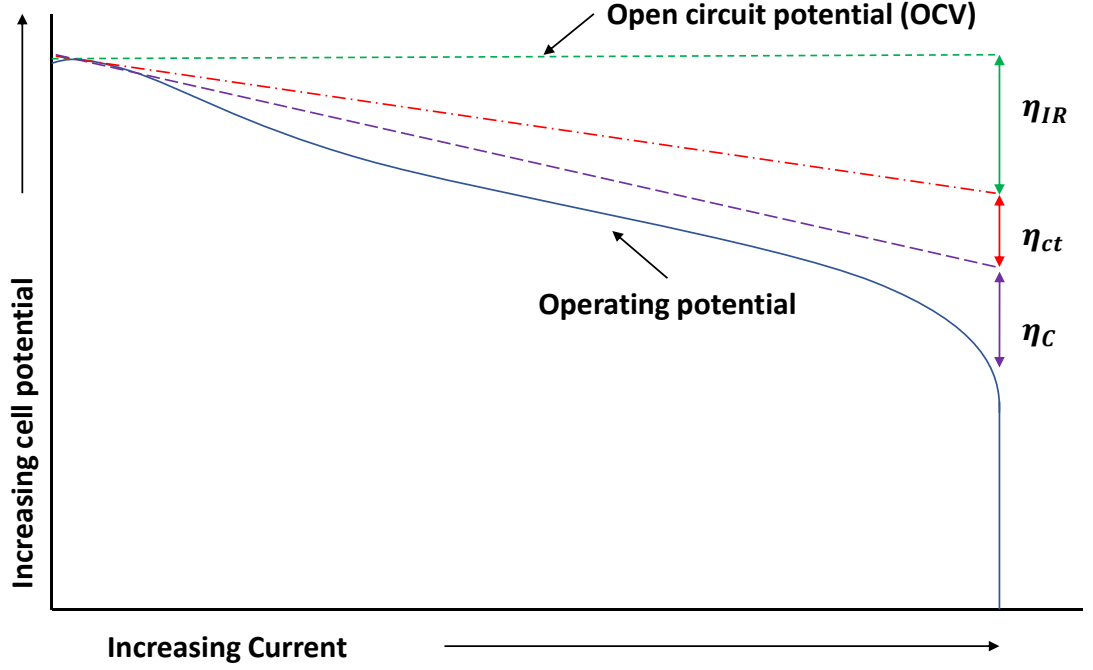


FIGURE 2-2 – CELL POLARISATION, AND SOURCES OF POTENTIAL DROPS ADAPTED FROM [65]

The potential drop  $\eta_{IR}$  is caused by the impedance in the bulk materials such as the electrode materials, electrolyte and current collectors, as illustrated in equation (7) where  $R_{bulk}$  is the Ohmic impedance of the cell bulk materials.

$$\eta_{IR} = IR_{bulk} \quad (7)$$

The second potential drop,  $\eta_{ct}$ , is related to the charge transfer resistance in the cell. For a net charge transfer to occur at an individual electrode and current to flow, an overpotential ( $\eta_{ct_{electrode}}$ ), defined in equation (8) must be overcome, where  $\phi_S$  is the potential of the solid electrode and  $\phi_E$  is the potential of the electrolyte.

$$\eta_{ct_{electrode}} = \phi_S - \phi_E - U_e^e \quad (8)$$

The overpotential relates to the current density ( $j_{cd}$ ) through the Butler-Volmer equation (9), where  $j_0$  is the exchange current density at equilibrium,  $T$  is the temperature,  $\alpha_A$  and  $\alpha_C$  are the anodic and cathodic exchange coefficients, relating to the rate of forward and backward reactions at the electrode surface and  $\alpha_A + \alpha_C = m$ , where  $m$  is the number of electrons involved in the reaction [66].

$$j_{cd} = j_0 \left[ \exp\left(\frac{\alpha_A n F \eta}{RT}\right) - \exp\left(-\frac{\alpha_C n F \eta}{RT}\right) \right] \quad (9)$$

At small values of  $j_{cd}$ , the overpotential and current density follow a linear relationship with regards to the charge transfer resistance ( $R_{ct_{electrode}}$ ) as shown in equation (10).

$$\eta_{ct_{electrode}} = j * R_{ct_{electrode}} \quad (10)$$

For larger values of  $j_{cd}$ , the relationship between overpotential and current density behaves in a non-linear manner. If  $j_{cd}$  is sufficiently large, the overpotential  $\eta$  is proportional to the log of the current and the Butler-Volmer equation simplifies to equation (11), where  $\alpha$  is the exchange coefficient.

$$j_{cd} = j_0 \exp\left(\frac{\alpha n F \eta}{RT}\right) \quad (11)$$

The change in potential at the electrode causes the surface of the electrode to take up a charge, attracting oppositely charged ions in the electrolyte to the electrode surface. This results in an electrical double layer providing capacitance ( $C_{dl}$ ). This double layer capacitance acts in parallel to the Butler-Volmer equation producing a current ( $j_{dl}$ ) as described in equation (12)[66].

$$j_{dl} = C_{dl} * \frac{d\eta}{dt} \quad (12)$$

Finally, the potential drop  $\eta_c$  is caused by concentration differences of active species at the reaction sites, and in the bulk material. As reactions occur, reactants are used resulting in localised concentration changes in electroactive species. The concentration polarisation is defined in equation (13), where  $C_B$  is the concentration of active species in the bulk, and  $C_E$  is the concentration of species at the electrode surface.

$$\eta_c = \frac{2.3RT}{nF} \log \frac{C_B}{C_E} \quad (13)$$

The active materials in LIBs are contained in porous electrodes, giving a larger interfacial area for chemical reactions. The effect of this is a reduction in charge transfer and concentration



polarisation. The interfacial area between electrolyte and electrode material depends on electrode porosity, particle size, and surface area per volume.

The overall polarisation increases with increasing current. On a full cell, this results in self-heating and irreversible heat losses following an  $I^2R$  relationship. As HP-BEV applications are likely to experience increased current compared to on-road driving, this will influence the magnitude of current density, and therefore the polarisation within the cell. Furthermore, these higher currents will tend to cause increased cell heating.

### 2.2.3 Temperature dependency

Many of the Li-ion battery cell's characteristics are largely influenced by temperature. The rate of chemical reactions within the cell increases with an increase of temperature and decreases with a decrease in temperature. Furthermore, mass transport kinetics such as diffusion rates increase with an increase in temperature and decrease with a decrease in temperature. As such, cells display higher capacity and power capability at increased temperature, and lower capacity and power capability at low temperature. This dependency is often described through an Arrhenius type relationship as described in equation(14), where  $\Psi_{ref}$  is the property value at the defined reference temperature ( $T_{ref} = 25\text{ }^\circ\text{C}$ ), and  $E_{act}^\Psi$  is the activation energy for the process.

$$\Psi = \Psi_{ref} \exp \left[ \frac{E_{act}^\Psi}{R} \left( \frac{1}{T_{ref}} - \frac{1}{T} \right) \right] \quad (14)$$

## 2.3 Electrode materials

The choice of active material dictates the open circuit potential and maximum specific power and energy, which a cell can deliver. Ideally, anode and cathode materials are chosen to deliver high specific charge capacity (measured in Ah/kg) and high charge density (measured in Ah/l) to optimise the weight and volume of a battery cell. Anodes should have a low potential, and cathodes have a high potential versus Lithium, respectively, to maximise the open circuit potential of the full cell. The de/intercalation process of lithium should always occur in a reversible manner without structural changes to the electrode, and the materials should operate within the electrochemical stability window of electrolyte components to prevent increased degradation. Furthermore, materials should be chemically stable at elevated temperatures. The

choice of anode and cathode combinations is a trade-off of reliability, safety and energy and power capability of the cell, examples of which are given below.

### 2.3.1 Anode materials

The characteristics of selected anode materials are listed in Table 2-1. For a more complete overview of anode materials, the author recommends the research presented within [67,68].

Anode Material	Potential vs Li	Charge Capacity	Ref
Lithium	0 V	3861 Ah/kg	[69]
Carbon	0.07-0.3 V	372 Ah/kg	[68,70–72]
$Li_4Ti_5O_{12}$	1.55 V	175 Ah/kg	[67,68,73,74]
Silicon	0.4 V	3500-4200 Ah/kg	[67,75]

TABLE 2-1 – PROPERTIES OF SELECTED ANODE MATERIALS

The first LIBs contained metallic lithium as their anode material. Under charging, metallic lithium is susceptible to dendritic growth posing a safety concern due to potential internal short-circuits and catastrophic failure, which makes this material unviable for commercial automotive applications. Modern commercial LIBs favour carbon based anodes, due to low cost, abundance, non-toxicity, and electrochemical properties of the material [46,47,76,77]. Graphite (G) is used commonly in batteries. It can achieve a high specific capacity of lithium concentration for carbon anodes, and in its lithiated state, i.e. charged to its maximum capacity, has a low potential close to 0 V versus lithium metal [68,70,71]. During ion de/intercalation, as illustrated in Figure 2-1, lithium diffuses between graphene layers. During this process the material undergoes only small volume changes below 10% during [47,71], which is desirable as it reduces the risk of structural damage to the electrode during dis/charging processes.

Carbon anodes operate outside the electrochemical stability window of common non-aqueous electrolytes within LIBs. At contact points between electrolyte and electrode the electrolyte decomposes at a potential of 0.8 V vs Li metal [61] resulting in the formation of a passivating layer on the surface contact region between the electrolyte and the solid electrode [78], irreversibly locking cyclable lithium within the layer. This solid-electrolyte interphase (SEI) layer [47,78–80], illustrated in Figure 2-3, is ionically conductive but blocks further contact between the electrolyte and the electrode, slowing down future side reactions. Over time, this SEI continues to grow and manifests as a degradation mechanism of the battery cell. The degradation of LIBs is discussed in more detail later.

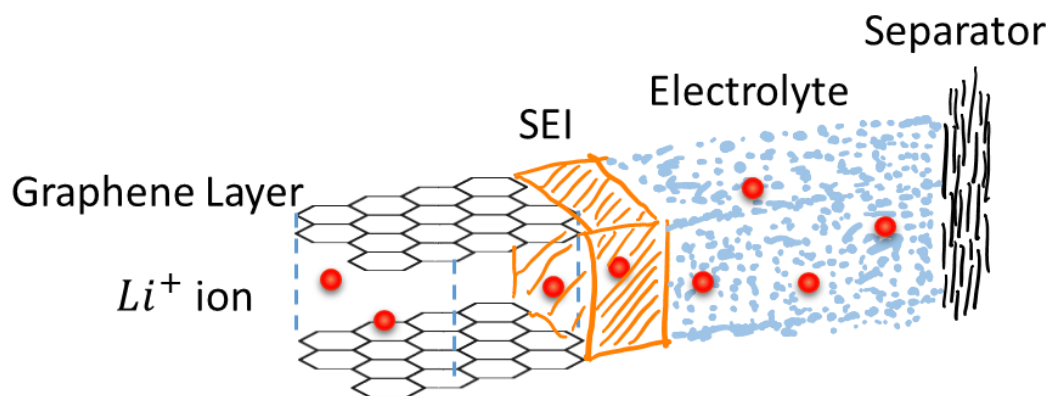


FIGURE 2-3 - SCHEMATIC DRAWING OF THE SEI LAYER

Two other anode materials of interest are silicon based anodes and spinel Lithium Titanium Oxide (LTO –  $Li_4Ti_5O_{12}$ ). Although silicon anodes offer a 10 times higher capacity than carbon anodes they are currently not used in automotive applications due to their low maturity and very limited cycle life which results from a 270% expansion/contraction during charge and discharge [68].

Similarly to carbon LTO is also non-toxic [81]. The potential of LTO vs lithium metal is higher than that of graphite at 1.55 V [82], and as such operates within the stability window of most electrolytes, preventing the formation of an SEI film. Furthermore, LTO is not susceptible to lithium dendrite growth [68], undergoes negligible volume changes during lithium de/intercalation [68,73,83], has lower heat generation than carbon anodes during operation [84], and a higher onset temperature for thermal runaway [85], making it a safer choice than graphite. However, the specific capacity and charge density of LTO is much lower than that of graphite. The high operating potential vs lithium metal also means that when paired with common cathode materials, the resulting cell operates at lower voltages around 2 V, making it less favourable for automotive applications.

### 2.3.2 Cathode Materials

Cathodes are the limiting of the two electrodes in terms of capacity. The cathode material used in commercial LIBs are predominantly metal oxides. An exception to this is Lithium Iron Phosphate (LFP ( $LiFePO_4$ )). Table 2-2 provides information on the characteristics of selected cathode materials found in commercial LIBs. For a more detailed review on cathode materials the author recommends the literature [68,86,87].

Cathode Material	Potential vs Li	Charge Capacity	Ref
$LiCoO_2$	3.7 - 4.2 V	140 - 150 Ah/kg	[61,88]
$LiNi_xCo_yMn_zO_2$	3.7 - 4.2 V	150-230 Ah/kg	[68,89]
$LiMn_2O_4$	4.1 V	120 Ah/kg	[89]
$LiFePO_4$	3.4 V	170 Ah/kg	[68,87]

TABLE 2-2 – PROPERTIES OF SELECTED CATHODE MATERIALS

Early commercial LIBs contained Lithium Cobalt Oxide – LCO ( $LiCoO_2$ ) electrodes. The material has a layered structure, allowing intercalation of lithium ions in between planes as illustrated in Figure 2-1. LCO in commercial cells has a voltage of 4.2V with respect to lithium metal corresponding to the cycling of 0.5  $Li^+$  ions per  $LiCoO_2$  and a useful capacity of 140-150 Ah/kg. Modern commercial batteries still contain Cobalt but the material bears several disadvantages over newer alternative electrode materials, being harmful to the environment, and relatively scarce and expensive. Furthermore, instability at high temperatures and proneness to thermal runaway at overcharge [79,88] make it less favourable for vehicle applications.

Another layered oxide material is Lithium Nickel-Manganese-Cobalt Oxide – NMC ( $LiNi_xCo_yMn_zO_2$ , where  $x + y + z = 1$ ). It is much cheaper and less toxic than LCO due to the reduced cobalt content, and safer in operation and storage [90]. The exact properties of the electrode material depend on the composition [91]. The achievable specific charge capacity of NMC mentioned in literature ranges between 140-230 Ah/kg, giving it a big advantage over LCO in terms of energy capacity. A further significant advantage over LCO cells is the higher power capability, making a preferred candidate for automotive use. The material in various compositions is used in several commercially available EVs [58], and was used within the batteries of Formula E racing vehicles [92] during sessions in years 2014 – 2018.

Lithium Manganese Oxide – LMO ( $LiMn_2O_4$ ) is an alternative to layered oxide. Its spinel structure is a different atomic structure to NMC and LCO cathodes. It is used in automotive applications as the main cathode for the cells comprising the battery system within the Nissan Leaf [87]. The material is relatively cheap compared to LCO, and has a better thermal safety behaviour than LCO with a higher thermal runaway temperature [86]. The voltages the cells can produce are similar those of LCO and NMC. However, the material has a lower charge capacity, and is outperformed by NMC by a factor of 2, making it less attractive for some automotive applications.

Unlike the other cathode materials, LFP is not a transition metal oxide but an iron phosphate with an olivine structure. Like LMO, the material is also non-toxic and cheaper than LCO [79], and

thermally more stable than LCO and NMC [93]. Compared to the cathode materials discussed above, LFP has a lower potential against lithium [86], and compared to NMC in particular a lower charge capacity [93], putting the material at a disadvantage for automotive use cases. Nevertheless, LFP is a popular candidate for high power applications and vehicles such as the Rimac Concept One [94], due to its high power capability and thermal stability [93].

Cells subjected to HP-BEV applications, as identified in Chapter 1, are likely exposed to high C-rates and thus more thermal loading. As such, cells intended for this use should have high rate capability and thermal stability. Furthermore, a key factor for racing applications is weight. As such, the selected cells should have a high specific capacity. Based on the existing literature, G-NMC and G-LFP cells appear suitable candidates for this application, where G represents the graphite anode.

## 2.4 LIB Degradation mechanisms

Over time, LIBs display a reduction of the useful energy capacity, and impedance augmentation. For EVs, these changes within the cell manifest themselves in a reduction of driving range and power capability for acceleration. This process, which is referred to as battery degradation, is coupled to structural and chemical changes within the cell called degradation mechanisms. Degradation within LIBs occurs at all times including resting conditions and can be further caused by fatigue during cell operation during charging and discharging, by mechanical stresses such as vibrations and shock impacts occurs over time, and by certain environmental conditions such as high temperatures.

Although the specifics of battery degradation such as rate and pathway are highly dependent on the choice of battery cell chemistry and format, the degradation is similar for a variety of chemistries of LIBs [47]. The most common degradation mechanisms for commercial LIBs, which are based on a carbon anode and a lithium-transition metal cathode, are illustrated within Figure 2-4 and described below. The overall degradation mechanisms can be broadly grouped into surface film effects, including SEI growth and lithium plating, structural changes to the bulk materials, mechanical changes, and parasitic side reactions [95]. The degradation of a battery cell is complex as all degradation mechanisms are interlinked and no mechanism occurs in isolation.

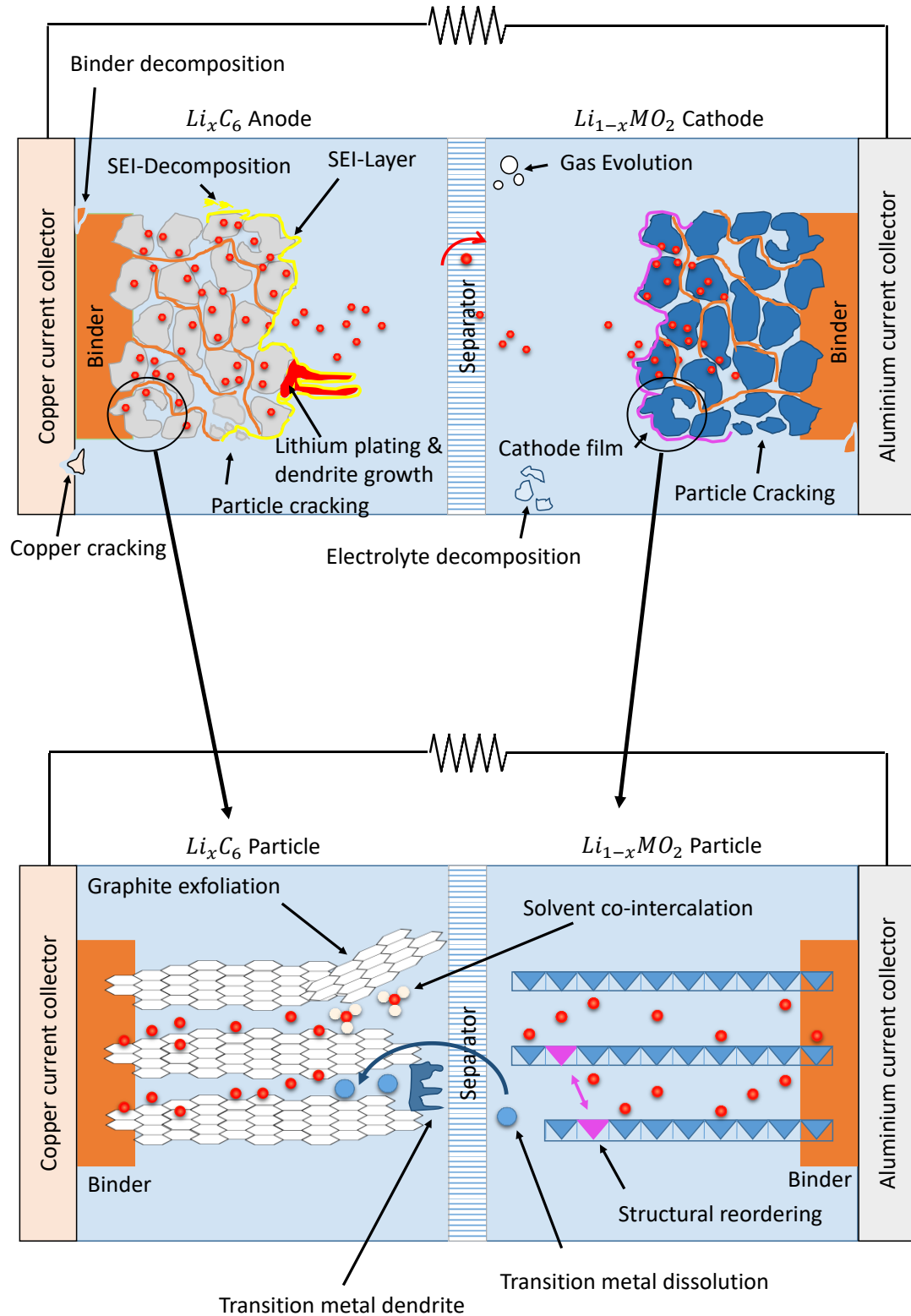


FIGURE 2-4 – COMMON DEGRADATION MECHANISMS OF A LIB

### 2.4.1 Surface film effects

During initial cycling, an SEI forms on anode surfaces, irreversibly locking cyclable lithium in the process. Throughout the lifetime of the cell, the SEI continuously grows, locking up further cyclable lithium, although at a much slower rate [96]. Elevated temperature operation and storage is known to accelerate the process of SEI growth at the carbon anode. The chemical composition and morphology of the SEI changes at elevated temperatures above 60-80 °C [97], resulting in a more porous layer. Furthermore, the SEI can decompose, exposing fresh graphite to the electrolyte. Under these conditions side reaction compounds such as phosphates, carbonates and  $LiF$  are formed, accumulate on graphite particles and form a barrier to  $Li^+$  ion diffusion causing an increase in cell impedance. Additionally more SEI is gradually formed, locking more  $Li^+$  ions in the process, causing capacity fade [47,78,97–99].

Lithium plating is the deposition of solid lithium metal on the anode surface during charging [47,78]. With increasing SOC [100], and at low temperatures [99,101] the diffusivity of lithium in graphite is reduced. At high charge current rates [102,103] the  $Li^+$  ions cannot intercalate into graphite layers quick enough to reach the theoretical capacity limit of the anode. This may lead to local areas on the electrode surface to be fully lithiated and subsequently lithium plating and dendrite growth occurs. Not only does this process reduce the amount of Li-ions available for shuttling between electrodes, but also acts as a potential failure mode. The metallic lithium subsequently reacts with fresh electrolyte, reducing charging efficiency and further increasing growth of the SEI [104–106]. Additionally to impedance rise and loss of cyclable lithium, lithium dendrites can penetrate the separator and cause an internal short circuit with the cathode causing catastrophic failure of the cell [68,71,79].

At the cathode, the formation of surface films similar to SEI on the anode has been reported within [107,108]. The formation of these films is accompanied by a reduction in cyclable lithium, and increased impedance. The decomposition and future growth of the passivating layer at the cathode surface is strongly related to charging the cells above a critical potential, which depends on the choice of cathode material. For example, charging NMC cells above 4.5 V results in significantly higher rate of layer growth than for 4.1 V [108].

### 2.4.2 Structural changes

Structural changes refer to changes in the electrodes at an atomic level, such as Jahn-Teller distortion and transition metal dissolution in spinel LMO cathode-based batteries [109]. In spinel LMO, Manganese is predominantly present as  $Mn^{3+}$  and  $Mn^{4+}$  ions. During discharging of the

battery cell, the cathode is being lithiated. As  $\text{Li}^+$ -ions diffuse much quicker within the electrolyte than in solid LMO particles, these ions may accumulate at the electrode surface and  $\text{Mn}^{4+}$  is reduced to  $\text{Mn}^{3+}$ . This causes a distortion in the atomic structure within the electrode material and a volume change within the electrode. The  $\text{Mn}^{3+}$  can then reduce further to  $\text{Mn}^{2+}$ , which is soluble in the electrolyte [29]. This process is augmented at low SOC, and high discharge rates, as a localised increase of  $\text{Li}^+$  [78].

The dissolution of Manganese into the electrolyte results in a reduction of active cathode material and electrolyte, and mechanical damage to the cathode material and thus a reduction in cyclable lithium capacity and increase in impedance. Furthermore,  $\text{Mn}^{2+}$ -ions can transfer to the anode through the electrolyte, deposit on the anode, and result in decomposition of the SEI [90,110].

#### 2.4.3 Mechanical changes

Mechanical changes are structural changes on a particle rather than atomic level, resulting predominantly in particle cracking. During de/intercalation of lithium in the electrodes, the active material particles can undergo expansion and contraction of up to 10% by volume for graphite [47], and up to 16% for LMO [78]. Over time, the repeated expansion and contraction of the electrode material can lead to cracking in the active particles due to fatigue. Not only does this expose electrolyte to fresh reaction sites, resulting in additional SEI formation, but also cause impedance rise through poor electric contact between active particles, binder, and the current collectors [111].

Another pathway for cracking is the co-intercalation of solvents from the electrolyte into the graphite anode [112]. The electrolyte reacts reductively, as in SEI formation, accompanied by gas release within the electrode particle. This can lead to the expansion of the graphite of up to 200%, resulting in particle cracking and exfoliation, resulting in a reduction in active material, and further SEI formation [47,61,71,113–115].

#### 2.4.4 Parasitic reactions

Parasitic reactions in LIBs involve the degradation of passive materials such as the current collectors and binders. On the anode side, the corrosion of copper current collectors can occur at low SOC, when the anode is highly delithiated [78,116]. At the cathode, at high SOC, the electrolyte decomposes and partly forms hydrofluoric acid ( $\text{HF}$ ), which corrodes the electrode material and aluminium current collector [117,118]. Both mechanisms result in a loss in electrical



contact and thus increase in cell impedance but are accompanied by some electrolyte loss and thus also result in further reduction in cyclable lithium.

Similarly, Binder decomposition occurs in both extremes of SOC (high and low)[116], and at high temperatures [119]. This causes a loss of electrical contact between the electrode active material particles and current collectors, manifesting itself in increased cell impedance. Furthermore, decomposed binder components can migrate to anode and cathode surfaces and block lithium diffusion pathways [119].

#### 2.4.5 Influencing environmental factors and operating parameters

The onset and progression of the discussed degradation mechanisms is influenced by various environmental conditions and operational parameters. A short summary of these differentiating factors and their effect on battery degradation is listed in Table 2-3. Notably, increased cell temperature and high operating currents accelerate most degradation mechanisms. As most chemical processes are assumed to follow an Arrhenius type relationship, an increase in temperature brings the system closer to the activation energy of unwanted side reactions, thus accelerates the degradation of the cell [116].

High electrical currents can cause rapid volume changes during intercalation and de-intercalation, which results in contact loss between the electrode and current collectors, changes in surface porosity of the electrode material, and subsequently expose fresh graphite to the electrolyte resulting in increased SEI growth on the anode. At the cathode large currents cause volume changes causing particle cracking resulting in increased cell impedance [50,120]. High currents are particularly damaging if a cell experiences uneven current distribution. Local areas within the cell will encounter larger currents than their surroundings causing localised hotspots coupled with SOC inhomogeneity resulting in localised ageing and further degradation of the cell [121].

Further information and detailed reviews on battery degradation can be found within [47,61,96,99,110].

Cause/ Aggravating factor	Affects	Causes	Reference
High Current	Anode	Lithium plating during charging at high SOC and subsequent SEI growth at locations where Li metal is exposed to electrolyte	[47,105,116]
		Volume changes resulting in contact loss of active material particles and particle cracking, exposing fresh graphite to the electrolyte and subsequently further SEI growth	[47,116]
	Cathode	Volume changes and tensile compressive stresses causing particle cracking	[50,120]
		Transition metal dissolution	[78]
High temperature	Anode	Decomposition of electrolyte resulting in loss of cyclable lithium and further SEI growth	[47,98,99,116]
		Increased SEI film growth decreasing accessible surface area	[47,99]
		Parasitic side reactions exposing fresh graphite to electrolyte and increased SEI growth	[47]
		Decomposition of binder causing mechanical instability	[47]
	Cathode	Oxidation of electrolyte causing gas evolution and loss of cyclable lithium	[46,77,116]
		Increase in phase changes in active material	[116]
		Dissolution of transition metal, and deposition on anode (LMO)	[47,50,99,116]
		Decomposition of binder	[119]
Low Temperature	Anode	Lithium plating during charging at high SOC	[47,122]
High DOD	Anode	Volume changes causing mechanical stresses and particle cracking with subsequent SEI growth	[47]
	Cathode	Volume changes causing mechanical stresses	[47,116]
		Crystal structure disorder causing particle cracking	[116]
High SOC	Both	Binder decomposition	[116]
		Electrolyte decomposition	[78]
	Anode	Lithium plating at high charging rates	[47,122]
	Cathode	Current collector corrosion	[78,116]
Low SOC	Both	Electrolyte decomposition	[78]
		Binder decomposition	[116]
	Anode	Current collector corrosion	[117,118]
	Cathode	Transition metal dissolution	[78]

TABLE 2-3 – LIB OPERATING CONDITIONS AND RESULTING DEGRADATION MECHANISMS FOR LIBS

## 2.5 Characterisation Testing

To characterise LIBs, and to identify and quantify battery degradation, researchers have employed a variety of invasive [123] and non-invasive [29] test methodologies. Invasive methods, such as scanning electron microscopy (SEM) can be used to measure physical characteristics. An example of this is the size of particles within the electrode active materials. They can also be used to detect surface film formation on particles, and mechanical changes such as electrode cracking within the electrode materials [124]. X-ray diffraction (XRD) can be used to identify structural changes on an atomic level. As such, these methods allow for the identification of the degradation mechanisms described previously, and for the parameterisation of electrochemical-physical models as described within [125]. However, these methods are destructive and require cell disassembly and complex sample preparation [126], thus cannot be easily done within an engineering framework outlined in Chapter 1. The use of destructive testing methods therefore is outside the scope of this work, and as such, only non-destructive methodologies are described in more detail.

Non-invasive testing methods are most commonly based on electrical characterisation tests and do not require deconstruction of the cell. Utilising these characterisation tests at regular intervals during a cell's useful life, and tracking their outcomes enables researchers to quantify the effect of degradation on the performance of the cells primarily in terms of energy capacity fade and impedance rise. The onset and progression of specific degradation mechanisms such as surface film effects can only be inferred, and only the effects of this degradation may be quantified, as discussed in detail below.

### 2.5.1 Galvanostatic energy capacity

Galvanostatic energy capacity tests are one of the most commonly used characterisation tests in research [127,128], and in industry as defined within industrial standards [34–36]. These tests determine the amount of electrical energy, which can be released from a fully charged cell under defined conditions. Typically, a cell is charged using a constant current-constant voltage (CC-CV) schedule as illustrated in the example in Figure 2-5 for a 53 Ah cell comprising a graphite anode, and NMC cathode. The specifics of data collection and post processing for this example are described in detail in Chapter 6.

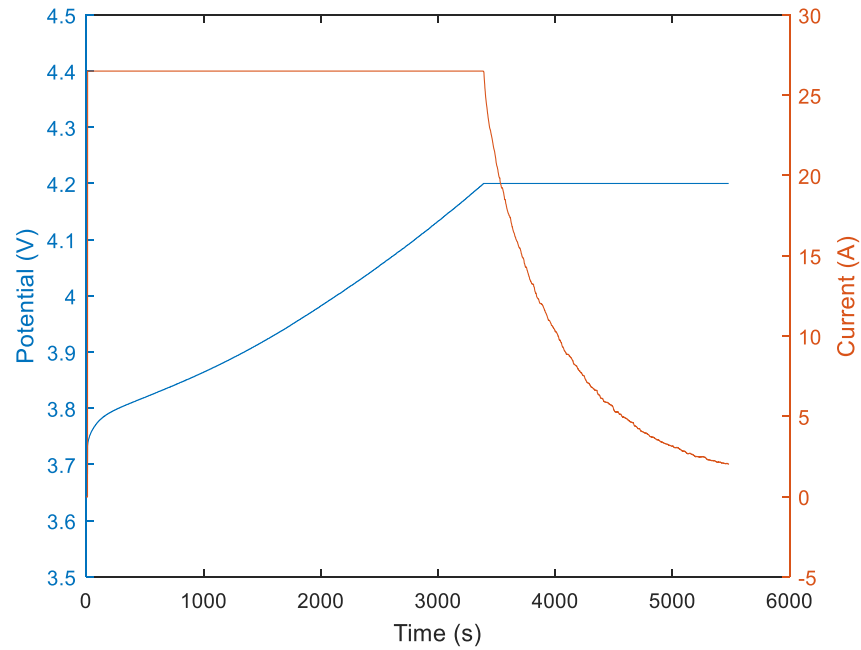


FIGURE 2-5 – CURRENT AND VOLTAGE PROFILE OF A 53 AH G-NMC CELL DURING CC-CV PROCEDURE.

Initially the cell is charged at a predefined C-rate until it reaches its maximum operating potential as specified by the manufacturer. The C-rate is a measure of the applied current compared to the manufacturer's rated capacity and a C-rate of 1C will discharge a cell in 1 hour [129]. Hence, for a cell with a capacity of 50 Ah, a C-rate of 1C would represent a current of 50 A. It is subsequently held at this potential with a decreasing current until the charging current drops below a predefined threshold, typically C/20 or less [104]. The cell is then left at open circuit potential for a set amount of time, typically 1h, to equilibrate, before being discharged at a constant current until the cell cut-off potential is reached. The discharge energy capacity is defined as the energy extracted during the discharge.

The magnitude of charging and discharging C-rates, as well as upper and lower cell potential limits influences the amount of energy, which can be extracted from the cell, and how much time is required to complete the test. As the C-rate is increased, more energy is lost as heat due to increases in polarisation, and the overall usable capacity in one cycle is decreased. As such, the measurements for capacity vary at different C-rates. This effect is illustrated in Figure 2-6. To track the capacity of a cell to determine the effects of degradation in terms of capacity fade, the test parameters must be kept consistent throughout the testing period.

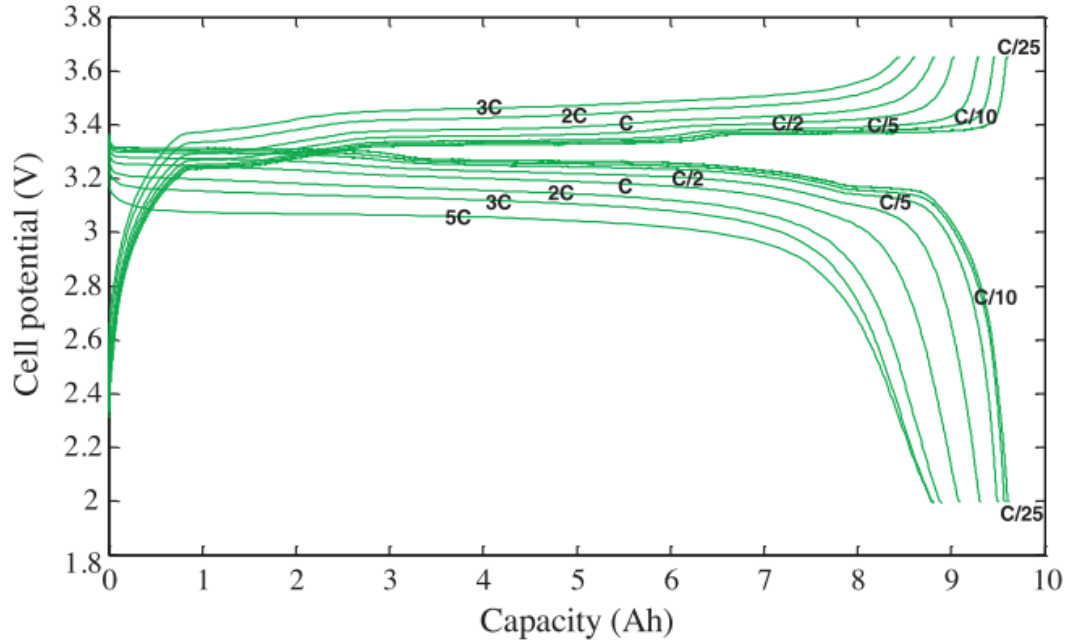


FIGURE 2-6 - GALVANOSTATIC CHARGE/DISCHARGE POTENTIAL PROFILES MEASURED AT VARIOUS C- RATES FOR A CARBON-LFP CELL AT 25°C. FROM [130]. INCREASES IN CURRENT REDUCE THE OVERALL ENERGY CAPACITY THAT MAY BE EXTRACTED FROM THE CELL, CAUSED BY INCREASED POLARISATION AND THERMAL LOSSES.

### 2.5.2 Pseudo-OCV testing and $dQ/dV$ analysis

The pseudo-OCV tests serves as a capacity test at a low C-rate and can be used for incremental capacity analysis, a method often used to identify gradual changes within LIBs [38,131–133] and to infer degradation through a non-destructive test process. The test can be conducted either during charging or during discharging. The test procedure is illustrated in Figure 2-7 for the same 53 Ah cell. The specifics of data acquisition for this example are detailed in Chapter 6.

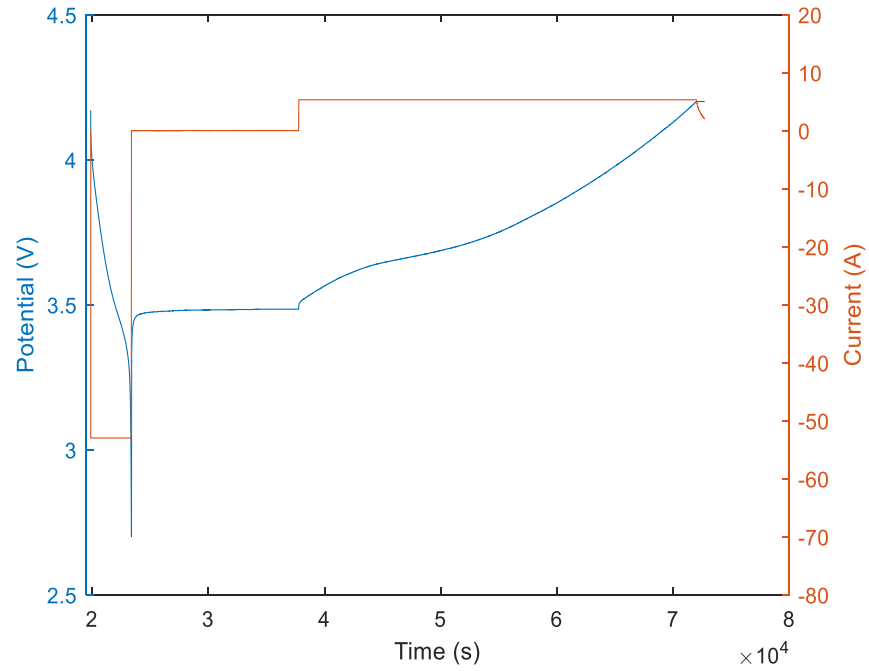


FIGURE 2-7 – CURRENT AND VOLTAGE PROFILE OF A 53 AH G-NMC CELL DURING PSEUDO-OCV MEASUREMENTS

The cell is discharged to 0% SOC, and left for a predefined duration to equilibrate (typically 1h). It is subsequently charged with a low C-rate under a CC-CV schedule, and voltage and capacity are recorded. The amplitude of the C-rate must be small enough to keep the cell in a state close to its OCV, but not so small as to fall within the accuracy limitations of the measurement and electrical loading equipment. Furthermore, the c-rate influences the duration of time it takes to complete the test. Pastor-Fernandez [134] et al suggest a rate of 0.1C or lower to find a compromise between test duration and data resolution. The corresponding capacity vs. potential curve (illustrated in Figure 2-8) is then differentiated to obtain the  $dQ/dV$  curve shown in Figure 2-9.

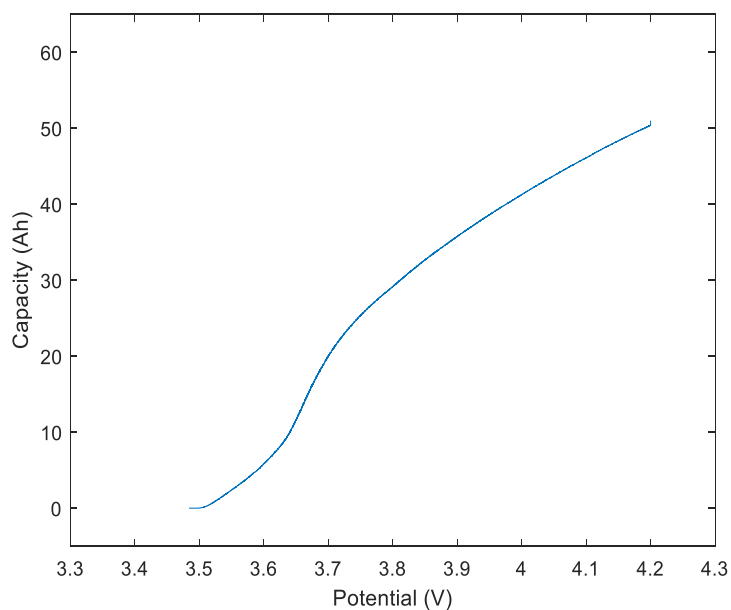


FIGURE 2-8 – CAPACITY VS CELL POTENTIAL CORRESPONDING TO THE P-OCV CHARGE IN FIGURE 2-7

The  $dQ/dV$  curves themselves are the derivatives of the charge vs. voltage, and the area under the curve equates to the capacity of the cell. Plateaus in the OCV curve are transformed to identifiable peaks on the  $dQ/dV$  curves (marked with red arrows).

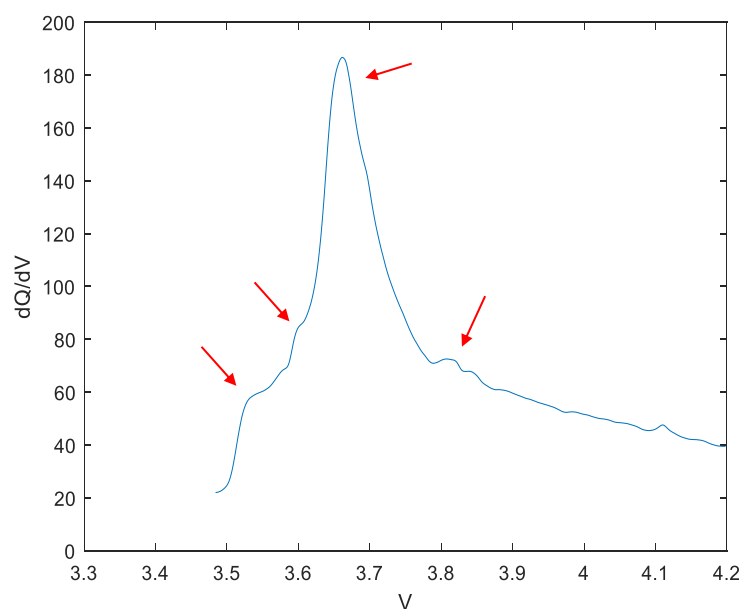


FIGURE 2-9 –  $dQ/dV$  CURVE DERIVED FROM FIGURE 2-8, RED ARROWS INDICATE PEAKS ASSOCIATED WITH PHASE CHANGES IN THE ACTIVE ELECTRODE MATERIALS DURING CHARGING

These peaks in  $dQ/dV$  curves, and plateaus in OCV curves are associated with phase transformations in the active materials. Conducting  $dQ/dV$  on individual electrodes reveals the phase changes within the materials individually, as illustrated in the example for graphite electrodes in Figure 2-10 [135].

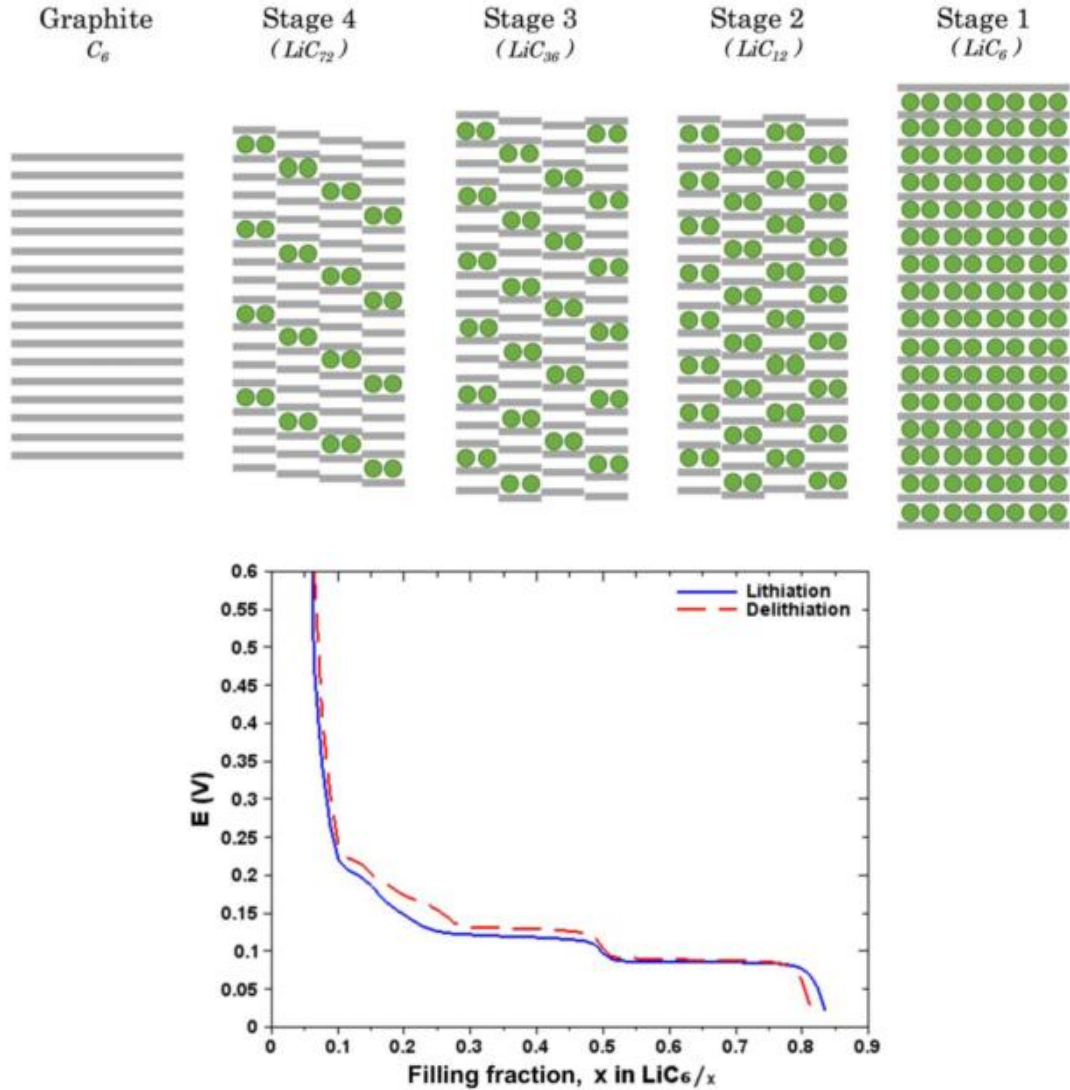


FIGURE 2-10 – OCV AND PHASES OF GRAPHITE AS A FUNCTION OF LITHIATION, ADAPTED FROM [135]

On a full cell, the analysis is more complex as the attribution to either electrode is not always straightforward. By monitoring changes in the shape and position of these peaks during cell life, crucial information about changes in the electrochemical properties of the cell can be extracted [133].



### 2.5.3 Hybrid Pulse Power Characterisation (HPPC)

When a discharging current is applied to a cell, the potential of the cell drops. For pure Ohmic systems, this potential drop is directly proportional to the current, which is applied and can be calculated if the internal resistance is known ( $\Delta U = \Delta IR$ ). The voltage response of LIBs to an applied current is not linear and is illustrated in Figure 2-11 on the same example cell as the previous two.

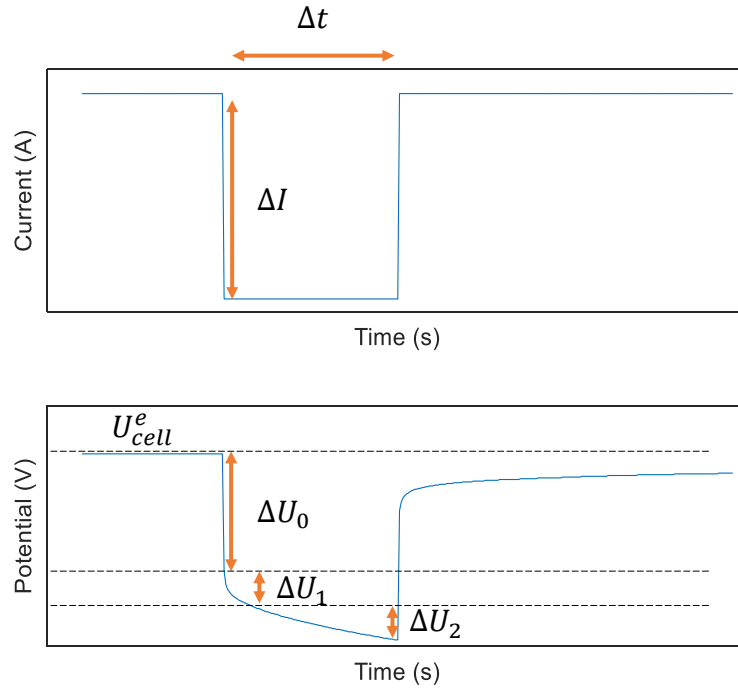


FIGURE 2-11 – VOLTAGE RESPONSE OF A CELL TO A DISCHARGING CURRENT INPUT

The total voltage drop within the cell can be divided into a static, and dynamic part [136]. The instantaneous voltage drop ( $\Delta U_0$ ) is caused by the pure Ohmic resistance within the cell. The dynamic part of the total voltage drop ( $\Delta U_1$ ) is caused by electrochemical changes within the cell. These electrochemical processes such as the concentration changes of reactants and products at the reaction sides in the electrodes are time dependent, thus the second voltage drop changes over time. The “Hybrid Pulse Power Characterisation” (HPPC) test consists of a sequence of alternating 10s discharge and charge current pulses of increasing C-rate applied at a pre-defined SOC and temperature with a rest-interval between each pulse to allow the voltage to equilibrate [137]. The duration of pulses is kept short at 10 s to limit the impact of SOC variation on the measurement.

The measured voltage response of these tests can then be used to parameterise an equivalent circuit model (ECM) for a specific SOC, temperature, and current input. ECMs of various degrees of complexity have been used in research to model the voltage response of lithium ion batteries for on-board SOC estimation in electric vehicles [138,139], and for estimating the state of health (SOH) of a cell by tracking the parameters for internal resistance over time [140]. An example of an ECM often utilised in research [134,136,139] is the Randles equivalent circuit consisting of a resistor, in series with two RC networks as illustrated in Figure 2-12.

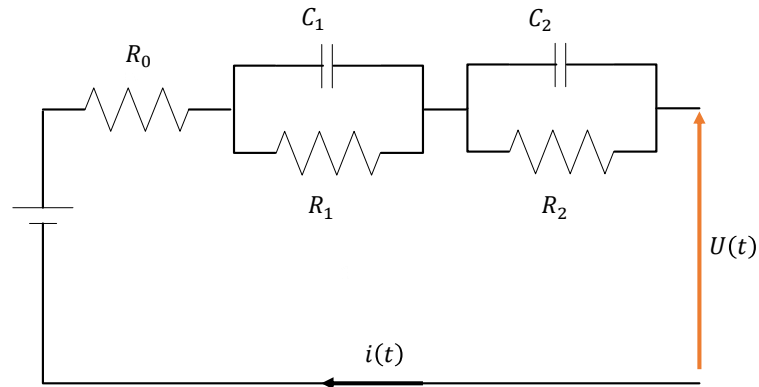


FIGURE 2-12 – RANDES ECM WITH 2 RC PAIRS,  $R_1$  REPRESENTS THE CHARGE TRANSFER RESISTANCE,  $C_1$  IS USED TO MODEL THE EFFECT OF THE DOUBLE LAYER CAPACITANCE. THE 2ND RC PAIR CAN BE USED TO MODEL THE EFFECTS OF THE SEI

In this example  $R_0$  represents the bulk Ohmic resistance in the bulk materials and current collectors,  $R_1$  represents the charge transfer resistance,  $C_1$  represents the double layer capacitance, and the second RC pair represent the electrical effects of the SEI.

#### 2.5.4 Pulse-Multisine Characterisation

The Pulse Multisine Characterisation (PMC) test, first introduced by Widanage et al. [141,142], is a characterisation test based on a similar principle as the HPPC test. The profile utilised for this test differs from the charging and discharging pulses used within the HPPC, as it is the result of a zero-mean multisine superimposed on a sequence of pulses, as illustrated in Figure 2-13. The resulting profile aims to charge sustaining and approximates the amplitude spectrum of a duty cycle derived from a real-world driving cycle. As such, the profile is more representative of the dynamics a cell is exposed to during operation. Within [142], the PMC test was successfully employed to characterise several different cell-types and provide the necessary dataset to parameterise an ECM which better captured non-linear behaviour of cells. The fundamentals of the method are briefly explained below, the MATLAB® code and scripts to design the PMC, and evaluate the test results were made available within [141,142].

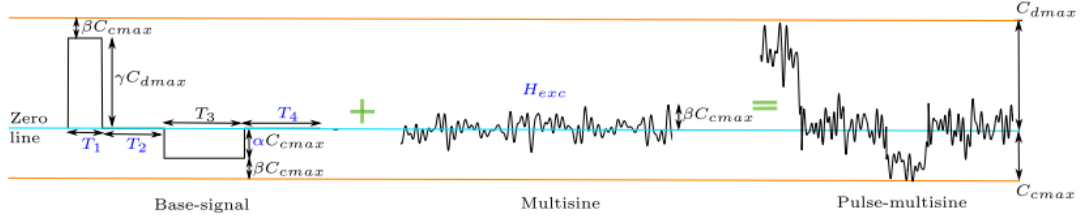


FIGURE 2-13 – PULSE MULTISINE CHARACTERISATION PROFILE FROM [141]. THE DYNAMIC MULTISINE SIGNAL IS SUPERIMPOSED ON THE MODAL BASE SIGNAL TO CREATE A MORE DYNAMIC PROFILE.

Several, typically 5, periods of the PMC signal ( $i(n)$ ) are applied to a cell and the voltage response ( $v(n)$ ) is recorded. This data can subsequently be used to parameterise a non-linear ECM (NL-ECM) as illustrated within Figure 2-14. The NL-ECM consists of linear ECM block coupled with a non-linear over-potential function and a parallel OCV model block.

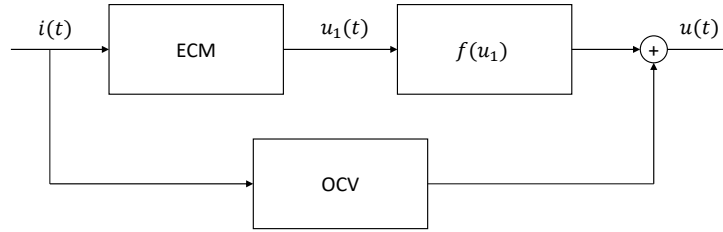


FIGURE 2-14 – NON-LINEAR ECM CONSISTING OF A LINEAR ECM, OCV BLOCK, AND NON-LINEAR OVER-POTENTIAL FUNCTION, ADAPTED FROM [142]

To parameterise the linear ECM, first the cell Impedance is estimated under steady state conditions. As such, to lessen the effect of transient behaviour, the first period of the measured current and voltage should be discarded. The measured voltage and current signals are then averaged over a single period as described in equations (15) and (16), where  $P$  is the number of periods of the PMC signal applied,  $N$  is the number of samples per period in the PMC signal, and  $n = 0, \dots (N - 1)$ .

$$\bar{i}(n) = \frac{1}{P-1} \sum_{p=2}^P i(N(p-1) + n) \quad (15)$$

$$\bar{u}(n) = \frac{1}{P-1} \sum_{p=2}^P u(N(p-1) + n) \quad (16)$$

In a further processing step, the mean voltage of the voltage response signal  $\bar{v}(n)$  is then subtracted from  $\bar{u}(n)$ , as it is interchangeable with the OCV for that particular SOC. The resulting signal  $\bar{u}_0(n)$  thus represents the over-potential arising from the applied current.

Subsequently, the Discrete Fourier Transform of the signals  $\bar{i}(n)$  and  $\bar{u}(n)$  are determined as described in equations (17) and (18), respectively, where  $k$  denotes the harmonic and  $k = 0, 1, \dots, N - 1$

$$I(k) = \sum_{n=0}^{N-1} \bar{i}(n) e^{-\frac{2j\pi n k}{N}} \quad (17)$$

$$U(k) = \sum_{n=0}^{N-1} \bar{v}(n) e^{-\frac{2j\pi n k}{N}} \quad (18)$$

This representation of the current and voltage signals within the frequency domain are linked via equation (19), where  $Z(k)$  is the impedance of the cell, and  $E(k)$  is an error term accounting for any non-linear behaviour.

$$U(k) = Z(k)I(k) + E(k) \quad (19)$$

From equation (19), the Impedance of the cell can be estimated whilst minimising the influence of  $E(k)$ . This is achieved through what the authors describe as a local-polynomial-method, where  $Z(k)$  is estimated locally around  $k$  via a low degree polynomial as described within [143]. Following the estimation of  $Z(k)$  a transfer function model  $Z_m(k)$  approximating the impedance is determined via the Frequency Domain System Identification Toolbox in MATLAB®. From this function, ECM parameters can be estimated via partial fraction expansion of  $Z_m(k)$ . Within [142]  $Z_m(k)$  was a 2<sup>nd</sup> order transfer function and was expanded as described within equation (20) to parameterise a 2<sup>nd</sup> order ECM, similar to that shown in Figure 2-12. The internal cell resistance is represented by  $R_0$ .  $R_1$  and  $R_2$  represent the polarisation resistances, and  $\tau_1$  and  $\tau_2$  the time constants.

$$Z_m(k) = -R_0 - \frac{R_1}{\tau_1 j \omega_k + 1} - \frac{R_2}{\tau_2 j \omega_k + 1} \quad (20)$$

The resulting ECM can then be used to model the voltage response  $v_1(t)$  to a current input  $i(t)$ . Any non-linear behaviour of the cell arising from reaction kinetics can be examined by plotting the measured over-potential  $\bar{u}(n)$  against the modelled over-potential. Within [142], non-linearity was observed predominantly for low temperatures, and modelled using a sigmoid function.

By conducting PMC testing on a regular basis and tracking changes of the estimated ECM parameters over time, changes within the cell could be inferred. In addition to the PMC requiring a shorter testing time than the HPPC, an additional advantage is the possibility to observe any changes in non-linear behaviour of the cell. This is beneficial since high current densities may result in non-linear behaviour of cells as identified above. Furthermore, the emergence of non-linear behaviour might occur over time due to electrochemical changes within the cell.

### 2.5.5 Electrochemical Impedance Spectroscopy

The voltage drops  $\Delta U_1$  and  $\Delta U_2$  measured in HPPC tests is caused by the combined effects of the electrochemical processes that occur within a cell. Each process has its own time constant [136,144], and as such the proportion that each process contributes to the voltage response cannot be easily extracted from HPPC data. Electrochemical impedance spectroscopy (EIS) offers the possibility of investigating each process individually [145].

EIS tests in galvanostatic mode are undertaken by applying an AC sinusoidal current ( $i(t)$ ), as defined in equation (21) to the cell and measuring the voltage response ( $u(t)$ ) as defined in equation (22).  $i_0$  is the magnitude of the excitation current,  $\omega$  is the excitation frequency, and  $\phi_1$  is the phase angle of the current signal.  $u_0$  is the voltage amplitude, and  $\phi_2$  is the phase angle of the resulting voltage response, which is different from  $\phi_1$  due to cell impedance [146,147].

$$i(t) = i_0 \sin(\omega t + \phi_1) \quad (21)$$

$$u(t) = u_0 \sin(\omega t + \phi_2) \quad (22)$$

The frequency domain representation of equations (21) and (22) are given in equations (23) and (24), respectively.

$$I(\omega) = I_0(\omega) e^{j\phi_1(\omega)} \quad (23)$$

$$U(\omega) = U_0(\omega) e^{j\phi_2(\omega)} \quad (24)$$

The impedance of the cell for a certain frequency ( $Z(\omega)$ ) can then be calculated from the above equations and as described in equation (25).

$$Z(\omega) = \frac{U(\omega)}{I(\omega)} = \frac{U_0(\omega) e^{j\phi_2}}{I_0(\omega) e^{j\phi_1}} = Z_0 e^{j(\phi_2 - \phi_1)} \quad (25)$$

The signal is applied throughout a range of frequencies (e.g. 10 mHz to 10kHz), and the calculated impedance,  $Z(\omega)$ , consists of a real and an imaginary component. This is represented on a Nyquist plot, where the imaginary part of the impedance is plotted on the y-axis and the real part of the impedance is plotted on the x-axis. A typical Nyquist plot for an LIB is illustrated in Figure 2-15.

The plot can be divided into three distinct regions: high-frequency inductive tail ( $>1\text{kHz}$ ), mid-frequency semicircle ( $1\text{kHz} - 10\text{Hz}$ ), and Warburg impedance at low-frequency ( $<10\text{Hz}$ ) [148]. The inductive tail in the high frequency region is associated with conduction through the bulk material of the cell, separator, electrolyte and wires. The pure Ohmic resistance can be extracted from the intersection of the inductive trail with the real axis. The semicircle in the mid-frequency region is attributed to charge transfer phenomena and reaction kinetics. The Warburg region of the plot correlates with diffusion and mass transport effects. The EIS frequency response can be used to parameterise an ECM, similar to that shown in Figure 2-12, to model the dynamic behaviour of the cell.

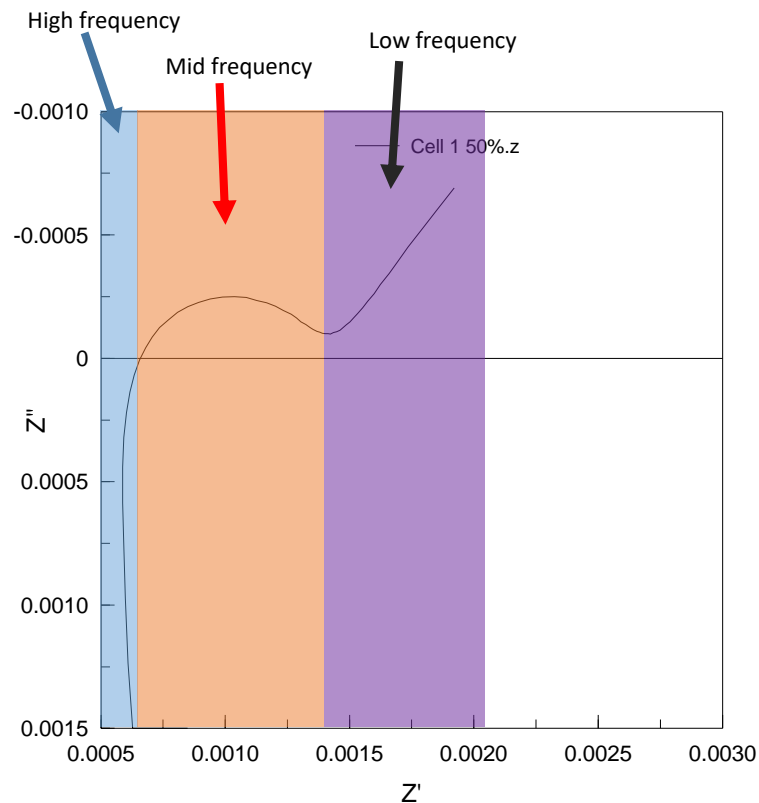


FIGURE 2-15 - TYPICAL NYQUIST PLOT FOR A LIB, SEPARATED INTO THREE DISTINCT FREQUENCY REGIONS.

In addition to characterising cell dynamics, EIS testing is commonly used to characterise the degradation of cells over time [149]. Through tracking changes in the shapes of the graphs and thus the resulting ECM parameters, it is possible to gather more detailed information about the degradation of cells. For example, a second semicircle is formed and appears on the Nyquist plots in the high- to mid-frequency over prolonged use of the cell. This semicircle is believed to originate from the growth of the SEI layer [107].

### 2.5.6 Ultrasonic testing

Unlike the previously discussed electrical characterisation tests, ultrasonic testing has been utilised in several studies as an alternative non-destructive means to determine the SOC and SOH of cells [150–153]. As ions intercalate and de-intercalate from an electrode, physical changes occur within the active material. As a result, the density and elastic modulus of an electrode changes as a function of its state of charge. A typical setup for ultrasonic testing is detailed within Figure 2-16.

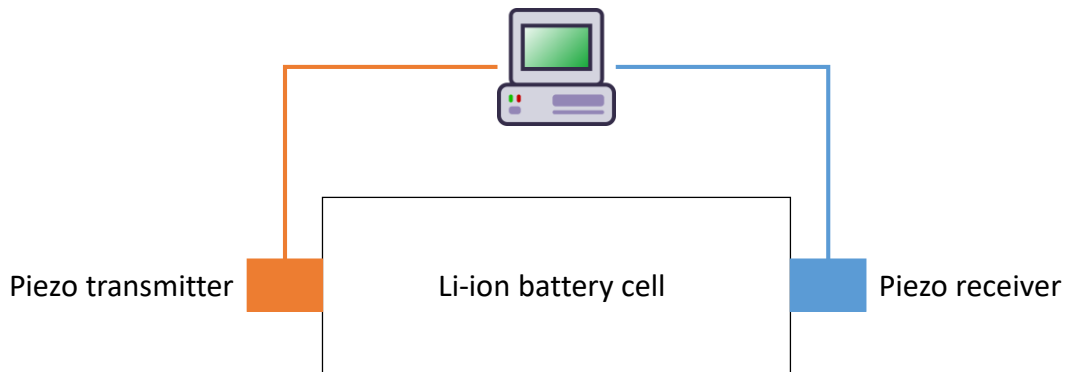


FIGURE 2-16 – SCHEMATIC OF ULTRASONIC TESTING SET UP

A piezo transmitter produces an acoustic signal pulse, which travels through the cell and is recorded at the receiver. The intensity of the measured pulse and time of flight can subsequently be correlated with the cell's SOC. Hsieh et al. [151] show that a strong correlation exists between a cell's SOC and the density distribution determined through ultrasonic measurements. Furthermore, they describe observable changes in measurements as the cell is cycled, indicative of degradation processes. They argue that ultrasonic testing offers an effective analysis technique regardless of cell chemistry and form factor. Gold et al. [153] show that within their study, the time of flight from piezo transmitter to receiver correlates approximately linearly with the SOC of a cell. However, the parameterisation of models that emulate the electrical behaviour of a cell is currently not possible. As such, ultrasonic testing will not be employed within this work.

In summary, the electrical characterisation tests described allow for the identification of cell characteristics such as internal impedance and energy capacity, and the parameterisation of models that emulate the dynamic behaviour of cells. The effects of LIB degradation can be measured by tracking the values of these parameters over the lifetime of a specific cell. The testing conditions such as C-rates, SOC range and testing temperature can be selected such that it replicates conditions encountered within a HP-BEV environment. The existing electrical characterisation testing framework is assessed as adequate to characterise LIBs for this use case.

## 2.6 Degradation Testing / Ageing

The typical process for degradation testing is illustrated in Figure 2-17 and detailed below.

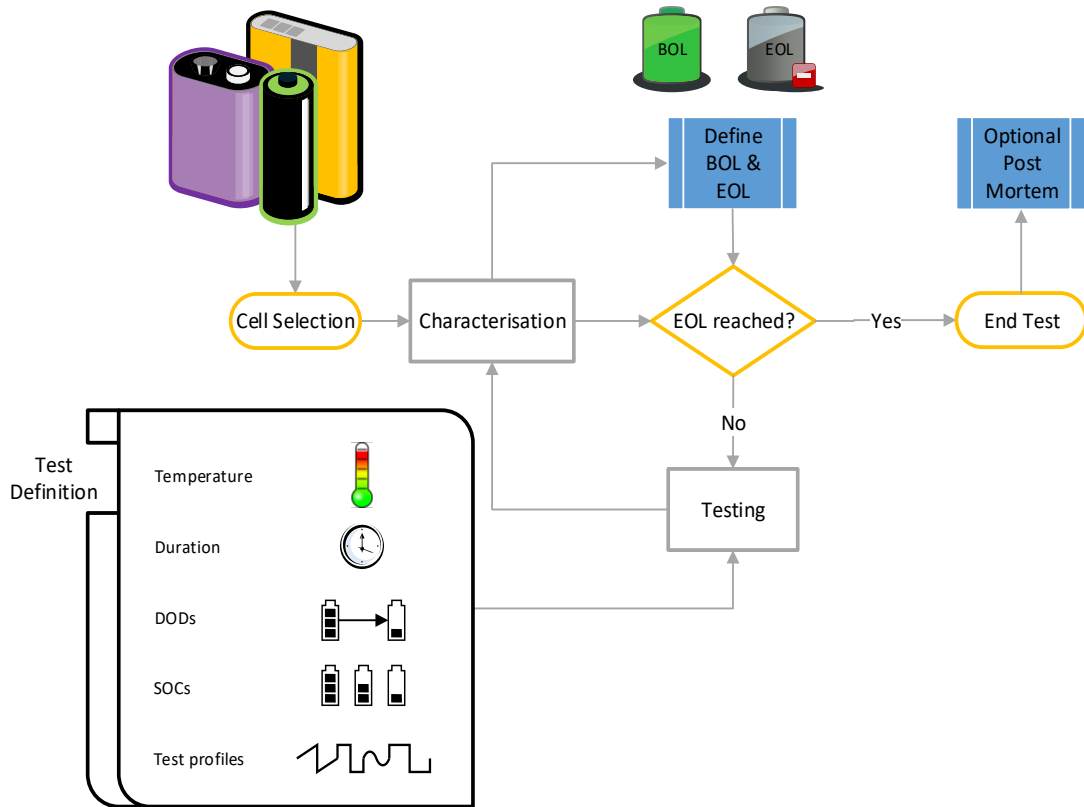


FIGURE 2-17 – TYPICAL PROCESS OF DEGRADATION TESTING.

Initially, a cell is selected considering form factor, chemistry and manufacturer. Subsequently, the cells are characterised to define their state at the cell's beginning of life (BOL). The specific methods chosen depend on each study, and comprise test described in the previous section. From this initial characterisation, the cells end of life (EOL) criteria are also defined based on the use case (usually 80% retained rated capacity, 100% impedance increase for automotive applications [36]). Cells then undergo testing to examine the influence of specific aspects of



operation on their degradation. This can be for example the influence of temperature under storage [55], or the influence of high current rates [154]. During testing, batteries are characterised periodically to monitor the progression of the effects of degradation, and testing is concluded if the EOL of the cells has been reached, or cells have undergone catastrophic failure. This is sometimes followed by post-mortem analysis to identify the degradation mechanisms. The research presented within this work focuses on storage and cycle degradation testing which are discussed in detail below. For more information on the degradation related to mechanical stresses the author recommends the research presented within [49,155,156].

### 2.6.1 Storage Testing – Calendar Ageing

Calendar ageing studies are used to investigate the degradation, which occurs over time without subjecting the cell to electrical loading. A typical experimental set-up involves storing LIBs at a predefined set of temperatures and SOC, and to observe the impedance rise and capacity fade over time [52].

An example of such a study is the work by Käbitz et al. [54], who tested 10Ah pouch-format cells comprising a graphite anode and NMC(0.33, 0.33, 0.33) cathode. Cells were stored under open circuit and constant voltage conditions at four different temperatures between 25°C and 60°C, and five different SOC between 20% and 100%. The degradation of the cells was measured based on impedance augmentation and capacity fade, by running pulse power tests and capacity tests, respectively every six weeks of storage. It was shown that the rate of impedance augmentation and capacity fade follows an Arrhenius-type relationship with respect to temperature and time. Cells stored at elevated temperatures experienced a greater rate of capacity fade and impedance augmentation, than those stored at lower temperatures. This was attributed to a relative increase in SEI growth and electrolyte decomposition compared to cells stored at lower temperatures. Cells stored at full charge (100% SOC) displayed higher impedance rise and capacity fade at the end of testing than cells stored at lower SOC, and little difference of effects could be observed for SOC between 90% and 50%. These observations are in accordance with those of a similar study investigating a different format type cell of similar chemistry [55].

Further extensive studies on storage and calendar ageing for a number of different format-type and cell chemistries and can be found within [52,157–160]. The results obtained from such studies provide information about optimum cell storage conditions with respect to SOH, and underpin the derivation of lifetime prediction models [140,161] to develop a better understanding of the ageing process during storage. These models are essential to simulate the

proportion of ageing which occurs whilst vehicles are parked, and to estimate differences in degradation rates for different geographic locations [95,162].

The environmental conditions, which HP-EVs experience during storage, could be assumed similar to those of standard road vehicles in the scenario of a vehicle being parked on a drive or in a garage. For a vehicle dedicated to racing applications, it can be argued that the storage conditions of the vehicle are optimised to minimise capacity fade and impedance rise of the cell. Gering et al. [163] have shown that the degradation during calendar ageing can be influenced if a cell is cycled in between calendar tests. Thus, the author asserts that the sequence of operating conditions as well as their nature directly influence the rate of ageing. This process is described as path-dependence. As such, to gain comparable results between two different studies, the sequence of tests should be kept the same. Provided, any differences in cycling profiles between HP-BEVs and standard passenger vehicles is taken into account, existing calendar ageing methodologies should be sufficient to provide datasets suitable for HP-EV applications. Hence, no further exploration into HP-BEV specific calendar ageing is covered within this work.

### 2.6.2 Cycle Testing

Cycle tests are suitable to provide several deliverables. Firstly, to identify the effect of specific cycling profile characteristics such as C-rate, depth of discharge ( $\text{DOD} = \Delta \text{SOC}$ ) and SOC cycling range on individual degradation mechanisms [29,54,164–166]. Secondly, to provide a dataset that underpins the development of an empirical degradation model to predict capacity fade and impedance augmentation for batteries in use such as electric vehicles [51]. Finally, to evaluate cell performance with respect to self-heating under operation [167,168], and to parameterise and validate electro-thermal models that predict the evolution of cell temperature and capacity under different testing conditions [125].

#### 2.6.2.1 Galvanostatic Profiles

In its most simple form, cycling tests are conducted using galvanostatic profiles. Ecker et al. [55] complemented their calendar ageing study with a cycle ageing study investigating the effect of DOD, and starting SOC on the degradation of an NMC cell. Cells were cycled at a rate of 1C at 35°C through 6 different DODs for a range of starting SOC. The degradation was measured in terms of capacity fade and impedance rise. Capacity fade was determined using a galvanostatic discharge at 1C, and impedance rise was determined using pulse power tests. The study found that cell degradation increases with increasing DOD, and that cycling around a mean of 50% SOC was least detrimental for the tested cells compared to lower and higher SOC. The faster

degradation rate was linked to cells crossing transitions in voltage plateaus in the individual electrodes, i.e. phase transitions in the active materials, thus resulting in higher mechanical stresses on the material particles.

Käbitz et al. [54], conducted similar tests, cycling cells using a current rate of 1C through different DODs at 4 different SOC levels at 40°C. Furthermore, they conducted full cycle tests from 100% SOC to 0% SOC at 25°C, 40°C and 60°C. They found that cycling at low DODs did not lead to any observable additional capacity fade, compared to the cells in their calendar ageing study at the same SOC levels. Discharging cells through higher DODs however did increase capacity fade. Impedance augmentation increased at elevated temperatures. At 25°C and high DOD, in contrast the impedance rise was lower than in the calendar ageing study over the same period. The reasons stated for this specific observation were believed to be complex interactions of volume increases and deposition reactions in the anode material during cycling [54].

Groot et al. [27] investigated the effects of symmetric and asymmetric cycle testing profiles at different temperatures, varying DODs, and resting periods between cycling on LFP cells. Symmetric profiles refer to tests where charging current rates and discharging current rates are of equal magnitude, asymmetric refers to situations, where different rates are used for charging and discharging respectively. Whilst for symmetric profiles capacity fade strongly related to current rate and temperature, the observed impedance augmentation did not directly correlate with capacity decrease. The increase in Ohmic resistance, measured using the EIS test technique, more closely related to the total test time, and the increase in low frequency impedance correlated well to the total capacity throughput and cycling temperature. For asymmetric cycles, i.e. situations where charging and discharging occurred at different current magnitudes, charging at elevated C-rates coupled with discharging at low c-rates lead to shorter cycle life than scenarios where the charging and discharging current magnitudes were reversed. Furthermore, in both cases degradation was worse than compared to high c-rate charge coupled with high c-rate discharge.

The cycling studies discussed above enable the investigation of the effects that some specific cycling conditions, namely DOD, SOC, C-rate and temperature, have on the characteristics of LIB degradation. The datasets obtained from such galvanostatic testing may underpin the development of degradation models under steady state and dynamic conditions allowing the user to make lifetime predictions.

One example is given by de Hoog et al. [51]. In this particular study 20 Ah pouch-format NMC cells were tested over 2.5 years with an extensive calendar life and cycle life test program, testing

several cells using a combination of 6 different temperatures, C-rates of C/3, 1C and 2C for symmetric and asymmetric cycling, 5 middle SOC, and 7 different DODs. The resulting dataset was used to develop a lifetime prediction model comprising separate calendar and cycling ageing components. The model was validated against test data of cells undergoing realistic, and accelerated duty cycle ageing utilising a scaled profile based on the WLTP driving cycle. Although the authors declared satisfactory accuracy for lifetime prediction capability of the model, the study did not explore higher charging or discharging current rates than 2C. As the effects of degradation cannot be extrapolated for higher current rates, this mapping approach is limited to the currents used. The authors stated that the charge and discharge current rate have a negligible effect on cycle ageing. Whilst this assumption may be acceptable for the described study, for cells being subjected to higher C-rates this is known to be not the case [27]. Specifically as identified in section 2.4, high currents can cause cracking of the electrode and extensive cell heating.

Although these tests provide some insights into the generic degradation of LIBs, the use of galvanostatic profiles however, is not representative of any passenger vehicle use case beyond charging or cruising on a motorway. As such, these tests are not suitable for the work presented within this thesis.

#### 2.6.2.2 Transient Profiles

Cycling tests using more complex and transient profiles are common practice in literature to determine the cycle-life and degradation of cells of LIBs under transient profiles and realistic EV duty cycles.

As part of their path-dependence study, Gering et al. [163] investigated how the relative magnitude and randomness of constant-power pulses could influence the degradation of 18650-format cells. 15 cells were tested on 5 different profiles (3 per test case), for which the time-average cumulative discharge energy was equal, but profiles varied in terms of pulse duration, pulse peak, and rest phases between pulses. Their initial analysis found that cells, which experience a higher frequency of higher magnitude power pulses, degrade faster than those, which experience lower magnitude pulses with the same energy throughput. This indicates that the shape of any duty cycle will be an influencing factor in the degradation, which may be observed.

Groot et al. [169] tested LFP cells with five different load cycles to determine the nature of cell degradation in HEV use cases. It was found that three of the tested cycles, which were similar in terms of SOC range and mean current rate yielded significantly different degradation rates and

characteristics, providing further evidence that degradation is heavily dependent on the duty cycles employed.

Ma et al. [170] used the profile of an electric Bus operating in Beijing to determine and quantify the degradation and cycle life for LMO cells for this particular use case. It was observed that a high DOD and elevated temperature negatively affected the capacity and impedance of the cells. However, the use of a realistic profile allows identifying dominant mechanisms under real world operation rather than specific profile characteristics. Through cross-referencing the observed degradation against literature, the likely degradation paths could be determined.

Friesen et al. [171] tested commercial 40Ah G-NMC pouch cells under a galvanostatic charging and discharging regime, and under a duty cycle derived from the common Artemis Driving Cycle between 80% and 20% SOC, at 25°C and 40°C. Regular characterisation tests were carried out to track discharge capacity and cell impedance at 50% SOC. EOL was defined as 200.000 km equivalent for the cell tested under the Artemis regime, and 80% retained capacity for the galvanostatic regime. The cells exhibited an approximately linear capacity fade until a retained capacity of 90% followed by accelerated degradation, and cells cycled at the higher temperature displayed worse degradation compared to the cells cycled at 25°C. A post-mortem analysis identified SEI growth and lithium plating as the main degradation mechanisms, and localised ageing near the tabs, which the authors attributed to a higher level heat generation.

A standardised approach to degradation testing is presented within the testing standards IEC 62660-1, ISO 12405-2, and DoE Battery Test Manual. These standards contain cycle life testing procedures to determine the degradation characteristics of battery cells and systems. An overview and comparison of the cycle life testing procedure for the three standards and guidelines is shown in Table 2-4. ISO 12405-2 and IEC 62660-1 cycle life tests both contain two testing profiles A and B. The objective of Profile A is to represent a battery profile associated with “typical driving” on a road, the objective of Profile B is to represent a battery profile of a vehicle driving uphill [34]. The Dynamic Stress Test (DST) as defined within the DoE Battery Test Manual uses a similar profile to Profile A. These profiles are illustrated in Figure 2-18, where discharging is identified by negative values, charging by positive values. The DST testing profile is a simplified version of the Federal Urban Driving Schedule (FUDS) with the same average value of net discharge power. The net discharge power is 12.7% of the peak discharge power; the mean discharge power is 25.5% of the peak discharge power. The FUDS is the power profile that is produced when the Federal Testing Procedure (FTP-75) driving cycle is applied to a specific EV [172]. A key assumption for this simplification is that the transient profile of the FUDS can be

simplified to a periodic profile utilising seven power amplitudes without affecting the outcome of degradation testing and cycle life. However, this assumption is problematic for degradation testing as the research discussed above suggests otherwise [163,169]

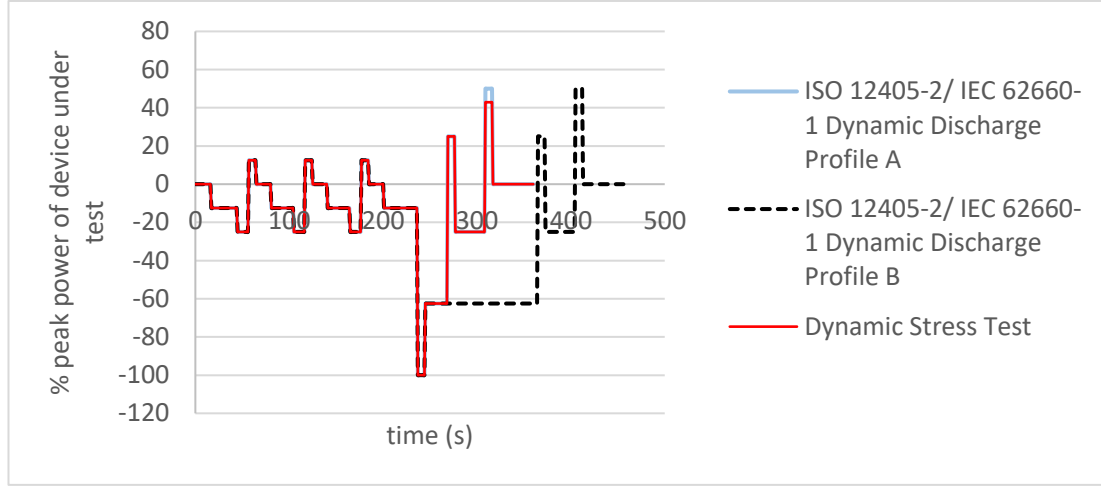


FIGURE 2-18 – CYCLE LIFE TESTING PROFILES

Although the testing profiles appear to be very similar for all three standards, the testing procedures and the testing peak of power vary substantially (see Table 2-4). The term peak power ( $P_{CLT}$ ) in Figure 2-18 is not uniformly defined as each testing procedure offers different, sometimes ambiguous definitions, for differing reference frames (cell, module, pack).

For the IEC-62660 standard  $P_{CLT}$  is equal to the maximum power required of the cell by the vehicle, if its value is smaller than the maximum power allowed by the cell manufacturer. For the ISO-12405-2 standard  $P_{CLT}$  on the y-axis is defined as the 10s discharge pulse power at room temperature (RT) and 35 % SOC. This is defined in equation (26).

$$P_{CLT} = P_{10s,dch} = U_{35\%,RT} * I_{DP,Max} \quad (26)$$

$I_{DP,Max}$  is the maximum rated pulse discharge current as defined by the manufacturer,  $U_{35\%,RT}$  is the average voltage of the battery during the test pulse [35].

$P_{CLT}$  in the DST is 470 W/kg on pack level and 700 W/kg on cell level for a 30s peak discharge pulse. These targets represent the technical requirements for the commercial viability for Li-ion battery use in EVs. The DST test requires 45kWh on a system level to be depleted in every test cycle, and a lifetime of 1000 cycles, equating to a total energy throughput of 45 MWh during the system's life.

Sequence	IEC-62660	ISO-12405	DoE-DST
Device tested	Cell	Battery system	Cell, module or system
Preconditioning	N/A	Discharge capacity test	C/3 constant current & HPPC
Reference Tests	Discharge capacity & dynamic discharge capacity test at 25 °C & 45 °C, HPPC	Discharge capacity at 25°C & -10°C	Discharge capacity, Low-current HPPC, Peak Power, HPPC verification
Cycle sequence	T = 45 °C ± 2 K 100%-20% SOC	T = 25 °C & 45 °C 100%-20% SOC	T = 30 °C SOC 100% - 20% SOC or agreed with manufacturer
Step 1	Full discharge	Standard discharge	Full charge
Step 2	Full charge	Standard charge	Discharge to specified SOC
Step 3	Profile A until $C_D = 50\% \pm 5\%$ Profile B Profile A until CD = 80%	Profile A - Profile B - Profile A until SOC = 20 % or $U < \text{limit}$	DST until net energy = 45kWh on a System level, or as specified by manufacturer at the cell level 15 min rest
Step 4	N/A	Charge to 100% SOC	Charge to 100% SOC
Step 5	Repeat Steps 1-3 for 28 days, proceed to characterisation if $U < \text{limit}$ during 3 - 5	Repeat Steps 3 and 4 for 28 days	Repeat steps 3 and 4 for 300-600 times (32 days)
Step 6: Reference Tests:	Capacity test & dynamic discharge capacity test (25 °C only), HPPC	Capacity & HPPC at 25 °C, standard charge <b>Every 8 weeks:</b> additional capacity and HPPC at -10 °C, standard cycle at 25 °C	C/3 constant current test Low-current HPPC test Peak Power Test HPPC Verification Test
	Repeat steps 1-6	Repeat steps 3-6	Repeat steps 3-6
Termination conditions	<ul style="list-style-type: none"> <li>- The test sequence is repeated 6 times</li> <li>- Any performance criteria measured &lt; 80% of the initial value</li> <li>- upper cell limit is reached during testing</li> </ul>	<ul style="list-style-type: none"> <li>- Cycle life test cannot be performed</li> <li>- Performance criteria can no longer be reached</li> <li>- Agreement between manufacturer and customer</li> </ul>	<ul style="list-style-type: none"> <li>- Test profile cannot be executed within Voltage limits</li> <li>- Performance criteria can no longer be reached</li> <li>- 1000 DST cycles</li> <li>- Capacity or peak power drops below target</li> </ul>

TABLE 2-4 – OVERVIEW AND COMPARISON OF CYCLE LIFE TESTS IN IEC-62660, ISO-12405, AND DoE BATTERY TEST MANUAL

Based on the literature discussed, the use of representative transient profiles for degradation testing is essential, as the shape of the testing profile is an influencing factor in the degradation of the cell under test. Although a number of research articles exist, in which transient degradation testing profiles are used, none of these studies explore testing profiles from a HP-BEV perspective. The discussed battery testing standards aim to provide a unified approach to produce comparable results between different cells, but are broadly based on driving cycles. Thus, they also do not cater toward HP-BEV applications.

## 2.7 Performance Testing

Performance testing partially overlaps with cycling degradation and characterisation testing. Instead of long-term degradation, other test outcomes such as range estimation and thermal performance of cells are the focus of these tests. Barcellona et al. [173] characterised cells to parameterise an ECM to predict EV range. To validate the model, cells were subsequently tested with duty cycles, which were derived from the New European Driving Cycle (NEDC) and SC03 driving cycles with the aid of an electric vehicle model, at 0°C, 25°C and 50°C. Based on these tests the driving range for the BEV was determined.

As increased cell temperature and cell temperature gradients have a detrimental effect on battery life, tests that determine the thermal behaviour of cells are particularly important to evaluate the requirements for a BMTS. Worwood et al. [6] developed a 1D electrochemical model coupled with a 3D thermal model for a 20 Ah G-LFP pouch cell. The model was validated against temperature measurements taken from a test cell subject to 1C, 3C and 5C continuous discharge conditions. The resulting model was used to determine the temperature increase of the cells when subject to an HP-BEV duty cycle, the development of which constitutes part of this thesis. In an additional study, Worwood et al. [3] developed a thermal model for cylindrical G-NCA 18650 cells with a capacity of 2.9 Ah. The model was validated by subjecting cells to a dynamic current profile at temperatures of 10°C and 25°C. The developed model facilitated the prediction of cell temperature under PHEV and a HP-BEV duty cycle and the conceptualisation and analysis of a radial tab cooling solutions suitable to deliver an acceptable cooling solution. Using these duty cycles, the authors investigated aluminium and copper as potential materials for a single edge fin cooling solution on G-NMC pouch cells [7].



## 2.8 Conclusion & Definition of the Knowledge Gap

The problem statement in Chapter 1 outlines that the differences in usage profiles between HP-BEV applications such as racing and those scenarios associated with driving on public roads will likely influence the thermal performance and long-term degradation of LIBs employed within EV energy storage systems. To address “Research Question 1: Do existing LIB testing methodologies adequately represent HP-BEV racing applications?”, this chapter has critically reviewed the fundamentals of LIB operation and degradation, as well as the existing body of literature regarding LIB characterisation, performance and degradation testing.

The electrical characteristics and performance of cells are largely determined by the choice of active materials. During use and storage, the performance of cells degrades. The degradation is broadly grouped into surface film effects including SEI growth and metal plating, structural changes on an atomic level such as Jahn-Teller distortions, mechanical changes on a particle level such as electrode cracking, and parasitic side reactions including binder decomposition. The onset and progression of degradation is complex, and no mechanisms occur exclusively. Furthermore, it is dependent on environmental conditions such as temperature and operational parameters such as current, SOC and DOD.

The onset and progression of LIB degradation over time can be identified through regular characterisation testing and tracking the test outcomes such as ECM parameters and energy capacity. Although specific degradation mechanisms cannot be quantified, their effect on performance characteristics can be measured through a combination of non-destructive techniques such as energy capacity and EIS testing.

The use of transient duty cycles within the LIB degradation and performance-testing framework for EVs focusses primarily on driving scenarios on public roads. This is exemplified through the common use of duty cycles derived from existing driving cycles, such as the cycle life testing profiles described in international standards. Research articles which do not utilise existing driving cycles often utilise duty cycles from recorded driving data. During everyday operation on public roads, all vehicles are typically restricted by traffic congestion and regulations. As such, the transient duty cycle profiles of HP-BEVs do not greatly diverge from those of the vehicles around them. For those specific scenarios, the existing testing procedures are believed to be sufficient to predict cell thermal behaviour and degradation.

### 2.8.1 Definition of the Knowledge Gap

On-road driving and HP driving on dedicated racing circuits are fundamentally different and so are the resulting electric loading profiles for batteries. Thus, the performance and long-term degradation behaviour of LIBs is expected to be different for those two use cases. As reviewed within sections 2.6 and 2.7, to obtain representative datasets, the experimental investigations into the behaviour of batteries should be underpinned by realistic duty cycles associated with the intended battery use. Whilst this is currently commonplace for public road driving, the existing body of literature pertaining LIB performance and battery degradation does not specifically cater to the fundamentally different driving scenarios encountered within HP and track driving. The results obtained from existing research are therefore assumed to be not transferrable to HP-BEV applications. The lack of experimental procedures required to conduct investigations into the performance and degradation of LIBs within HP-BEV applications constitute a knowledge gap, as illustrated in Table 2-5.

Procedure	On-Road driving	HP-BEV application
Characterisation Testing	☑	☑
Performance Testing	☑	☒
Degradation Testing	☑	☒

TABLE 2-5 – KNOWLEDGE GAP IN EXISTING TESTING PROCEDURES

This knowledge gap is compounded by a lack of suitable HP-BEV testing cycles that may underpin experimental investigations or simulation studies. As such, prior to any experimental study, a strategic requirement exists to define a methodology that may be used to create a representative HP-BEV duty cycle.

## 3 A Review of Duty Cycle Construction Methods

---

### 3.1 Introduction

The transient duty cycles utilised within existing research concerning the performance and degradation of LIBs in passenger vehicles are often derived from driving cycles with the aid of a suitable vehicle model [36,173,174]. These driving cycles are usually based around real world driving data, for example the ARTEMIS driving cycles [175,176], or synthetically produced as in the case for the soon to be phased-out New European Driving Cycle (NEDC). The topic of degradation and performance testing of LIBs in the context of HP-BEV and racing applications remains largely unexplored within the existing body of literature. To progress the research into a better understanding of the performance requirements and cell degradation of LIBs within HP-BEVs it is first necessary to conduct experimental work with a suitable HP-BEV duty cycle. Battery duty cycles associated with driving on a race circuit are defined through the performance parameters of the vehicle being used, the ability of the driver, and the physical aspects of each individual track. To test every possible duty cycle within a laboratory setting is not feasible within the context of a PhD studentship. Instead, testing should be conducted using a battery test cycle that is representative of a larger number of HP-BEV use cases. Currently there is no such duty cycle available within the literature, which consequently leads to another research question:

#### 3.1.1 Research Question 2: How can a duty cycle representative of HP-BEV racing applications be defined?

A representative duty cycle should capture the signal characteristics and conditions that are responsible for degradation and ageing of LIBs in a representative manner. It should contain a realistic composition of these operating conditions in appropriate proportions and ensure those operating conditions which mostly affect cell ageing such as high current amplitudes, the frequency of their occurrence [47,105,116] and the resulting cell-heating [47,98,99,116] are preserved. The resulting testing data from batteries undergoing those cycles should provide information about representative cell-heating profiles, ageing rates, the most prevalent ageing mechanisms and what conditions should be avoided to improve battery life. To underpin this study, this chapter provides a critical review of methods for the derivation of a representative duty cycle.

### 3.2 Driving Cycle Methods

The underlying principle of driving cycle construction is to develop a profile whose properties match specific criteria extracted from a database of recorded driving scenarios. Most of these construction methods follow broadly the same steps. Initially, real-world driving data is collected, secondly, the driving data is segmented into shorter sections, these segments are rearranged to construct several cycles, and lastly these cycles are evaluated, and a final profile is selected. Although the measured quantities of driving cycles (speed vs. time) and duty cycles (battery power demand vs. time) are different, the assertion is that the methodologies employed within driving cycle research lend themselves to the development of a HP duty cycle.

### 3.3 Data Collection

For driving-cycles based on real world driving data, there are two main approaches to driving data collection: on-board measurements, and the car-chase method. On-board measurements are obtained by instrumenting privately owned vehicles of volunteers or lending out instrumented vehicles to volunteer drivers for their everyday use. This approach has been used amongst other studies for the development of the FTP-75 [177], and the ARTEMIS project [175,176]. For the car-chase method a single or several vehicles are equipped with driving data recording instrumentation and follow randomly selected vehicles along a chosen route or within a certain geographic location at an approximately constant distance recording their velocity and acceleration. This method has been employed successfully in several driving cycle studies, for example within Hong Kong [178,179], Los Angeles [180], Athens [181], and Sydney [182].

An advantage of the on-board method is that data is collected straight from the vehicle thus providing a more accurate measurement of driving conditions compared to the car-chase method. One disadvantage identified with the on-board method is that the driver's knowledge of being recorded may influence their driving behaviour [183]. In contrast, the drivers of vehicles followed for the car-chase method are assumed unaware that their driving patterns are being recorded, thus their driving should remain uninfluenced.

Driving patterns on public roads vary significantly depending on geographic regions [180]. Furthermore, traffic and population density, frequency of junctions, and traffic lights influence the magnitude, frequency and duration of steady state speed, acceleration and deceleration events in urban, rural and motorway driving [180]. As such, driving cycles are often specific to a certain geographic location and road type. Depending on the goal of the study, the routes over

which driving is recorded include home-to-work trips [184], following a specific route during “rush-hour” [185], or general vehicle use over a prolonged period of time [175]. Other factors influencing driving pattern are driver demographic and vehicle performance [186,187], with average driving speeds and accelerations being systematically higher for higher powered vehicles [175,176]. To capture a broad range of driving, studies using the on-board method often use a fleet of different drivers and vehicles rather than employing just one driver and vehicle type [175,176,188,189].

Within the context of HP duty cycles, regarding data collection there are two main factors to be considered compared to the methods presented within the existing driving cycle literature. Firstly, rather than collecting speed vs time traces the battery power demand should be recorded through voltage and current measurements. Secondly, the use case of HP driving on dedicated circuits is restricted by fundamentally different limitations compared to driving on public roads. Driving on racing circuits, and thus the resulting battery power profiles are predominantly limited by driver ability, vehicle power and handling limits and the layout of the circuit, instead of traffic volume, road regulations and road type as is the case for public roads. As such, data should be recorded directly from the driven vehicle via on-board measurements, as following a vehicle at a fixed distance at handling limits is an unrealistic task for most drivers.

### 3.4 Data Segmentation, Processing & Cycle Construction

#### 3.4.1 Random Microtrip Cycles

A common cycle construction method utilises a random selection of microtrips. The data processing and construction sequence is illustrated within [Figure 3-1](#) and described below.

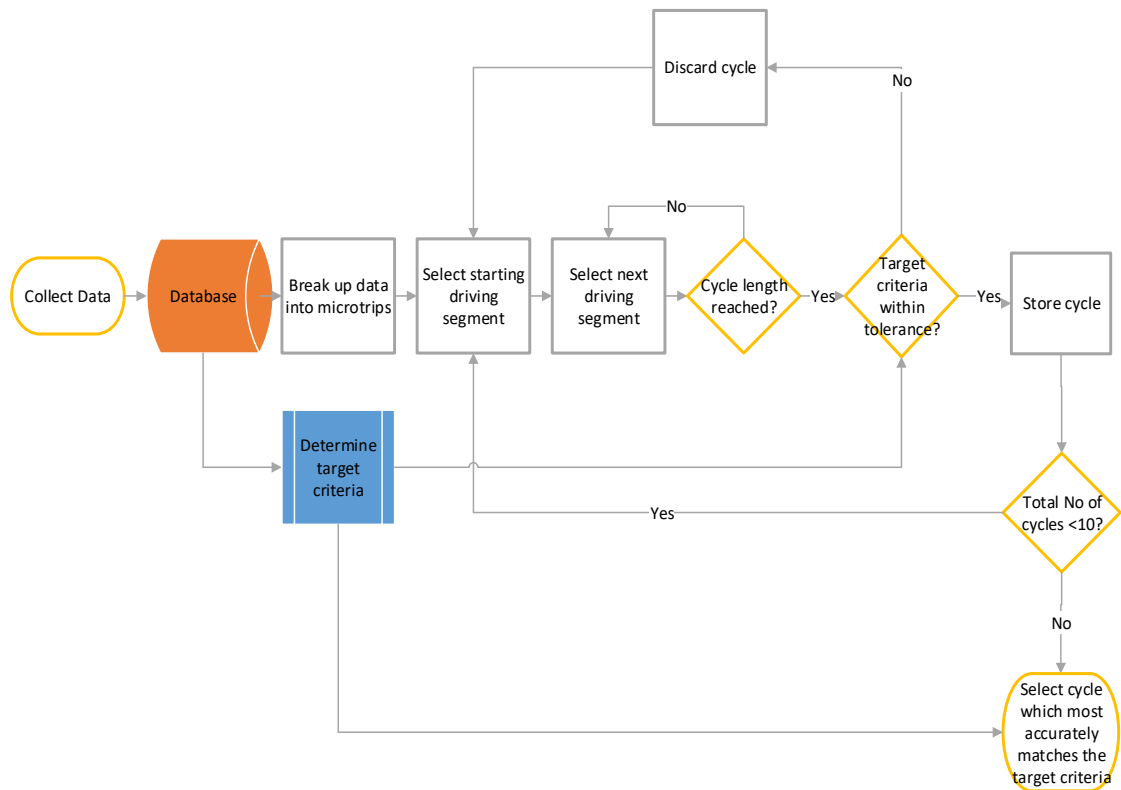


FIGURE 3-1 - THE PROCESS OF DETERMINING A RANDOM DRIVING CYCLE, AS DESCRIBED WITHIN [178,179,184,189]

Following data collection, the vehicle speed-time traces are broken up into microtrips. A microtrip can be defined in several ways. In most cases, it represents a driving segment bound by stopping phases as illustrated in Figure 3-2 on the LA 92 driving cycle. For long sections of highway driving where a stop does not occur, they can alternatively be defined by an arbitrary duration of time, or change in driving mode such as acceleration or braking [188].

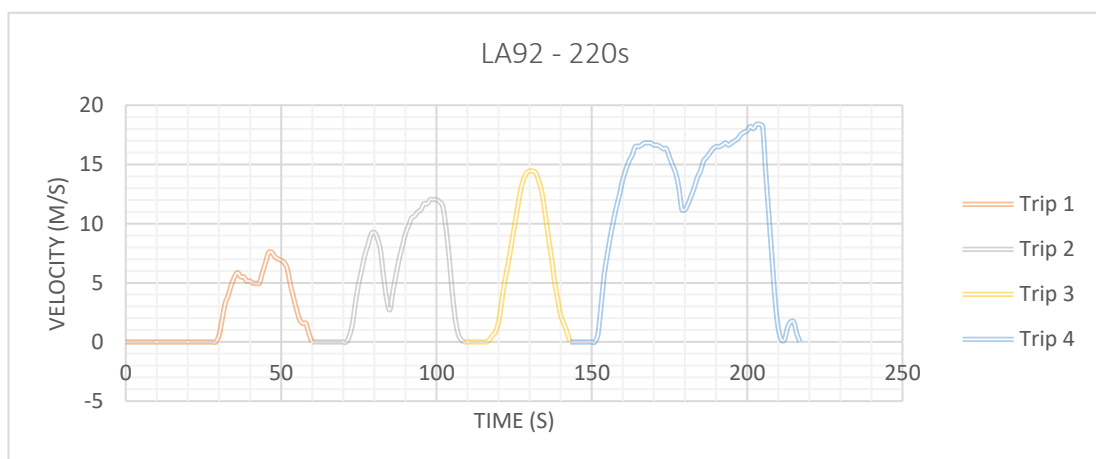


FIGURE 3-2 - MICROTRIPS FOR THE FIRST 220S OF THE LA92 CYCLE [188]

In a second step, the desired cycle length is chosen and target criteria for a driving cycle are determined. These target criteria serve as a tool for comparison between the constructed driving cycle and the source driving data. By matching the target criteria of a constructed cycle to that of the source data a statistically representative cycle may be found [188]. In the case of driving cycles, the choice of target criteria is often based on driving features that correlate to exhaust emissions and fuel consumption. The emphasis is put on average speed, average running speed, acceleration, idle time, and the speed-acceleration frequency distribution (SAFD) [178,182–184,190,191]. The SAFD expresses the amount of time spent at each instantaneous speed and acceleration. An example is illustrated in Figure 3-3 reference.

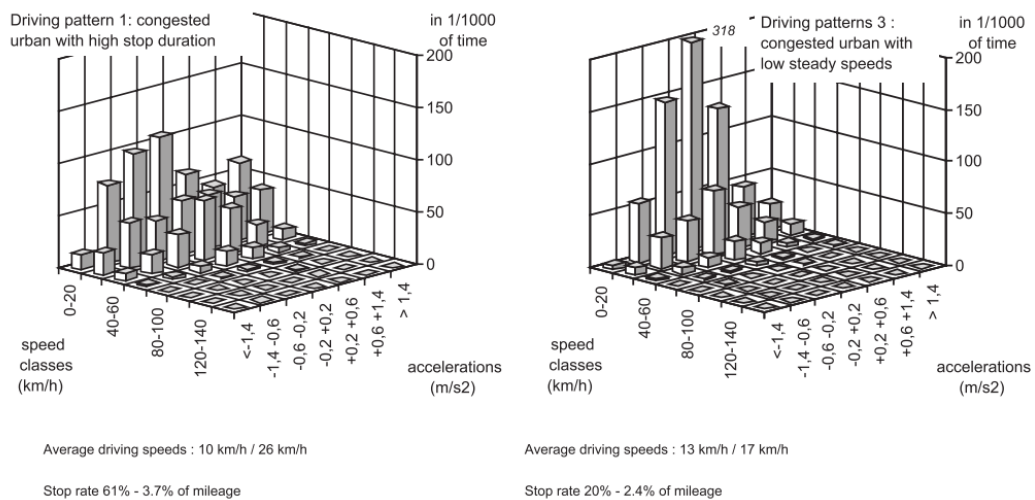


FIGURE 3-3 - ILLUSTRATION OF SPEED ACCELERATION CROSS DISTRIBUTIONS OF TWO URBAN DRIVING SCENARIOS FROM [175]

For cycle construction, microtrips may be selected randomly or quasi-randomly until the desired cycle length is reached. Quasi-random selection refers to studies where microtrips are selected to match the overall SAFD before final comparison. The resulting cycle is referred to as a candidate cycle, which is then analysed and the target criteria and deviation from the source data are calculated. A candidate cycle is accepted when the characteristics from the cycle are within a certain threshold, typically 5% or 10% [178,179] of the target criteria of the source data. This process is repeated until 10 or more [178,179] of those cycles have been found, from which the cycle that most accurately matches the target criteria, based on a lowest cumulative error, is chosen. One difficulty with such a construction method is the appropriate selection of target criteria. By choosing statistically average values, more severe conditions may be underrepresented within the resulting driving cycle. For example, two driving segments with similar average velocities and duration may vary substantially with respect to instantaneous values of velocity and instances of high and low acceleration and deceleration rates, which in the

context of BEVs may not affect the overall energy requirement for a segment but influences the required power rating of the energy storage system.

The microtrip method can be adapted to duty cycles. Instead of vehicle speed traces, battery power profiles could be segmented into “duty-pulses” which are separated by instances, where no charging or discharging occurs. Using this criterion for segmentation may be suitable for driving recordings on public roads, as the resulting segments would directly relate to microtrips. For HP driving scenarios, this approach is impractical, since driving on a circuit does not contain frequent instances at which the vehicle stops, and no power is drawn from the traction battery. Instead, the power demand profile should be broken up into individual charging and discharging pulses, thus segmentation would be based on a zero crossing of electrical current. The selection of target criteria, rather than concentrating on driving features should focus on those aspects of the battery profiles that have a direct impact on battery degradation and heating. Reconstruction of a new cycle can then be undertaken following the same remaining steps as the driving cycle method illustrated in Figure 3-1 above.

#### 3.4.2 ARTEMIS Cycles

The construction of the ARTEMIS driving cycles, described within [175,176], follows a probability based approach. A database of driving records is split into segments of equal size (i.e. a time duration of 120 seconds), similar to microtrips. Each segment is analysed with respect to idling duration and SAFD. The segments are subsequently classified using correspondence analysis based on the chi-squared distance of their respective SAFDs. The chi-squared distance ( $d$ ) between two normalised histograms  $x = [x_1, x_2, \dots, x_n]$  and  $y = [y_1, y_2, \dots, y_n]$ , with  $n$  bins each can be calculated using equation (27).

$$d(x, y) = \sum_{i=1}^n \frac{(x_i - y_i)^2}{2} \quad (27)$$

From the equation above the smaller the chi-squared distance between the SAFDs of two segments, the more similar they are. Using this information, segments are then clustered and sorted into bins associated with specific driving conditions. In the study described within [175,176], conditions such as congested urban, free-flow urban extra-urban, motorway, etc. were identified through data measured under known conditions, as identified by researchers in the measuring vehicle.



The overall driving data is analysed further to in terms of trip history based on the driving conditions to establish a typical composition of driving cycles in urban, rural, and motorway driving scenarios. Cycles are then constructed from the segments by selecting successive segments from bins to match observed probabilities for successive driving conditions. The selection of individual segments to optimise the distance of each segment from their cluster centre, and to match target criteria, such as start and end speed of each segment, road specific SAFDs, and the composition and chronology of driving conditions.

Several facets of this methodology need to be adapted to make it suitable for the creation of a HP duty cycle. In principle, each profile could be split into homogeneous segments and each segment could be analysed through a power demand vs rate of change in power demand frequency distribution, similarly to the SAFD. The segments could then be clustered based on their current amplitude and sorted into bins using the same method as described by Andre et al. [175,176].

For any circuit, a driving cycle, and the battery power profile associated with it would be expected to be approximately periodic in nature, with each period limited to a few minutes. The driving conditions encountered over a lap could be associated with the physical layout of the circuit, i.e. there is expected to be several straight sections of varying length, and several corners of different radii. As such, an obvious way of classifying the data is to associate segments of the recorded battery profiles with different types of corners and straights. When a vehicle is coming to the end of a straight and entering a corner, the driver would be expected to apply the brakes. This would result in a change from discharging power to charging power for vehicles with, or alternatively to a battery rest period for vehicles without regenerative braking capability. Once the desired cornering speed is reached, a driver would be expected to apply the accelerator pedal again, thus changing to a new period of discharging power demand. As such, a much more practical approach would be to use a segmentation of charging and discharging pulses as discussed in the previous section, and subsequent clustering into pulses based on pulse duration.

A disadvantage of the methodology employed within the ARTEMIS project is the amount of data required. To classify the data into several driving classes requires a dataset large enough to achieve meaningful clustering results. The specific size would need to be determined experimentally. The dataset used within the study by Andre et al. [175] utilised more than 2000 hours of recorded real-world driving traces from several countries, drivers and vehicles. This is not achievable with the monetary and time constraints associated with this work.

### 3.4.3 Markov Chain Cycles

Lin et al. [192] introduce a Markov chain approach to derive a vehicle driving cycle. A Markov chain is a stochastic model describing a sequence of events in which the probability of each event occurring depends only on the state in the previous event. Considering a set of states ( $S$ ) displayed in equation (28).

$$S = \{s_1, s_2, \dots, s_n\} \quad (28)$$

The starting state is defined by an initial probability distribution on  $S$ , and moves successively from one state to another. This state change occurs according to a transition probability (defined below) that only depends on the current state. Assuming the process starts in state  $s_i$  and moves to state  $s_j$ , the probability of this change is given by  $p_{ij}$ . The probability of the state remaining in  $s_i$ , is given by probability  $p_{ii}$ . A Markov chain with  $m$  states has  $m^2$  transition probabilities. The transition probability matrix is displayed in (29) and (30).

$$Q_{ij} = P(s_{n+1} = j \mid s_n = i) \quad (29)$$

$$Q_{ij} = \begin{bmatrix} s_1 \rightarrow s_1 & s_2 \rightarrow s_1 & \cdots & s_m \rightarrow s_1 \\ s_1 \rightarrow s_2 & s_2 \rightarrow s_2 & \cdots & s_m \rightarrow s_2 \\ \vdots & \vdots & \ddots & \vdots \\ s_1 \rightarrow s_m & s_2 \rightarrow s_m & \cdots & s_m \rightarrow s_m \end{bmatrix} \quad (30)$$

The current state is  $s_n$ , the next state is  $s_{n+1}$ , and  $P$  is the transition probability from  $s_n$  to  $s_{n+1}$ .

Within [192], each journey was broken into segments based on acceleration and deceleration and sorted into modal event bins based on average, minimum, and maximum speeds and acceleration rates. These modal event bins containing original journey segments were then defined as the states in the state space form. The transition probability matrix was populated based on observations of the frequency of one state changing to another. The segmentation of the source data could also be done according to microtrips and trips could be clustered into bins representing different states associated with specific driving conditions.

A starting segment is chosen according to desired initial criteria, the next modal event bin is selected using a random number generator weighted with the transition probability matrix based on the current modal event bin. The best-fit segment within the bin is chosen. Within [192], best-

fit is determined by matching the initial speed of the new segment to the end speed of the previous segment to within 0.5mph, and by matching the SAFD of the resulting profile to the desired SAFD. These steps are repeated until the cycle length reaches the desired trip length to produce a candidate cycle. This process is repeated to generate several candidate cycles, from which a single representative cycle is chosen, based on desired target criteria, as for the random process approach.

An example of the implementation of a Markov chain approach for the development of several duty cycles for battery degradation and cycle-life testing is presented by Groot et al. within [169,193]. A HEV prototype bus was driven along a city-bus route in Gothenburg, Sweden, and battery current, voltage, SOC and temperature were recorded using a sampling rate of 10 Hz. The current vs time profile was subsequently filtered with a 10-point moving average filter in combination with a sample-and-hold filter, resulting in a stepwise profile with a minimum step duration of 1s. This is illustrated in Figure 3-4. It can clearly be seen that within the filtered profile, some dynamics are not preserved. Within [169] the author states that this processing step is necessary to reduce the likelihood of differences between profile setpoints and actual values during subsequent experimentation, thus improving test robustness. Although this may not be a problem for testing within heavy-duty HEV applications, this processing step may be problematic for HP applications. The reason for this are frequent transient changes that may be expected during racing driving.

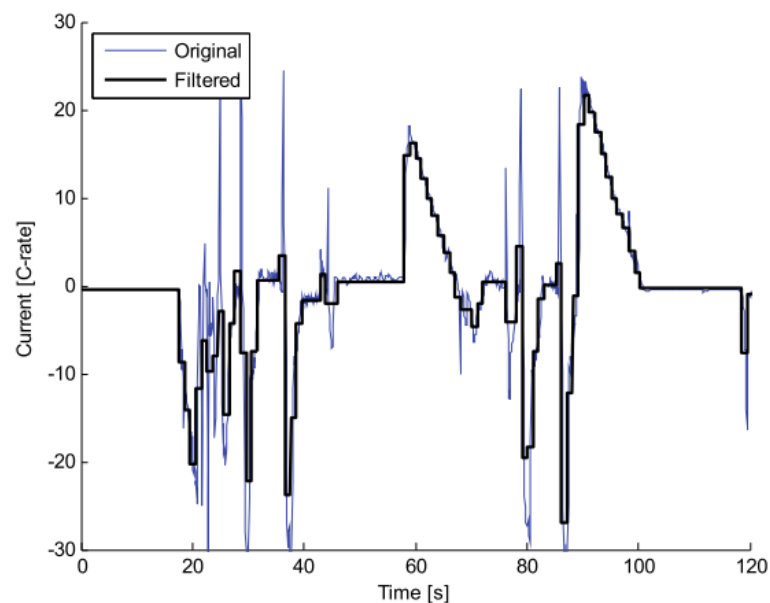


FIGURE 3-4 - HEV DUTY CYCLE RECORDING AND FILTERED VERSION. MANY OF THE DYNAMIC CHANGES ARE NOT PRESERVED WITHIN THE FILTERED PROFILE. FROM [169].

To comply with the rating of the cells employed within the research, the author further scaled the profile down to 80% of its original value, and reduced the peak charging current. Furthermore, to reduce the risk of accelerated ageing from high average SOC and increased temperatures, the target SOC range of the filtered profile was adjusted to a range between 25% and 55% SOC, and the target temperature modified to fall between 25°C and 45°C. This cycle was subsequently used as a reference load cycle from which new synthetic profiles were derived using a Markov chain process.

The reference cycle was defined to contain  $m$  unique states, corresponding with unique values of the profile itself. The  $m \times m$  transition probability matrix ( $Q$ ) was populated by stepping through each sample and incrementing the corresponding state  $Q_{ij}$ . Subsequently, each value in a column was normalised with the total number of samples in each column, such that the sum of each column equalled 1. Within [193], the author details that this process of populating the probability matrix can be expanded to any number of duty cycles, provided they all are sampled at the same rate, and the total number of cycle samples are used to normalise the columns. A duty cycle was then created, using a random number generator and a support matrix  $Q_s$ , where the probability values in each column were replaced by the cumulative column sum of  $Q$ , and the element closest to the generated number was selected as the next state.

As HEVs are required to operate within a narrow SOC operating range, the author within [193] implemented an SOC estimation algorithm based on a single resistance ECM to modify the amplitude of the selected state to prevent a duty cycle to cause a battery to exceed SOC limits of a cell under test. Due to the relatively narrow SOC range and temperature operating windows, a constant OCV and resistance was suggested. This simplification would not be appropriate if the target application required larger temperature and SOC operating ranges. Furthermore, the restriction of the cycle construction based on SOC range is not necessary for BEV applications operating throughout the entire operating range. This process was followed to create several candidate cycles, which were subsequently compared to the original reference cycle with respect to the SOC over the duration of the cycle, RMS power and maximum energy window, difference in power and energy distribution.

Although the construction method varies for the two discussed Markov chain construction approaches by Lin et al. [192] and Groot et al. [193], the underlying principle is still to match the final duty cycle to some desired target criteria. As such, they contain similar limitations to the previous construction methods, which is the selection of appropriate targets. The approach as suggested by Groot et al, which requires the filtering and smoothing of data is problematic for

the derivation of a duty cycle for HP applications, as fast transient changes and dynamics could be lost. Within [169] it is stated that the excluded fast transients in the original cycle are not believed to have a significant impact on cycle life, but no evidence is given to support this. As fast transient changes are an intrinsic element to HP automotive applications, as will be shown in detail within Chapter 4, the author asserts that such a filtering process would not be suitable in this case. Without smoothing, the number of individual states would be inadequately large, especially if a large number of duty cycles were to be employed.

#### 3.4.4 Best-fit Cycles

Rather than deconstructing a database and subsequently reassembling duty cycles, another approach is to select a specific duty cycle from within the database, which most closely matches some target criteria extracted from the database. One example of this approach is the development of the Edinburgh Driving Cycle (EDC) [194].

For the EDC, six pre-determined routes in the city centre of Edinburgh, Scotland were driven at four different times of day and data was recorded using the car-chase method. The routes were chosen to represent typical commuting journeys. Additional information such as abnormal traffic and weather conditions, distances and start and end times of each segment of the route were recorded by an assistant who was in the car with the driver, and traffic volume flow data for major roads in the city centre was provided by the City of Edinburgh Council.

The resulting speed-time traces analysed were analysed with respect to the amount of time spent at five specific speed intervals. A number-code was generated for each journey by going through the data second by second and incrementing a counter in a specific speed interval bin for each second at that speed. This is illustrated on the example in Figure 3-5, where a journey contained 402 s at a speed of 0 mph, 208s between 0 and 15 mph, and so forth, resulting in the final code 402-208-103-165-167.

Code for route 1 on 13.8.1999 at the morning period

	Code	402	208	103	165	167
Time	Vehicle speed (mph)	0	0–15*	15–20	20–25	25–30
8:32:51	28.1					1
8:32:52	28.4					1
–	–	–	–	–	–	–
8:33:28	20.4				1	
8:33:29	21.3				1	
–	–	–	–	–	–	–
8:34:08	15.8			1		
8:34:09	18.07			1		
–	–	–	–	–	–	–
8:36:02	14.0		1			
8:34:03	11.2		1			
–	–	–	–	–	–	–
8:36:05	0.0	1				
8:36:06	0.0	1				
–	–	–	–	–	–	–
Total seconds		402	208	103	165	167

\*The interval designates a speed greater than zero and less than 15.

FIGURE 3-5 - TABLE CONTAINING THE CODE FOR A JOURNEY ANALYSED BY TRAFIX METHOD, FROM [194]

The total number of codes was reduced to 72 by calculating average codes for each of the six routes, at the three measured periods, one for weekdays, one for Saturdays, and one for Sundays. The supplementary traffic information was used to determine which routes were travelled on most, at what times, and which were most representative of the average traffic in the city. Weighting factors were calculated based on the traffic volume flow along each route compared to the overall traffic volume flow within the city. These weighting factors were then used to calculate a final weighted code for the EDC cycle. This final code was then compared to the database of all original driving recordings, and the recording with the closest matching code was selected as the EDC.

To adapt this method to battery duty cycles, instead of speed interval bins, appropriate power level bins need to be defined, and codes can be generated for a lap of each circuit. The sampling frequency of 1 Hz used within the EDC development may not be sufficient for the dynamics of a HP application, and thus a higher frequency should be used. The use of weighting factors with respect to traffic volume would not be applicable for track driving, and as such the method could be simplified. One concern with this approach is that by choosing a single individual cycle, some features present in other duty cycles may be lost.

### 3.5 Frequency Domain Methods

The existing driving cycle analysis and construction methods discussed operate primarily within the time domain. Driving data is recorded as a time series, and in most cases analysed using

several easily identifiable traits such as average speed, time on idle, or acceleration rates. An alternative, relatively unexplored approach would be to analyse the data within the frequency domain and construct a signal with a specific amplitude spectrum. Recent publications by Widanage et al. [141,142] show that the consideration of target amplitude spectra in the design of excitation signals for cell characterisation tests can positively affect the representativeness of the testing procedures. The research identifies that pulse tests often used to parameterise ECMs do not cover the same bandwidth as the validation test cases such as dynamic duty cycles. As such, the resulting ECMs can underperform when simulating a dynamic scenario, as the parameterisation dataset does not contain the same excitation frequencies and amplitudes as the validation profile.

Since the voltage response of an LIB to a current input is dependent on the current input amplitude spectrum, this should be taken into account for the design of long term degradation testing. As discussed within Chapter 2, the operating potential of a cell is the culmination of the OCV and polarisation caused by internal cell resistance, charge transfer phenomena and concentration changes. As such, any profile employed to conduct cell degradation testing for a specific test case should not only be representative within the time domain but also within the frequency domain as to excite the cell under test over a representative frequency range [141,142].

The amplitude spectrum of a periodic time-based function  $x(n)$  describes how much power the signal contains at each frequency  $f$ . This spectrum may be obtained from the Fourier series. The Fourier series of a time-based function  $x(n)$  is defined in equation (31).

$$x(n/f_s) = A_0 + \sum_{k=1}^{\infty} A_k \sin(2\pi n f_k + \phi_k) \quad (31)$$

$A_k$  is the amplitude and  $\phi_k$  is the phase of the  $k^{th}$  harmonic,  $f_k$  is the frequency at  $k^{th}$  harmonic and is  $f_k = k f_s / N$  with  $f_s$  the sampling frequency, and  $N$  is the number of samples per period. A detailed discussion into the derivation and use of Fourier Series for signal analysis is presented within a number of educational text, such as [195–197]. As such, provided a target amplitude spectrum is known, a profile can be synthesized using equation (31), which satisfies the desired target criteria within the frequency domain.

However, a desired amplitude spectrum alone may not be sufficient to design an appropriate testing profile. The selection of phases  $\phi_k$  has a direct impact on the shape of the profile within the time domain, such as influencing the resulting profile's crest factor, defined as the ratio of the profile's absolute maximum value over its root mean square (rms) [198,199], and magnitude distribution or histogram [200]. As discussed in Chapter 2, the magnitude and duration of charging and discharging pulses are directly linked to cell self-heating and degradation, as is the total energy throughput over time. Consequently, the phases should be selected to result in a testing profile representing these features within the time domain.

The research presented within [200] describes a time-frequency domain swapping algorithm by which a signal is constructed which matches a user imposed amplitude spectrum in the frequency domain and whose phases are optimised to match a desired inverse Cumulative Distribution Function (iCDF) in the time domain. The Cumulative Distribution Function (CDF) for a quantity  $y$  that takes a real value at random is defined in equation (32). The right-hand term describes the probability that a given variable  $y$  has a value less than or equal to a specific value  $B$ . The function  $F(B)$  is limited by boundaries of 0 and 1 and is non-decreasing.

$$F_y(B) = P[y \leq B] \quad \text{for} \quad B \in \mathbb{R} \quad (32)$$

Within a battery duty cycle, if  $y$  is the amplitude of the power profile at a given point, then  $F_y(B)$  is the probability that the amplitude of that operating point is equal to or less than  $B$ . For a profile with  $N$  data points the empirical cumulative distribution function (eCDF) is a step function increasing by  $1/n$  at each data point. The iCDF is simply the inverse of the eCDF and is described in equation (33).

$$g(P) = F_x^{-1}(P) \quad (33)$$

Provided, a database of HP-BEV duty cycle recordings is available, the amplitude spectrum of each individual duty cycle can be extracted from the Fourier series, via the Fast Fourier Transform (FFT) routine; the iCDF can be determined through equation (33). As the resulting profile solely depends on the amplitude spectrum and iCDF, the selection of the former and the latter in the profile design stages is of paramount importance.

A potential disadvantage of this approach is that the resulting cycles would no longer be reconstructed from the database source data, but synthesized from functions, which



approximate a target amplitude spectrum and iCDF. As every approximation involves a loss of information, some aspects of the database may not be captured in the resulting cycles. Although frequency domain approaches are a proven methodology for the design of excitation signals in system identification research [141,198,200], their application for the development of a duty cycle for degradation and performance testing of batteries is currently unproven.

### 3.6 Conclusion & Definition of the knowledge gap

To address “Research Question 2: How can a duty cycle representative of HP-BEV racing applications be defined?” this chapter critically reviewed both, time domain and frequency domain approaches, to develop a representative testing profile.

The discussed time-domain approaches are predominantly used within driving cycle research. As part of this review, for each methodology necessary key modifications to the data collection, processing and reconstruction steps were identified to optimise each process for the development of a duty cycle for performance and degradation testing of BEV batteries. The majority of the discussed methods are analysed and evaluated with respect to measures and targets extracted from the time-domain. As such, to develop a profile that is representative of a larger database of recordings, a multitude of target criteria, which best describe the generic shape of the profiles must be defined. Targets need to be selected such that key aspects pertaining battery degradation and self-heating, such as current amplitude, pulse duration, and energy throughput are preserved.

Another approach reviewed in this chapter requires the analysis of data within both, the time-domain and frequency-domain. Rather than selecting several target measures exclusively from within the time domain, the evaluation and design criteria would be a target amplitude spectrum in the frequency-domain and a target iCDF in the time-domain. A potential advantage of this method would be that a specific bandwidth of excitations could be selected, and the final profile could be optimised where limitations such as peak power demand for charging and discharging are not exceeded.

#### 3.6.1 Definition of the knowledge gap

As identified within Chapter 2, a knowledge gap exists with respect to the experimental procedures required to conduct investigations into the performance and degradation of LIBs representative of HP-BEV applications. This knowledge gap can be addressed through the

definition of a new experimental procedure, which itself must be underpinned by a representative duty cycle. The literature review presented within this chapter further highlights a second knowledge gap regarding the need for a suitable methodology to derive such a duty cycle.

Although the use of driving cycles coupled with a suitable BEV model may be adequate to derive a representative duty cycle for on-road driving scenarios, this approach is not suitable for HP-BEV applications. The design of LIB testing profiles from a database of battery measurements is limited to few examples such as [169,193] discussed in section 3.4.3, which as highlighted in their current format are not suitable for HP-BEV applications. Furthermore, all other discussed approaches to duty cycle development require extensive adaptations. Therefore, Table 2-5 can be extended as illustrated in Table 3-1 to define the complete knowledge gap pertaining to the research problem.

Procedure	On-Road driving	HP-BEV application
Characterisation Testing	☑	☑
Performance Testing	☑	☒
Degradation Testing	☑	☒
LIB test cycle construction	☑	☒

TABLE 3-1 – KNOWLEDGE GAPS IN THE EXISTING TESTING FRAMEWORK

The author asserts that the shortcomings of established experimental procedures and cycle construction methodologies render the existing framework for performance and degradation testing insufficient for HP-BEV applications. It is believed that other automotive applications, whose typical usage profiles do not conform to established testing standards, are disadvantaged by similar shortcomings. As such, the author proposes the development of an additional framework for LIB performance and degradation testing, illustrated within Figure 3-6, to supplement existing testing procedures for applications, where existing testing standards are unrepresentative of the typical usage profile.

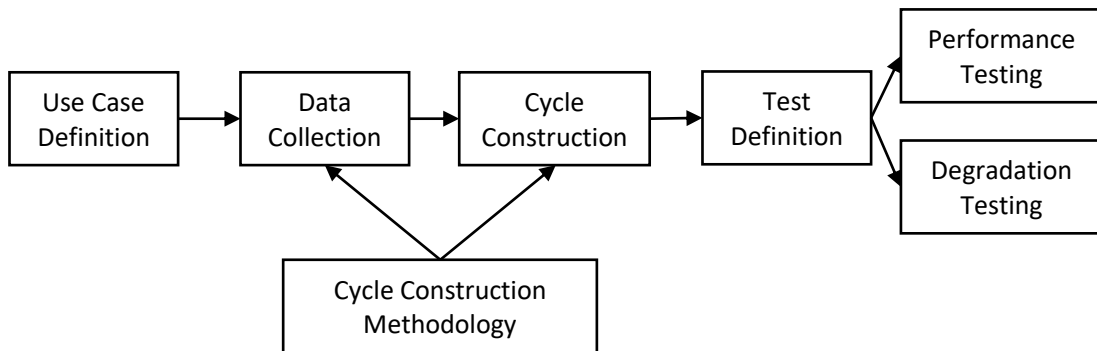


FIGURE 3-6 – PROPOSED ADDITION TO THE EXISTING TESTING FRAMEWORK

Following the definition of the use case, a database is required that describes those usage profiles encountered during operation, that are outside the scope of the established testing procedures. The proposed framework specifies a methodology through which a representative duty cycle for LIB performance and degradation testing may be derived from the database, thus addressing the shortcomings of existing cycle construction methodologies. Based on a more representative duty cycle, an experimental procedure for additional performance and degradation testing is defined to address the knowledge gap identified within Chapter 2.

The following chapters present a series of research tasks, summarised within Table 3-2, that are required to develop and implement this new testing framework within the context of HP-BEV applications. Further, academic publications relating to each research task are highlighted within Table 3-2 for completeness.

**3.6.2 Research Task 1:** Collate a database of battery duty cycles representative of HP-BEV racing applications.

A common prerequisite to determining a methodology for the derivation of a battery duty cycle is the existence of a database of real world recordings, from which the target design and assessment criteria can be extracted. This task is addressed within Chapter 4, in which the development of a duty cycle database that is representative of HP-BEV track driving scenarios is described. The methodology presented within this chapter has been published within [1,4].

**3.6.3 Research Task 2:** Define a methodology, from which a duty cycle that is suitable for LIB performance and degradation testing may be derived.

Chapter 5 presents two novel methodologies that may be used to develop a generic duty cycle. Both methodologies have been published within [1]. Within this context, “suitable” refers to

preserving profile traits that are known to be detrimental to LIB degradation and heat generation. To address the knowledge gap identified within Chapter 3, the methodologies should not be exclusive to the use-case of HP-BEVs but be applicable to any application, where LIB degradation is a concern.

**3.6.4 Research Task 3:** Devise an experiment to conduct LIB performance and degradation testing to investigate differences between HP-BEV applications and standard testing procedures.

Based on the literature review presented within Chapter 2, Chapter 6 presents the experimental set-up and testing procedures required to conduct LIB cell characterisation, performance and degradation testing. The experiment is designed such that any difference in cell behaviour over time can be ascribed to the use case in question. The experimental procedure has been published as parts of the publications [2,5].

**3.6.5 Research Task 4:** Analyse the experimental results and determine any use-case specific behaviour between HP-BEV applications and standard testing procedures.

Chapter 7 presents the results from the experimental investigation and provides a detailed analysis of the observations made. The work surrounding this has been published within [2].

Knowledge Gap	Framework Step	Research Task	Chapter	Pub
Duty Cycle Design Methodology	Data Collection	<b>Research Task 1:</b> Collate a database of battery duty cycles representative of HP-BEV racing applications.	4	[1,4]
	Cycle Construction & Methodology	<b>Research Task 2:</b> Design a methodology, from which a duty cycle that is suitable for LIB performance and degradation testing may be derived.	5	[1]
Performance & Degradation testing	Test Definition	<b>Research Task 3:</b> Devise an experiment to conduct performance and degradation testing and investigate differences between HP-BEV applications and standard testing procedures.	6	[2,5]
	Performance & Degradation Testing	<b>Research Task 4:</b> Analyse the experimental results and determine any use-case specific behaviour between HP-BEV applications and standard testing procedures.	7	[2]

TABLE 3-2 – RESEARCH TASKS COMPLETED WITHIN THIS THESIS

## 4 Development of a High-Performance Duty Cycle Database

---

### 4.1 Introduction

To support the design of a generic HP duty cycle, and to fulfil “**Research Task 1:** Collate a database of battery duty cycles representative of HP-BEV racing applications.”, a database of real-world HP duty cycles is required, from which key performance indicators (KPIs) can be extracted. Ideally, this dataset would comprise actual vehicle data recorded over a diverse range of different race circuits. However, there are obvious financial and logistical challenges associated with obtaining this data within the context of this initial study. In this chapter, a method is presented, using the commercially available simulation software IPG CarMaker, to simulate race circuits, a HP-BEV and a driver to generate a database that defines a range of HP duty cycles that are deemed representative of the real-world use of a HP-BEV. The IPG CarMaker software packages are simulation tools commonly used within the automotive industry. The model capability has been validated for some use cases [201–203]. The author asserts that these tools are thus fit for purpose. It is beyond the scope of this thesis to present the full derivation and validation of the mathematical models that underpin the IPG software packages. This information is contained within [204–206] and will therefore not be repeated.

### 4.2 Vehicle model

#### 4.2.1 Target vehicle

Vehicle performance characteristics are a limiting factor within HP driving and racing scenarios. Therefore, the choice of vehicle has a substantial effect on the resulting battery duty cycle. Within the HP vehicle market, performance characteristics such as acceleration times, top speed, and system power can vary substantially, as illustrated in Table 4-1. As such, a target vehicle sub-segment must be chosen for which a duty cycle database is constructed.

Vehicle Model	0-100 km/h	0-200 km/h	Top-Speed	Peak Power
Tesla Model S P85D	3.5 s	14.7 s	249 km/h	515 kW
Jaguar I-Pace	4.5	-	200 km/h	294 kW
NIO – EP9	2.9 s	7.1 s	313 km/h	1000 kW
Rimac Concept_1	2.5 s	6.2 s	355 km/h	913 kW
VW ID-R	2.3 s	-	-	507 kW
Conventional “Supercar”	≈ 4.0 s	≈ 13 s	≈ 300 km/h	≈ 300 kW

TABLE 4-1 – COMPARISON OF SELECTED PERFORMANCE CHARACTERISTICS OF DIFFERENT COMMERCIALLY AVAILABLE AND CONCEPT EVs, DATA FROM [94,207–210]

The target vehicle for this research is situated within what is referred to as the “Supercar” segment in popular media. This segment was chosen, as it is a strategically important market for the sponsoring companies. Examples of traditionally powered vehicles within this segment are the Jaguar F-Type R, Audi R8, and Aston Martin V8 Vantage. Although no concrete definition exists on what makes a vehicle a “Supercar”, there are certain commonalities with respect to the performance parameters, listed in the last row of Table 4-1. As such, the conceptualized HP-BEV within this work is benchmarked against these performance parameters of existing, traditionally powered vehicles within this segment. A list of vehicle model parameters are presented within Table 4-3 and discussed below

#### 4.2.2 Chassis and handling

The starting point for the vehicle model is the conventionally powered Audi R8 demonstration vehicle that is made available within the IPG CarMaker software. This is a model of a typical vehicle within the “Supercar” segment. Within this model, all key vehicle subsystem models, including the vehicle suspension, hydraulic brakes, hydraulic steering, tyre and powertrain models are preconfigured and parameterised.

For the model used within this work, it was decided that only the powertrain sub-model would be replaced to represent that of an HP-BEV. Although each individual model provided within the software can be parameterised by the user to represent the specific characteristics of real components much of the information required to do so is proprietary for each OEM, and thus not readily available. Due to the associated time and cost efforts to reverse engineer those subsystems, it was decided that the models for the suspension, hydraulic brakes steering and tyres models remained unchanged from the original model.

The overall vehicle mass of 1564 kg was also left unchanged, with a 50-50 mass distribution between the front and rear of the vehicle. This mass is approximately 300kg lighter than the Rimac Concept One [94], 180 kg lighter than the NIO EP9 [209], and 650 kg lighter than the Tesla Model S P85D [207], and Jaguar I-Pace[208]. To achieve this for a commercially available electric road vehicle would be challenging and require extensive engineering effort due to the mass of the traction battery system required to provide power to the vehicle. However, this goal is achievable, exemplified through the battery utilised in the 2017-18 Formula E vehicles, which has a specific peak power exceeding 860 W/kg [211]. An example of how this mass saving could be achieved is illustrated within Table 4-2, where negative values indicate a mass saving and positive values indicate a mass gain.

Component	approx. mass (kg)	Notes
Motor/inverter assemblies	150 ± 20	2 lightweight assemblies
Battery pack	440 ± 60	Assuming 60kWh pack
Engine	-300 ± 50	4.2l supercharged V8 wet weight
Air system	-40 ± 10	exhaust, catalytic converters, etc
Seats	-50 ± 10	Carbon fibre vs standard
Wheels	-15 ± 5	lightweight sport wheels
Fuel Tank and lines	-10 ± 5	Assuming empty tank
Air conditioning	-35 ± 10	Optionally stripped out for racing
Infotainment cluster	-25 ± 10	Optionally stripped out for racing
<b>Total mass balance</b>	<b>115 ± 170</b>	

TABLE 4-2 – ESTIMATED MASS SAVING POTENTIALS TO ACHIEVE TARGET VEHICLE MASS

#### 4.2.3 Powertrain

A schematic of the HP-BEV powertrain model as conceptualised within CarMaker is shown in Figure 4-1. It comprises two drive sources, composed of an electric machine (EM) – inverter assembly mechanically coupled through an automated two-speed gearbox and differential to the front and rear axles respectively, a power supply representing the traction battery, and a powertrain control unit comprising a battery control unit (BCU), motor control unit (MCU), and traction control unit (TCU).



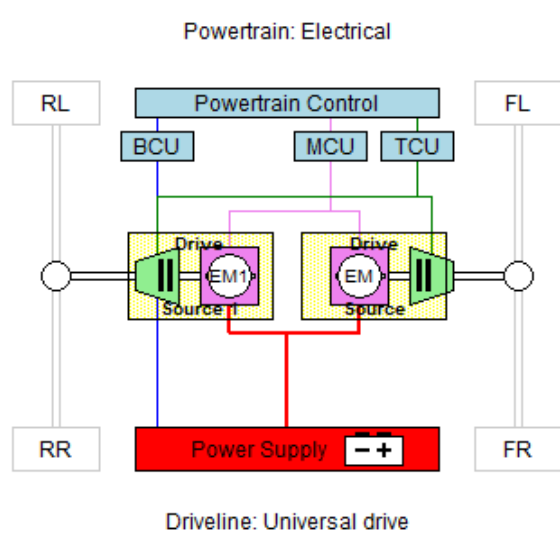


FIGURE 4-1 — POWERTRAIN SCHEMATIC OF THE HP-BEV WITHIN CARMAKER COMPRISING TWO DRIVE SOURCES COMPOSED OF AN EM-INVERTER ASSEMBLY, A 2 SPEED GEARBOX, AND A DIFFERENTIAL FOR EACH, A POWER SUPPLY REPRESENTING THE BATTERY, AND A POWERTRAIN CONTROL SYSTEM, COMPRISING A BATTERY CONTROL UNIT (BCU), MOTOR CONTROL UNIT (MCU), AND TRACTION CONTROL UNIT (TCU).

Most vehicles within the HP segment use a rear-wheel drive (RWD) or all-wheel drive (AWD) powertrain architecture. An RWD architecture is lighter than AWD systems, as the resulting powertrain contains fewer components, resulting in better acceleration at higher speeds than a similarly powerful AWD system. During friction braking, the largest portion of braking energy is dissipated into heat. In contrast, the utilisation of separate front and rear electric machines for an AWD architecture allows for a larger proportion of the braking force to be used for regenerative braking. Furthermore, AWD can provide more traction during acceleration, resulting in faster acceleration rates at low speed, and usually allow for better handling in situations where limited traction is available [212]. To increase vehicle range through regenerative braking, and for the benefit of better acceleration, the AWD architecture was chosen with a power-split of 50-50 between the front and rear axle as recommended within [213].

The power supply within the model was parameterised to provide an ideal power source capable of delivering and receiving 300 kW of electrical power throughout operation at a constant voltage. This approach was selected to gather data in which the battery performance does not derate. This is not always representative of real life situations, as a BMS may derate battery power output and input to prevent excessive battery degradation due to temperature, current, voltage, and SOC limitations [214].

Figure 4-2 illustrates the typical voltage dependency of electric machines, whereby a decrease in voltage due to SOC results in an earlier onset of the knee-point on the torque-curve. The knee-point is the instance at which operation changes from constant torque to constant power mode.

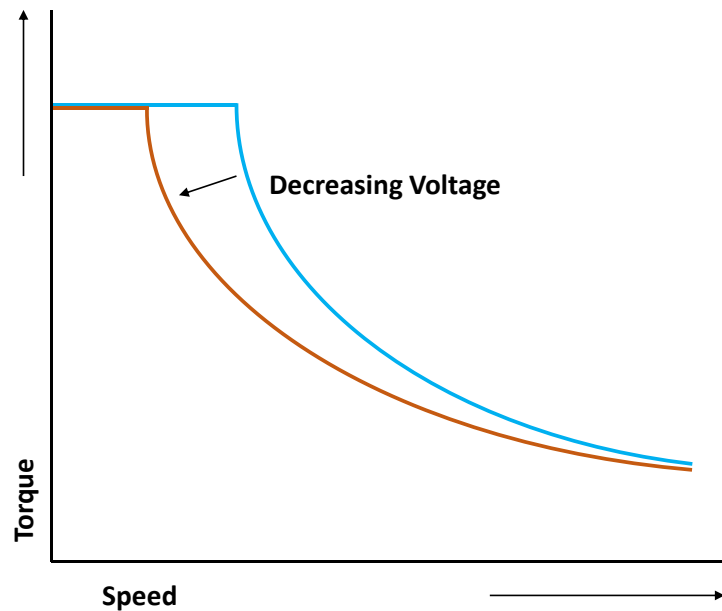


FIGURE 4-2 – TYPICAL TORQUE-SPEED CHARACTERISTICS OF ELECTRIC MACHINES

The energy efficiency maps of the EM-inverter assembly models for acceleration and regenerative braking are shown in Figure 4-3.

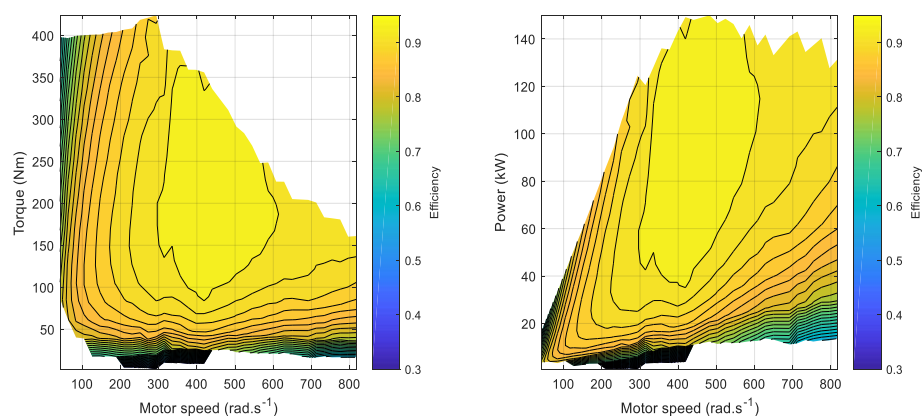


FIGURE 4-3 – EM-INVERTER EFFICIENCY MAPS FOR FRONT AND REAR DRIVE SOURCES; THE DATA WAS PROVIDED BY AN INDUSTRIAL PARTNER.

The efficiency is defined as the ratio of mechanical output power to electrical input power and quantified as a function of machine speed and torque. The source data used for parameterisation of this model within this work was based on real-world test data from commercially available

systems. The source data was provided by an industrial partner and scaled to 150 kW for each motor to match the desired battery power output of the target vehicle. To maximise energy recovery during regenerative braking, a sequential braking strategy was implemented, where mechanical brakes are only in use for braking torques that exceed the EM's regenerative capability. The automated gearboxes, and final drive are assumed to have an efficiency of 95% [215]. Gear ratios were parameterised by simulating straight-line accelerations from 0 km/h to top speed and iteratively adjusting gearing to achieve typical performance for acceleration times and top speed within the target sector. Ancillary loads for power steering or air conditioning were not considered within the model as their impact on the overall power demand is not expected to exceed 1%.

Parameter	Value
Vehicle body	Rigid body
Vehicle mass	1564 kg
Combined motor input power	300 kW
Combined motor torque	850 Nm
Height of center of gravity	0.5m
Wheelbase	2.67m
Longitudinal drag coefficient	0.3
Effective frontal area	2.0 m
Gearing ratio 1 <sup>st</sup> gear	1.4 : 1
Gearing ratio 2 <sup>nd</sup> gear	0.45 : 1
Final drive gear ratio	5.8 : 1
Tire rolling resistance $k_{rr}$	0.01
Tire friction coefficient $\mu_r$	1
Tire radius $r$	0.27 m
Axle power split	50-50
0 - 100 km/h	3.8 s
0 - 200 km/h	12.4 s
Top speed (km/h)	300 km/h

TABLE 4-3 – VEHICLE MODEL PARAMETERS USED WITHIN THE IPG SOFTWARE

### 4.3 Circuit Models

The circuit design affects the resulting driving profile, and subsequently battery duty cycle. The selection of circuits forming the basis of a HP duty cycle database should capture as many different HP driving scenarios as possible. As such, to avoid any potential bias with regard to racing class, or circuit length, the database should contain a number of circuits from different geographic locations, and differentiating track design concerning length, number of corners, and target racing class. Within this work, an arbitrary number of circuits (12) compliant with these targets were chosen. Table 4-4 summarises, for each race-circuit, the location, a summary of popular use, actual and modelled circuit length, and the associated percentage error. The track models deviate from official circuit length from 6m to 272m. This deviation translates to an error in track length of 2.5% in the worst case but lower than 1% in most cases, which was deemed acceptable.

The modelling process for the circuits is illustrated within Figure 4-4 on the example of the Nürburgring GP and Nürburgring Nordschleife tracks, and described below. IPG Road allows for the modelling of road segments or tracks by two means. Firstly, individual segments can be created manually, parameterised through length, road width, corner radius and road inclination. Alternatively, geographic coordinates can be imported in the “.kml” file format, and the software automatically computes splines between these waypoints and generates a road model with a constant, user-defined width. Due to restricted resources in terms of required survey data to recreate models of the racing tracks, it was decided to opt for the simpler approach of importing geographic coordinates, recorded from Bing Maps Satellite images.

Waypoints were collected by manually retracing the centreline of the road on each circuit. The road width chosen within this work is 12m, as it is the minimum width for any new Formula 1 circuit [216]. Furthermore, most circuit operators state a track width between 10m and 14m. Road elevation and inclination and thus gradient was not included in the model, as this data is not readily available. One exception is the Nürburgring Nordschleife, for which GPS data linked with an altitude profile can be found online [217]. To assess the effect of road inclination on the resulting duty cycles, the Nordschleife circuit is included twice within the Database, once with elevation included, and once without elevation. The implications of this are discussed in further detail in section 4.6.2.



FIGURE 4-4 - LEFT TO RIGHT, NÜRBURGRING GP AND NORDSCHLEIFE TRACKS TRACED IN BING MAPS, BIRDS' EYE VIEW OF NÜRBURGRING GP TRACK IN IPG ROAD, NÜRBURGRING NORDSCHLEIFE IN IPG ROAD

Racing-circuit	Location	Use	Model length (km)	Official length (km)	Delta (%)
Anglesey International Circuit	UK	TD	3.294	3.381	-2.57
Bahrain GP	Bahrain	F1, TD	5.439	5.412	0.50
Brands Hatch Grand Prix Circuit	UK	DTM, GT, F3	3.908	3.917	-0.23
Dunsfold Park	UK	Top Gear	2.852	2.818	1.22
Goodwood Full Circuit	UK	TD	3.853	3.832	0.55
Lausitzring Automobilsport	Germany	DTM	4.551	4.534	0.37
Le Mans Circuit de la Sarthe	France	End.	13.626	13.629	-0.02
Magny Cours GP	France	(F1), TD, GT, End.	4.436	4.411	0.57
Nürburgring GP	Germany	F1, DTM, GT	5.142	5.148	-0.12
Nürburgring Nordschleife	Germany	(F1), TD	20.800	20.832	-0.15
Nürburgring Nordschleife (with altitude)	Germany	(F1), TD	20.560	20.832	1.31
Silverstone GP	UK	F1, End., GT	5.920	5.892	0.46
Suzuka GP	Japan	F1, GT	5.828	5.807	0.36

TABLE 4-4 – RACING-CIRCUIT MODEL OVERVIEW – NOMENCLATURE: TRACK DAY (TD), DEUTSCHE TOURING MASTERS (DTM), FORMULA 3 (F3), FORMULA 1 (F1) ENDURANCE (END.)

The road conditions can be described through a coefficient of adhesion between the tyres and the road surface. Typically, for dry asphalt this value ranges between 0.75 and 1 depending on the condition of the tyre and the vehicle speed. In wet and icy conditions, this coefficient may decrease to 0.1. Special racing compounds exist providing coefficient of up to 1.8 on dry asphalt [212]. The coefficient of adhesion within this model was set to 1 as it is the best case [212] for a typical road tyre, and the maximum possible within the software.

#### 4.4 Driver Model

IPG Driver is an artificial intelligence (AI) driver model which can be parameterised to follow a course and a speed on a given track [204,205]. The software provides a model, which can be parameterised by the user (User Driver) and a closed loop artificial intelligence (AI) racing driver (Racing Driver). For either driver model, a static path is calculated along the circuit. The user can influence this calculation through a corner cutting coefficient which dictates how much of the road width the AI driver may use, with a value of 1 allowing the driver to utilise the entire width of the track, a value of 0 forcing the driver to drive along the centre of the road.

The Racing Driver can learn the dynamic vehicle limits through an in-built simulation procedure called "Driver Adaption". The dynamic behaviour of the User Driver can be manually parameterised in terms of aggressiveness, tuneable with respect to both, lateral and longitudinal dynamics (see Figure 4-5).

Initially, the Racing Driver model was employed for driving simulations. However, during the simulations for three circuits (Dunsfold, Lausitzring, and Nordschleife), the vehicle left the road and the simulation was automatically stopped. This could be avoided by reducing the corner-cutting coefficient for those circuits track, effectively resulting in less aggressive driving. To provide a reproducible process, it was decided to parameterise the User Driver model. A description of the tuneable parameters and their final values are detailed within Table 4-5 and Table 4-6. The process of parameterisation is described below.

**Driver** Close

Mode: ☒ User parameterized Driver ☐ Racing Driver

Standard Parameters | Traffic | Race Driver | Misc. / Additional Parameters

**General**

Cruising Speed  km/h dt Change of Pedals  s

Corner Cutting Coefficient  Min. dt Accel./Decel.  s

☐ Use Handbrake for Driveway

Driveway Options ☐ Traction Control: reduce throttle if wheelspin occurs

**Accelerations, g-g Diagram**

Max. Long. Acceleration  m/s<sup>2</sup> ●

Max. Long. Deceleration  m/s<sup>2</sup> ●

Max. Lat. Acceleration  m/s<sup>2</sup> ●

Exponent of g-g Diagram (ax/ay dependency)

Speed [km/h]	Accel.	Decel.
25	2	2
50	1.3	1.2
100	1	0.95

FIGURE 4-5 – IPGDRIVER PARAMETERISATION. EACH PARAMETER IS TUNEABLE TO INCREASE OR DECREASE DRIVER AGGRESSIVENESS WITH RESPECT TO LONGITUDINAL AND LATER VEHICLE DYNAMICS.

Parameter	Description	Value
Cruising speed	The speed the driver will aim to reach during driving unless otherwise limited	300 km/h
Corner Cutting Coefficient	Defines how much of the track width may be used. A value of 1 allows the driver to use full track width, a value of 0	1
Max Long. Acceleration	The longitudinal acceleration in the direction of travel that the driver will aim to achieve	10.5 m/s <sup>2</sup>
Max Long. Deceleration	The longitudinal deceleration the driver will aim to achieve	8.7 m/s <sup>2</sup>
Max Lat. Acceleration	Maximum allowed maximum lateral acceleration during cornering	9.0 m/s <sup>2</sup>
g-g Diagram	representation of the speed dependent maximum longitudinal and lateral acceleration, similar to friction circle for tyres	See Table 4-6

TABLE 4-5 – MODEL PARAMETERS AND EXPLANATIONS FOR THE PARAMETERISATION FOR IPG DRIVER

Speed (km/h)	Acceleration	Deceleration
25	2.00	2.00
50	1.30	1.20
100	1.00	0.95
150	0.65	0.60
200	0.30	0.30
250	0.10	0.10
300	0	0

TABLE 4-6 – G-G DIAGRAM EXPONENTS DESCRIBING THE SPEED DEPENDENT DRIVER BEHAVIOUR WITH RESPECT TO LONGITUDINAL AND LATERAL ACCELERATION DURING CORNERING

For the driver parameterisation and to start with an extremely aggressive driver, the initial value for cruising speed was set to the maximum vehicle speed of 300km/h, lateral and longitudinal acceleration values were set to 9 m/s<sup>2</sup>, and all g-g exponents to 2. To optimise the longitudinal acceleration parameter, straight-line acceleration simulations were conducted and the parameter value was iteratively increased in increments of 0.1 m/s<sup>2</sup> until no improvement of acceleration times could be recorded any more. This process overlaps with that of gearing



optimisation described in section 4.2.1. Deceleration was optimised by running straight-line deceleration tests and a value of  $8.7 \text{ m/s}^2$  was chosen at which the wheels did not lock up.

To calibrate the lateral dynamic driving behaviour, consecutive simulations of the Lausitzring circuit were conducted. The g-g exponent values resulted in several aborted simulations as the driver left the track and crashed. For each of those instances, the gg-exponents were reduced iteratively, until a crash was avoided. The final parameters are displayed in Table 4-6. This user-parameterised driver could be used to complete simulations without crashing and achieved faster lap times than the built in Racing Driver AI on every circuit. There is currently no feature within the used software to automate the parameterisation process, as a failed driving scenario, where the vehicle leaves the road, ends the simulation program.

## 4.5 Simulation & Data processing

The processes that constitute the simulation work and subsequent data processing are illustrated within Figure 4-6 and discussed below.

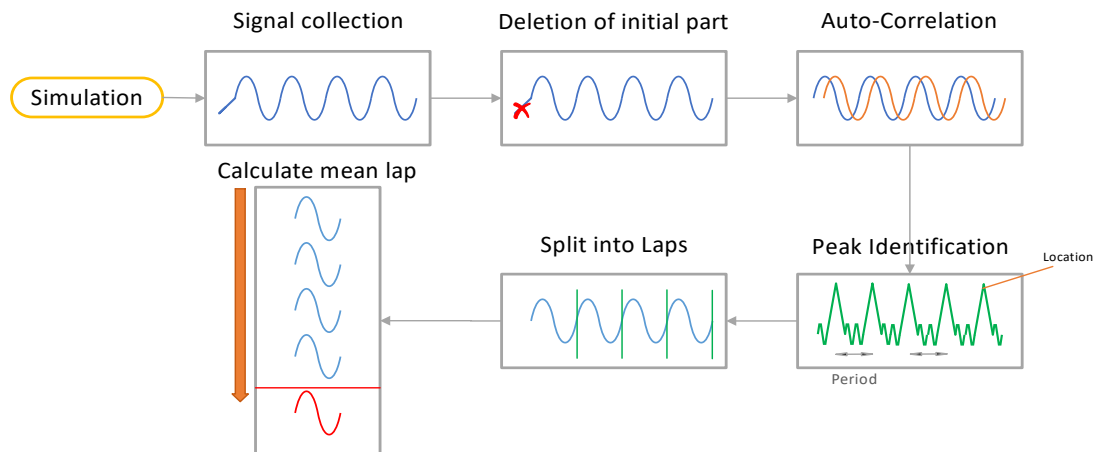


FIGURE 4-6 – SUMMARY OF THE DATA PROCESSING STEPS. FOLLOWING SIMULATION WORK, THE SIGNALS FOR VELOCITY AND POWER DEMAND ARE RECORDED. AN INITIAL PART OF THE SIGNAL IS DELETED TO AVOID THE STANDSTILL PORTION OF EACH SIMULATION. THE PERIOD, I.E. LAP LENGTH OF EACH CIRCUIT IS DETERMINED THROUGH AN UNBIASED AUTO-CORRELATION. THE COLLECTED SIGNAL IS SPLIT INTO INDIVIDUAL LAPS, FROM WHICH A MEAN LAP IS CALCULATED.

A simulation was carried out for each circuit. The data extracted from simulations are the vehicle speed and battery power profiles at the power source terminals as illustrated within Figure 4-7a and Figure 4-7b, respectively, on the example of the Silverstone circuit simulation. Each simulation starts with the vehicle at standstill and 1800 seconds of driving are recorded for each racing-circuit. This is done to ensure that each recorded power demand profile contains at least

one complete lap without a start from standstill. The sampling frequency was set to 10 Hz, which is the maximum sampling frequency of the available battery testing equipment, discussed in more detail in Chapter 6. For real-life data, sampling at higher frequencies would be useful to analyse the effect of traction limiting scenarios such as tyre slipping, free spinning, or locked up wheels, on the power profiles. However, this level of fidelity cannot be achieved with the current models.

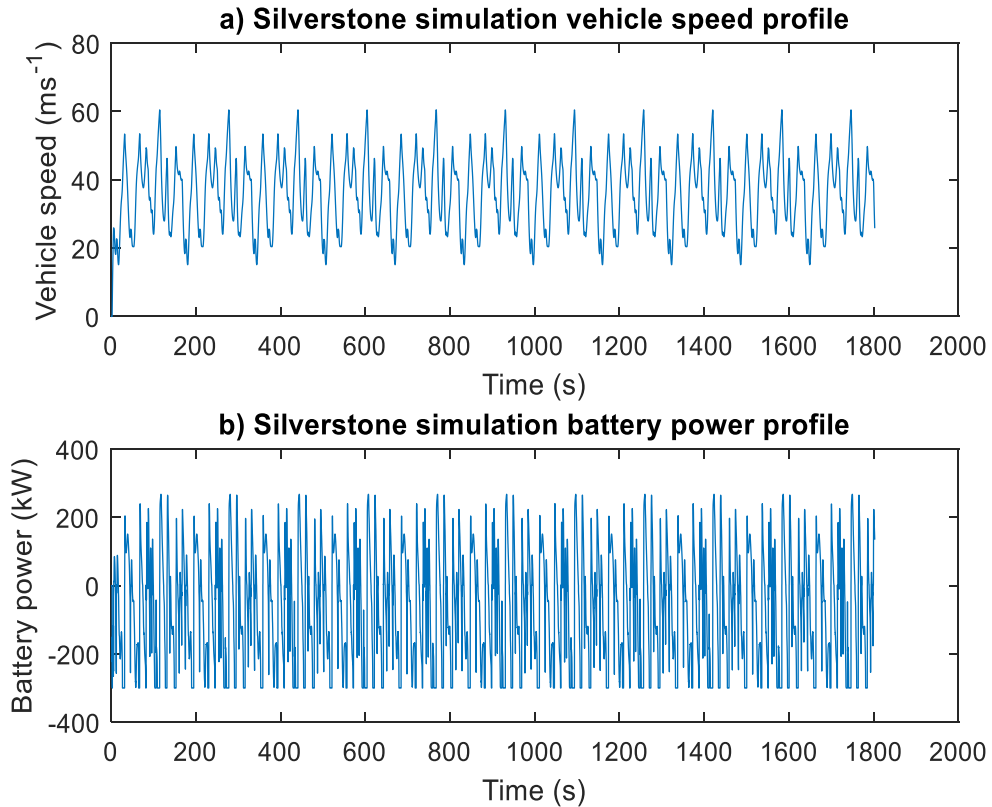


FIGURE 4-7 – A) VEHICLE SPEED RECORDED FROM THE SILVERSTONE SIMULATION; B) ASSOCIATED BATTERY DUTY CYCLE PROFILE FROM THE SILVERSTONE SIMULATION

Both, the vehicle speed and the battery power profile follow a periodic pattern, with almost identical profiles for every lap, as would be expected for a racing driver. As such, a typical duty cycle for each circuit can be approximated as a mean lap from the simulations. An initial step in this process is to determine the period, thus lap duration, of each profile. To reduce the effect of the standing start on each mean lap, the initial portion of each power profile is eliminated. This initial starting point can be defined at the the first point at which charging of the power source exceeds a minimum threshold, or after a specific amount of time has passed. Within this work, a minimum charging threshold value of 10kW was chosen arbitrarily. From this reduced profile, the

number of individual periods and their duration can be determined through an unbiased auto-correlation function [218].

Assuming the recorded data is a signal  $x(n)$  containing  $N$  data points as described in equation (34).

$$x(n) = [x_0, x_1, \dots, x_N] \quad (34)$$

The unbiased auto-correlation ( $R_{xx}$ ) of  $x(n)$  is the unbiased correlation of  $x(n)$  with a shifted copy of itself as a function of the shift ( $m$ ) as described in equation (35), where  $x^*$  is the complex conjugate of  $x$ .

$$R_{x,x,unbiased}(m) = \frac{\sum_{n=0}^{N-m-1} x_{n+m} \cdot x_n^*}{N - |m|} \quad (35)$$

$$m = [0, 1, \dots, N - 1] \quad (36)$$

The calculated correlation function is unique for each power profile. The peak values for  $R$  have a different amplitude for each individual circuit. To ease the processing of multiple profiles within MATLAB®, the values of each correlation function are normalised through equation (37) to provide values between a maximum and minimum limit of 1 and -1, respectively.

$$R_{Norm} = \frac{R}{\max(R)} \quad (37)$$

A plot of  $R_{Norm}$  vs the lag  $m$  for the Silverstone profile is shown in Figure 4-8.

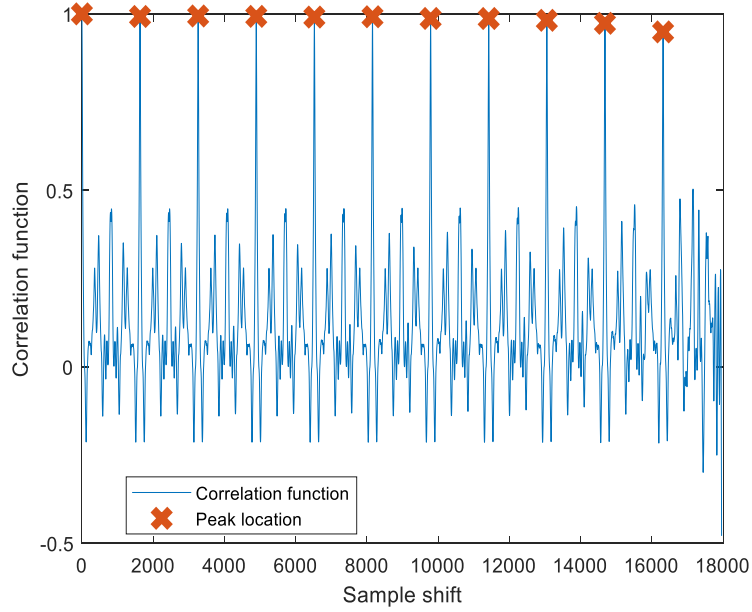


FIGURE 4-8 – NORMALISED UNBIASED AUTOCORRELATION VS SAMPLE SHIFT. THE RED CROSSES MARK THE LOCATION OF THE HIGHEST PEAKS, INDICATING COMPLETION OF A FULL LAP. THE NUMBER OF SAMPLE POINTS BETWEEN PEAKS IS EQUAL TO THE SAMPLES CONTAINED WITHIN EACH LAP.

The number of samples for each period, thus lap, is equal to the number of samples between the highest peaks marked by a red cross. These are determined through use of the MATLAB® “findpeaks” function. The number of peaks and their location indices ( $loc = [loc_0, loc_1 \dots loc_I]$ ) with respect to the sample shift are stored. The definition for a single lap profile ( $x_i(n_i)$ ), is described in equation (38) and equation (39), where  $i$  denotes the lap number, and  $I$  is the number of peaks in Figure 4-8.

$$x_i(n) = [x_{loc_i}, x_{loc_0+1}, \dots, x_{loc_{(i+1)}-1}] \quad (38)$$

$$i = [1, 2, \dots, I - 1] \quad (39)$$

The resulting power profiles for the laps are shown in Figure 4-9a. As the data stems from simulations, the individual laps vary only by one sample, i.e. 0.1 s. For the Silverstone simulation, the shortest period contains 1631 samples, and the longest period 1632 samples. The shorter period length was used for every lap, and the last data sample for longer laps was omitted, such that all laps have the same length. A typical lap profile ( $P(t)$ ) is then approximated as the mean lap over the periods displayed in Figure 4-9b.

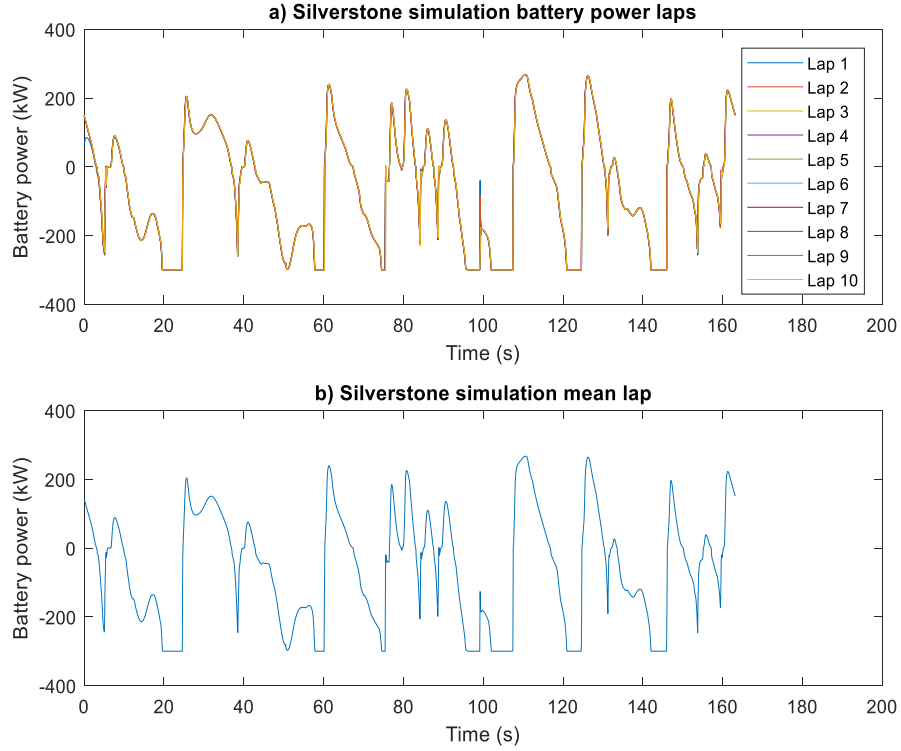


FIGURE 4-9 – A) LAP PROFILES EXTRACTED FROM ORIGINAL RECORDING FOR THE SILVERSTONE SIMULATION; B) MEAN LAP CALCULATED FROM THE LAPS SHOWN IN SUBFIGURE A).

This approximation is only justifiable as each simulation returns lap profiles, which are almost indistinguishable from one another. For real world data, where more variation is expected, an intermediate data processing step may be required. For larger differences between individual periods, each lap profile could be scaled and interpolated onto the same time vector, as suggested within [219], and a mean lap calculated.

#### 4.5.1 Normalised duty cycles

Normalisation of the mean lap power profiles with equation (40) allows decoupling of the power profile from battery and system parameters with the resulting profiles containing values between -100% and 100%. This processing step allows the scaling of the profiles to a subsystem or cell level, as it is independent of the internal design features of the power management system.

$$P_{Norm}(t) = \frac{P_{Cycle}(t)}{\max(P_{System})} \quad (40)$$

$P_{Norm}(t)$  is the normalised power profile, referred to as a duty cycle within this work,  $P_{Cycle}(t)$  is the power demand profile resulting from the simulation, and  $\max(P_{System})$  is the peak power that the power source can supply to the electric machines. These resulting duty cycles, although dimensionless, are still fully dependent on the specific properties of the vehicle and driver models, and race-circuit selection. As such, they relay information about their intensity as a function of the system's peak capability, without eliminating crucial information about differences between individual profiles. Furthermore it enables direct comparison with the battery testing profiles within the ISO 12405-2, IEC 62620-1 and Battery Test Manual [34–36], that aim to represent the best practice approach for LIB testing.

## 4.6 Results

### 4.6.1 Recorded profiles

Table 4-7 provides for each circuit, the mean values of speed, absolute power, discharge power after considering regenerative braking, RMS of the absolute power, and peak power when modelled within the CarMaker software. The mean value for each of the columns within Table 4-7 are displayed in Figure 4-10, where error bars represent one standard deviation.

The peak power demand for each driving scenario is limited by the vehicle capability, reaching a maximum of 300 kW. Most circuits lie within a narrow band of values for each measure, except for the Anglesey International circuit and Le Mans Circuit de la Sarthe. The Anglesey International circuit is the second shortest in terms of length but its layout features a relatively high portion of tight corners, requiring slow passing speeds. The Le Mans circuit in contrast is well known for long sections of straight track, thus resulting in higher speeds and large portions of time spent at full power.

Racing-circuit	Mean speed (m/s)	Mean absolute Power (kW)	mean Power (kW)	Peak discharge power (kW)
Anglesey International Circuit	29.0	118.3	43.6	300
Bahrain GP	33.7	176.6	73.9	300
Brands Hatch Grand Prix Circuit	34.0	135.9	53.2	300
Dunsfold Park (Top Gear)	33.1	137.8	55.8	300
Goodwood Full Circuit	42.4	153.0	77.5	300
Lausitzring Automobilsport	31.9	132.9	52.8	300
Le Mans Circuit de la Sarthe	44.9	201.3	109.9	300
Magny Cours GP	34.5	161.0	68.4	300
Nürburgring Nordschleife	39.9	142.7	76.0	300
Nürburgring Nordschleife (with altitude)	40.8	145.5	75.8	300
Nürburgring GP	32.5	138.5	59.3	300
Silverstone GP	35.9	143.3	59.8	300
Suzuka GP	33.0	139.2	60.6	300

TABLE 4-7 – RACING CIRCUIT MODEL AND SIMULATION RESULT OVERVIEW

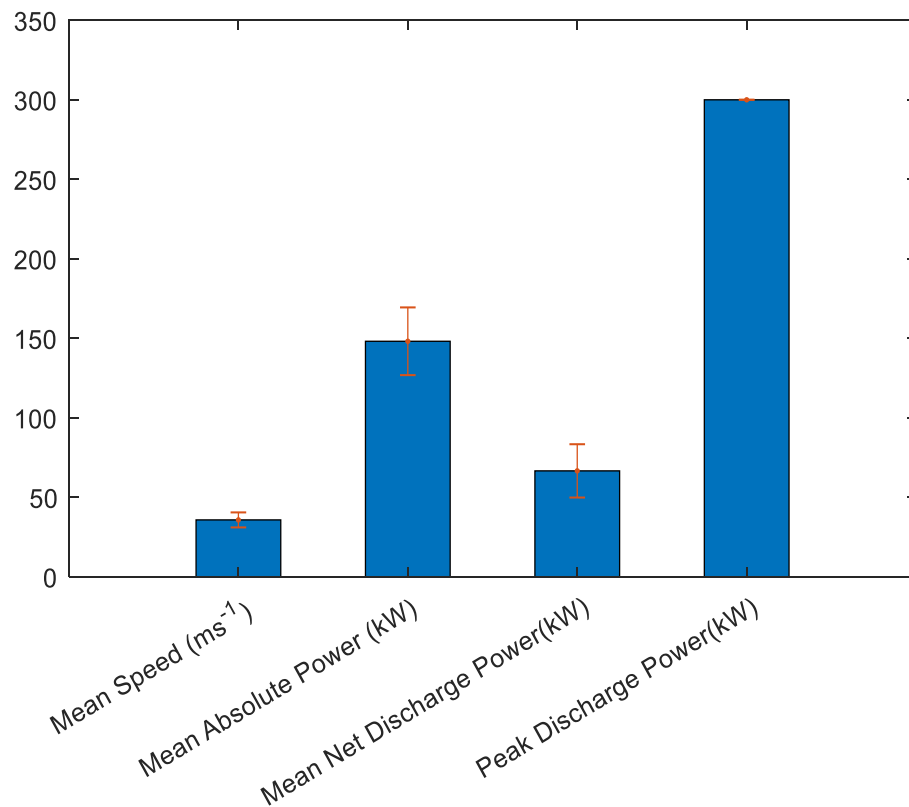


FIGURE 4-10 – MEAN VALUES FOR THE MEASURES LISTED IN TABLE 4-7. ERROR BARS REPRESENT ONE STANDARD DEVIATION FROM THE MEAN. ERROR BARS REPRESENT ONE STANDARD DEVIATION FROM THE MEAN

#### 4.6.2 Effect of road inclination

Ignoring road inclination and the resulting gravitational forces on the vehicle influences both, the vehicle speed and power demand profile of a vehicle driving on a track. As it is expected that a driver will push the vehicle to its performance limits. With reference to power demand, driving uphill would result in a longer demand in power for propulsion and a shorter braking duration. Similarly, for driving downhill, the duration of peak power demand will be shorter, whereas the braking duration increases. This simplification is equivalent to a vehicle driving on a circuit with longer/shorter straights.

Comparing the results for the two versions of the Nürburgring Nordschleife track as tabulated within Table 4-7, there are only minor differences between both. Except for mean vehicle speed, the three other measures, which relate to the characteristics of the power profiles, lie well within one standard deviation of the mean values shown in Figure 4-10. As such, it was deemed that both simulation results are treated as individual entries in the database.



#### 4.6.3 Normalised profiles

The normalised battery power profile for the Silverstone circuit is shown within Figure 4-11a, and the IEC 62660-1 Cycle Life Profile A, as described within the IEC 62660-1 standard [34], is shown within Figure 4-11b. Visual comparison of these two profiles reveal obvious differences. These are the frequency of changes between charging and discharging, the amplitude of charging and discharging power and the portion of the profile at high amplitudes. This further strengthens the arguments for performance and degradation testing to be conducted with a bespoke HP-BEV duty cycle.

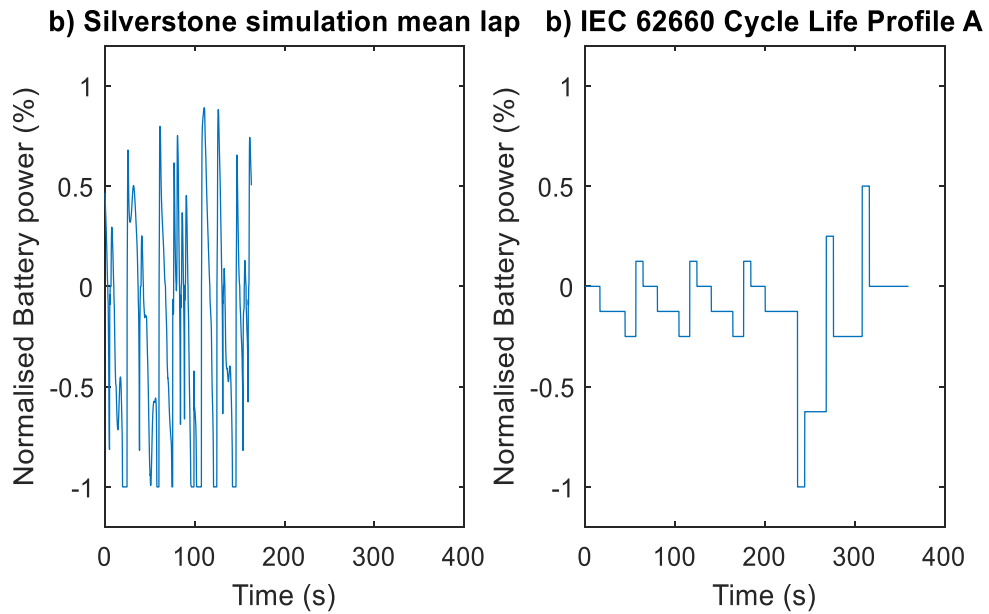


FIGURE 4-11 – A) NORMALISED PROFILE OF THE MEAN LAP FROM THE SILVERSTONE CIRCUIT SIMULATION, B) IEC 62660-1 CYCLE LIFE PROFILE A

#### 4.7 Duty cycle selection

Two options are considered for duty cycle selection to conduct performance and degradation testing. Either, the most demanding cycle in terms of mean absolute power, mean net power and RMS power from the database could be chosen, or a generic duty cycle representative of the database as a whole could be developed.

Testing with the most demanding duty cycle would provide a dataset, which is specific to one particular scenario rather than the database as a whole. If this data were to be used for the specification of BTMS requirements, the resulting system would be able to cope with the thermal requirements for all HP duty cycles present in the database. Further, within the context of

degradation testing, this would provide a worst-case scenario dataset, thus provide a benchmark for minimum battery life rather than representative degradation over a wider variety of scenarios. If the most demanding profile is rare in occurrence, any system specified to these requirements could be potentially over-engineered (e.g. heavy and costly) for the majority of other use cases. Similarly, if a generic duty cycle is to be used, the resulting data should provide an estimation of thermal management requirements and degradation for a large portion of the HP-BEV use case, but any system specified to cater to these requirements might be unsuitable for the most demanding scenarios. To gain an initial understanding of the performance and degradation of LIBs within the HP-BEV use cases as identified within Chapter 2, the author asserts that a generic cycle representative of the database should be chosen.

## 4.8 Limitations of the database

There are limitations associated with the approach described within this chapter that must be explored. First is the use of simulations instead of real-world data, which could not be obtained due to financial and resource limitations. However, the software packages used to develop the models and simulate the duty cycles are tools used within industry and the model capability has been validated for comparable use cases [201–203]. Secondly, there is a lack of data, which may underpin the development of more accurate and higher fidelity models. As such, assumptions and simplifications needed to be made to formulate and parameterise the models discussed in sections 4.2, 4.3 and 4.4.

Much of the required information to build a representative vehicle model is proprietary and not easily accessible within the public domain. As such, the vehicle model developed within this chapter is only conceptual and not a real vehicle. The approach of benchmarking the performance of the HP-EV model against performance targets of ICE powered vehicles that operate within the same market segments, and, where available using real-world measurements to parameterise models, offers a degree of confidence that the vehicle model is representative of the target market. Additional validation of vehicle subsystem and component models would improve the overall accuracy of the full vehicle model. Furthermore, as vehicle performance is one of the limiting factors in circuit driving, each vehicle segment would require its own bespoke database, as duty cycles between two vehicle classes would differ significantly.

The driver model parameterised within this work emulates a vehicle user with a high level of ability to control the vehicle, and consistency with respect to driving on a racing circuit. For professional racing drivers this approximation may be suitable. However, taking a sample from

the general populous, a group of real human drivers would be expected to display much larger variability in terms of ability and consistency, thus duty cycles. As such, an expansion of the duty cycle database through additional simulations with different driver parameter settings may be required for future studies.

The circuits are currently modelled without considering road inclination, or differing road surfaces. Concerning road inclination, it was shown within section 4.6.2 that the resulting error from this simplification is relatively small and thus deemed acceptable. Although the current number of circuits within the database is relatively small, the resulting duty cycles are very similar with respect to the measures listed within Table 4-7. The database itself can be expanded through the inclusion of additional circuits. To expand the database through different road conditions is outside the scope of this thesis but should be addressed in further studies.

The process to develop a database of duty cycles as described within this chapter is the most accurate approximation to collecting real-world data with the information available to the author. The accuracy and fidelity of the data obtained through this process could be improved through the inclusion of models that are more accurate and proprietary information currently not available in the public domain. These limitations, however, do not invalidate the method presented.

## 4.9 Conclusion

The work presented within this chapter fulfils the requirements demanded from “**Research Task 1:** Collate a database of battery duty cycles representative of HP-BEV racing applications.” In this chapter a method to develop a duty cycle database of previously unexplored HP-BEV driving on racing circuits, based on simulations has been discussed. A description of the vehicle, circuit and driver models underpinning the simulation work has been given, and the model parameterisation process was discussed on detail. The HP-BEV model represents a hypothetical vehicle operating in the “Supercar” segment; its acceleration and speed has been validated against existing ICE-powered vehicles operating within the same segment. The driver is parameterised to resemble a racing driver, and 13 internationally known circuits of varying length, geographic location, and main use were modelled for driving simulations. As such, this database supports the development of a generic HP duty cycle, the derivation of which is discussed in Chapter 5.

## 5 Development of a generic HP duty cycle

### 5.1 Introduction

This chapter addresses “**Research Task 2:** Define a methodology, from which a duty cycle that is suitable for LIB performance and degradation testing may be derived.” Two methodologies to develop a duty cycle are presented. The resulting methodologies constitute a key component of the framework outlined within Figure 3-6, and address the knowledge gap identified within Chapter 3, pertaining to the scarcity of appropriate duty cycle design methodologies.

Each methodology is used to generate a duty cycle representing 12 out of the 13 duty cycles established in the previous chapter. The 13<sup>th</sup> profile, chosen arbitrarily as the duty cycle derived from the simulation for the Bahrain circuit is used as a validation profile to determine the validity of the presented methodologies and resulting profiles. The process for each methodology and selection of target criteria are described in full detail below.

Secondly, results are presented that quantify the differences in performance requirements for a cell based on HP duty cycles compared to the IEC 62660 Dynamic Discharge Profile A (IECC), initially described in Chapter 2. Finally, results from a thermal modelling simulation are reported that highlight the level of heat generation within a cell under HP-BEV applications and compares this to that predicted using established battery test methods.

### 5.2 Method One: HP Random Pulse Cycle (HP-RPC)

The first of the two methods extends the research described in [178,179]. This new method, illustrated in Figure 5-1, follows the same principle as the random microtrip methodology initially discussed in Chapter 3.4.1. The key differences between this new method and the existing established driving cycle method are highlighted with a red box within Figure 5-1. Firstly, the source data, which are normalised duty cycles instead of driving profiles, is segmented into duty pulses, defined as the time signal between two zero crossings. Secondly, to ensure the resulting cycle is suitable for LIB performance and degradation testing, the target criteria is selected to represent those aspects of the database, which mainly influence cell heating and degradation. These are defined later within the chapter. Duty cycle construction subsequently involves randomly selecting pairs of discharging and charging pulses and combining them to generate the complete HP duty cycle. The resulting cycle is called a “HP Random Pulse Cycle” (HP-RPC). The

specifics of data processing, target criteria selection, and cycle generation are described in detail below.

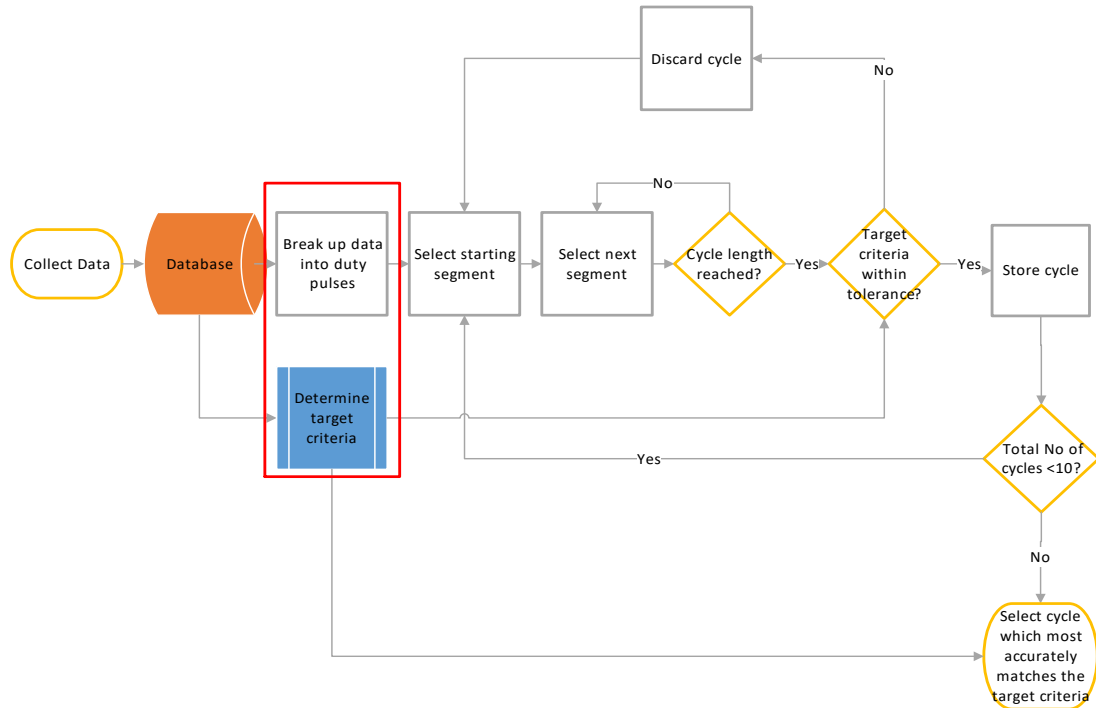


FIGURE 5-1 – DUTY CYCLE CONSTRUCTION PROCESS AS SUGGESTED FOR THE HP-RPC.

### 5.2.1 HP-RPC Data Processing and Target Criteria

The target criteria for the first method comprises several measures in the time-domain. A profile matching these criteria should represent the generic shape of the original profiles in the database. Furthermore, key profile features pertaining to battery degradation and self-heating should be preserved.

As described in detail in Chapter 2, cells cycled at higher C-rates, i.e. higher power, are known to display reduced cycle life [27,220] which should be reflected in the target criteria. Preliminary results presented within [163] indicate that both, charging and discharging pulses, at peak power cause a higher capacity loss over time than a pulse with the same cumulative energy but lower magnitude. Pulsed profiles also appear to cause more capacity fade than a constant current discharge with the same cumulative discharge energy [154]. Accurate representation of the magnitude and duration of charging and discharging pulses is therefore deemed necessary. As the anode and cathode degrade under different ageing mechanisms [47] it is also required to

take into account the duration the cell is being charged and discharged respectively to ensure that this is equally represented within the derived HP duty cycle.

To extract information such as power pulse duration and magnitude from the duty cycles, the following process was followed. Each normalised race circuit duty cycle signal ( $P_{Norm}(t)$ ) was divided into a set of duty pulses ( $p(t)$ ). As mentioned, this is defined as the time signal between two zero crossings. This is similar to the definition of a microtrip often employed within drive-cycle construction studies [180]. The entire database is broken down into a finite number of duty pulses and expressed as a single set  $\mathbb{P}$  with  $k$  number of duty pulses in the database.

$$\mathbb{P} = \{p_1(t), p_2(t), p_3(t), \dots, p_k(t)\} \quad (41)$$

Furthermore, the set  $\mathbb{P}$  is broken down into two subsets,  $\mathbb{D}$  and  $\mathbb{C}$  containing all recorded discharging ( $d_i(t)$ ) and charging ( $c_i(t)$ ) pulses, respectively, where  $i$  is the  $i^{th}$  pulse contained within in each set. The conditions for a pulse of duration  $L$  to be classified as a discharging or charging pulse are defined in equations (42) and (43) respectively.

$$p(t) = d(t), \quad \text{for } \int_0^L p(t) dt < 0 \quad (42)$$

$$p(t) = c(t), \quad \text{for } \int_0^L p(t) dt > 0 \quad (43)$$

As such:

$$\mathbb{P} = \mathbb{D} \cup \mathbb{C} \quad (44)$$

$$\mathbb{D} = \{d_1(t), d_2(t), \dots, d_j(t)\} \quad (45)$$

$$\mathbb{C} = \{c_1(t), c_2(t), \dots, c_j(t)\} \quad (46)$$

The two subsets  $\mathbb{D}$  and  $\mathbb{C}$  can be further arranged into racing-circuit specific duty pulses as

$$\mathbb{D} = D_1 \cup D_2 \cup \dots D_M \quad (47)$$

$$\mathbb{C} = C_1 \cup C_2 \cup \dots C_M \quad (48)$$

where  $M$  ( $M = 12$ ) is the number of racing-circuit duty cycles in the database. Each subset ( $D_m$ , and  $C_m$ ) contains the duty pulses  $d_i^m(t)$  and  $c_i^m(t)$ , where  $m$  is the index for a specific racing-circuit and  $i$  is the index for a particular duty pulse.

$$D_m = \{d_1^m(t), d_2^m(t), \dots, d_i^m(t)\} \quad (49)$$

$$C_m = \{c_1^m(t), c_2^m(t), \dots, c_i^m(t)\} \quad (50)$$

Duty pulses for charging and discharging are easily associated with driving manoeuvres on a racing circuit as illustrated within Figure 5-2, whereby discharging pulses are associated with driving on straights and accelerating out of corners, and charging pulses are associated with braking into a corner.

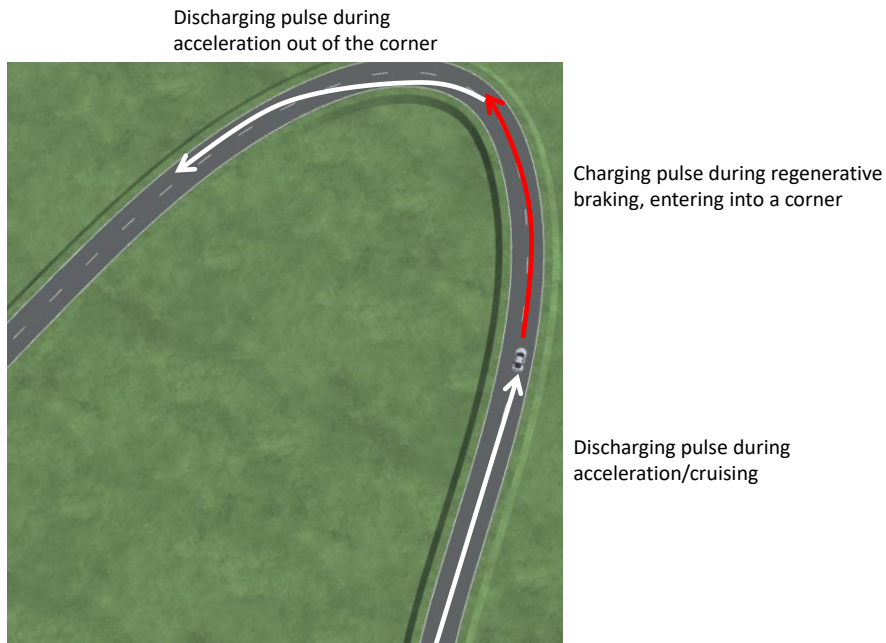


FIGURE 5-2 – ILLUSTRATION OF DUTY PULSES AND ASSOCIATED DRIVING MANOEUVRES

The racing-circuits in this study produce a total of 189 charging and 189 discharging pulses. Based on this knowledge, the race circuit driving cycle database is analysed in terms of the parameters ( $\zeta_{cycle}$ ) described in Table 5-1.

No	Parameter ( $\zeta_{cycle}$ )	Description	Value from database
1	$P_{DC}$	Normalised mean duty cycle discharge power	57.06%
2	$P_C$	Normalised mean duty cycle charge power	34.95%
3	$P_{net}$	Normalised net duty cycle discharge power	22.02%
4	$P_{abs}$	Normalised mean duty cycle absolute power	48.59%
5	$\kappa_{DC}$	% of time on discharge	61.6%
6	$\kappa_C$	% of time on charge	38.4%
7	$\tau_{AvgDC}$	Mean discharge pulse duration	8.3s
8	$\tau_{maxDC}$	Maximum discharge pulse duration	23.4s
9	$\tau_{AvgC}$	Mean charge pulse duration	4.7s
10	$\tau_{maxC}$	Maximum charge pulse duration	10.4s
11	$t_{cycle}$	Duration of the cycle	204.8s

TABLE 5-1 - RANDOM PULSE CYCLE TARGET PARAMETERS

$P_{DC}$  and  $P_C$  represent the average power sunk or sourced from the battery system during a duty cycle.  $P_{net}$  is the net power demand that indicates how much power is demanded on average at every instant.  $P_{abs}$  defines the mean absolute power throughput describing how much power is either supplied to or demanded from the battery.  $\kappa_{DC}$  represents the fraction of time the battery is discharging. Conversely,  $\kappa_C$  is the fraction of time the battery is charging over the course of a duty cycle. As the peak power demand for charging and discharging within this study is vehicle limited, the peak pulse amplitudes do not require an individual measure. These target parameters, collectively, describe the amount of energy supplied to and extracted from the system and the proportions in which this occurs.

The arithmetic mean and maximum duration of discharge pulses,  $\tau_{AvgDC}$  and  $\tau_{maxDC}$  are chosen to represent the shape and composition of the different discharge pulses. The target parameter for maximum pulse duration ( $\tau_{maxDC}$ ) ensures that a wide range of pulses are used and therefore the potential effects arising from prolonged high power demand are not excluded from the duty cycle. Finally, the target duration of the duty cycle ( $t_{cycle}$ ) defines the length of one period of the test profile.



## 5.2.2 HP-RPC Construction

Using the target parameters from Table 5-1 in conjunction with the sets  $\mathbb{D}$  and  $\mathbb{C}$  it is possible to construct a representative duty cycle following the steps illustrated in Figure 5-3 and described in detail below.

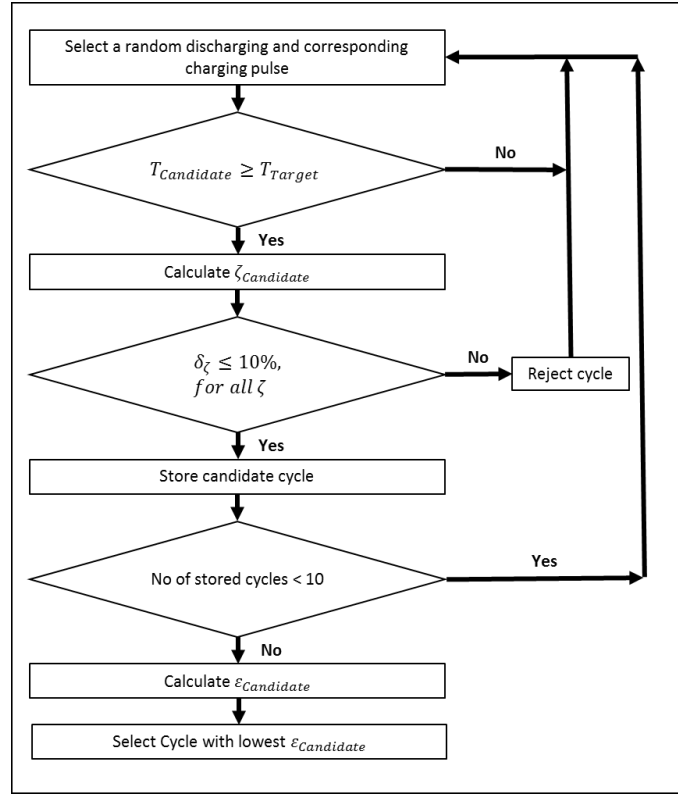


FIGURE 5-3 – RANDOM PULSE CYCLE (HP-RPC) CONSTRUCTION METHODOLOGY

A uniform random number generator using the MATLAB® function “rand” determines an integer index  $m$  with the condition  $1 \leq m \leq 189$  for the sets  $\mathbb{D}$  and  $\mathbb{C}$ . The indexed discharging pulse is selected from the set  $\mathbb{D}$  followed by the charging pulse with the same index resulting in a duty cycle as described in equation (51), where  $l$  is the number of generated indices.

$$P_{Candidate}(t) = [d_1, c_1, d_2, c_2, \dots, d_l, c_l] \quad (51)$$

Once a pulse has been selected, it is not excluded from the set. Selecting the charging pulse with the same index as the previous discharging pulse ensures a realistic sequence of charge and discharge pulses is created. This avoids the occurrence of a short discharging pulse followed by a long charging pulse, which may not be possible within a real-world application since it results in a battery over-charge condition. This stage of the process is repeated and the pulses are

concatenated until the target time duration  $t_{cycle}$  is reached or exceeded as shown in equation (52). This resulting cycle is referred to as a “*candidate cycle*”.

$$t_{Candidate} \geq t_{cycle} \quad (52)$$

The candidate cycle is subject to an assessment test to evaluate its suitability. Each of the eleven assessment parameters from Table 5-1 ( $\zeta_{cycle}$ ) are calculated for the candidate cycle ( $\zeta_{Candidate}$ ). The error ( $\delta_\zeta$ ) is calculated for each  $\zeta_{cycle}$  using equation (53).

$$\delta_\zeta^{Candidate} = \left| \frac{\zeta_{Candidate} - \zeta_{cycle}}{\zeta_{cycle}} \right| \quad (53)$$

A cycle passes the assessment test if it fulfils the condition in equation (54) for each target parameter.

$$\delta_\zeta^{Candidate} \leq 10\%, \quad \text{for all } \zeta \quad (54)$$

In [178,179] a cycle is only accepted as a candidate cycle if each of the assessment parameters is within a 5% error margin. Within this work however, a relaxation of the convergence criteria was required to ensure a candidate-cycle satisfied the criteria within an acceptable number of iterations. With  $\delta_\zeta$  set to 10%, it was found that 200 iterations of the process were required before suitable candidate cycles were identified. Conversely, with  $\delta_\zeta$  set to 5% more than 40,000 iterations failed to return an acceptable candidate cycle. The excessive computational time required with a reduced error margin was therefore deemed to reduce the usefulness of the method. A larger database with greater variation of pulses may return a cycle that matches a more stringent selection criterion with a reduced number of iterations.

The evaluation process is repeated until 10 cycles are found that pass the assessment test. The cumulative error ( $\varepsilon_{Candidate}$ ) is calculated as the sum of errors from  $\delta_\zeta^{Candidate}$  for a particular candidate cycle as in equation (55), and the cycle with the smallest ( $\varepsilon_{Candidate}$ ) is chosen as the HP-RPC.

$$\varepsilon_{Candidate} = \sum_{\zeta} \delta_\zeta^{Candidate} \quad (55)$$

### 5.3 Method Two: HP Multisine Cycle (HP-MS)

The second of the two methods utilises the frequency domain approach presented within [200], and initially described in section 3.5. Using a frequency-time domain swapping algorithm, a duty cycle is derived from a user defined amplitude spectrum and iCDF. The choice of target amplitude spectrum and iCDF are described in detail below.

#### 5.3.1 HP-MS Data Processing and Target criteria

The amplitude spectrum for each of the normalised duty cycles contained within the database can be determined from a Fourier series first described in equation (31), and again in equation (56), where  $P_{Norm}(t) = x\left(\frac{n}{f_s}\right)$ , and each profile  $P_{Norm}(t)$  contains  $n$  samples, sampled at frequency  $f_s$ . This is obtained via the Fast Fourier Transform (FFT) routine in MATLAB®.

$$x\left(\frac{n}{f_s}\right) = A_0 + \sum_{k=1}^{\infty} A_k \sin(2\pi n f_k + \phi_k) \quad (56)$$

This approach assumes that the profile  $P_{Norm}(t)$  is periodic. In a real-world scenario this is not entirely the case due to small lap-to-lap variations that are expected from human driving. However, the author asserts that this assumption is acceptable due to the nature of driving on a closed circuit. In the analysis stages, the amplitude component at 0 Hz frequency (the DC component  $A_0$ ) can be removed as long as it is accounted for at the cycle design stage. Therefore, the mean (averaged over time) of each duty cycle is removed to produce a zero-mean duty cycle  $P_{Norm,zm}(t)$ . This processing step is required to aid function fitting as discussed later.

The iCDF was initially shown in equations (32) and (33), and again equations (57) and (58). Again,  $y$  is the amplitude of the power profile at a random point,  $F_y(B)$  is the probability that the amplitude of that operating point is equal to or less than  $B$ , and the iCDF in equation (58) is the inverse of the eCDF in equation (57). As the iCDF is a representation of a histogram, it contains similar information to the target parameters associated with the random pulse method (see Table 5-1), except for the pulse duration parameters ( $\tau$ ).

$$F_y(B) = P[y \leq B] \quad \text{for} \quad B \in \mathbb{R} \quad (57)$$

$$g(P) = F_y^{-1}(P) \quad (58)$$

Figure 5-4(a) shows the amplitude spectra (in dB<sup>1</sup>) for each  $P_{Norm,zm}(t)$ , as well as a function approximating the mean of the 12 duty cycles. The exclusion of the component  $A_0$  simply removes the amplitude at a frequency of 0 Hz. The remaining shape and values of the amplitude spectra are unaffected. The values of the amplitude spectra lie within a certain band and all retain a similar shape with a broad spread of values at low frequencies converging to a narrower spread at higher frequencies. The mean spectrum lies within the band of spectra and follows the general shape and thus captures the characteristic in the frequency domain [141]. The mean amplitude spectrum here is approximated by a rational function  $f(f_k)$  as expressed in equation (59).

$$f(f_k) = \frac{\sum_{i=0}^4 a_i f_k^i}{\sum_{l=0}^5 c_l f_k^l} \quad (59)$$

In this case, the function most accurately representing the mean amplitude spectrum  $f(f_k)$  (obtained by running a MATLAB curve-fitting algorithm) is composed of a 4<sup>th</sup> order polynomial in the numerator and 5<sup>th</sup> order polynomial in the denominator.

---

<sup>1</sup>  $dB(x) = 20 \log(x)$

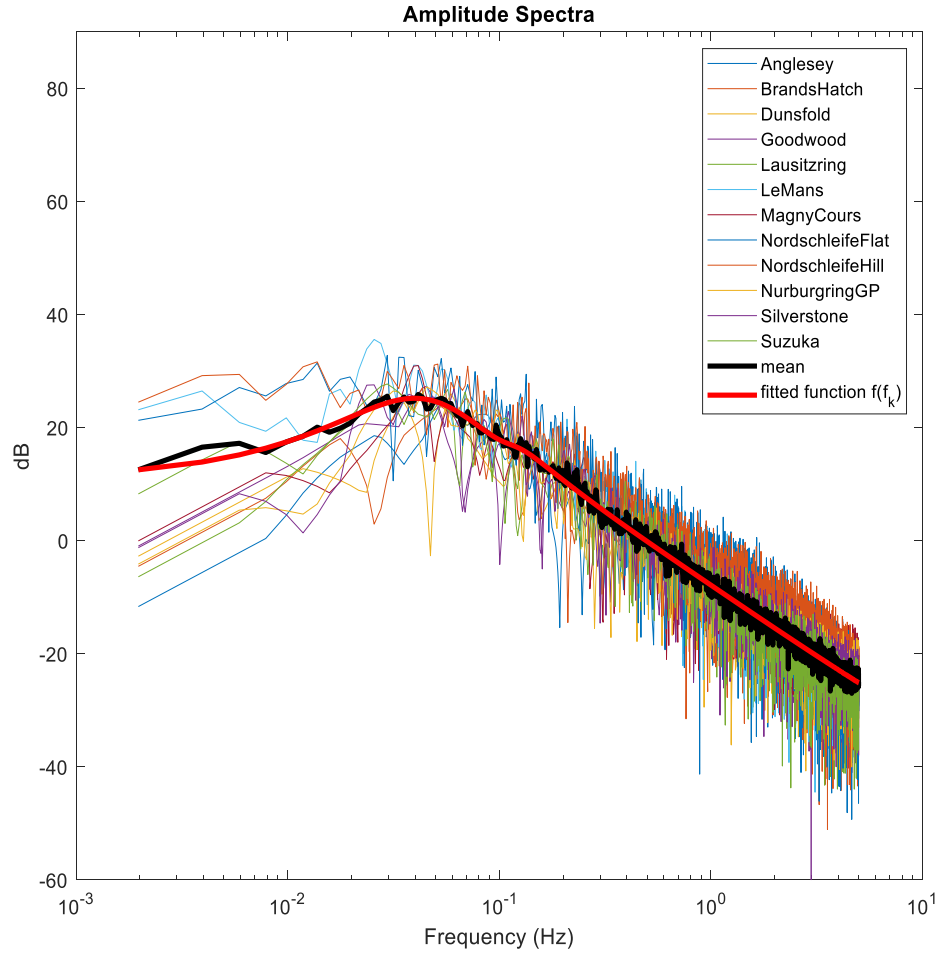


FIGURE 5-4 – AMPLITUDE SPECTRA FOR  $P_{Norm,zm}(t)$  FOR 12 CIRCUITS OF THE DATABASE; MEAN AMPLITUDE SPECTRUM; FUNCTION APPROXIMATING THE MEAN AMPLITUDE SPECTRUM

Figure 5-5 shows the iCDF for each zero-mean duty cycle in the database as well as the mean and a fitted function. The removal of the DC component results in a shift of the iCDF without influencing its shape. The functions all lie within a certain band and follow the same trend in terms of shape. An outlier in the results presented is the Le Mans racing-circuit (Table 4-7) duty cycle. This circuit is known for long straights associated with extended high-power discharge pulses and fewer corners relating to fewer braking opportunities and thus fewer charging pulses. This makes the Le Mans racing-circuit a more aggressive but not improbable scenario. Therefore, it is not excluded from further analysis. The mean of the iCDFs is approximated by a rational function  $g(P)$  as shown in equation (60). This forms the desired iCDF for the signal generation method.

$$g(P) = \frac{\sum_{i=0}^5 a_i P^i}{\sum_{l=0}^4 c_l P^l} \quad (60)$$

The function best approaching the mean inverse CDF ( $g(P)$ ) contains a 5<sup>th</sup> order polynomial in the numerator and 4<sup>th</sup> order polynomial in the denominator. The parameters for both the mean amplitude spectrum (equation (59)) and iCDF (equation (60)) functions are estimated using the MATLAB<sup>®</sup> function fitting toolbox. Out of the tested functions in MATLAB<sup>®</sup>, the rational function with the highest  $R^2$  value and narrowest 95% confidence intervals for the coefficients was chosen.

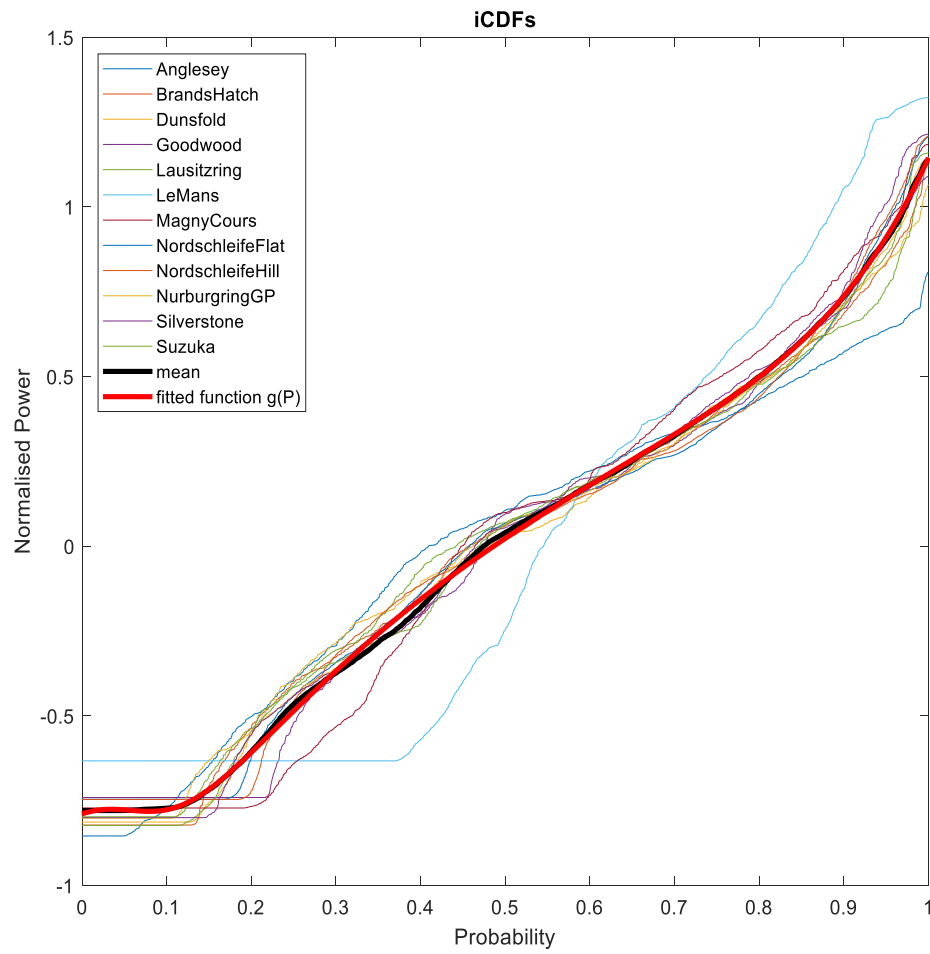


FIGURE 5-5 – iCDF for  $P_{Norm,zm}(t)$  FOR 12 CIRCUITS OF THE DATABASE; MEAN AMPLITUDE SPECTRUM; FUNCTION APPROXIMATING THE MEAN AMPLITUDE SPECTRUM

## 5.3.2 HP-MS Construction

The process for the construction of the HP-MS is summarised within the flowchart in Figure 5-6 and described below. The progression of the implemented time-frequency swapping algorithm is illustrated in Figure 5-7. The derivation and explanation of this algorithm is discussed within [200].

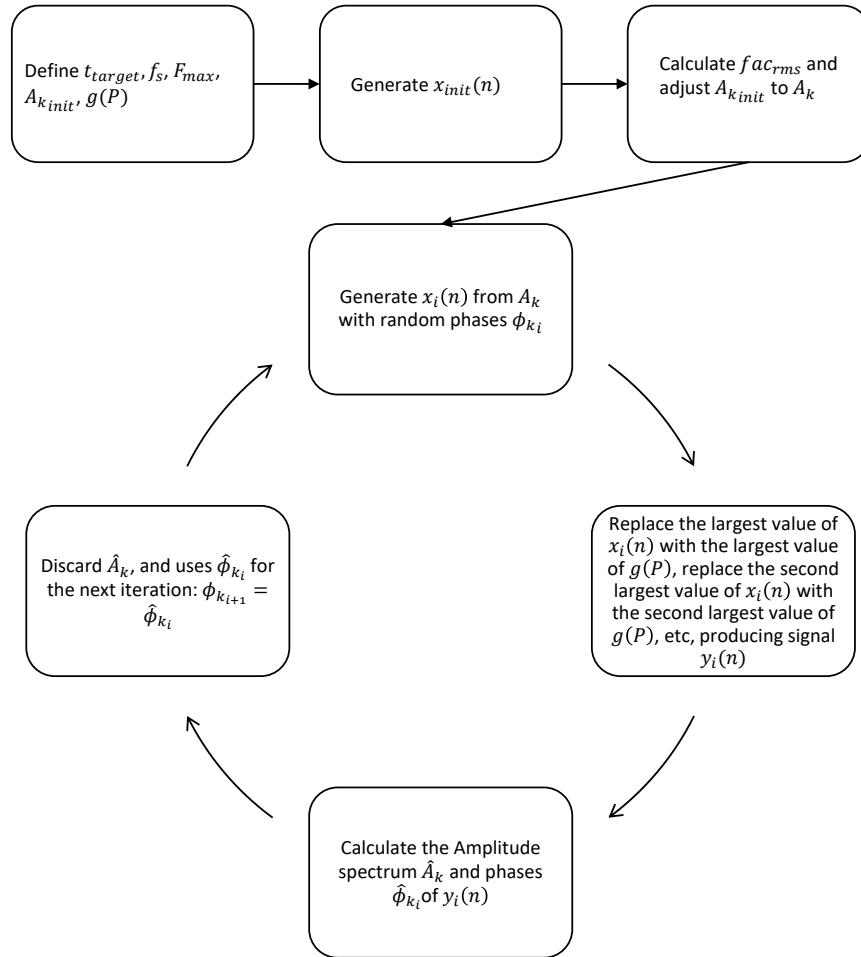


FIGURE 5-6 – HP-MS CONSTRUCTION PROCESS

The algorithm starts by generating a single period of a random phase multisine, which is a series of superimposed sinewaves with random phases (uniformly distributed between 0 and  $2\pi$ ), as defined in equation (61).

$$x_i(n) = \sum_{k=1}^F A_k \sin(2\pi n f_k + \phi_k) \quad n = 0, 1, \dots, N-1 \quad (61)$$

Again,  $f_k$  is the frequency at the  $k^{th}$  harmonic and is  $f_k = kf_s/N$  with the sampling frequency  $f_s$  (10 Hz),  $N$  is the number of samples per period ( $N = t_{target}f_s$ ), where  $T$  is the period in seconds. For this duty cycle  $t_{target}$  is set to the HP-RPC target of 204.8s, which in combination with the 10 Hz sampling rate results in 2048 samples. The amplitudes  $A_{k_{init}}$  for frequencies  $f_k = \frac{f_s}{N}, \frac{2f_s}{N}, \dots, F_{max}$  are determined from equation (62), where  $F_{max}$  denotes the highest frequency of interest.

$$A_{k_{init}} = f(f_k) \quad (62)$$

The function  $f(f_k)$  approximates the mean amplitude spectrum as described in equation (59) and shown in Figure 5-4. It can also be seen in Figure 5-4 that the majority of power in the amplitude spectrum is contained within the range from 0 – 0.3 Hz. As such  $F_{max}$  is set to 0.3 Hz and a total of  $F$  amplitudes are determined for the first  $F$  frequencies where  $F = \frac{F_{max}}{f_1}$ . The phases  $\phi_k$  for the  $F$  harmonics are initially chosen at random between 0 and  $2\pi$ . Subsequently, the values for the desired iCDF ( $g(P)$ ) are determined by using equation (60) for  $P = \frac{1}{N}, \frac{2}{N}, \dots, 1$ .

At first, as only a reduced spectrum is selected, the initial profile of  $x_{init}(n)$  and  $g(P)$  have different RMS values. For the algorithm to work it is necessary that the values of  $A_{k_{init}}$  are adjusted to account for this using a correction factor ( $fac_{rms}$ ) as described in equation (63), and adjusting  $A_{k_{init}}$  as described in equation (64). The value of this correction factor is dependent on the frequency bandwidth of choice.

$$fac_{rms} = \frac{rms(g(P))}{rms(x_{init}(n))} \quad (63)$$

$$A_k = A_{k_{init}} \cdot fac_{rms} \quad (64)$$

This produces the desired amplitude shown in Figure 5-7-b.

Following this adjustment, another random phase multisine is generated using the adjusted spectrum. This signal has the desired spectrum but the random phases do not produce the desired iCDF (see Figure 5-7-c) for this random phase multisine signal (see Figure 5-7-a). The time-frequency domain swapping algorithm enforces the desired iCDF ( $g(P)$ ) and the desired amplitude spectrum ( $f(f_k)$ ) iteratively until a convergence criterion is met as described below.



The sample values of the random phase multisine ( $x_i(n)$ ,  $i$  denotes the iteration index) are sorted in ascending order and the indices of the values original position are recorded. These values of  $y$  are the iCDF of  $x_i$  (the zero-mean HP duty cycle at the  $i^{\text{th}}$  iteration). The position variable ( $\varphi$ ) serves as a timestamp indicating at which time in the duty cycle the value  $y$  occurs. It can be seen in Figure 5-7-c that the iCDF differs from the desired mean iCDF as described equation (60) in and shown in Figure 5-5.

To match the desired iCDF, a new duty-cycle ( $y_i(n)$ ) is created by replacing each value in  $x_i(n)$  with the corresponding value of  $g(P)$ . This implies that the smallest of the calculated values of  $g(P)$  replaces the smallest value in  $x_i(n)$ , the second smallest value of  $g(P)$  replaces the second smallest value in  $x_i(t)$ , and so forth. This process is repeated for all  $y$  resulting in a new duty cycle with a changed amplitude spectrum and phases. The phases of this new duty cycle are determined via the Discrete Fourier Transform and used to generate a new duty cycle using the desired amplitude spectrum. This process is repeated, each time using the updated phases until a defined convergence between  $\text{sort}(x_i(n))$  and  $g(P)$  is met.

The convergence criteria chosen in this work is met if the change in the sum of errors between desired and optimised inverse CDF is smaller than  $10^{-7}$ . This value was chosen as a compromise between accuracy and computational effort. The progression of this is shown in Figure 5-7-d, the resulting zero-mean cycle is shown in Figure 5-7-a. The HP Multisine Cycle (HP-MSC) is obtained once the mean DC component, synonymous with  $P_{net}$  in Table 5-1 is added. The final HP-MSC contains instances where peak discharge demands exceed the -100% limit. This is attributed to the approximation of the mean iCDF by a function. Instances where the HP-MSC exceeds the discharging limit are constrained to -100%.

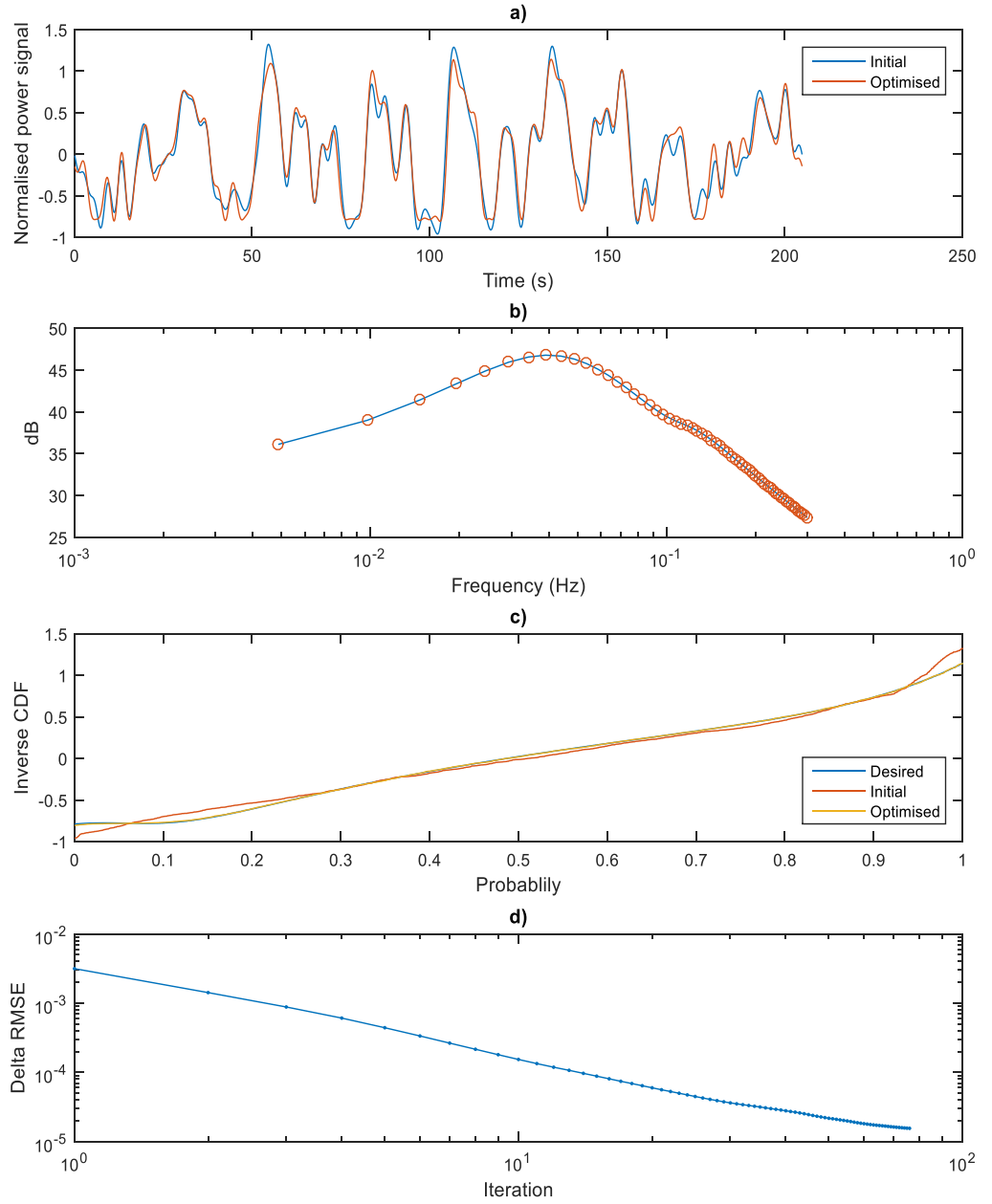


FIGURE 5-7 - OVERVIEW OF ALGORITHM OUTCOME A) A SINGLE PERIOD OF THE ZERO-MEAN MULTISINE CYCLE; B) THE AMPLITUDE SPECTRUM UP TO 0.3 Hz; C) DESIRED, INITIAL AND OPTIMISED INVERSE CUMULATIVE DISTRIBUTION FUNCTION; D) PROGRESSION OF POWER ROOT MEAN SQUARED ERROR (RMSE)

## 5.4 Results

To verify the new duty cycles that represent HP driving scenarios three different studies were undertaken. Firstly, the HP-MSC and HP-RPC are validated, using the assessment criteria for HP-RPC and HP-MSC, against the duty cycle for the Bahrain International Circuit (Bahrain). The selection of this circuit was arbitrary and made prior to the development of the duty cycles.

Secondly, the HP-RPC and HP-MSC are compared to the IECC [34] to further highlight the differences in these realisation of a HP duty cycle compared with traditional and widely accepted test and characterisation cycles. The power-time traces of HP-RPC, HP-MSC, Bahrain, and IECC are shown in Figure 5-8.

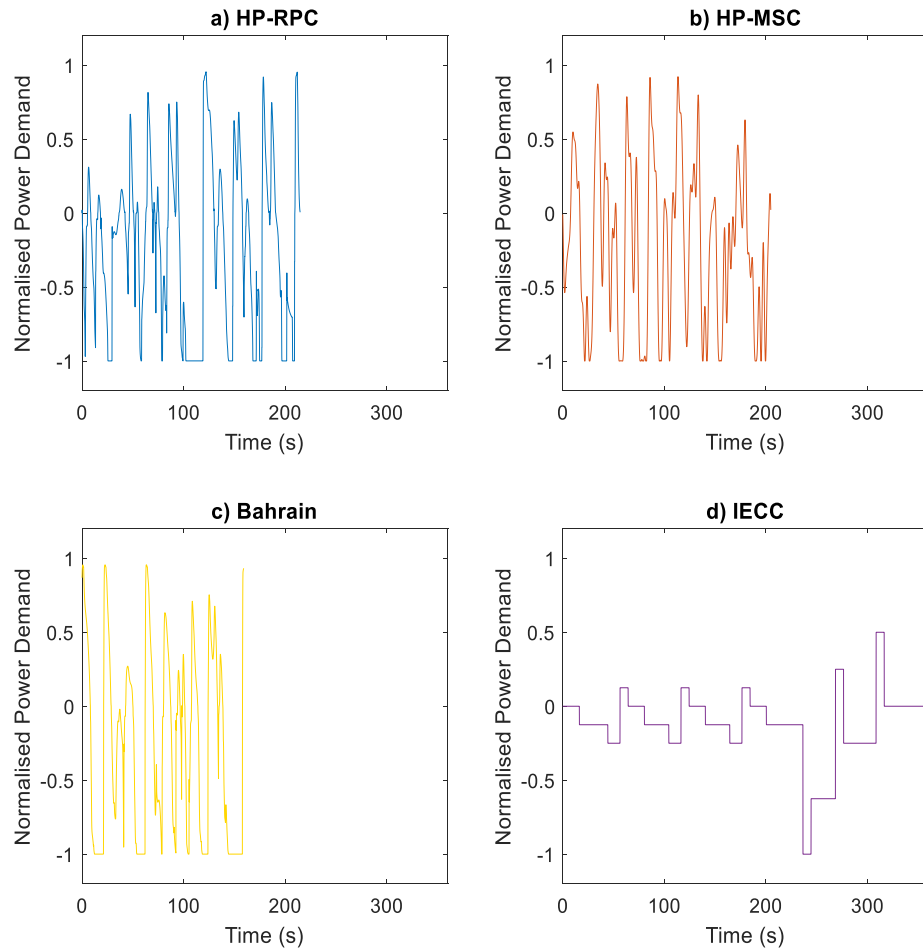


FIGURE 5-8 - A) MULTISINE CYCLE; B) RANDOM PULSE CYCLE; C) BAHRAIN RACING-CIRCUIT SIMULATION DUTY CYCLE; D) IEC 62660-1 CYCLE LIFE TEST PROFILE A

Finally, a thermal simulation study is undertaken for HP-RPC, HP-MSc, Bahrain, and IECC to estimate cell heating and the average volumetric temperature profile for a discharge from 100% to 10% SoC. As identified in the introduction, cell temperature is a main contributor to battery degradation and as such, the self-heating of a cell during electrical loading should be considered as an influencing factor when considering cell degradation and the usefulness of the battery duty cycle.

#### 5.4.1 Validation of HP-MSc and HP-RPC

Figure 5-9a and b show the design parameters, described in Table 5-1, calculated for HP-RPC, HP-MSc and the Bahrain duty cycle. Despite the different methodologies applied to design each duty cycle, the calculated parameters for HP-RPC and HP-MSc are very similar. Compared to the Bahrain cycle, a lower demand for mean discharge power ( $P_{DC}$ ) and mean charge power ( $P_C$ ) may be observed for both HP-RPC and HP-MSc. In turn, this results in corresponding lower values for net discharge power ( $P_{net}$ ) and mean absolute power ( $P_{abs}$ ). The difference between HP-RPC and the Bahrain cycle for these parameters range from 12.9% to 19.9%. Conversely, when comparing the HP-MSc and Bahrain circuit profile, the differences range from 11.6% to 20.7% respectively (see Figure 5-9c). The percentage of time the battery is subjected to discharge ( $\kappa_{DC}$ ) and subjected to charge ( $\kappa_{DC}$ ) is similar between all cycles with differences of less than 8%.

Similar variations can be found for the time-based parameters, except for the maximum discharge pulse duration ( $\tau_{MaxDC}$ ) and cycle duration ( $T$ ). Further analysis of the profiles, illustrated in Figure 5-8 a, b and c, reveals that the longest discharge pulse for the HP-RPC is 23.7s compared to 22.1s for the HP-MSc and 19.2s for the Bahrain Cycle. The difference in peak pulse duration is small, in absolute terms, but amounts to 23.4% between Bahrain and HP-RPC, and 15.1% between Bahrain and HP-MSc.

Figure 5-9d shows the amplitude spectra for the HP-RPC and Bahrain cycle up to 5 Hz and for the HP-MSc up to the design frequency of 0.3Hz as presented in section 5.3.1. The HP-MSc, HP-RPC and Bahrain cycle amplitude spectra follow the same general trend and as such all signals carry similar characteristics within the frequency domain.

The flatness in peak power demand represented by the HP-RPC and Bahrain cycle is not captured in the HP-MSc. This observation is due to the exclusion of higher frequencies in the selection of the amplitude spectrum in the HP-MSc approach. Inclusion of higher frequencies (in the range of 0.3Hz to 5Hz) would allow for a flattened peak demand for discharge pulses, but also results in

more frequent periods of charging and discharging. The performance of the HP-MS against the time-based parameters in Figure 5-9b may be adversely affected by fluctuations around zero amplitude, causing increased switching between charging and discharging. The performance of HP-MS against target parameters, shown in Figure 5-9a, and the cycle duration ( $T$ ) remain unaffected by the inclusion of higher frequencies.

The iCDFs for all three cycles are displayed in Figure 5-9e. They show that the discharge power demand for HP-RPC remains at peak power ( $P < -0.9$ ) for 20.6% of the cycle duration compared to 16.7% for the HP-MS and 29.2% for the Bahrain cycle. The proportion of power demand for discharging and charging, respectively, is similar between all cycles, an observation which is synonymous with the results presented in Figure 5-9a, b and c.

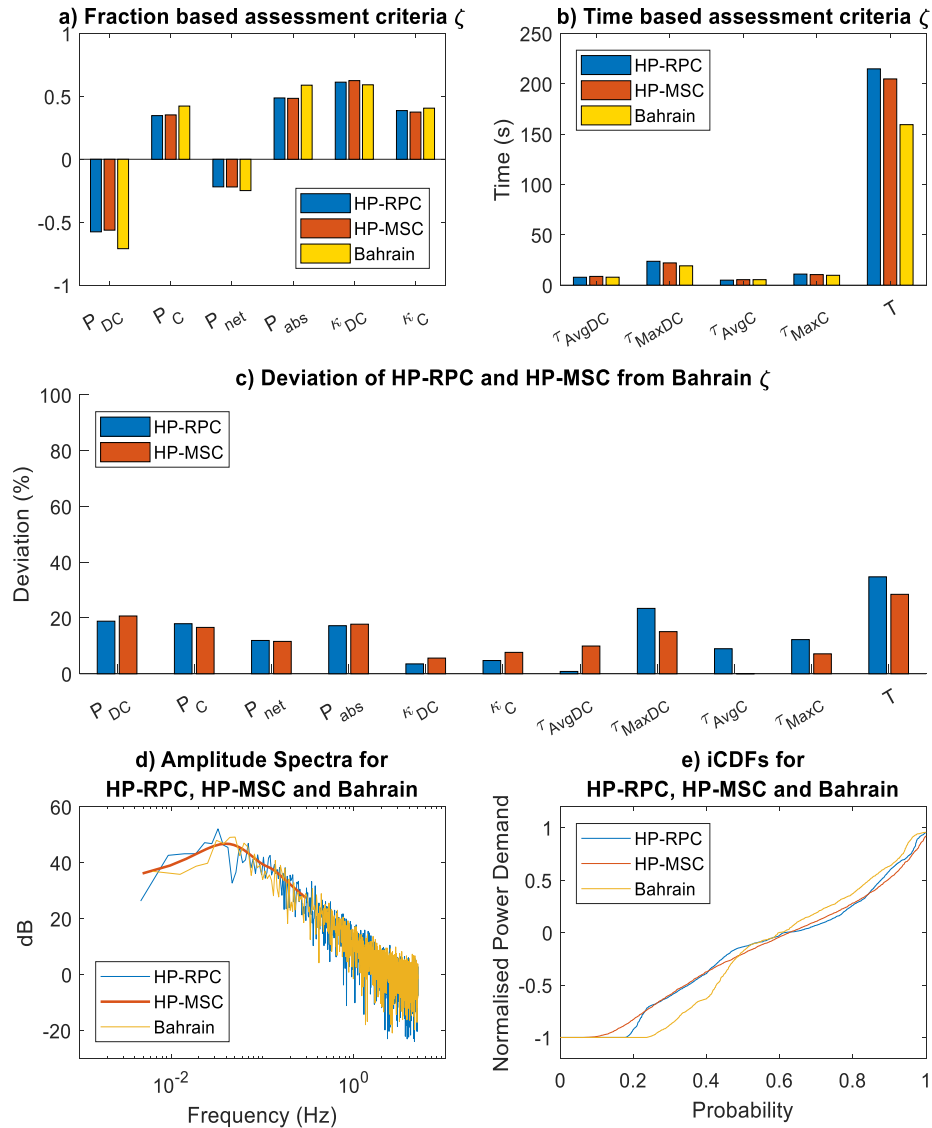


FIGURE 5-9 – VALIDATION OF HP-MSC AND HP-RPC AGAINST THE BAHRAIN CYCLE BASED ON HP-RPC AND HP-MSC DESIGN CRITERIA. A) FRACTION BASED CRITERIA; B) TIME BASED CRITERIA; C) DEVIATION OF HP-MSC & HP-RPC FROM BAHRAIN CYCLE BASED ON HP-RPC CRITERIA; D) AMPLITUDE SPECTRA FOR HP-RPC, HP-MSC AND BAHRAIN; E) iCDF FOR HP-RPC, HP-MSC AND BAHRAIN.

#### 5.4.2 Comparison between HP cycles and the IEC Test standard

To highlight the difference between the realisation of a generic HP duty cycle and a traditional automotive testing duty cycle, HP-RPC and HP-MSC are compared to the cycle life test profile A (IECC) defined within the IEC 62660-1. The IECC contains only 8s of peak discharging power demand per period compared to the previously identified 23.7s for the HP-RPC and 22.1s for the

HP-MSC. In conjunction with a much longer period, this results in a very low value for the mean discharge power ( $P_{DC}$ ) of 0.255. As shown in Figure 5-10a, similar observations can be made for mean charge power  $P_C$ . As such, the values for net discharge power ( $P_{net}$ ) and mean absolute power ( $P_{abs}$ ) also adopt much lower values for the IECC compared to the HP profiles. The percentage of time the battery is on discharge ( $\kappa_{DC}$ ) is comparable between the HP cycles and standardised cycle. However, as the IECC contains resting periods at zero power demand and the HP profiles do not, their respective values for percentage of time the battery is on charge ( $\kappa_C$ ) do not correlate.

The maximum and mean pulse duration for charging and discharging are shown in Figure 5-10b and highlight further large differences. Although  $\tau_{AvgDC}$  and  $\tau_{MaxDC}$  indicate much longer individual discharging pulses for the IECC, the amplitude of the pulses is up to 70% lower and as such would result in much lower instantaneous heat generation. Assessing the deviation of HP-RPC, HP-MSC and IECC from the HP-RPC design targets as illustrated in Figure 5-10c, reveals that the smallest deviation of the IECC from HP targets can be found for  $\tau_{MaxC}$  at a value of 25.3% (except for  $\kappa_{DC}$ ). Conversely, the largest deviation is for  $\tau_{AvgDC}$  at a value of 410%.

As expected from a visual inspection of the cycles in Figure 5-8, and the discrepancies between the different duty cycles (HP-RPC, HP-MSC, and the IECC) shown in Figure 5-10a-c, the amplitude spectra of HP-RPC, HP-MSC and IECC (Figure 5-10d) follow separate trends. The excitation amplitudes for the IECC is lower than that of the HP-MSC, RPC, and Bahrain circuit for a broad bandwidth. As such, the IECC is deemed not to be representative of HP driving scenarios within the frequency domain. Similarly, for the iCDFs in Figure 5-10e, there is no identifiable correlation between these three cycles.

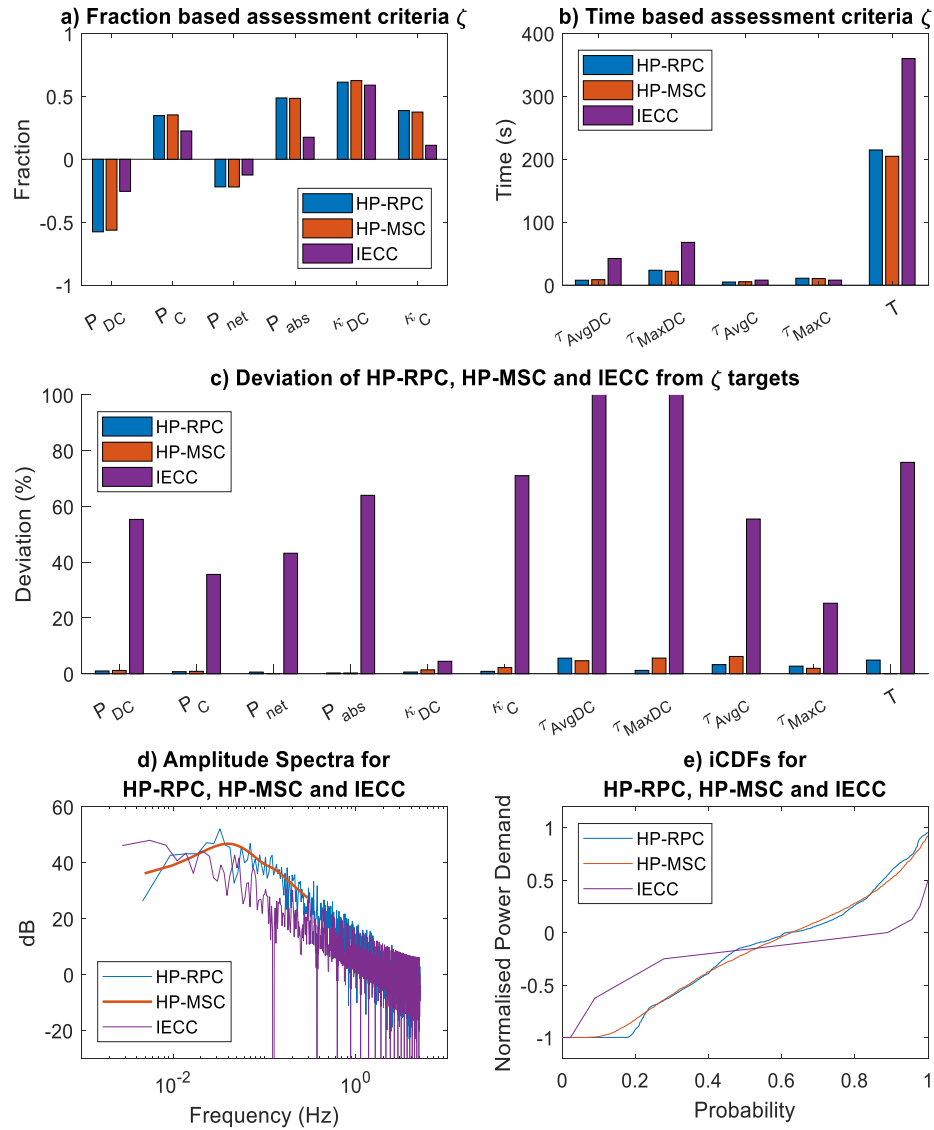


FIGURE 5-10 - DIRECT COMPARISON BETWEEN HP-RPC, HP-MSC AND IECC IN TERMS OF A) FRACTION BASED CRITERIA; B) TIME BASED CRITERIA; C) DEVIATION OF HP-RPC, HP-MSC AND IECC FROM HP-RPC TARGETS CRITERIA; D) AMPLITUDE SPECTRA FOR HP-RPC, HP-MSC AND IECC; E) iCDF FOR HP-RPC, HP-MSC AND IECC



### 5.4.3 Thermal simulation study

To further illustrate the discrepancies between the IECC and HP duty cycles, defined as part of this work and also to further highlight the correlation between the HP-RPC, HP-MSD and Bahrain cycle, a thermal simulation was undertaken to estimate the value of self-heating during a discharge from 100% to 10% SOC for each of the cycles.

A coupled 1D electrochemical-thermal model, developed through a complementary research activity within the University, for example [6], was employed. The commercial software Comsol Multiphysics was employed for the numerical simulation. The validated thermal model was developed for a 20 Ah pouch cell, where the anode is made of graphite and the cathode material is LFP. The model has been validated at different C-rates, 0.5C, 1C, 3C, 5C and 10C under 20°C ambient temperature. During this simulation study, the input power of each cycle was scaled to cell level. The maximum C-Rate for discharge was set at 8, a value that resides within the validated range of the model. The maximum charge rate of the profile was subsequently limited to 3 to comply with the manufacturer's specification for the cell. The ambient temperature of the simulation was set to 20°C, and the heat transfer coefficient from the cell surface to the surroundings was defined as  $10 \text{ Wm}^{-2}\text{K}^{-1}$  to emulate natural convection. Natural convection refers to a condition in which fluid motion for heat exchange is not generated by any external source, such as a fan or ventilator.

The derivation and parameterization of this model does not constitute part of this thesis. This and the numeric results were provided by the main author of the research presented within [6].

The results from this study are tabulated in Table 5-2 and presented in Figure 5-11. The terms temperature and heat generation refer to the average volumetric temperature and average volumetric heat generation respectively within the cell.

Cycle	Duration (s)	Max. Temperature (°C)	Mean volumetric heat generation ( $\text{kWm}^{-3}$ )	Mean heat generation (W)
HP-RPC	1491	44.0	107	28.3
HP-MSD	1530	43.9	106	27.9
Bahrain	1280	47.5	135	35.5
IECC	3121	30.0	30	7.9

TABLE 5-2 - THERMAL SIMULATION RESULTS FOR 20AH POUCH CELLS

Figure 5-11-a shows the volume average cell temperature for all four use cases. For the HP cycles the maximum temperature is reached at the end of discharge. This translates to 1280s for the Bahrain cycle, 1491s for HP-RPC, and 1530 for HP-MSD and ranges from 43.9°C to 47.5°C. As the Bahrain cycle is more aggressive, as shown by Figure 5-9a, than HP-RPC and HP-MSD respectively, the end of electrical loading is reached within a shorter time. In contrast, a cell undergoing the IECC schedule requires more than twice the time for the energy discharge to occur and reaches a peak temperature of only 30.0°C.

The cell heat generation for all four cycles is displayed in Figure 5-11-b-e. As expected, the three HP cycles show a good correlation to each other. The highest recorded instance of heat generation is similar between all cycles to within 3%. However, the mean heat generation for the duration of the cycles varies significantly, with Bahrain displaying the highest heat generation term of 135kW.m<sup>-3</sup>. The mean heat generation for the IECC is of a lower order of magnitude at 30kW.m<sup>-3</sup> resulting in a much lower temperature rise through electrical loading.

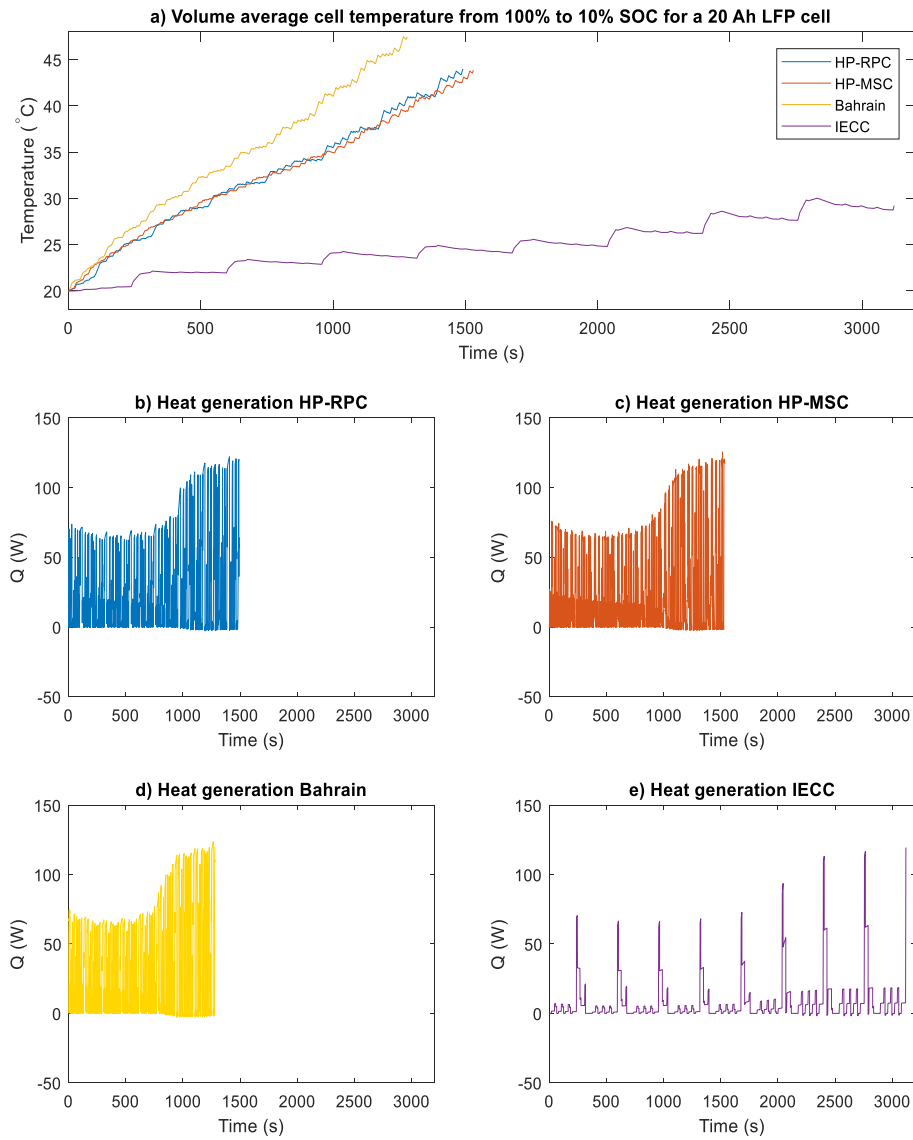


FIGURE 5-11 – A) AVERAGE CELL TEMPERATURE IN DEG C DURING CYCLING FROM 100% - 10% SOC FOR A 20 AH LFP CELL; B) CELL HEAT GENERATION FOR HP-RPC; C) CELL HEAT GENERATION FOR HP-MS; D) CELL HEAT GENERATION FOR BAHRAIN; E) CELL HEAT GENERATION FOR IECC

## 5.5 Discussion

### 5.5.1 Validation of the HP duty cycles for the Bahrain International Circuit

Validation of the cycles has shown a good degree of correlation between HP-RPC, HP-MS and a cycle chosen at random from the database representing the Bahrain International Circuit.

Although some differences such as power demand and time spent at peak have been observed, the results presented in section 5.4.1 clearly show that the HP-MSC and HP-RPC offer a good approximation for this particular HP scenario with the average error between HP-RPC and HP-MSC compared with the Bahrain cycle of 14.0%, and 12.8% respectively. The amplitude spectra of all cycles follow a similar shape highlighting the similarity between the profiles. As discussed within Chapter 3, the representation within the frequency domain is desirable, as the amplitude spectrum of the current input signal influences the voltage response of the LIB, thus the electrochemical processes taking place. Over time, this will affect the outcome of degradation.

The iCDFs show clearly that the Bahrain cycle is more aggressive and demanding than the generic cycles. To cater for more demanding cycles, the database for HP-RPC may be expanded with further aggressive duty cycles. For the HP-MSC generation method, an adjustment of the desired iCDF would be sufficient to tune the nature of the cycle to better represent this facet of the target HP duty-case.

Power demand and energy throughput for the Bahrain cycle are higher, but the longest pulse at peak power is smaller than that from the HP-RPC and HP-MSC. As shown in Figure 5-11, this results in higher heat generation during electrical loading for the Bahrain cycle. The largest discrepancy between the cycles is the period ( $T$ ) with a 34.8% deviation for HP-RPC and 28.5% deviation for HP-MSC. Arguably due to the repetitiveness of the pulses the shorter period of the Bahrain cycle by itself may be of lower significance to the profile as combined effects of  $\tau_{MaxDC}$ ,  $\tau_{MaxC}$  and  $T$  are indirectly captured in the parameters  $P_{DC}$ ,  $P_C$ ,  $P_{net}$  and  $P_{abs}$ . The Bahrain cycle is only one particular scenario falling within the band of HP cycles, and as such, both HP-MSC and HP-RPC are deemed satisfactory to represent a typical HP cycle.

### 5.5.2 Comparison of the HP Duty cycles against Standard Test and Characterisation Cycles

The subsequent comparison of the HP scenarios with standardised tests shows large discrepancies between the cycles based on the HP-RPC and HP-MSC design criteria. This was confirmed by the thermal simulation study which showed much smaller peak temperatures and self-heating effects for the IECC compared to the HP cycles. As such, it can be concluded that there is too little commonality between the standard IECC and HP duty cycles to warrant representation of the latter by the former.

## 5.6 Conclusion

This chapter has addressed “**Research Task 2:** Define a methodology, from which a duty cycle that is suitable for LIB performance and degradation testing may be derived.” Two methods to design HP battery duty cycles for cycle life and performance evaluation have been derived. The methodologies are not limited to HP-BEVs but provide a step-by-step guide for engineers and researchers to develop their own duty cycles for other applications, where standard testing procedures are not representative of real-world use and therefore address the first knowledge gap defined within Table 3-2. Either of the two methodologies can be used as part of the framework proposed within Chapter 3 and illustrated within Figure 3-6.

As discussed within a number studies, for example [221,222], a representative duty cycle supports a range of additional engineering functions such as component sizing, energy management, simulation and testing of the complete vehicle powertrain and key subsystems. As a result, the two methodologies are highly transferable to a number of different sectors that are investigating opportunities for electrification and the integration of battery systems. These include the electrification of marine and aerospace systems [223], either for more energy efficient propulsion or because of the inclusion of more electrically powered ancillaries. Further areas are the hybridisation of off-highway or construction vehicles [224,225], where the diverse usage patterns prohibit the creation of a generic drive-cycle such as the NEDC or US06 that are common within the road transport sector.

The HP-RPC method extends a well-established technique from the literature for drive-cycle construction [178,179] by randomly selecting alternating charging and discharging power pulses. The target criteria for cycle evaluation can be assessed to reflect the engineering challenge under investigation. The relative error margins between each candidate cycle and the criteria can be selected by the engineer to optimise the inherent trade-off between computation time and cycle accuracy. For this research, the error was set to 10% for each target criterion.

The second method evaluated for HP cycle definition follows a frequency-time swapping algorithm [200]. This generates a cycle that matches a user defined amplitude spectrum and an iCDF. Both functions can be chosen by the design engineer, following the general criteria presented in section 5.3.1. The choice of amplitude spectrum and iCDF in this work are based on the mean of the spectra and iCDFs within the HP duty cycle database, representing different international race circuits. It has been shown that the HP-MSC method can be tuned to match the same targets as the HP-RPC by adaption of the iCDF. An advantage of this method is the

relatively small amount of data required to generate a duty cycle. Only the two design target functions are required in contrast to an entire database of duty pulses.

Direct comparison of the HP-RPC, and HP-MSD with the Bahrain duty cycle has shown good agreement between the newly constructed cycles and the target use case within both, the time and frequency domain. Representation within the time domain ensures that both, average and peak charge and discharge power demand are matched to within a small margin. Representation within the frequency domain ensures that the LIB under test is excited over a representative frequency range. If either cycle was used in degradation testing, this should result in comparable degradation patterns between the target use case and the developed duty cycles. Further comparison with the IECC highlight that the new HP duty cycles provide a more representative duty cycle compared to traditional battery test standards. Hence, both the HP-RPC and HP-MSD are deemed suitable for LIB performance and degradation testing.

As the HP-MSD was designed with a target amplitude spectrum, this duty cycle will be further utilised in this thesis to conduct extensive performance and degradation testing on battery cells. This is described in the following chapters.

## 6 Experimental Assessment of Cell Performance and Degradation

---

### 6.1 Introduction

This chapter presents the cell selection process, hardware set-up and experimental procedures required to fulfil “**Research Task 3:** Devise an experiment to conduct LIB performance and degradation testing to investigate differences between HP-BEV applications and standard testing procedures.” Building upon the previous research tasks, tabulated within Table 3-2, and utilising the HP-MSC as a suitable duty cycle, this chapter presents the test definition part of the proposed framework illustrated within Figure 3-6.

The experimental procedures entail characterisation testing, performance testing, and degradation testing of a 53Ah pouch cell of G-NMC chemistry. Characterisation testing ensures there is little spread between cells prior to performance and degradation testing. Performance testing is conducted to build upon the findings of the simulation study presented within Chapter 5. Although this test utilises different cells to those described by the model in the previous chapter, it further refines the validity of the HP-MSC through an experimental assessment, specifically with regard to the instantaneous electrical behaviour and heat generation of cells.

The degradation study investigates the possible effects and consequences of continuous HP cycling on the electrical characteristics of the cells. Within the duty cycle degradation study, two test groups of cells are subjected to continuous cycling using the HP-MSC and IECC standard profiles to identify the rate and nature of changes in cell behaviour. These changes are identified through regular characterisation of the cells during electrical cycling. As all conditions except the duty cycle are kept the same for both sets of cells, this offers a systematic approach to identify any use-case specific LIB behaviour and thus investigate differences between HP-BEV applications and standard testing procedures as demanded by the research task.

## 6.2 Experimental set-up

### 6.2.1 Cell selection

The cells selected are large format pouch cells with G-NMC chemistry at a rated C/2 Capacity of 53 Ah (196 Wh); key cell parameters are listed in Table 6-1. The cell format features a larger surface area-to-volume ratio compared to cylindrical cells and as such, the cell is described by the manufacturer as having better heat dissipation. According to the manufacturer, the cells target high-energy applications such as energy storage for HEVs and EVs, grid storage, marine vessels, and locomotives. The combination of high power capability, low internal resistance and higher heat dissipation capability compared to cylindrical cells makes this cell a suitable candidate for HP-EV applications. Another factor influencing the choice of cells was that they were provided free of cost by an industrial partner.

Performance Characteristics	Typical Value (2016)
Capacity at C/2	53 Ah
Nominal Voltage	3.7 V
Discharge Energy (C/2)	196 Wh
Weight	1.15 kg
DC Resistance (10s @ 50% SOC)	1.33 mΩ
Peak Discharge C-Rate (10s @ 50% SOC)	8.0 C
Upper Voltage Limit	4.2 V
Lower Voltage Limit	2.7 V
Charge Temperature Range	0°C ~ 45°C
Discharge Temperature Range	-20°C ~ 60°C
Cell Dimensions (LxWxT)	225x225x11.8 mm

TABLE 6-1 – CELL CHARACTERISTICS

### 6.2.2 Test equipment

The experimental rig required to facilitate this research is described below. Hosseinzadeh et al. [125] conducted experiments on the same type of cells as used within this research to develop an electrochemical-thermal model. They have shown that when subject to a galvanostatic discharge of 5C at an environmental temperature of 25 °C under convection cooling, these cells can reach peak temperatures in excess of 60 °C. As such, due to the intensity of the employed testing profiles, for performance and degradation testing an active cooling system is required to



keep cells within their thermal safety window. As such, the requirement for the experimental rig is to provide a suitable housing for a cooling system, and to facilitate a means of connecting individual cells to a battery cyclers.

The experimental rig described below was conceptualised and manufactured in collaboration with other research involving active thermal management of pouch cells [7]. The experimental rig was modelled using the commercially available software Solidworks. A computer drawing of the test rig is provided in Figure 6-1a, a picture of the completed assembly is shown in Figure 6-1b, the dimensions of components are tabulated in Table 6-2 for reference. A description of its design features, as well as an outline of the assembly process is provided below.

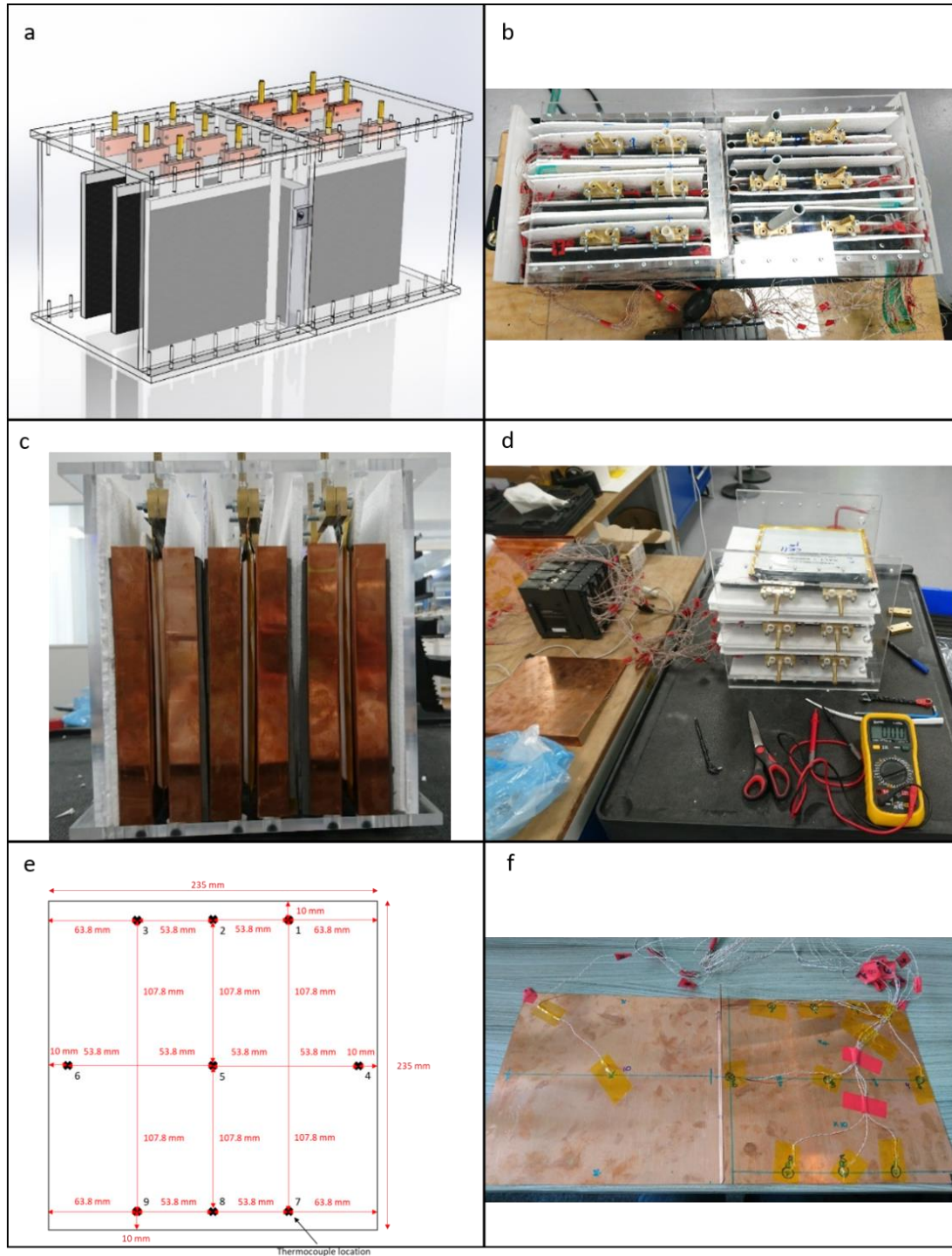


FIGURE 6-1 - TEST RIG DESIGN PROCESS ILLUSTRATION; A) TEST RIG CAD MODEL B) TOP VIEW OF THE ASSEMBLED EXPERIMENTAL RIG; C) FRONT VIEW OF HALF RIG WITH BENT COOLING PLATES; D) FOAMGLAS® AND POLYSTYRENE PACKING OF GAPS BETWEEN CELLS; E) POSITIONS OF THERMOCOUPLES; F) INSTRUMENTED COOLING FINs.

The test rig comprises two Perspex casings, housing a total of 6 cells and an external cooling system. In each casing, three pouch cells are suspended by their tabs, clamped between two

brass blocks, which serve as the connection terminal for the battery cycler and allow for in situ EIS testing. Technical drawings for the design of the brass blocks are provided within Figure 6-2.

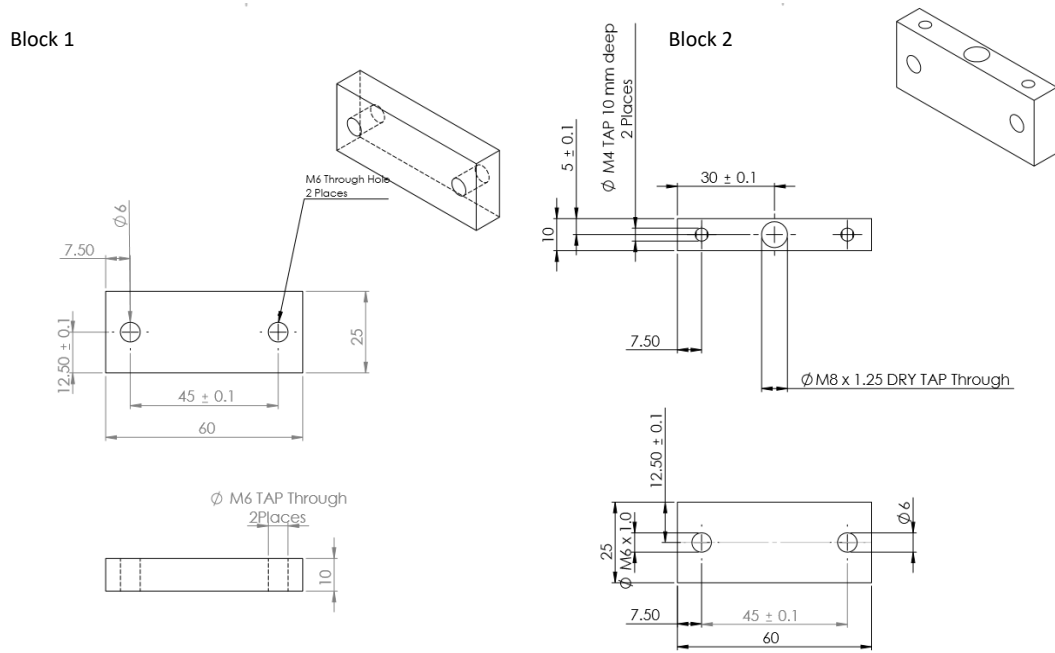


FIGURE 6-2 — BRASS BLOCK DESIGN AND DIMENSIONS; TAPPED HOLES IN BLOCK 2 ALLOW FOR IN SITU EIS TESTING.

The cooling circuit consist of an aluminium cooling plate with internal ducts and a Lauda Thermostat, with the former being located in one of the Perspex casings. The front and back face of each cell are in contact with a pair of L-shaped copper cooling fins. The short edge of each fin is bent at 90° with a radius of 1mm to form a 25mmx210mm patch as shown in Figure 6-1c. These patches are in contact with the aluminium cooling plate, thus providing a means of heat extraction from the testing assembly by means of single edge fin cooling. Space between cooling fin faces of adjacent cells is filled with slabs of polystyrene and FOAMGLAS®, resulting in a densely packed layered structure, thereby ensuring good thermal contact between the cooling fins and cell surface, as shown in Figure 6-1d. The FOAMGLAS® slabs are incompressible and enable even pressure to be applied along the length of the cooling fin edge onto the cold plate via hand tightened ratchet straps. Each pair of cooling fins is instrumented with 10 T-type thermocouples connected to a “HIOKI® 8423 HiLogger”.

Of the thermocouples, 9 are placed on the fin contacting the front face of a cell, and 1 on the fin contacting the back. This serves to investigate the development of cell temperature and thermal gradients during cell cycling. Figure 6-1e shows a schematic of the thermocouple locations for the front facing fin, with a pair of instrumented fins photographed in Figure 6-1f. Given the good contact between the cooling fins and the cell surface, the thermocouple measurements are used

as pseudo-cell surface measurements [7]. The testing rig was placed in an ESPEC PL-3KPH environmental chamber. Each cell is individually connected to cell cycling channels of a “BITRODE MCV 16-100-5” cycler, which can provide a maximum current of 400 Ampere per cell. In addition to the thermal instrumentation, a thermocouple from the Bitrode cycler is installed for safety temperature monitoring at the cell edge next to position 4. The sample frequency for data acquisition of this system for cell voltage and current is 10 Hz. For all tests the maximum charging currents were limited to 106 A per cell (defined by the manufacturer), and discharging currents were limited to 400 A as per test-equipment limitation. Due to limited availability of BITRODE testing equipment, cells 1, 4, 5 and 6 were connected to a cycler with firmware of type “kj”, cells 2 and 3 were connected to a cycler with firmware type “dC”. According to the equipment manufacturer, the type of firmware should not influence testing outcomes.

Component	Height (mm)	Length (mm)	Thickness (mm)
Aluminium cooling plate	210	250	30
Copper cooling fin (fin-cell body)	220	235	0.52
Copper cooling fin (fin-plate contact patch)	220	25	0.52

TABLE 6-2 - TEST RIG COMPONENTS DIMENSIONS

The accuracy, operating range, accuracy and resolution of the HIOKI logger, Bitrode cycler and espec chamber are detailed within Table 6-3.

Component	Operating range	Accuracy	Maximum sampling Frequency
HIOKI® 8423 HiLogger	-100 °C to 100 °C	±0.05% full scale (°C)	100 Hz
BITRODE MCV 16-100-5	0 A to 100 A 0 V to 5 V	±0.1 % full scale	10 Hz
Espec Thermal Chamber	-40 °C to 150 °C	± 1 °C	n/a

TABLE 6-3 – TESTING HARDWARE OPERATING RANGES

### 6.3 Cell characterisation testing

A total of six cells were provided by an industrial partner for the experimental work. To ensure a small spread of variation between individual specimens and ensure robustness of the testing

outcomes, a full characterisation of the cells' attributes prior to performance and degradation testing was deemed to be required. The characterisation process employed within this research is defined in Table 6-4 and discussed below. A full characterisation refers to the entire table; a partial characterisation refers to those tests marked in bold. Implementation of either a full or partial characterisation test is discussed below.

Unless otherwise stated, all tests were conducted using the "BITRODE MCV 16-100-5" system. The sampling rate for cell current and voltage measurements during charge and discharge were set to 10 Hz, the fastest sampling rate available with the equipment. During resting periods, where a less dynamic cell response is expected, the sampling rate was set to 1 Hz to reduce the amount of data collected. The results from the initial characterisation tests are presented and discussed within the next chapter in section 7.2.

Assessment Test	Description	SOC	C-Rate
Discharge energy capacity	Standard test to determine the discharge capacity of every cell	100-0%	1C
Slow charge capacity/ p-OCV Test	Slow charge/p-OCV test. Can be used for DQ/DV analysis	0-100%	C/10
PMC Test	A characterisation test to characterise an equivalent circuit model, similarly to the HPPC test	10%, 20%, 50%, 80%, 95%	max 7.5C discharge (equipment limited), max 2C charge (cell limited)
EIS Test	Used to investigate the behaviour of the cell. Response can be used to infer degradation mechanisms	<b>10%</b> , 20%, <b>50%</b> , 80%, <b>95%</b>	n/a

TABLE 6-4 – CHARACTERISATION TESTS. TESTS IN BOLD CONSTITUTE PARTIAL CHARACTERISATION TESTS DURING DUTY CYCLE DEGRADATION STUDY.

### 6.3.1 Galvanostatic energy capacity

The galvanostatic energy capacity tests are reviewed within section 2.5.1. This test is selected as it is commonly used to identify the energy content that can be extracted from a cell during discharge, or stored within a cell under charge. As the amount of energy which can be stored or

extracted is current dependent, the current used is kept the same throughout the duration of testing. Tests were conducted for charging and discharging.

For each discharge energy capacity test, cells were charged using a CC-CV schedule with a charging current of 26.5 A (0.5 C) up to the upper voltage limit of 4.2V. Subsequently, the cells were kept at this voltage until the current dropped below 2A, after which the cells were left to equilibrate for 1 hour. This state was defined as fully charged or 100% SOC. Following this rest period, the cells were discharged to the lower voltage limit of 2.7V with a current of 53 A (1 C), followed by another resting period of 1 hour to let the cells equilibrate again. The discharge energy capacity was defined as the recorded dissipated energy capacity during the discharge.

Following the discharge capacity tests, cells were subsequently charged with a smaller current of 5.3 A (0.1C) up to the cells' upper potential limit of 4.2 V, and again held there until the charging current dropped below 2 A. This lower current was chosen such that the resulting voltage vs. capacity profile could be used for  $dQ/dV$  analysis during degradation testing as described within section 2.5.2. For a true pOCV analysis, to minimise effects of polarisation, some researchers suggest that the currents employed should ideally be at C/25 or lower [38]. However, the internal resistance of the cells employed within [38] was reported to be 0.18  $\Omega$ , compared to 0.0013  $\Omega$  for the cells employed within this research. With the constrained access to experimental facilities associated with this work, and accounting for the low internal impedance declared by the cell manufacturer, the current of C/10 was deemed acceptable. The  $dQ/dV$  curves can be obtained by differentiating the capacity vs voltage data. The charge capacity was then defined as the total energy sunk into each cell during this charging step. The results of this test are presented and discussed within section 7.2.1.

### 6.3.2 Pulse-Multisine Characterisation

Within this study, the Pulse Multisine Characterisation (PMC) test is chosen over the HPPC test, that is defined within the IEC 62660 standard [34], to characterise cell internal resistance. Unlike the HPPC test, the PMC test does not require a 30-minute equilibration time between each individual current pulse. As such it requires less testing time whilst providing equally reliable characterisation results [142].

Testing was carried out at five different SOC, at 95%, 80%, 50%, 20% and 10%. Each cell was charged to 100% SOC using the same CC-CV schedule as the one prior to the discharge capacity test. Following this charging step, the cell was left to equilibrate for 1 hour before being discharged at 26.5 A to 95% SOC. SOC intervals were determined via coulomb counting based on

the rated coulombic capacity of the cell; i.e. a 5% DOD discharge from 100% SOC to 95% SOC requires the dissipation of 2.65 Ah. Following the SOC adjustment, the cells were left to equilibrate for another hour before they were subject to five consecutive repetitions of the PMC profile during which voltage and current measurements are acquired. Upon completion of this test, the cells were left for 1 hour to equilibrate and for their temperatures to drop back down to 20 °C, followed by the next SOC adjustment period from 95% to 80% SOC. These steps were repeated for all five SOC levels at which the tests were conducted. The composition of the PMC profile used is illustrated within Figure 6-3.

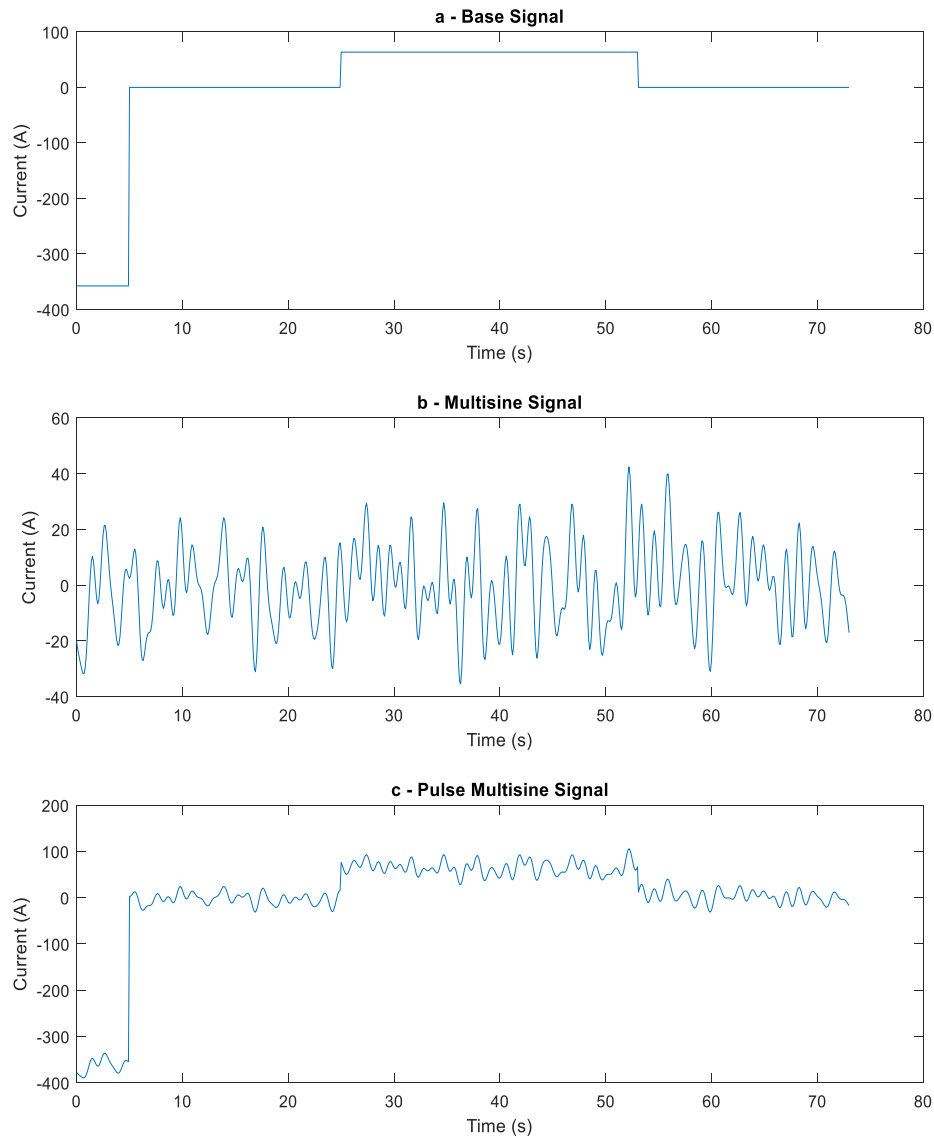


FIGURE 6-3 – PULSE MULTISINE PROFILE COMPOSITION: (A) BASE SIGNAL WITH PULSES OF 357.6 A DISCHARGING AND 67.6 A CHARGING CURRENT AMPLITUDE; (B) ZERO-MEAN MULTISINE SIGNAL WITH A PEAK AMPLITUDE OF 43.4 A; (C) COMBINED PULSE MULTISINE SIGNAL USED FOR PMC CHARACTERISATION TESTS

The profile consists of a charge-neutral base signal illustrated in Figure 6-3a, which is superimposed with a zero-mean multisine signal (illustrated in Figure 6-3b), resulting in a charge sustaining combined profile as shown in Figure 6-3c. The base signal comprises a 5 second discharging pulse with a magnitude of 357.6 A, followed by a resting period of 20 seconds. This is followed by a charging pulse with an amplitude of 63.6 A followed by another 20 second resting period. To maintain charge neutrality, the duration of the charging pulse is 28.1 seconds. The multisine signal is a random-phase multisine as defined within [141]. It has a flat spectrum with



a uniform distribution of random phases between  $-\pi$  and  $\pi$  radians. This results in a zero mean profile in which the magnitudes of the profile have a normal distribution. The peak amplitude of the multisine is 43.4 A such that the peak discharging and charging currents of the combined signal do not exceed 400 A and 106 A, respectively. The recorded current and voltage signals are subsequently processed to parameterise an NL-ECM, the structure and parameterisation of which are initially described within section 2. The results of this test are described and discussed within section 7.2.2.

### 6.3.3 Electrochemical Impedance Spectroscopy

As identified within the literature review, the Nyquits plots resulting from EIS testing can be used to model the response of cells to different frequency inputs and map this response to the SEI, charge transfer phenomena, and diffusion effects. Thus this test gives a deeper insight into the processes occurring within the cell.

Electrochemical Impedance Spectroscopy (EIS) testing was carried out at five different SOC levels at 95%, 80%, 50%, 20% and 10% during full characterisation tests and at 95%, 50% and 10% SOC during partial characterisation tests. The charging and SOC adjustment procedures prior to each EIS test followed the same protocol as for the PMC tests. Following SOC adjustment, an extended equilibration period of at least 4 hours was employed as recommended by Barai et al. [145], to allow the dynamics of the cell to stabilise before measurements were made. The EIS tests were carried out in galvanostatic mode using a *Solartron EnergyLab XM* system with a 2-Ampere booster. Each cell was excited with a sinusoidal AC current with an RMS value of 1.41 A, and cell impedance was measured in a frequency range from 10 mHz to 10 kHz with 10 frequency points per decade as suggested within [136]. To analyse the impedance measurements, the resulting Nyquist plots were subsequently fitted to an ECM using “*Scribner® ZView2*”. The process of ECM fitting and results of these tests are detailed within section 7.2.3.

## 6.4 Performance testing

One of two key components required to fulfil research task 3 is to define a procedure to conduct performance testing. Emphasis is placed on energy throughput and cell temperatures, as those are often identified as key contributors to cell degradation [47] and are known to greatly influence cell performance. Additionally, building upon the work presented within section 5.4 this test serves to provide experimental data for the validation of the HP-MSC. The HP-RPC has not been included in the experimental study. Given the similarity between the HP-RPC and HP-

MSC that were identified within the previous chapter, the author assumes the use of the HP-MSC sufficient for the purpose of performance testing and cycle validation.

To investigate differences between HP-BEV applications and standard testing procedures, three different tests are designed based on the three duty cycles shown in Figure 6-4: The HP-MSC (a), the IECC (b), and the duty cycle from the Bahrain International circuit (Bahrain) simulation (c). Six cells are subject to one test cycle of each profile.

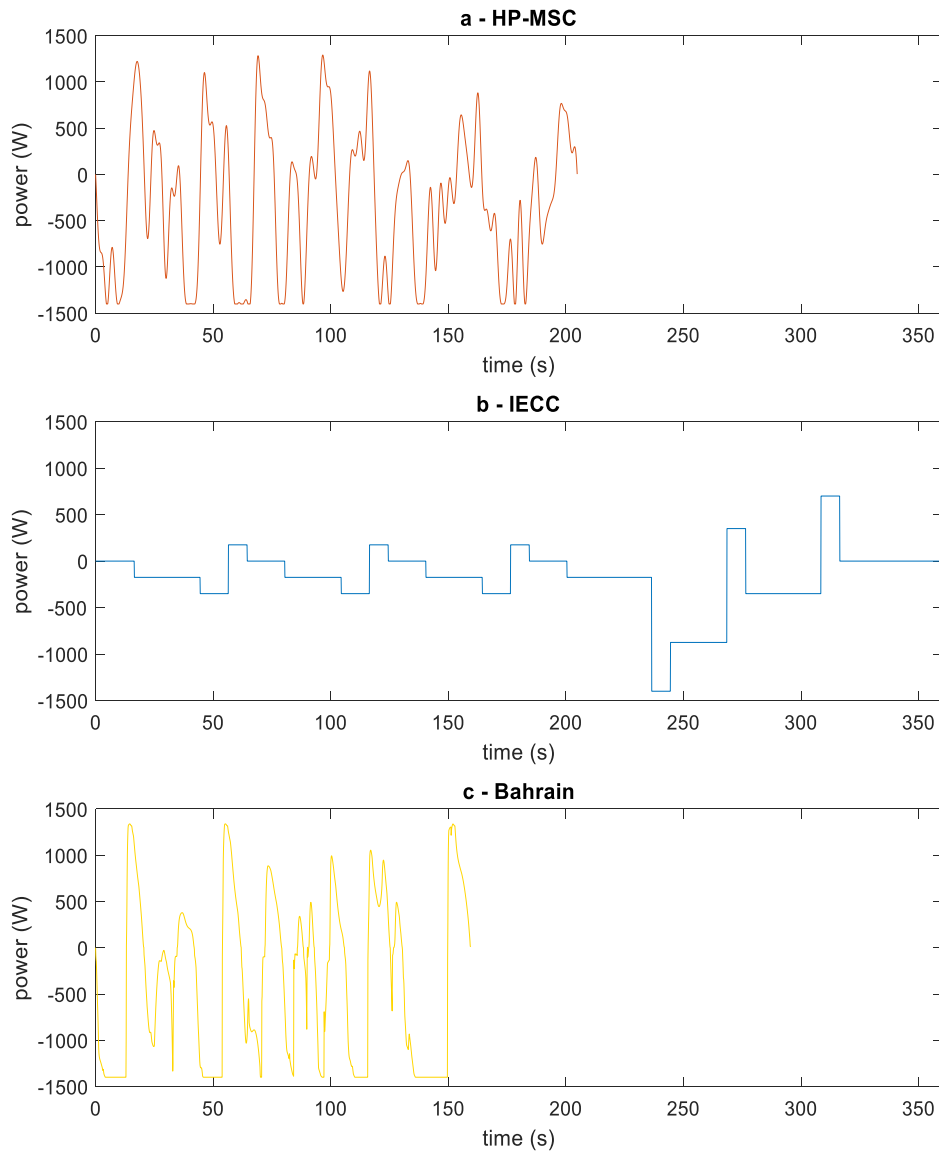


FIGURE 6-4 — A SINGLE PERIOD OF THE THREE DUTY CYCLES SELECTED FOR TESTING: A — HP-MSC; B — IECC; C — BAHRAIN

Within this context, a test cycle comprises the following. Cells are charged to the upper cut-off voltage of 4.2 V using the CC-CV procedure discussed within section 6.3.1, followed by a rest period of 1 hour allowing the cells to equilibrate. They are then discharged to 95% SOC at 0.5C, followed by another 1-hour rest period. Subsequently the cells are subjected to repetitions of one of the three duty cycles shown within Figure 6-4 until either they reached a SOC of 10%, resulting in a 85% DOD (45.05 Ah) charge depletion, or the peak cell surface temperature reached the thermal safety limit of 65 °C (defined by the manufacturer). The SOC operating window and DOD can be chosen in accordance with the defined use case. Within this thesis, the value of 85% DOD was chosen after discussions with the partnering companies. A resulting test cycle on the example of the IECC is shown within Figure 6-5.

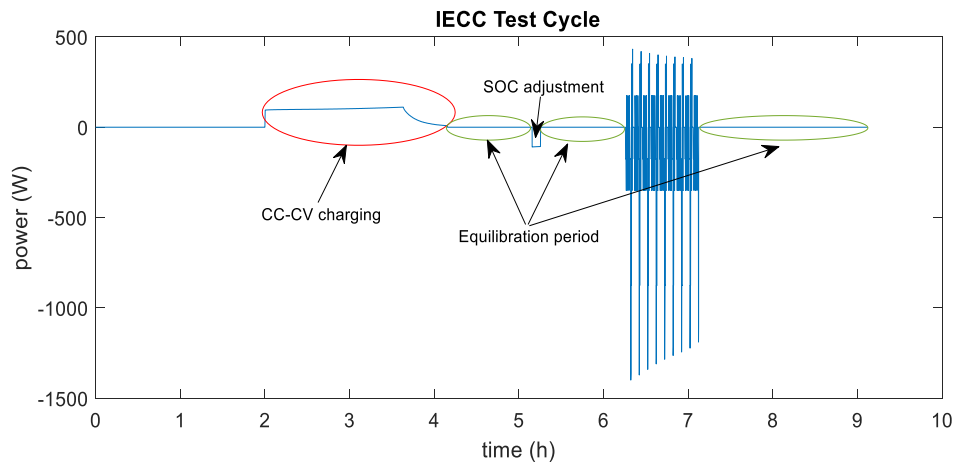


FIGURE 6-5 – ANNOTATED IECC TEST CYCLE: RED – CC-CV PERIOD, GREEN – EQUILIBRATION PERIODS

Rather than scaling each profile to a maximum C-rate as done for the simulation study in the previous chapter, each profile is scaled to a peak power demand to more accurately portray a realistic duty profile. Peak power per cell is defined as 1400 W. This value is chosen as a compromise between maximising the power demand and keeping cells within the thermal safety window throughout testing. Negative values of power represent cell discharging, whereas positive values represent charging.

Comparison between the results from the HP-MS test and the test employing the Bahrain duty cycle will further refine the validity of the duty cycle construction methodology described within section 5.3. Further comparison between the tests employing the HP-MS and IECC, respectively will allow for direct comparison of thermal performance of LIBs between HP-BEV applications and standard testing procedures. The results of all three test cycles are presented and discussed within section 7.3.

## 6.5 Duty cycle degradation study

To complete research task 3 and assess the longer-term effects of HP-BEV applications on LIBs, a duty cycle degradation study is required to investigate how the differences between duty cycles representing HP-BEV application, and standard duty cycles affect the electrical characteristics of LIBs in the long-term. Following the full characterisation (defined in Table 6-4), the cells are split evenly into two sets, and tested simultaneously with two different usage profiles.

In this study, cells No. 1-3 were cycled using the test cycle based on the HP-MSC as discussed in the previous section. Cells No. 4-6 were cycled using the test cycle based on the IECC. Again, a test cycle within this context refers to a single completion of the protocol used for the performance testing described within section 6.4, followed by a 2-hour rest period for cells to cool and equilibrate.

Both sets of cells underwent 200 test cycles with regular partial characterisations. These partial characterisation tests were employed at regular intervals as detailed within Table 6-5 to detect whether any effect on the cells' attributes could be observed. Once each cell completed 200 duty cycles, a full characterisation test was once again undertaken. The complete test schedule is summarised in Table 6-5.

Throughout the duty cycle degradation study, both test groups, i.e. all six cells, are subject to the same characterisation tests at the same time. As tests are conducted simultaneously, the only differentiating factor between the two test groups is the test cycle itself. Thus any differences in cell characteristics, which may emerge between the two test groups during the degradation study, can be attributed to the test cycle used.

Based on the literature review in Chapter 2, it would be expected, that cells undergoing the HP-MSC schedule will degrade at an earlier point, and more rapidly than the group undergoing the IECC schedule. This assessment is primarily based on the higher frequency of high amplitude currents and expected increased temperatures, the HP-MSC groups are experiencing.

Number of cycles	Total cycles	Test
0	0 (start of test)	Full characterisation
10	10	Partial characterisation
10	20	Partial characterisation
10	30	Partial characterisation
20	50	Partial characterisation
20	70	Partial characterisation
20	90	Partial characterisation
20	110	Partial characterisation
40*	150	Partial characterisation
10*	160	EIS at 50%
Laboratory closure due to construction work		
40*	200 (end of test)	Full characterisation

TABLE 6-5 - TEST PROGRAM FOR SHORT TERM CYCLING STUDY, \* INDICATES OCCURRENCES WHERE HARDWARE MALFUNCTIONS WERE ENCOUNTERED

During the timeframe of the experimental work, the laboratory facilities underwent major refurbishment and construction work. As such, after 160 cycles, testing was suspended for 5 weeks, during which the experimental-rig was disconnected from the BITRODE equipment and stored at 20°C, with all cells at 50% SOC. EIS testing was conducted on all cells prior to storage (Figure 6-6-blue plot), and again post storage at 50% SOC (Figure 6-6-red plot). As the cells were not cycled during the refurbishment work, no SOC adjustment was conducted prior to the second measurement.

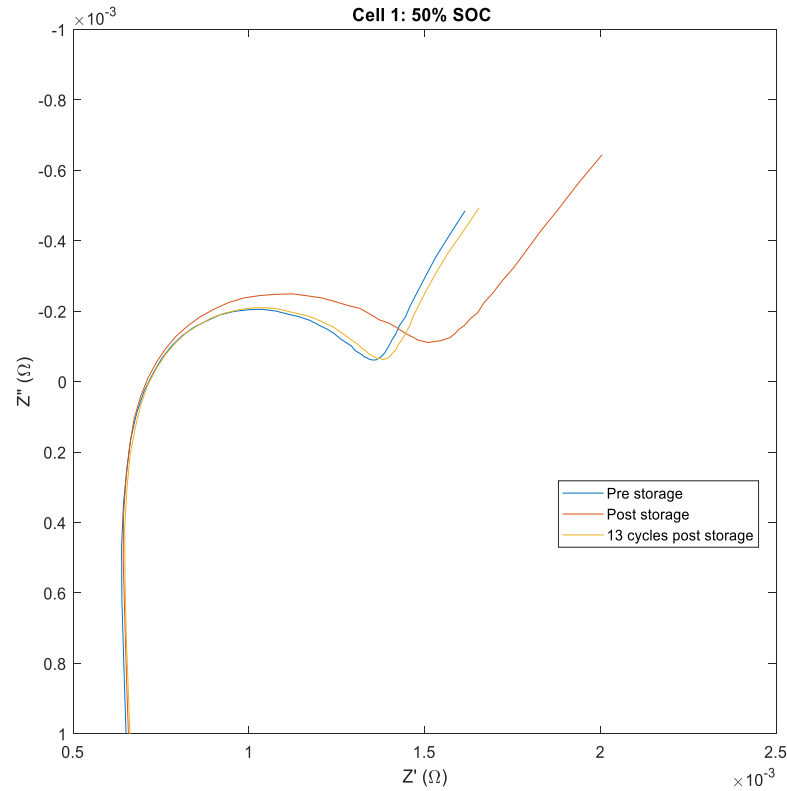


FIGURE 6-6 – NYQUIST PLOTS OF EIS MEASUREMENTS AT 50% SOC PRE STORAGE, POST STORAGE AND 13 GALVANOSTATIC 1C DISCHARGES POST-STORAGE

Figure 6-6 reveals a significant increase in charge transfer resistance for the test post storage compared to those tests conducted 5 weeks prior. This was attributed to reversible changes, which may occur within the cells post use and during storage as reported within literature [53]. As such, prior to commencing the degradation study, each cell was subject to 13 galvanostatic charge-discharge cycles following the same regime as the energy discharge capacity test (1C discharge, C/2 charge). After 13 cycles, there were only minimal differences between the Nyquist plots (Figure 6-6-yellow plot) and those taken prior to the laboratory closure. These differences were deemed satisfactory, and subsequently testing was commenced with the HP-MSC and IECC test cycles. The results of the completed degradation study are presented and discussed within section 7.4.

#### 6.5.1 Hardware malfunctions

In addition to the prolonged resting period, BITRODE hardware malfunctions were encountered on multiple occasions. These are tabulated within Table 6-6, as well as the action taken post

interruption. On all occasions, where testing was interrupted, cells had been cycled through approximately 5% DOD.

Cell No	Cycling interval	Occurrences	Action
Cell 1	160 – 200	10	Continue cycling program
Cell 2	111 – 121	1	Trouble-shooting – Bitrode-engineer attributed fault to broken voltage sensor. Restart test program with reduced loops
	121 – 127	2	1 <sup>st</sup> instance: Continue cycling program, 2 <sup>nd</sup> instance: Trouble-shooting – Bitrode-engineer identified firmware as potential cause. Restart test program with reduced loops
	127 – 200	17	Continue cycling program
Cell 3	111-121	1	Fault-finding: No error could be found Restart test program with reduced loops
	121 – 129	2	1 <sup>st</sup> instance: Continue cycling program, 2 <sup>nd</sup> instance: Trouble-shooting – Bitrode-engineer identified firmware as potential cause. Restart test program with reduced loops
	129 – 150	1	Continue cycling program

TABLE 6-6 – LIST OF BITRODE MALFUNCTIONS DURING LONG TERM TESTING FOR THE HP-MSC TEST GROUP.

The first of these instances were encountered during cycle No 121, where the equipment stopped the experimental run for both, both, cell 2 and cell 3. A broken voltage sensor was identified by a BITRODE service engineer on the leads connected to cell No 2. No issue could be identified with the circuitry connected to cell No 3. The faulty component was replaced by the service engineer, and the testing program was restarted with a reduced number of loops to account for the complete cycles. Despite no other failure being identified, the hardware continued to malfunction and halt cycling on several occasions. Testing on cells 2 and 3 was suspended one further time, whilst trouble shooting was conducted on the BITRODE hardware. A firmware limitation was subsequently stated by the equipment manufacturer as a possible cause of the malfunctions. However, prior to cycle 121, no issues had been encountered with the same testing equipment, making a firmware limitation unlikely. Following trouble-shooting, cells were charged back to 100% SOC. This resulted in cells 2 and 3 being subject to two additional charging cycles compared to cell 1. As this amounts to less than 1% of the total number of charging events, it is not expected to influence the overall outcome of the experimental work.

Following the 5-week break in testing, the HP-MSG group was connected to equipment with “kj”-type firmware, the IECC test group was connected to equipment with “dC”-type firmware. This decision was made, as prior to this point no testing issues were encountered on cell 1, which had previously been connected to a cycler with “kj”-firmware. However, this did also not resolve the issue and subsequently, testing issues were encountered on cells 1 and 2, but not on cell 3.

As no error source could be identified by either, the laboratory staff or service engineer, and to minimise the interruption to the test plan, it was decided to continue the test program in all instances where cycling was interrupted due to a fault. When testing was continued following a malfunction, a cell would cycle from the last recorded point down to 10% SOC, thus completing a full cycle. However, for those cycles with a forced break, the recorded cell surface temperatures at the end of discharge were lower than during uninterrupted cycles, as shown in Figure 6-7, where the difference in the peak surface temperature is 4.2°C. The impact of this difference in temperature on the outcomes of the degradation study is deemed small due to the low number of total occurrences, which are 10% for cell 2, 5% for cell 1, and 2% for cell 3.

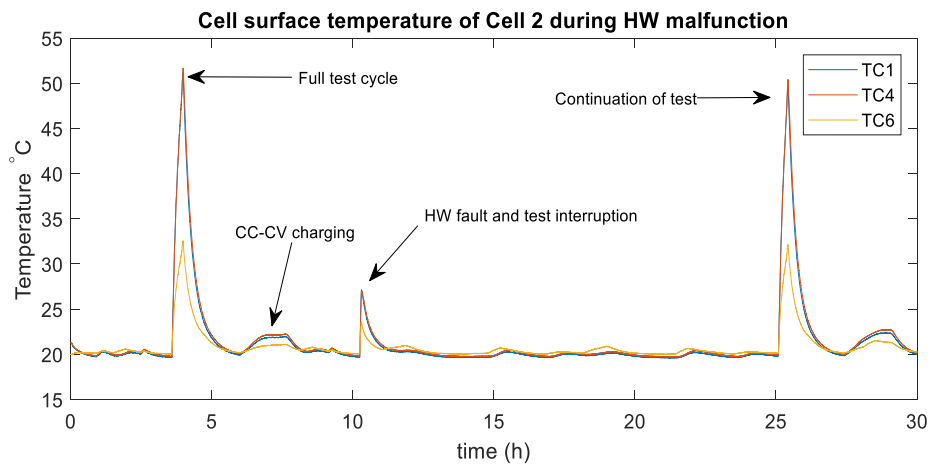


FIGURE 6-7 – CELL SURFACE TEMPERATURE ON THERMOCOUPLE POSITIONS 1, 4, AND 6 ON CELL 3 DURING BITRODE MALFUNCTION. TEMPERATURE DIFFERENCE AT HOTTEST POINT OF 4.2 °C FOR TC4 AND 0.3°C FOR TC6.



## 6.6 Conclusion

This chapter satisfies “**Research Task 3:** Devise an experiment to conduct LIB performance and degradation testing to investigate differences between HP-BEV applications and standard testing procedures.” It presents the cell selection process, hardware set-up, and experimental procedures required to conduct characterisation, performance and degradation testing for LIBs within the context of HP-BEV applications. The definition of the required experimental procedures constitute part of the proposed framework illustrated within Figure 3-6, and fulfils part of the requirements to address the knowledge gap pertaining to the lack of experimental studies within the HP-BEV segment as illustrated within Table 3-1.

The selection and parameterisation of the characterisation tests that provide a detailed description of cell behaviour follows the best practices as discussed within the literature review in Chapter 2. The procedure suggested for performance testing is designed to provide datasets to evaluate the thermal and electrical performance of LIBs subject to three test cycles: The HP-MSC test cycle, representing typical HP-BEV applications, IECC test cycle, representing a standard testing profile, and the Bahrain test cycle, representing a specific HP-BEV use case. The results from this test will enable direct comparison between standard and HP-BEV testing scenarios and further serve as a validation exercise for the duty cycle construction methodologies presented within Chapter 5.

The methodology employed for degradation testing investigates how the characteristics of LIBs change over prolonged use within both, HP-BEV applications, and when subject to standard testing cycles. This is achieved through regular characterisation testing throughout the degradation study. Any changes in cell characteristics occurring over the course of the experiment between the two test groups are a function of the test cycles employed and thus use case specific. The results from the experimental procedures described within this chapter are presented and discussed within Chapter 7.

## 7 Experimental Results & Discussion

### 7.1 Introduction

This chapter addresses “**Research Task 4:** Analyse the experimental results and determine any use-case specific behaviour between HP-BEV applications and standard testing procedures.” It presents and discusses the results obtained from the testing procedures described in Chapter 6, thus completing the tasks required to address the knowledge gaps listed within Table 3-1. Furthermore, it addresses the final step of the framework illustrated within Figure 3-6.

The results from cell characterisation tests provide a set of control values against which changes in cell characteristics throughout the duty cycle degradation study may be compared. The results from performance testing are analysed to provide a greater level of insight into the thermal performance of LIBs under standard and HP-BEV scenarios. The results from the duty cycle degradation study are analysed to identify and explain the divergence of cell characteristics for the HP-MSC and IECC test groups.

### 7.2 Cell characterisation testing

The results presented within this section correspond with the experimental procedure described in section 6.3.

#### 7.2.1 Galvanostatic energy capacity

The voltage vs energy capacity plots of all six cells for a 1C discharging and 0.1C charging rate are shown within Figure 7-1(a) and (b), respectively. The final recorded energy and coulombic capacities for both tests are tabulated within Table 7-1.

The mean discharging capacity is 52.01 Ah with a standard deviation of 0.29 Ah. For the charge capacity test at 0.1C the mean charging capacity is 51.47 Ah with a standard deviation of 0.38 Ah. The measurement spread between the cells for charging and discharging capacity is small as expected and falls within 0.7% and 0.6%, respectively. As currents of different magnitude were used for both tests, the measured capacity between charge and discharge varies. The lower charging current of 0.1C results in lower polarisation and thermal losses during charging, compared to the higher discharging current of 1C. Although the Capacity is measured in Ah and

is larger for the higher discharging current, the total amount of energy transferred into the cell (measured in Wh) is larger for the lower current.

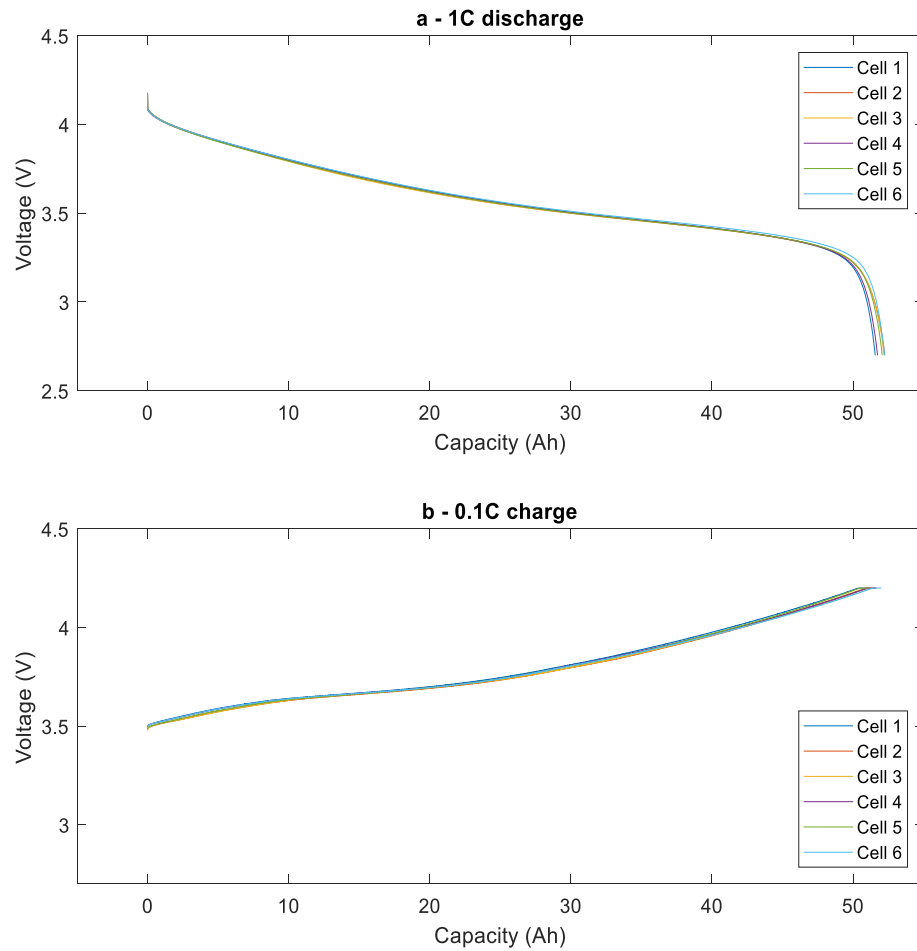


FIGURE 7-1 - CAPACITY TEST RESULTS. (A) DISSIPATED ENERGY CAPACITY DURING A 1C DISCHARGE, (B) TOTAL ENERGY DURING CHARGE

Test	Cell 1	Cell 2	Cell 3	Cell 4	Cell 5	Cell 6
1C Discharge Capacity (Ah)	51.57	52.25	52.20	51.74	52.07	52.24
0.1C Charge Capacity (Ah)	50.99	51.61	51.49	51.66	51.09	52.00
1C Discharge Capacity (Wh)	184.52	186.44	186.22	184.97	185.92	186.97
0.1C Charge Capacity (Wh)	192.00	193.85	193.43	194.45	192.01	195.78

TABLE 7-1 – ENERGY CAPACITY TEST RESULTS FROM INITIAL CHARACTERISATION TESTS

### 7.2.2 Pulse Multisine Characterisation

Figure 7-2(a) and (b) show the cell voltage and surface temperature response, respectively, to the current input signal ( $i(n)$ ) of the PMC (Figure 6-3) for cell 3 at 50% SOC. The temperature was measured using the Bitrode thermocouple. The magnitude of the voltage response to the high current pulse decreases steadily over the five periods, with the largest change occurring primarily over the first two periods. This change could be attributed to the increase in cell temperature over the same period. As the impedance should be estimated under steady state conditions, the first two periods of the measurement were eliminated prior to further processing as described within Chapter 2.

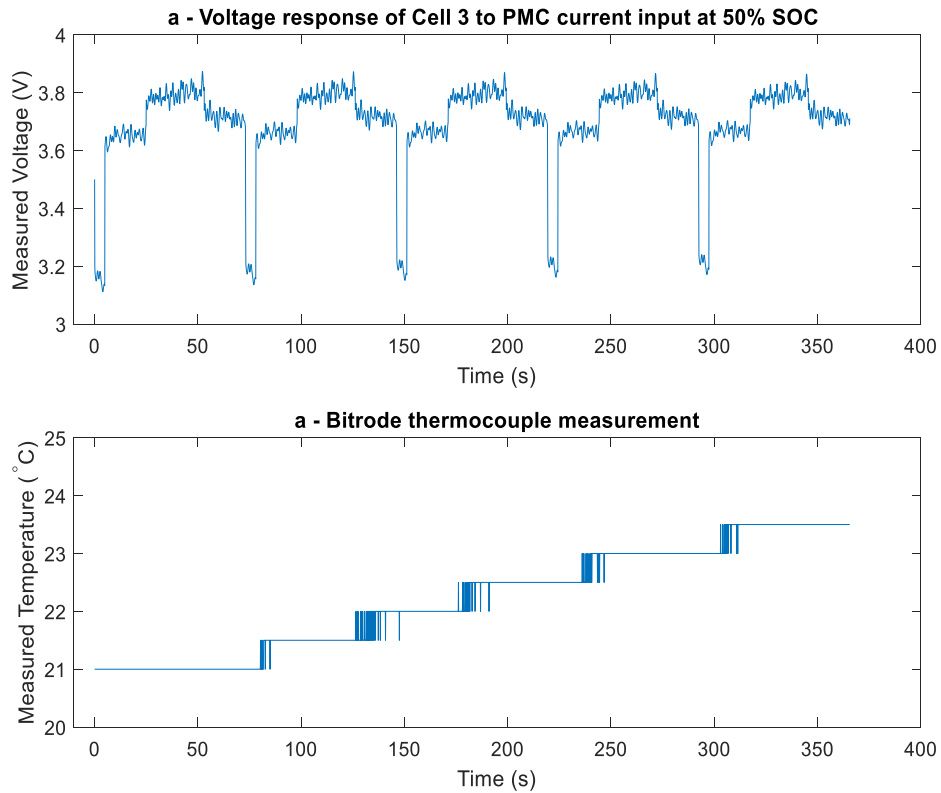


FIGURE 7-2 – VOLTAGE AND TEMPERATURE RESPONSE OF CELL NO 1 AT 50% SOC, INITIAL CHARACTERISATION TEST (A) MEASURED VOLTAGE RESPONSE TO THE PMC SIGNAL. (B) BITRODE SAFETY THERMOCOUPLE MEASUREMENT

Figure 7-3 shows the cell impedance ( $Z(k)$ ) as estimated from equation (19), and a fitted first order transfer function ( $Z_m(k)$ ) as described within equation (65), where  $\omega_k = \frac{2\pi k f_s}{N}$ , and  $a_n$  and  $b_n$  are transfer function coefficients.

$$Z_m(k) = -\left(\frac{b_1 j \omega_k + b_0}{a_1 j \omega_k + a_0}\right) \quad (65)$$

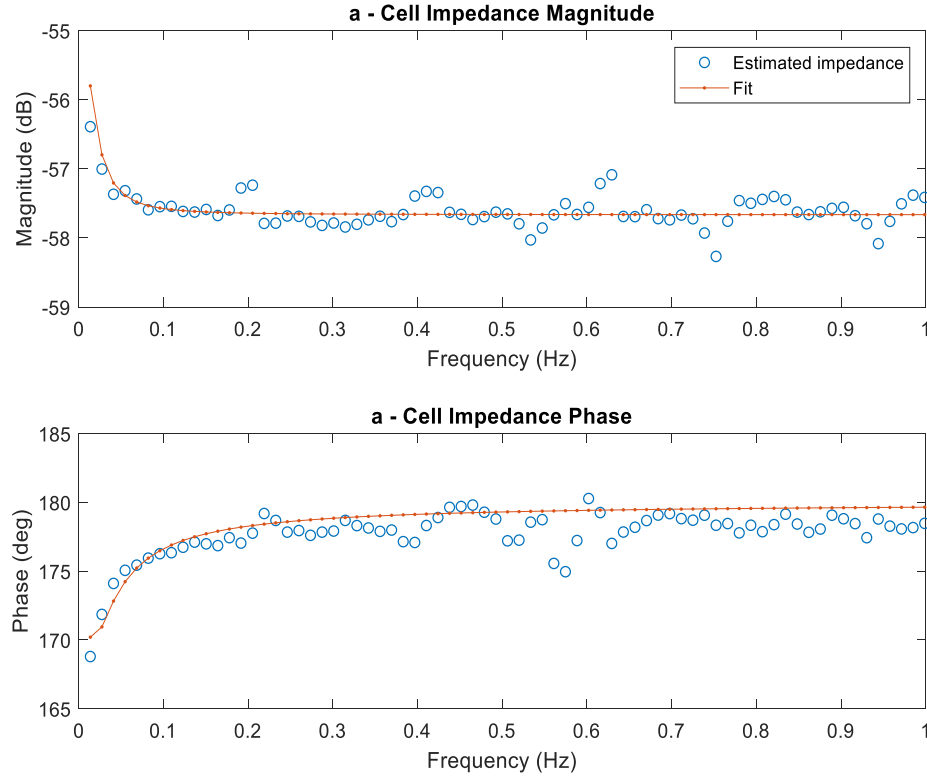


FIGURE 7-3 – ESTIMATED CELL IMPEDANCE AND 1<sup>ST</sup> ORDER TRANSFER FUNCTION FIT.

From Figure 7-3-a and b it can be seen that a first order function offers a good fit for the estimated impedance. The transfer function is subsequently expanded via a partial fraction expansion to produce a function as described within equation (66), yielding the parameters for a 1<sup>st</sup> order ECM as illustrated within Figure 7-4. The model comprises a series resistor  $R_{0-PMC}$  representing the cells internal resistance and an RC pair, where  $R_{1-PMC}$  represents the polarisation resistance,  $\tau_{1-PMC}$  the time constant, and  $\tau_{1-PMC} = R_{1-PMC}C_{1-PMC}$ .

$$Z_m(k) = -R_{0-PMC} - \frac{R_{1-PMC}}{\tau_1 j \omega_k + 1} \quad (66)$$

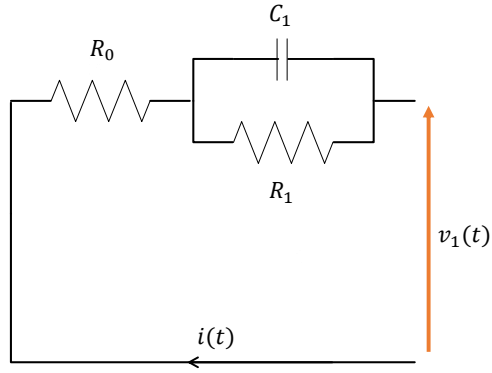


FIGURE 7-4 – 1<sup>ST</sup> ORDER EQUIVALENT CIRCUIT MODEL COMPRISING A SERIES RESISTOR WITH ONE RC PAIR USED TO MODEL THE OVER-VOLTAGE RESPONSE.

By plotting the measured over voltage  $v(n)$  vs the modelled overvoltage  $v_1(n)$  resulting from the current  $i(n)$  being applied to the ECM, the presence of any non-linear behaviour associated with high current densities can be detected. Figure 7-5(a-e) shows the measured vs modelled data points for 95%, 80%, 50%, 20%, and 10% SOC for cell 3 as well as a fitted sigmoid function described in equation (67), where  $c_{NL1}$  and  $c_{NL2}$  are coefficients estimated via the `lsqcurvefit` function from the MATLAB® Optimisation Toolbox.

$$f(\bar{v}_1) = \frac{c_{NL1}\bar{v}_1}{\sqrt{1 + c_{NL2}\bar{v}_1^2}} \quad (67)$$

A linear relationship between the measured and modelled over voltage is observed for all SOCs except 10%, where the fitted function indicates some non-linear behaviour. However, voltage clipping was encountered during PMC testing at 10% SOC, as illustrated by the red circles within Figure 7-6, meaning the desired current input could not be achieved due to cell voltage limitations. As such, with the available data, it is not possible to conclude whether or not non-linear cell behaviour is present.

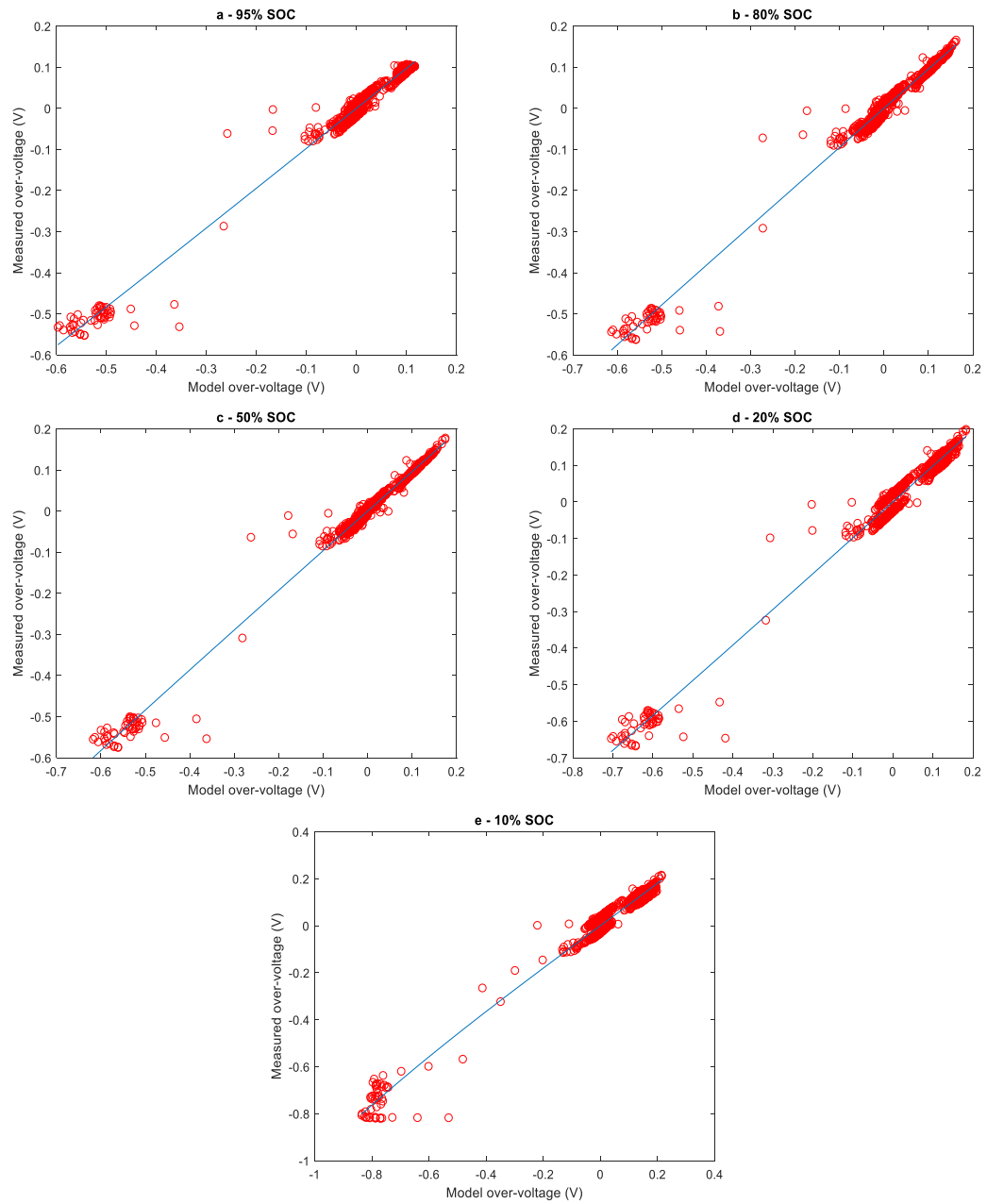


FIGURE 7-5 — MEASURED OVER-VOLTAGE VS MODELLED OVER-VOLTAGE MODELLED FROM ECM. A LINEAR RELATIONSHIP BETWEEN MODELLED AND MEASURED OVER-VOLTAGE CAN BE OBSERVED; SOME NON-LINEAR TENDENCY FOR 10% SOC

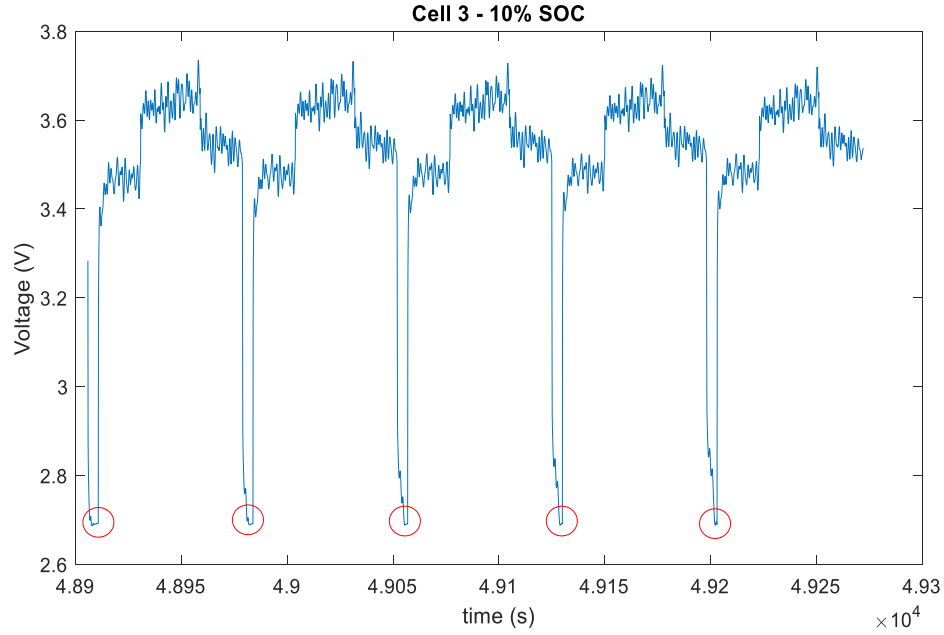


FIGURE 7-6 – PMC VOLTAGE RESPONSE FOR CELL 3 AT 10% SOC DURING INITIAL CHARACTERISATION. RED CIRCLES INDICATE OCCURRENCES, WHERE THE CELL VOLTAGE SAFETY LIMIT WAS REACHED, RESULTING IN CURRENT DERATING.

Table 7-2 presents the mean values for the ECM parameters and non-linear coefficients  $c_{NL1}$  and  $c_{NL2}$  as well as their standard deviation for 95%, 80%, 50%, 20%, and 10% SOC. Figure 7-9(a – c) shows the fitted ECM parameters for those cells under the PMC for a single RC pair ECM. The data points represent the mean value for all six cells, and the error bars the standard deviation from the mean.

	95% SOC	80% SOC	50% SOC	20% SOC	10% SOC
$R_{0-PMC}$ ( $m\Omega$ )	$1.31 \pm 0.04$	$1.32 \pm 0.04$	$1.38 \pm 0.04$	$1.53 \pm 0.05$	$1.60 \pm 0.04$
$R_{1-PMC}$ ( $m\Omega$ )	$0.40 \pm 0.03$	$0.50 \pm 0.03$	$0.50 \pm 0.03$	$0.33 \pm 0.03$	$0.62 \pm 0.04$
$\tau_{1-PMC}$ (s)	$5.91 \pm 0.51$	$7.26 \pm 0.52$	$9.90 \pm 0.61$	$3.42 \pm 0.55$	$1.06 \pm 0.05$
$c_{NL1}$	$0.966 \pm 0.005$	$0.950 \pm 0.002$	$0.962 \pm 0.001$	$0.987 \pm 0.014$	$0.905 \pm 0.007$
$c_{NL2}$	$0.004 \pm 0.035$	$-0.052 \pm 0.019$	$-0.052 \pm 0.004$	$0.073 \pm 0.076$	$-0.179 \pm 0.021$

TABLE 7-2 – MEAN AND STANDARD DEVIATION OF THE ESTIMATED ECM PARAMETERS FOR THE DC INTERNAL RESISTANCE AND CHARGE TRANSFER PHENOMENA FROM SIX G-NMC 53AH CELLS.

For the PMC, the impedance is determined for frequencies up to 1Hz, and the cell internal resistance  $R_{0-PMC}$  is estimated from the partial fraction expansion described in equation (66). As



such this parameter does not only represent the pure Ohmic resistance of the bulk materials, but is also influenced by some charge transfer phenomena occurring within the cell under discharge [147]. Similarly to HPPC test results reported within literature,  $R_{0-PMC}$  displays an SOC dependency with higher values at the low SOC's at 10% and 20%, and a flat profile between 50% and 95% SOC [226,227].

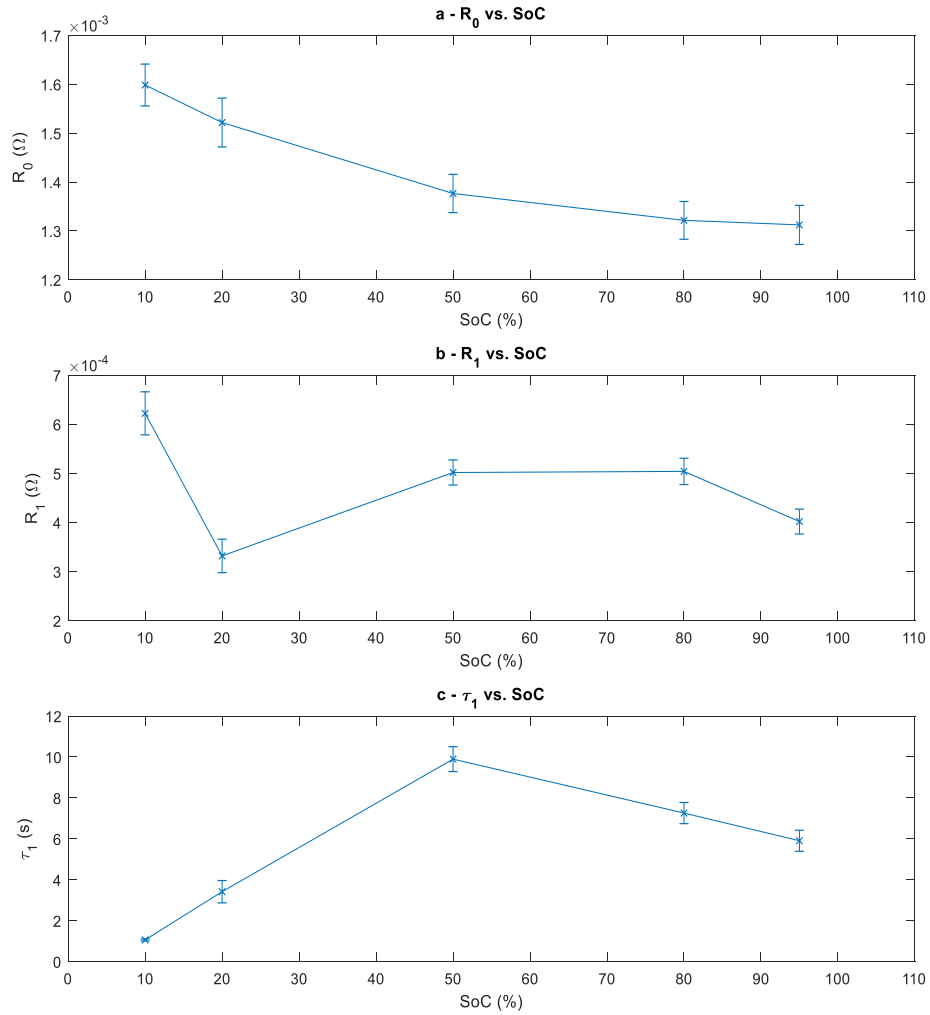


FIGURE 7-7 – PMC MEAN ECM PARAMETERS AND STANDARD DEVIATION. (A) DC RESISTANCE  $R_0$ . (B) CHARGE TRANSFER AND DIFFUSION RESISTANCE  $R_1$ . (C) TIME CONSTANT  $\tau_1$ .

The resistance  $R_{1-PMC}$  and time constant  $\tau_{1-PMC}$ , shown within Figure 7-7(b) and (c), respectively, are associated with the continual voltage response as charge transfer and diffusion phenomena dominate the cell dynamics. As voltage clipping occurred during the high current discharge pulses at 10% SOC, the values for  $R_{1-PMC}$  and  $\tau_{1-PMC}$  may not be completely reliable, and are omitted from all further analysis. Values for  $R_{1-PMC}$  would usually be expected to follow

a bathtub shape with higher values for low SOC, and very high SOC, as polarisation and charge transfer phenomena influence cell behaviour. However, the opposite can be observed within Figure 7-7(b), which can partially be attributed to the fact that part of the charge transfer phenomena are accounted for within  $R_{0-PMC}$ . The combined resistance ( $R_{0-PMC} + R_{1-PMC}$ ) for the cells results in a flat profile around 1.8 mΩ for all cells. As  $\tau_{1-PMC}$  and  $R_{1-PMC}$  are co-dependent, the overlap in resistances also influences the values of the time constant used to model the remaining dynamic voltage response.

### 7.2.3 EIS tests

Figure 7-8 shows a Nyquist plot of the measured EIS response for cell 3 at 50% and the modelled EIS response when fitted to the second order ECM at the bottom of the figure. The imaginary part of the impedance is plotted on the y-axis, and the real part of the impedance is plotted on the x-axis. The shape of the Nyquist plot is in agreement with those found within literature [227–229], displaying the traits as described within Chapter 2, i.e. high-frequency inductive tail, mid-frequency semicircle, and Warburg impedance at low-frequency.

The software “Scribner® ZView2” was used to parameterise the model to fit the EIS response for all SOC. To decide upon a suitable equivalent circuit model, each of the three distinct regions was examined individually and a partial ECM was parameterised. Subsequently, these models were combined to a full ECM and the software’s parameter optimisation tool was run to generate an optimised set of ECM parameters. The optimisation step is achieved through the use of a non-linear least squares algorithm. The inductive tail and skin effect [229] was modelled using an inductor  $L_i$  in parallel with a resistor  $R_i$ . The intersection of the inductive tail with the real axis corresponds with the pure Ohmic resistance, represented by a single resistor  $R_{0-EIS}$ . The mid-frequency semicircle is modelled by two Resistor-Constant-Phase-Element pairs ( $R_{1-EIS} - CPE_1$  and  $R_{2-EIS} - CPE_2$ ) to model effects caused by charge transfer phenomena and the electrochemical double layer. The local minimum at the end of the semicircle is associated with the charge transfer resistance ( $R_{ct-EIS}$ ) and corresponds with the values of  $R_{1-EIS} + R_{2-EIS}$ . Finally, an open Warburg element is used to model behaviour caused by mass transport effects [229].

Although a first order model with a single R-CPE pair is suggested to be sufficient for Nyquist plots which only present one suppressed semi-circle [136], the inclusion of a second R-CPE pair generally resulted in a lower sum of squares error between modelled and measured value. Furthermore, as the cells are used a second semicircle associated with continued SEI growth

often appears over time as the cell degrades. To avoid alternating between different order ECMs for a comparison between the initial characterisation and subsequent tests it was thus decided to use the model shown within Figure 7-8.

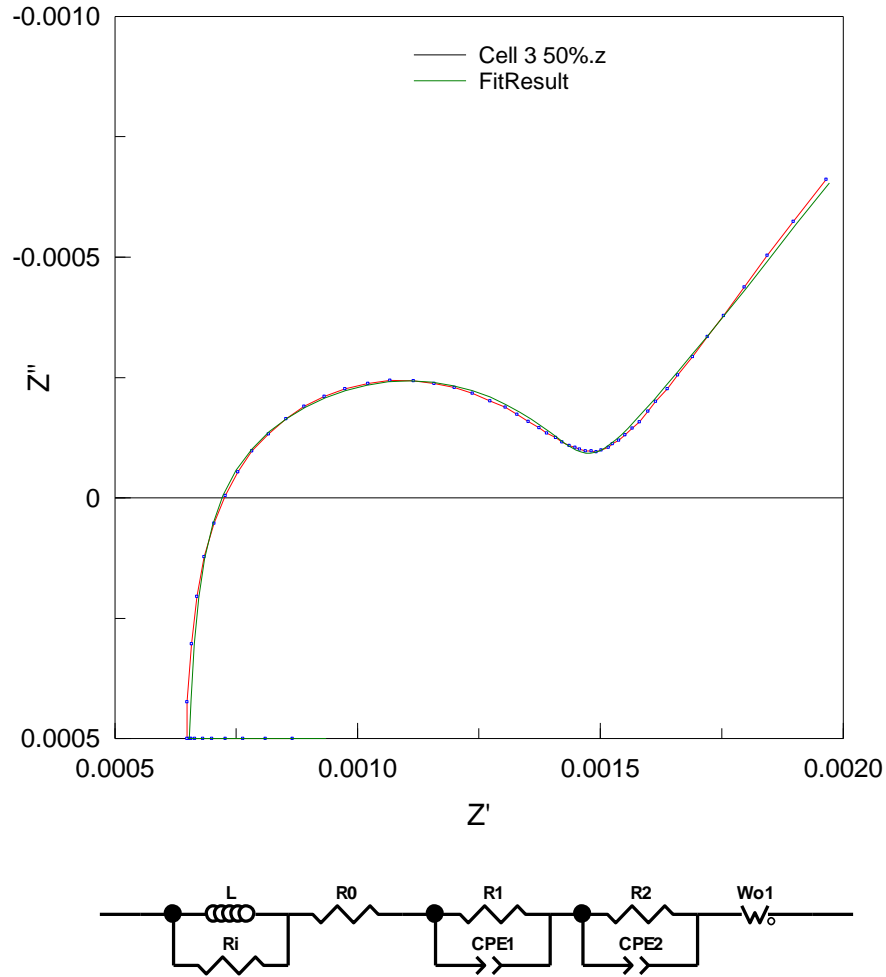


FIGURE 7-8 – SECOND ORDER ECM USED TO MODEL THE IMPEDANCE RESPONSE OF A CELL UNDER EIS WITHIN SCRIBNER® ZVIEW.

Figure 7-9 shows the Nyquist plots for initial EIS characterisation at 95%, 80%, 50%, 20% and 10% SOC for all cells. All cells display similar characteristics. Figure 7-10 shows the mean value and standard deviation of the Pure Ohmic resistance, charge transfer resistance, and total combined resistance  $R_{Total-EIS}$  for 95%, 80%, 50%, 20% and 10% SOC over all six cells. Similarly to findings within literature [227,230,231] the cells display little variation of the pure Ohmic resistance throughout the SOC range. In contrast, a large SOC dependency can be observed for the charge transfer resistance  $R_{ct-EIS}$  from the position of the local minimum of the semicircle within Figure

7-9, and the mean values portrayed within Figure 7-10. Values are lower in the in the middle SOC window, and a distinct increase can be observed at the lower SOC of 20% and 10%. This is assumed to be caused by changes in the lithium concentration within, and physical characteristics of the electrode materials as described within Chapter 2.

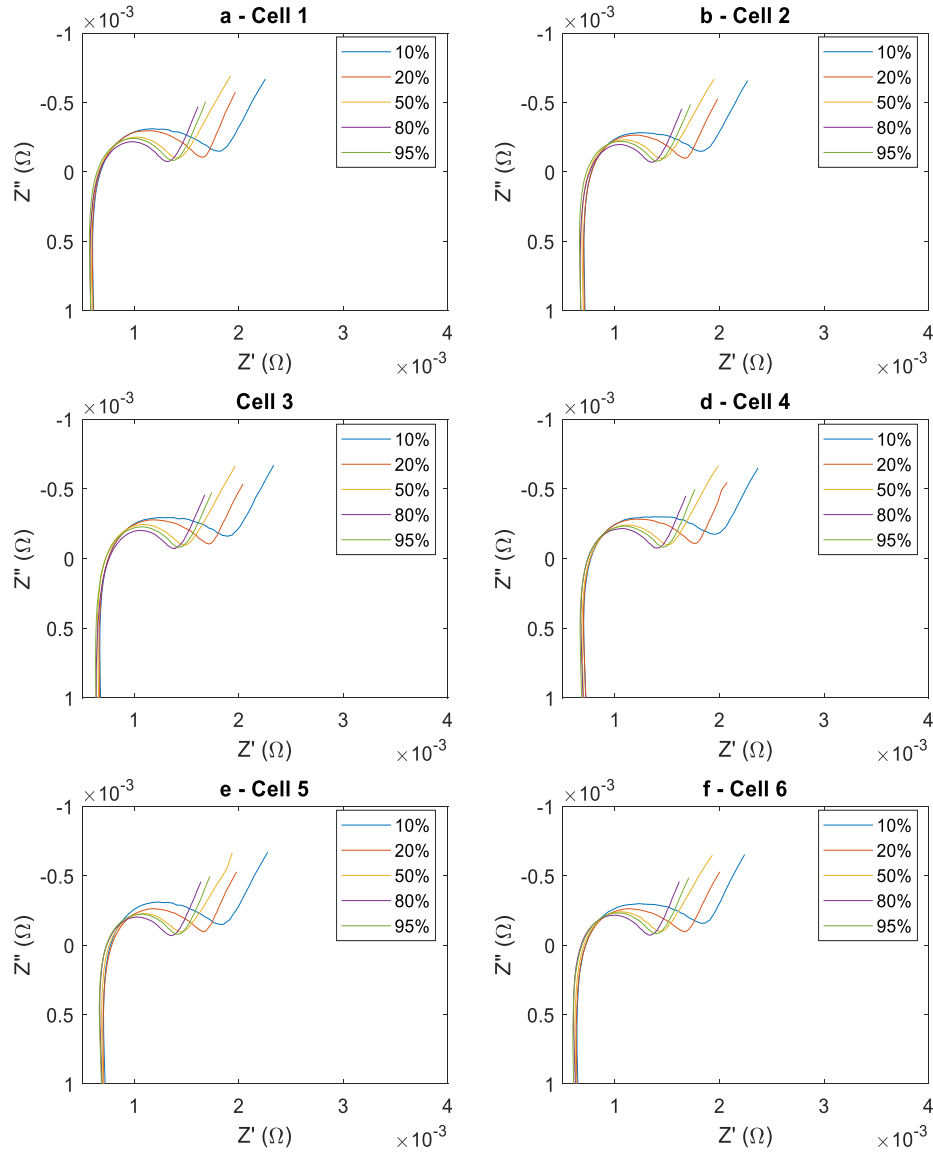


FIGURE 7-9 – NYQUIST PLOTS FOR EIS MEASUREMENTS AT 95%, 80%, 50%, 20% AND 10% SOC.

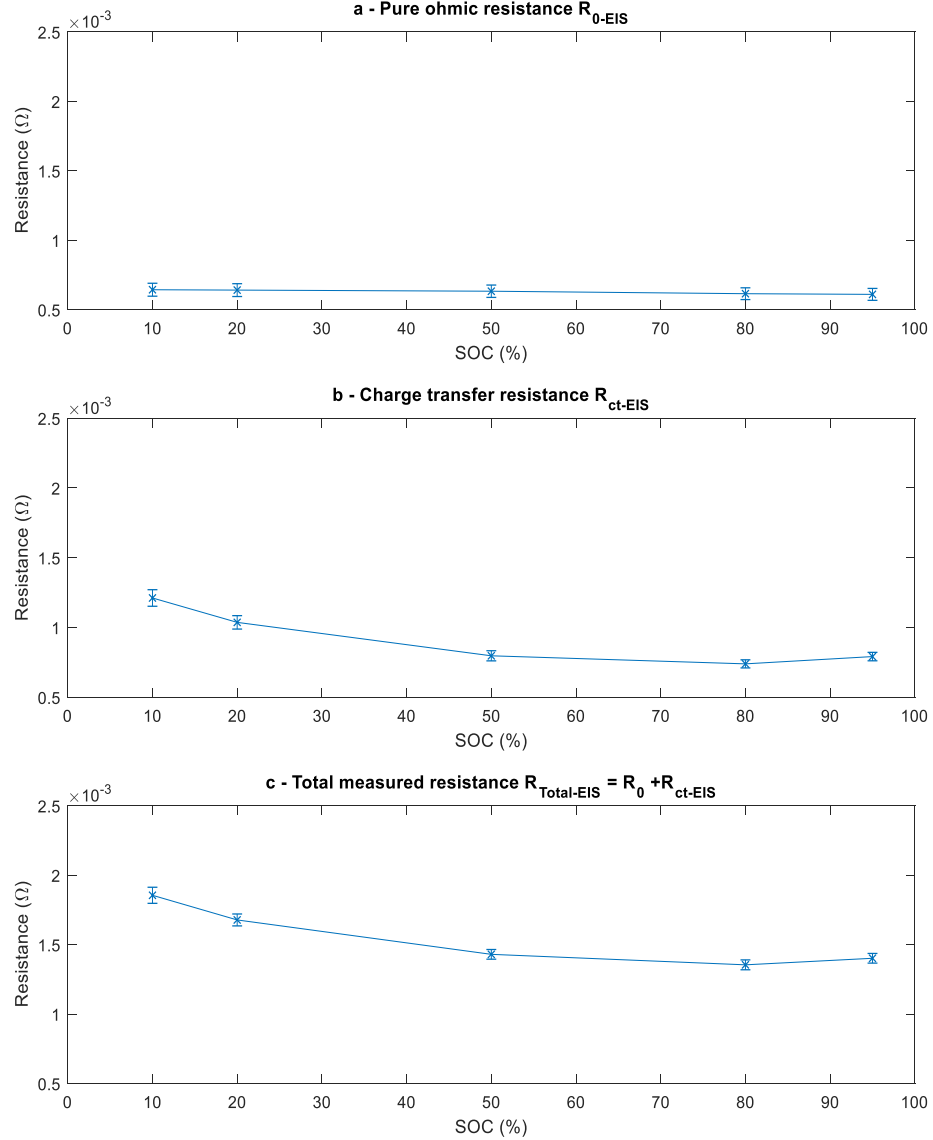


FIGURE 7-10 — RESISTANCE PARAMETERS DETERMINED FROM EIS MEASUREMENTS. (A) PURE OHMIC RESISTANCE ( $R_0$ ). (B) CHARGE TRANSFER RESISTANCE  $R_{ct-EIS}$ . (C) COMBINED RESISTANCE

By comparison of the findings between the PMC and EIS tests, it can be seen that for the PMC tests, values for  $R_0$  are higher than those found for the EIS tests by a factor of up to 2. This observation is attributed to the measurement timescale utilised in each test [147]. As the maximum frequency applied for the PMC test is 1 Hz, a more suitable comparison would be to compare those values with the EIS impedance measured at 1 Hz ( $R_{1Hz-EIS}$ ), as illustrated within Figure 7-11 for cell 3 at 50% SOC. For cell 3 this returns a resistive value of 1.469 m $\Omega$ , which corresponds well with the  $R_{0-PMC}$  value from the PMC test of 1.402 m $\Omega$ .

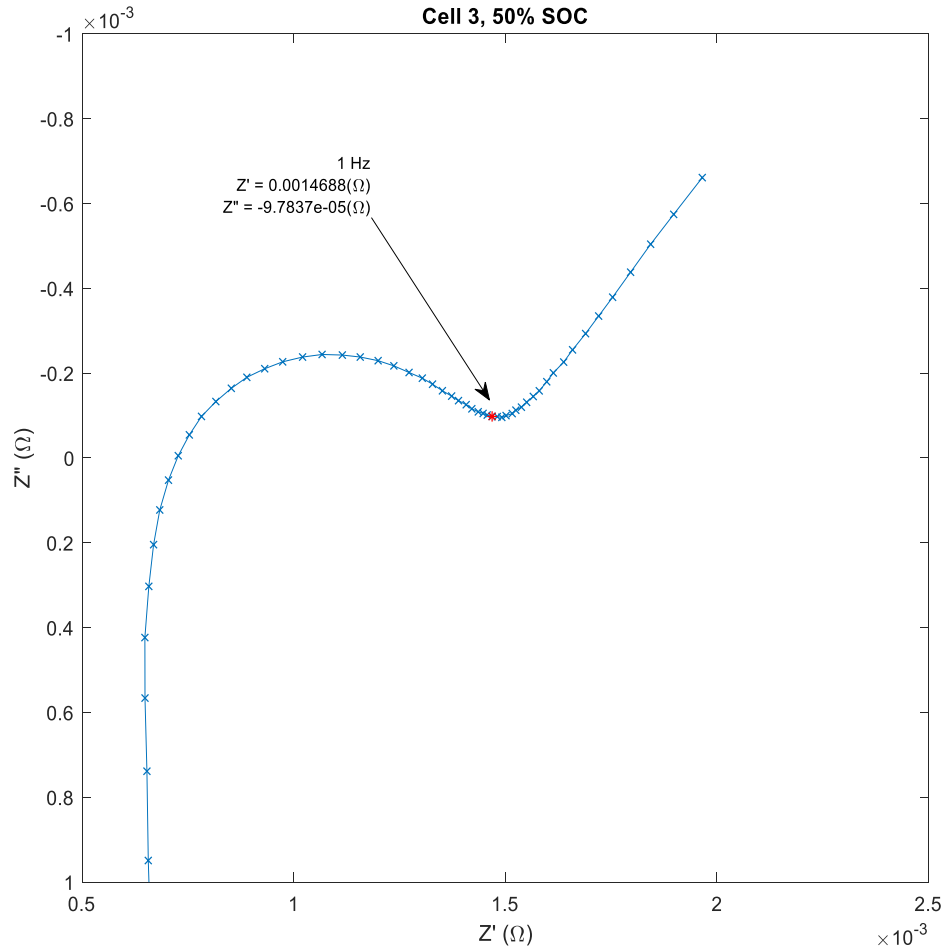


FIGURE 7-11 – NYQUIST PLOT FOR CELL 3 AT 50% SOC. THE 1HZ IMPEDANCE HAS A RESISTIVE VALUE OF 1.469  $m\Omega$ . THIS CORRESPONDS WELL WITH THE  $R_{0-PMC}$  MEASUREMENTS

#### 7.2.4 Initial characterisation summary

Based on the initial characterisation test, little differences are observed between the cells with regards to cell capacity, DC resistance as measured via PMC tests, and AC Impedance measured via EIS. From the PMC test results, the cells have shown to display linear characteristics between 95% and 20% SOC, which can be accounted for by a first order ECM. It is currently inconclusive whether non-linear behaviour is present at 10% SOC or not. Values for  $R_{0-PMC}$  increase for 20% and 10% SOC, combined values for  $R_{0-PMC} + R_{1-PMC}$  result in a flat resistance profile around 1.8  $m\Omega$  between 95% and 20% SOC. Due to voltage clipping occurring for PMC tests at 10% SOC, values from these specific measurements are unreliable and need to be omitted from further analysis. For other SOC's, Comparison between  $R_{0-PMC}$  and  $R_{1Hz-EIS}$  indicates good agreement between PMC and EIS testing outcomes. The small spread of values between cells for energy

capacity, PMC and EIS tests, shows that there is little variation between individual cells at the beginning of testing. As such, any divergence of characterisation test outcomes between the two test groups during the degradation study will enable the identification of use-case specific degradation behaviour.

### 7.3 Performance testing

The results presented within this section correspond with the experimental procedure detailed within section 6.4. Figure 7-12, Figure 7-13 and Figure 7-14 show the duty cycle profile, voltage response, and cell surface temperature for an 85% depth of discharge (DOD) on cell No. 4 for the HP-MS, IECC, and Bahrain duty cycle, respectively. This cell was chosen as all installed thermocouples operated without interruption throughout the duration of all tests, and as such provides the most reliable thermal test data. Table 7-3 lists the mean time taken for each duty cycle ( $\bar{\theta}$  time), and the mean energy throughput ( $\bar{\theta}$  Wh) for the set of cells with the associated standard deviation ( $\sigma$ ) for each measure. Whilst the HP-MS takes 1406 seconds to complete with an absolute energy throughput of 230 Wh, the IECC requires 122% longer duration with a 13% lower energy throughput and the Bahrain cycle is 42% shorter with only a 9% lower energy throughput. It is clear that the IECC lacks the dynamic behaviour, which both the HP-MS and Bahrain cycle exert on the cells. As the HP-MS is aimed to be representative of a variety of HP duty cycles and the Bahrain cycle is only a single example of the target use case, the differences between these two cycles concerning duration and energy requirements are deemed acceptable.

Cycle	$\bar{\theta}$ time(s)	$\sigma$ time	$\bar{\theta}$ Wh throughput	$\sigma$ Wh
HP-MS	1406.1	0.4	230.18	0.73
IECC	3121.1	0.0	199.41	0.52
Bahrain	826.0	0.1	209.49	0.95

TABLE 7-3 — MEAN DURATION OF THE DISCHARGE FOR EACH DUTY CYCLE, MEAN ENERGY THROUGHPUT AND THE ASSOCIATED STANDARD DEVIATION FOR EACH MEASURE FOR THE SET OF CELLS

The vast differences in intensity of the HP-MS and Bahrain duty cycle compared to the IECC is further illustrated in the three sub-graphs Figure 7-12c, Figure 7-13c, and Figure 7-14c and the data presented within Table 7-4. The figure presents the measured cell surface temperatures during discharge for cell No. 4, the table lists the mean peak temperatures ( $\bar{\theta}$  peak °C) for the hottest and coldest part of the cells, and the peak temperature differences across the cell surface for each cycle, as well as one standard deviation ( $\sigma$ ) for each measure. The hotspot on every cell is generally measured on the thermocouple placed at the edge of the cell furthest away from the

cooling plate (Pos. 4 – see Figure 6-1b). The position underneath the tab, which is furthest away from cooling (Pos. 1), experiences similar temperatures. This, however, is not always the case, when Pos. 1 displays marginally hotter temperatures than Pos. 4. This observation may be a feature of individual cells, as reported within [232] or, alternatively, attributed to uneven pressure distribution across the cell surface arising from an uneven surface of the polystyrene and FOAMGLAS® slabs, the swelling of cells during cycling, or a shift in position of the thermocouples. The cold-spot of the cell is always measured on the edge of the cell, located closest to the cooling plate in Pos. 6.

The intensity of the HP-MSC and Bahrain cycle cause cell surface temperatures to reach much higher peak temperatures compared to the IECC. The cell surface hotspots for the IECC reach similar temperature levels to the cold-spots for the HP-MSC, but remain 6.31 °C below the cold spot of cells undergoing the Bahrain cycle. Surface temperature gradients for the IECC reached a mean of 8.34 °C across the cell samples, whereas the surface gradients of the HP-MSC and Bahrain cycle were 200% and 300% of that value respectively.

Increased cell temperatures in excess of 45 °C have long been identified as a key contributor to accelerated cell degradation, due to accelerated growth of the passivating solid-electrolyte interface (SEI) layer at the anode and increased rate of undesired side reactions as reported within [54,89,99]. Furthermore, temperature gradients within cells through the central plane have been reported to also contribute to accelerated degradation [121,233]. Parts of the cell at elevated temperatures are expected to have a lower resistance, allowing more current to flow through it, in turn heating up more via a positive feedback process between unique layers that are electrically connected in parallel and localised parts in the same layer. This in turn may lead to localised aging, and accelerate the ageing process [234]. For realistic cycle life studies the choice of a testing profile which results in representative cell self-heating is therefore of paramount importance. From a thermal perspective, it may be argued that within the HP use case, international testing standards such as IEC 62660-1/2 and ISO 12405-1/2 are inadequate for evaluating cycle life and thermal design requirements and that the presented HP-MSC offers a more realistic target profile.



Cycle	Ø peak °C hotspot	σ	Ø peak °C coldspot	σ	Ø peak surface °C gradient	σ
HP-MS	54.00	1.56	36.75	0.93	17.24	1.97
IECC	36.93	0.66	28.40	0.81	8.34	0.71
Bahrain	67.30	1.99	43.24	1.76	24.06	2.53

TABLE 7-4 – MEAN PEAK TEMPERATURES OF THE HOTSPOT, COLDSPOT, AND GRADIENTS FOR THE SET OF CELLS.

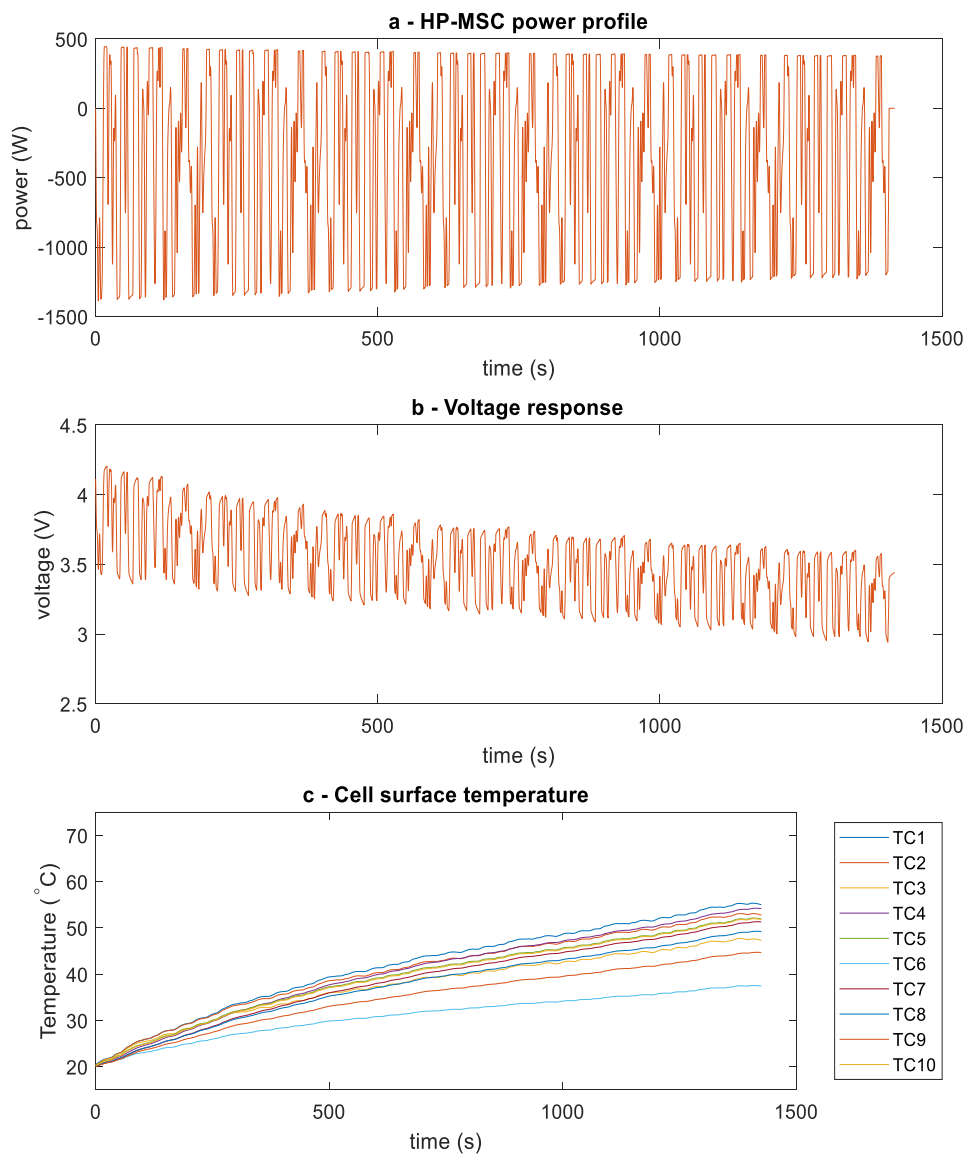


FIGURE 7-12 – PERFORMANCE TEST RESULTS FOR THE HP-MSC FOR CELL 4 FOR A DYNAMIC DISCHARGE FROM 95-10% SOC. (A) POWER PROFILE. (B) MEASURED VOLTAGE RESPONSE. (C) MEASURED CELL SURFACE TEMPERATURE

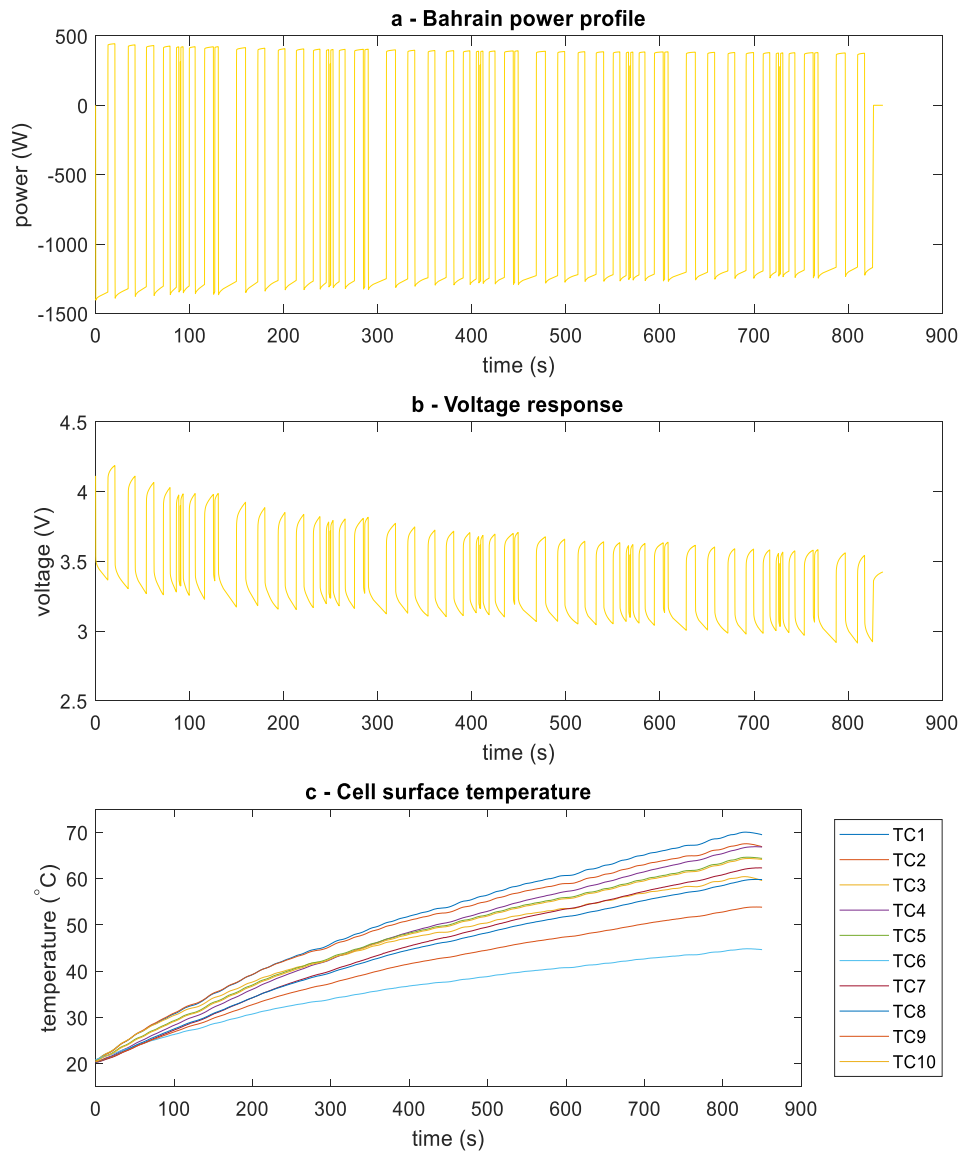


FIGURE 7-13 – PERFORMANCE TEST RESULTS FOR THE BAHRAIN CYCLE FOR CELL 4 FOR A DYNAMIC DISCHARGE FROM 95-10% SOC. (A) POWER PROFILE. (B) MEASURED VOLTAGE RESPONSE. (C) MEASURED CELL SURFACE TEMPERATURE

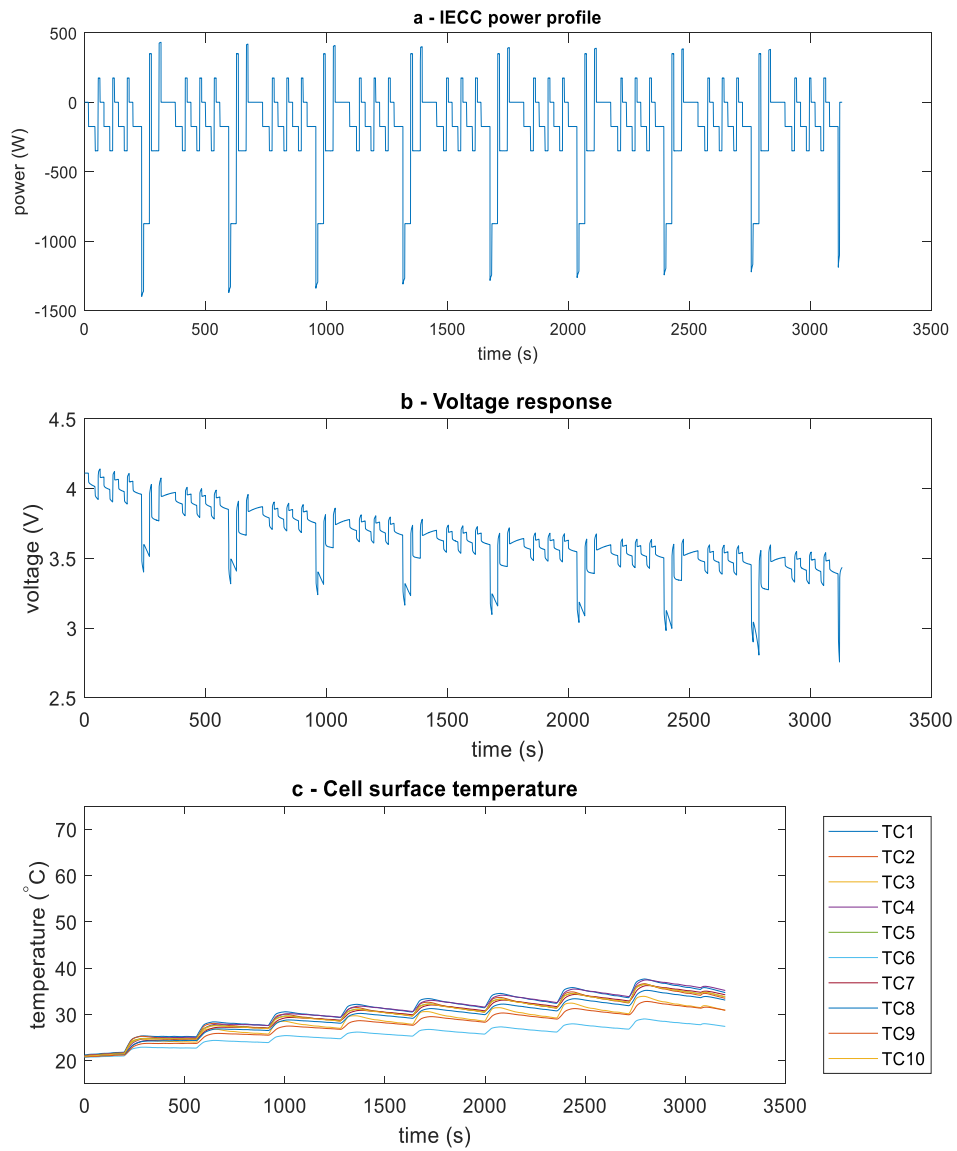


FIGURE 7-14 – PERFORMANCE TEST RESULTS FOR THE IECC FOR CELL 4 FOR A DYNAMIC DISCHARGE FROM 95-10% SOC. (A) POWER PROFILE. (B) MEASURED VOLTAGE RESPONSE. (C) MEASURED CELL SURFACE TEMPERATURE.

## 7.4 Duty Cycle Degradation Study

This section presents and discusses the results obtained from the experimental procedure detailed within section 6.5. Figure 7-15 presents for both, the HP-MSG Group and IECC Group, the progression of cell capacity retention against the cells' energy throughput from HP-MSG and IECC cycling, respectively, throughout the duty cycle degradation study, as measured during each partial characterisation test. The discharge capacity extracted from the 1C discharge tests is shown in the top two graphs, the charge capacity, determined during C/10 charging is shown in the bottom two graphs. The data points represent the mean of each group, with the error-bars measuring one standard deviation. Both, the discharge and charge capacity increases throughout testing for both test groups. The initial and final charging and discharging capacities for both test groups, and the calculated change ( $\Delta$ ) are tabulated in Table 7-5.

	Initial Ah	Final Ah	$\Delta$ %	Initial Wh	End Wh	$\Delta$ %
IECC (discharge)	52.02	53.28	2.42	186.00	189.70	1.99
HP-MSG (discharge)	52.01	53.04	1.98	185.70	188.90	1.72
IECC (charge)	51.58	53	2.75	194.10	198.80	2.42
HP-MSG (charge)	51.36	52.62	2.45	193.10	197.30	2.18

TABLE 7-5 - CHARGE AND DISCHARGE CAPACITY FOR THE HP-MSG AND IECC TEST GROUPS

The highest measured capacity for the HP-MSG group is at 53.15Ah (189.4 Wh), in the penultimate characterisation, before reducing to 53.04Ah (188.9 Wh) at the final characterisation, whereas the IECC group's capacity is still steadily increasing. However, the capacity measurements of the HP-MSG group are within the error of the previous measurement and overlap with the error of the IECC group. From the capacity measurements alone, no definitive start of capacity fade can be asserted from the experimental data.

Increases in cell capacity at the early stages of cycling for cells of similar chemistry and format have been reported within [166] and [51]. Jalkanen [166] et al. tested 3 Dow Kokam<sup>®2</sup> 40Ah pouch at room temperature, 45°C and 65°C for continuous 1C charge and discharge cycling. All three cells initially have a higher discharge capacity than the nominal capacity declared by the manufacturer, and capacity increases to a maximum, before decreasing. Based on the presented

<sup>2</sup> Dow Kokam rebranded to XALT Energy

results, the cell discharged at 45 and 65 °C reach their maximum capacity within the first 100 cycles, the cell cycled at room temperature reaches a first peak at around 200 cycles and a second at 500 cycles. The rate of subsequent decrease in capacity is marginally fastest for the cell cycled at 65°C, which gave a shorter cycle life than the other two cells.

De Hoog et al. [51] tested EIG® 20Ah NMC pouch cells to formulate a model which separates calendar and cycle ageing. They observed an initial increase in cell capacity for calendar ageing and combined calendar and cycle ageing tests, an effect which was more pronounced for cells stored at low states of charge, and subject to lower DOD.

Both studies explained their observations with a process referred to as electrochemical milling. During charge and discharge electrodes expand and contract, resulting in internal stresses, which in the case of non-uniform stress distribution within the electrode may result in micro-cracks forming in the electrode material, exposing fresh sites and pathways for lithium ion intercalation [235]. This in turn causes a widening of the operating voltage window of the electrodes, the extent of which can be determined using reference electrode tests. Provided parasitic side reactions are minimal, and fractured particles maintain good electronic contact, this may result in an increase in the energy capacity and a reduction of the internal resistance. As discussed within [50] cracking in electrode material can be caused by high currents and high DOD. Both duty cycles tested reach c-rates exceeding 7.5C, making electrode cracking a possible pathway for changes in the electrode particles. Hence, the capacity increase observed in both test groups within this work may also be correlated to the onset of electrochemical milling. However, based on these results alone, it is not possible to fully validate this hypothesis.

Another possible explanation for the capacity increase observed within this study is a potential gradual decrease in external pressure applied to the cells over time. As the cells are densely packed at the beginning of cycling, continual cycle testing, and the associated expansion and contraction of cells may lead to deformations in the packed polystyrene slabs that will in turn reduce the lateral force on the cells. Barai et al. [236] reported a decrease of cell capacity coupled with an increase in impedance for NMC pouch cells which had an external pressure applied to them. They observed a 2% capacity decrease for an external pressure of 0.8 bar. The author asserts that a pressure difference of 0.8 bar resulting from deformed polystyrene slabs is unlikely. Furthermore, a change of this magnitude would result in significantly worse and observable cell cooling nearer the end of the duty cycle degradation study. However, no such observation could be made within the recorded data. As such, the more plausible cause of capacity increase is that of electrochemical milling. However, it is noteworthy that based on the capacity test data alone,

without further observations from within the cells themselves, it is not possible to make a definitive conclusion.

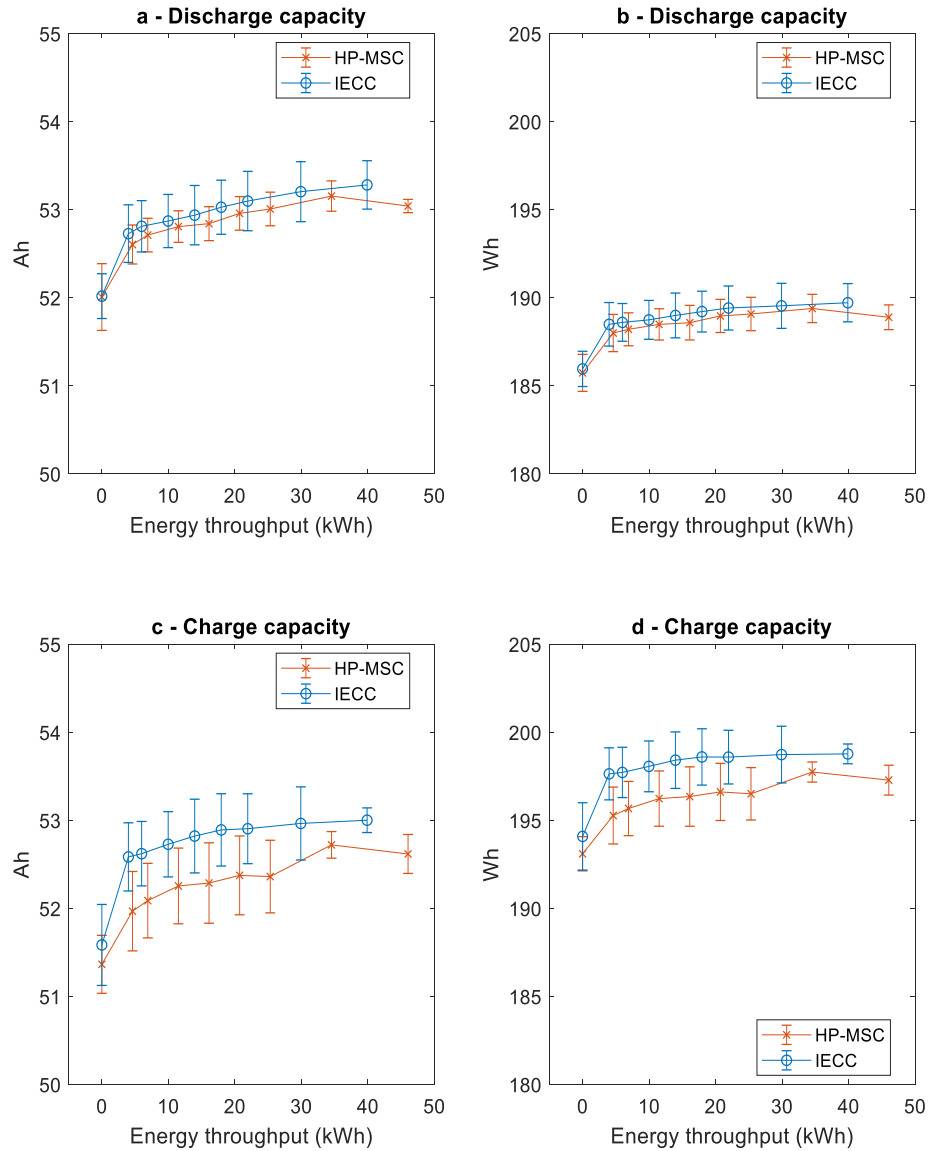


FIGURE 7-15 - CELL CAPACITY THROUGHOUT TESTING AT CHARACTERISATIONS.

Graphs for differential capacity analysis for both test groups are presented in Figure 7-16. The curves show the derivatives of the charge vs. voltage ( $dQ/dV$ ) curves recorded for the 0.1C charge for the p-OCV test, with the area under the curve equating to the energy capacity of the cell. The upper subplots show the results for both test groups at the initial and final characterisation tests, respectively. The lower subplots present a direct comparison between the initial and final

characterisations for the HP-MSD and IECC groups, respectively. An advantage of these plots is that changes in the p-OCV and voltage vs. capacity plots can be seen more easily. The underpinning theory behind the analysis of these graphs is discussed in detail in [38,131–133].

Based on the Initial characterisations, three regions of interest were investigated and displayed in magnified areas within Figure 7-16a, b and c. The features of the curves displayed in the initial characterisation graph are explained as follows. At 0% SOC, the graphite electrode is almost completely delithiated. During charging,  $\text{Li}^+$  ions intercalate into the graphite layers and the material transitions through several phases as the lithium content within the material increases [135,148]. One of these phase transitions is indicated in the peak around a full cell potential of 3.52 V in Figure 7-16a, in which a wide spread of peak height can be observed within the cells in terms of the height of the  $dQ/dV$  peak. Cells No. 2 and 3 display the most pronounced peak whilst Cell No.1's peak is least defined.

At the beginning of charge, the NMC electrode material is almost fully lithiated in a hexagonal O3 layered structure [79]. During charge, as lithium is extracted, a phase change occurs from the hexagonal to a monoclinic lattice [237], manifesting in the peak identified in Figure 7-16b around a cell potential of 3.66V. Similarly, to the peak in Figure 7-16a, a wide spread of peak height can be observed for the test groups. Cells No. 6, 4 and 1 have the three highest peaks, respectively, with the remaining cells showing similar behaviour. Between 3.75 V and 4.2 V NMC then displays a steady potential with the material in the solid-solution region. The third region of interest is located at the beginning of charge in Figure 7-16c. All 6 cells display a similar OCV between 3.46 V and 3.48 V. However, the initial  $dQ/dV$  values vary significantly.

Comparing the observations of the initial full characterisation to the results displayed for the final full characterisation, significant differences may be observed. Firstly, by comparing Figure 7-16a with Figure 7-16d, the intensity of the peak in the latter appears to have increased whilst the spread of intensity between cells has been greatly reduced. The increase in area underneath this peak indicates that a larger amount of energy capacity may be attributed to the phase change process associated with the graphite electrode compared to initial measurements. The order of peak intensity as seen for the initial characterisation test has also changed, with the HP-MSD group having slightly lower peak intensity than the IECC group. Furthermore, a shift in the peak position toward the lower cell potential is observed, which is associated with a shift to a lower impedance within the cell [131]. By examination of Figure 7-16-g the peak for the HP-MSD group after 200 cycles shifted approximately 10 mV from 3.53 V to 3.52 V, whereas the shift for the IECC group (Figure 7-16k) is slightly larger at 20 mV from 3.53 V to 3.51 V.



Secondly, by comparing Figure 7-16-b and Figure 7-16-e, a smaller spread in peak height for final characterisation tests can be seen, but no clear trend in height gain or reduction for either the HP-MSC (Figure 7-16-h) or IECC (Figure 7-16-l) group. Whilst cells No. 1, 4 and 6 show a decrease in peak height, cells No. 2 and 5 show an increase, and no significant change can be observed for cell No 3. However, a horizontal shift of the peaks toward higher cell potentials is observed, with the shift of the HP-MSC group being slightly larger, which may indicate a higher internal resistance.

Thirdly, linking region f) to region c), a significant change in the starting OCV is observable with a mean shift of 85 mV for the HP-MSC group (Figure 7-16j), and a mean shift of 63 mV for the IECC group (Figure 7-16m) toward a lower potential, in conjunction with a lower spread in initial  $dQ/dV$  values for both test groups. Inspection of Figure 7-16f and j also reveal an additional peak at a potential of 3.45 V. Based on the information provided within [135,148], this new peak is most likely resulting from a phase change in the earlier lithiation process of the graphite electrode. This decrease of the OCV is directly related to the increase in energy capacity. An increase in the OCV of a cell, as reported by Stiaszny et al. [228], is caused by a reduction in cyclable lithium stemming from the NMC electrode as lithium is irreversibly used in SEI layer formation and growth. The reduced OCV observed in this study thus requires an increase in cyclable lithium.

A possible source for these observations may be minor cracks in the NMC material, providing fresh reaction sites, which previously were not accessible due to diffusion or mass transfer limitations in the electrode particles or porous electrode matrix, respectively. Without reference electrode tests it is not possible to assign definitively the observed changes in the OCV to changes in either the graphite, or NMC electrode, but these results, combined with evidence from the literature [235] provide further indication that cells experience electrochemical milling. Further work required to reaffirm this conclusion is presented in section 7.6.

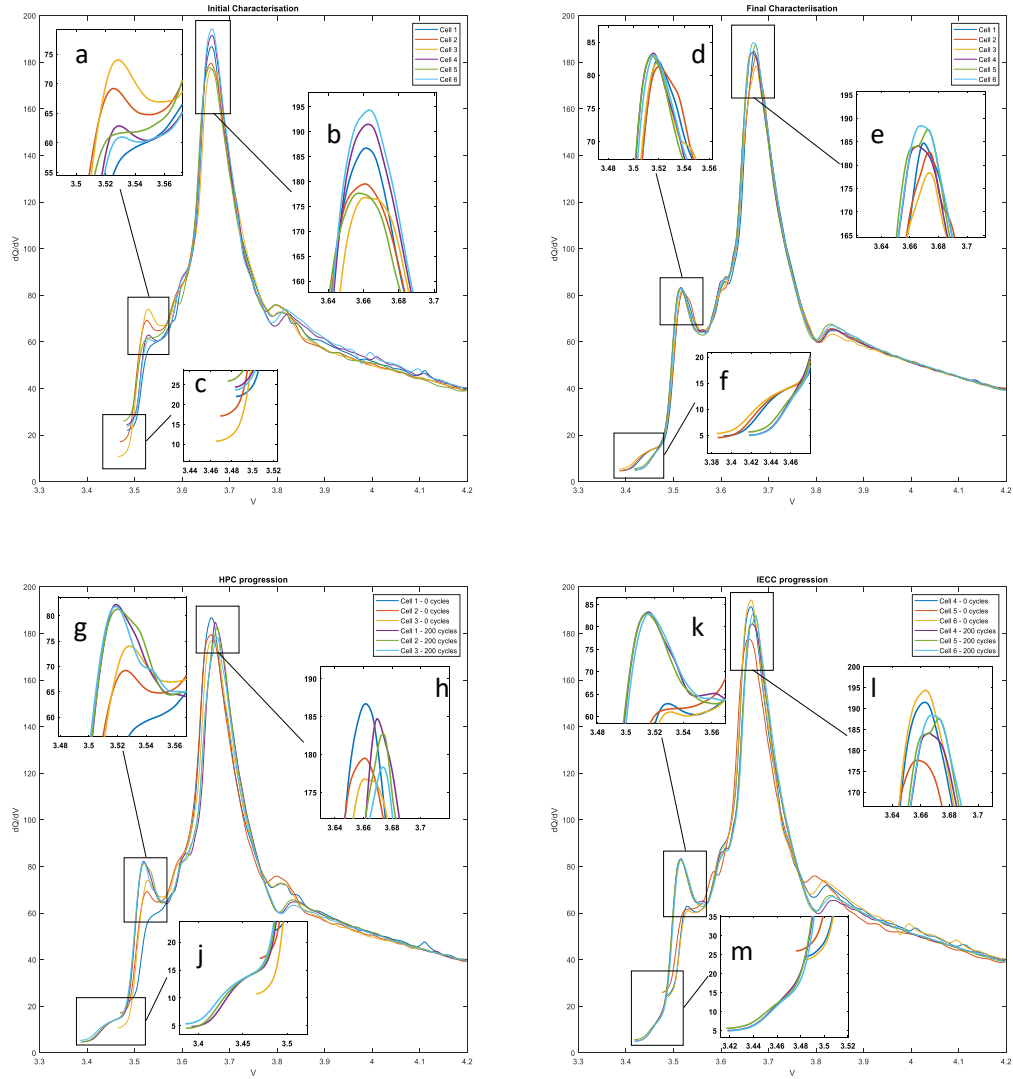
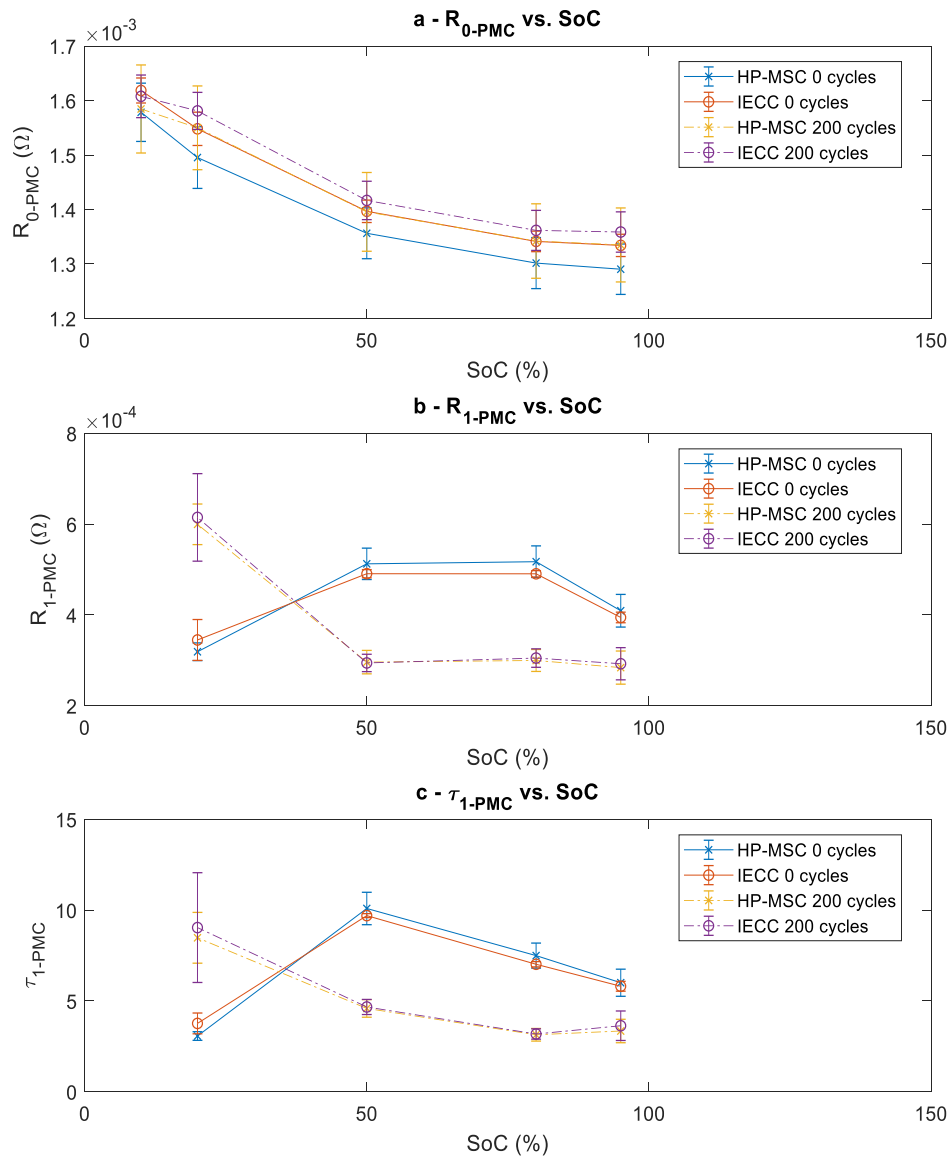


FIGURE 7-16 - INCREMENTAL CAPACITY ANALYSIS - TOP LEFT: INITIAL CHARACTERISATION; TOP RIGHT: FINAL CHARACTERISATION; BOTTOM LEFT: HP-MSC CELL PROGRESSION; BOTTOM RIGHT: IECC CELL PROGRESSION

Figure 7-17 (a – c) illustrates the change in ECM parameters, extracted from the PMC tests of the two test groups during the duty cycle degradation study. Table 7-6 tabulates the percentage change for each ECM parameter. Values for  $R_0$  show an increase from their initial values through to their final characterisation for both test cycles. With the HP-MSC group having a slightly higher increase throughout the SOC range. Values for  $R_1$ , partially associated with charge transfer and diffusion phenomena, decrease after cycling for SOC of 50%, 80% and 95%, and show an increase for an SOC of 20%. The increase in  $R_1$  at 20% SOC is linked to the change in peak between 3.5 V and 3.56 V in Figure 7-16d. Values for  $R_{1-PMC}$  and  $\tau_{1-PMC}$  at 10 % SOC have been excluded from the results as the cell lower voltage limit of 2.7 V was reached during characterisation tests.

FIGURE 7-17 – PROGRESSION OF ECM PARAMETERS AS DERIVED FROM PMC TESTS FOR A –  $R_0$ ; B –  $R_1$ ; C –  $\tau_1$ .

Parameter	Group	95% SOC	80% SOC	50% SOC	20% SOC	10% SOC
$R_{0-PMC}$	HP-MSC	3.45%	3.11%	2.90%	3.65%	0.39%
	IECC	1.84%	1.51%	1.43%	2.12%	-0.66%
$R_{1-PMC}$	HP-MSC	-30.59%	-42.05%	-42.23%	88.01%	[-]
	IECC	-25.84%	-37.83%	-40.04%	78.28%	[-]
$\tau_{1-PMC}$	HP-MSC	-44.27%	-58.15%	-54.53%	176.17%	[-]
	IECC	-37.41%	-54.70%	-51.86%	140.18%	[-]

TABLE 7-6 – PERCENTAGE CHANGE FOR MEAN VALUES OF PMC-ECM PARAMETERS FROM INITIAL TO FINAL CHARACTERISATION.

Figure 7-18-a and Figure 7-18-b show the Nyquist plots derived from the EIS tests for Cell No. 1 from the HP-MSC group at the initial characterisation and after 200 cycles, respectively, for a number of SOCs. Figure 7-18-c and Figure 7-18-d, show the same Nyquist plots for cell No. 4 from the IECC test group. For both cells, a shift of the intersection of the inductive trail toward higher values of  $Z'$  is observed. The position of the local minimum in the mid-frequency semicircles, however, does not show any obvious signs of movement from its original location.

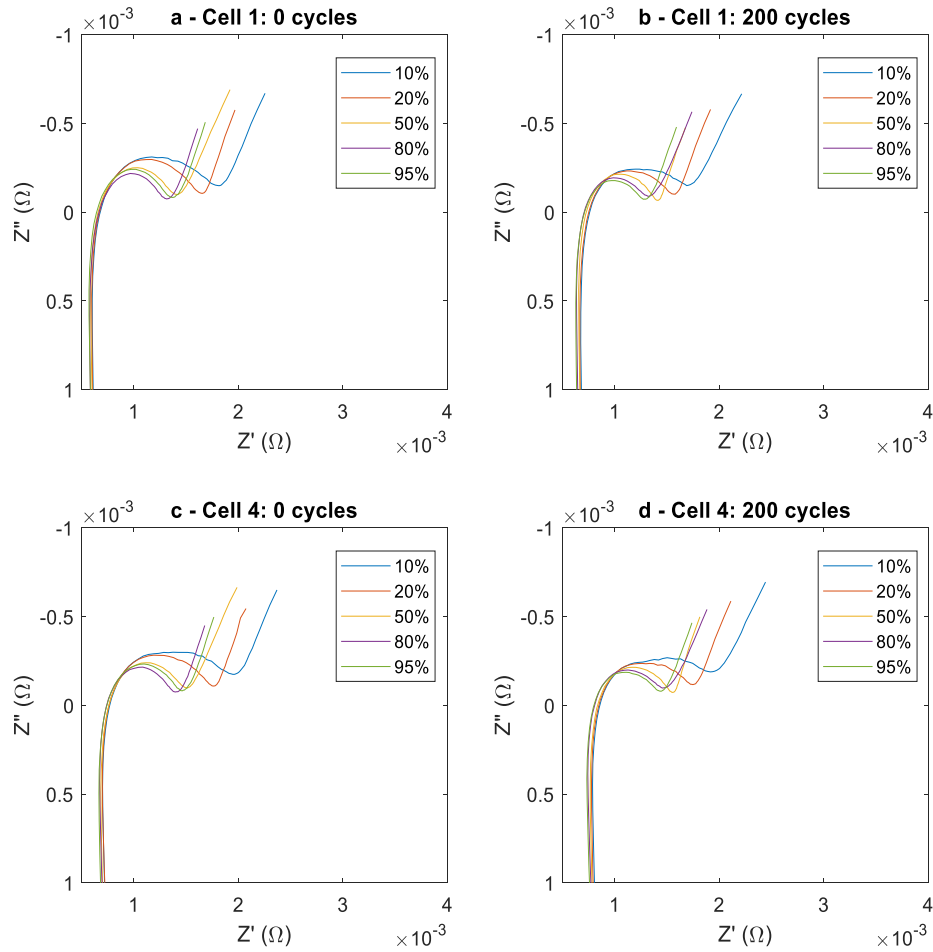


FIGURE 7-18 – NYQUITS PLOTS: A – NYQUIST PLOTS FOR CELL 1 AT BEGINNING OF TESTING; B – NYQUIST PLOT FOR CELL 1 AFTER 200 CYCLES; C – NYQUIST PLOTS FOR CELL 4 AT BEGINNING OF TESTING; D – NYQUIST PLOT FOR CELL 4 AFTER 200 CYCLES

The mean values of the pure Ohmic resistance ( $R_{0-EIS}$ ), as extracted from the Nyquist plots, for the HP-MSC and IECC groups, is presented in Figure 7-19-a, with the error bars representing one standard deviation from the mean. Table 7-7 lists the percentage change of the mean EIS-ECM parameters. Values of  $R_{0-EIS}$ , which is attributed to the resistance of the bulk electrode material and electrolyte, show an increase for both test groups throughout the SOC range. This

observation is in agreement with the increase for  $R_0$  from the PMC test. It indicates changes in the cell bulk material, likely associated with degradation mechanisms, such as potential particle cracking. The values of the charge-transfer resistance, ( $R_{ct-EIS}$ ), associated with the local minimum of the mid frequency semicircle in the Nyquist plots, show a decrease after the completion of the study, as shown in Figure 7-19-b. This downward shift is known [145] to be linked to improved transfer kinetics at the electrode electrolyte interfaces in the porous electrode. As discussed within [51,235,238], one reason for this may be an increase in active surface area for Li-ion intercalation which could have been caused by electrode cracking. This shift appears to be of a larger magnitude for the HP-MSC test sample.

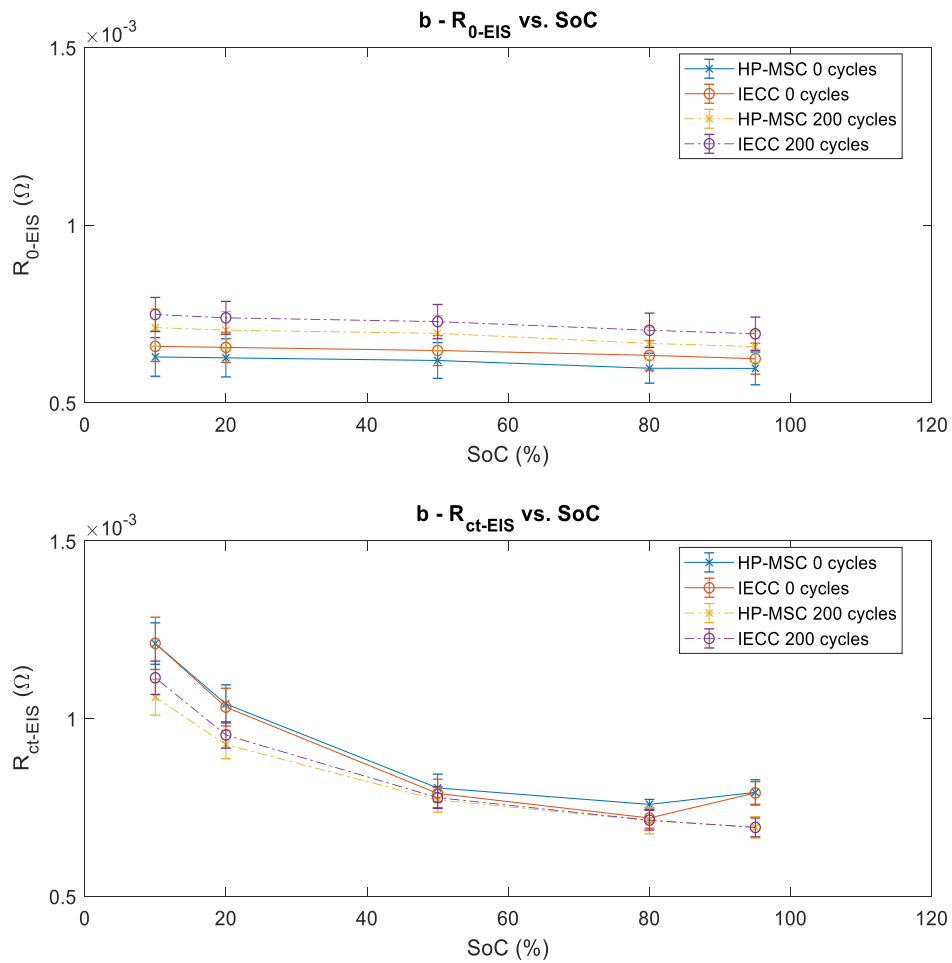


FIGURE 7-19 – A – MEAN OHMIC RESISTANCE OF TEST GROUPS DERIVED FROM NYQUIST PLOTS, B – MEAN CHARGE-TRANSFER RESISTANCE OF TEST GROUPS DERIVED FROM NYQUIST PLOTS.

Parameter	Group	95% SOC	80% SOC	50% SOC	20% SOC	10% SOC
$R_{0-EIS}$	HP-MSC	10.25%	11.70%	12.35%	12.45%	13.13%
	IECC	11.25%	11.16%	12.56%	12.69%	13.63%
$R_{ct-EIS}$	HP-MSC	-12.41%	-6.00%	-4.21%	-10.97%	-12.47%
	IECC	-12.28%	-0.86%	-1.51%	-7.60%	-8.01%

TABLE 7-7 - PERCENTAGE CHANGE OF MEAN VALUES OF EIS-ECM PARAMETERS FROM INITIAL TO FINAL CHARACTERISATION

The reduction in charge transfer resistance in combination with the increase in bulk resistance is a further indication that electrochemical milling may be occurring during the test. As previously suggested, the introduction of micro-cracks in the electrode material may allow fresh sites, some of which may have previously been diffusion limited, to be exposed to the electrolyte. This in turn would result in an increased surface area of reaction sites, transfer kinetics, and allow for a greater amount of lithium to be used for cycling reactions, thus providing a plausible explanation for the decrease in  $R_{ct-EIS}$ , and increase in cell energy capacity. The increase in bulk resistance in this case is assumed to stem from a degradation of the electrolyte and slightly worsened electrical contact of the electrode material. As high-currents are a known pathway for electrode particle cracking, the higher reduction of  $R_{ct-EIS}$  for the HP-MSC group as shown in Figure 7-19j is plausible, as their cycling profile more frequently utilises high currents.

## 7.5 Further Discussion on the Results of the duty cycle degradation Study

Both test groups show a minor increase in the pure Ohmic resistance, and small decrease in the charge transfer resistance, and an increase in the overall cyclable capacity. At the end of the study (200 cycles) the cells from the HP-MSC group appear slightly more degraded in terms of impedance rise and capacity retention in direct comparison with the cells from the IECC test group. However, these differences cannot completely be correlated to the aggressiveness of the HP-MSC cycle profile, as the overall energy throughput of the HP-MSC group's cells is higher, and the spread of experimental results within both test groups overlap. These observed changes of cell characteristics are likely ascribed to micro-cracking in the electrode material, or electrochemical milling. However, to eliminate any doubt about this hypothesis, additional testing is required. Initially, a reference electrode test would enable the analysis of the graphite and NMC electrodes separately. Secondly, post-mortem testing, such as XRD and SEM can be used to confirm if micro-cracking or milling is present in electrode materials in their current state. Similar investigations have been reported within [239].

It is currently not known whether the observations made within this work are solely conditional on the use of high electrical currents, or if the cells are designed to operate in this fashion. If testing were to be continued, it would be expected that, once the cell side reactions overtake the milling effect, the micro-cracking in the cells would cause accelerated degradation over time compared to cells that would not expect this cracking. A possible way to test for this eventuality would be to cycle a further test group with the same mean current as the HP-MSC or IECC, but lower peak currents. From the test results it can then be observed, whether cells tested under these conditions also display an initial increase in energy capacity, and decrease in charge transfer resistance, and at which rate these changes occur. The author aims to continue the experimental work and report further results in future articles.

Concerning temperature related behaviour, as previously identified, cells subject to elevated temperatures, and high temperature differences across the cell surface, are known to experience accelerated degradation mechanisms and ageing. Elevated temperatures enable increased parasitic side reactions between the electrolyte and the carbon electrode, leading to increased SEI growth and a reduction in energy capacity. The rate of this degradation is known to follow the Arrhenius law [99]. However, at the end of the duty cycle degradation study within this work, neither the HP-MSC, nor the IECC group show significant signs of temperature related ageing. Even for the HP-MSC group, which is exposed to significantly higher temperatures during cycling than the IECC group, no temperature related ageing has yet been observed. Although average cell temperature in the HP-MSC cells regularly exceeds 40 °C during cycling, the total duration of these instances is relatively small due to active cooling of the cells during cycling and rest periods, possibly explaining the absence of temperature related degradation indicators. Although no observations of this nature could be made, it is possible that, with continued testing, the cells within the HP-MSC group would show signs of temperature related degradation before the cells in the IECC group.

The atypical degradation behaviour observed within this study has several implications for the design and operation of battery management systems concerning SOC and SOH estimation. Traditionally, SOC is determined via coulomb counting and OCV, whilst SOH is estimated through the observation of a reduction in cell energy capacity and increase internal resistance [214]. As such, the observed widening of the OCV window and capacity increase demand more complex methods of SOC estimation. Furthermore, the non-linearity in degradation observed in this case may mean that BMS identifies little to no change in energy capacity and cell impedance for a prolonged period, identifying a high SOH, followed by rapid decrease in usability of the cell, resulting in driver dissatisfaction.

## 7.6 Limitations of the experimental study

The duty cycle degradation study presented within this work is limited to 200 cycles (circa 180 days) and cells show only little degradation in their electrical characteristics. The expected degradation sequence has not been observed yet and further testing is required to confirm whether the cells within this study follow a typical degradation profile. As such, the author recommends continued testing of the cells until their end of useful life (80% retained capacity, 100% impedance increase) can be verified. To confirm the occurrence of micro-cracks in the electrode material, further testing of the cells in their current state is also recommended. Firstly, reference electrode tests can be performed to identify whether the change in cell characteristics are underpinned by changes in the anode or cathode, secondly XRD and SEM tests to check for visible structural changes within the electrode.

The observations and assessments made regarding the cycling study within this work are only valid for the type of cell used, and for the thermal constraints of the tests. The experimental rig set-up was primarily designed to maintain the safe operating temperature of the cells, and to maximise their operating window. As such, its intended use is constrained to experiments within a laboratory environment and in its current form it is not proposed as a vehicle solution for cell thermal management. For these research findings to be applicable to vehicles, a battery thermal management system would be required to extract the same amount of heat from the cells as the experimental rig within this study.

It is noteworthy that the cells are designed for long cycle life and high-power applications as they have a lower energy density and internal resistance than standard automotive cells. Furthermore, the manufacturer of the cells used within this study is a supplier to FIA Formula-E. The effect of HP cycling on batteries with different chemistries and form factors cannot be known without further testing, although testing on standard automotive cells (i.e. higher energy density and internal impedance) would be more likely to show degradation at earlier stages and would reveal the impact of HP scenarios when compared to standard road vehicles. The author also recommends that the testing procedure within this work is repeated without active cooling efforts to identify the effect of thermal management on the results of the duty cycle degradation study.

The tests within this work only consider the effects of electrical loading and ignore other degradation modes caused through mechanical and thermal loading. It is known that vehicle vibrations contribute to the degradation of cells [49,156] and as such a combined testing study



with vibration and cycling demands further exploration. Lastly, the effect of AC current ripples, as discussed within [149] in the system during cell operation, as may occur during operation in an EV, is not considered due to the fidelity of the testing equipment.

## 7.7 Conclusion

This chapter successfully addresses “**Research Task 4:** Analyse the experimental results and determine any use-case specific behaviour between HP-BEV applications and standard testing procedures.” The completion of this task fulfils the remaining requirements to address the knowledge gap relating to a lack of LIB performance and degradation testing within HP-BEV applications, as illustrated within Table 3-1. The findings of this chapter exemplify the outcomes of the proposed framework, illustrated within Figure 3-6, when applied to the Use case of HP-BEV applications. They provide an insight into the evolution of cell characteristics within this use case, and highlight the limitations in the understanding of cell degradation in this area. Furthermore, they deliver important information pertaining to the thermal management requirements of cells within the HP-BEV segment. These findings will enable additional activities regarding the operation and degradation of cells used within HP-BEVs.

The results obtained from the performance study illustrate the necessity for the additional testing framework to conduct representative performance testing for HP-BEVs. By direct comparison of the HP-MSC with the Bahrain duty cycle and the IECC, it has become evident that the new proposed HP-MSC is more representative of HP driving scenarios than existing procedures. The disparity between the heat generation within cells during the IECC and the HP-MSC further highlights that the use of a representative duty cycle is vital when benchmarking cells for design activities pertaining to battery thermal management. The considerable differences in thermal behaviour of the two test cases also underpins the requirement that cycle-life studies employ the HP-MSC over the IECC to characterise cells for their usable cycle-life in automotive HP scenarios.

The requirement for the proposed framework to conduct representative degradation testing is less conclusive, based on the experimental results from the duty cycle degradation study. Over 200 duty cycles, counterintuitively, the cells in both test groups have shown an increase in cyclable energy capacity, a reduction in charge-transfer resistance, and an increase in pure Ohmic resistance. Although the cells within the HP-MSC test sample have shown larger changes in cell characteristics than those in the IECC group, the results have to be treated as inconclusive, due to the higher overall energy throughput of the HP-MSC group, and overlapping values spread of experimental results. The cells used within this study can deliver a total of 200 track driving

sessions without showing signs of capacity decrease or significant overall impedance rise, provided active cell cooling is present.

The atypical progression of cell characteristics observed in this work, suggest that the changes in cell characteristics could be caused by cracking of the electrode material, although no definitive conclusion can be drawn without further reference electrode testing and destructive SEM and XRD tests. From a review of the academic literature [47,50,116], the high electrical currents employed within the tests have been identified as a likely source. This in turn indicates future accelerated degradation such as a reduction in energy capacity and impedance rise due to extensive cracking and the associated worsened electrical contact with continued use compared to cells, which do not show signs of cracking. The higher frequency of occurrence of high electrical current pulses in the HP-MSD group compared to the IECC group furthermore suggests that with continued cycling, cells within the HP-MSD test group will degrade at a faster rate as electrical testing continues.

Temperature dependent degradation effects have not yet been observed within either test group. The higher cell temperatures and surface temperature differences observed in the HP-MSD test group suggest that, with continued use, accelerated capacity loss and impedance rise due to faster SEI growth may also be observed compared to the IECC cells.

## 8 Conclusions and future direction

The motivation underpinning this thesis as described in Chapter 1 is to investigate the instantaneous performance and long-term degradation of LIBs within the context of HP-BEV and racing applications from an engineering perspective. Following a critical review of the existing literature relating to LIB characterisation, performance and degradation testing within Chapter 2, it was concluded that the existing testing methods for performance and degradation testing currently do not fully address the requirements of HP-BEV applications, and that the results obtained from existing research are not transferrable to this use case. Therefore, a lack of experimental investigations into the performance and degradation of LIBs within HP-BEV applications was identified as a first knowledge gap.

Furthermore, it was found that the absence of experimental studies within this field could be partially attributed to a lack of representative testing profiles suitable for experimental investigations. As such, a prerequisite for testing is to develop a new testing profile. To address this, Chapter 3 critically reviewed methodologies to construct representative test cases. It was found that there is no systematic approach to generate a duty cycle for the use of LIB performance and degradation testing from vehicle battery recordings. Based on these shortcomings, it was concluded that the existing framework for performance and degradation testing is insufficient for HP-BEV applications.

### 8.1 Contributions to knowledge

The key contribution of this work is the definition and implementation of a framework for LIB performance and degradation testing for applications, where existing testing standards are unrepresentative of the typical usage profile. This framework is illustrated within Figure 8-1.

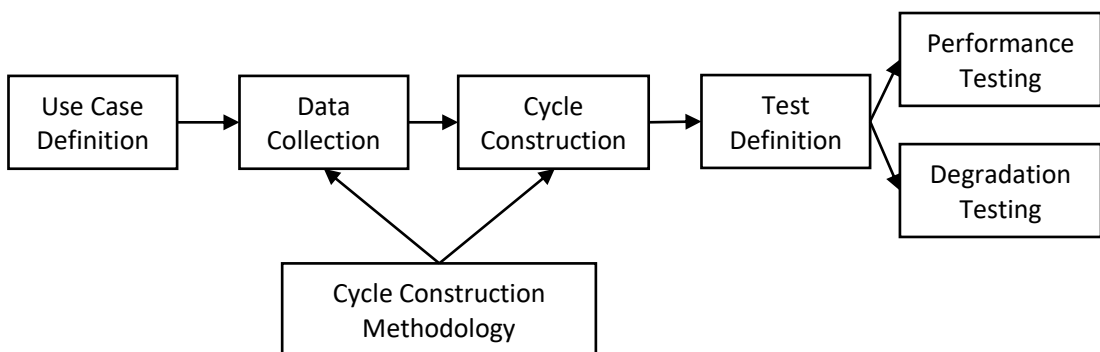


FIGURE 8-1 – PROPOSED FRAMEWORK FOR PERFORMANCE AND DEGRADATION TESTING

The development and implementation of this framework on the use case of HP-BEV applications has addressed the research gaps identified within Chapters 2 and 3, as illustrated within Table 8-1. This was achieved through a series of four research tasks.

Procedure	On-Road driving	HP-BEV without framework	HP-BEV with framework
Characterisation Testing	☑	☑	☑
Performance Testing	☑	☒	☑
Degradation Testing	☑	☒	☐
LIB test cycle construction	☑	☒	☑



TABLE 8-1 – KNOWLEDGE GAPS IN THE EXISTING FRAMEWORK FOR LIB PERFORMANCE AND DEGRADATION TESTING; ☑ - ADDRESSED, ☒ - NOT ADDRESSED, ☐ - INCONCLUSIVE

The first process was defined in “**Research Task 1:** Collate a database of battery duty cycles representative of HP-BEV racing applications.” This task is representative of the data collection step of the new framework illustrated within Figure 8-1. Data collection within this thesis consists of extensive modelling and simulation work to produce a duty cycle database of previously unexplored HP-BEV driving on racing circuit, the specifics of which are covered in Chapter 4. It requires the modelling and parameterisation of a conceptual HP-BEV in accordance with the sponsoring companies’ ambitions, the modelling of racing circuits, and the parameterisation of an AI racing driver. Although the resulting database is based off simulation, this approach offers the most accurate approximation to collecting real-world data with the information available to the author and lays the foundation for the development of a generic duty cycle.

The second stage of the process was defined in “**Research Task 2:** Define a methodology, from which a duty cycle that is suitable for LIB performance and degradation testing may be derived.” This encapsulates the cycle construction methodology and cycle construction steps of the new framework. Chapter 5 presented the successful adaption of two signal design approaches to develop methodologies that allow for the derivation of testing profiles, which accurately capture signal traits that influence battery performance and degradation, thus addressing the research gap pertaining to LIB test cycle construction as indicated through the ☑-symbol in column 4 within Table 8-1. Both methodologies presented within Chapter 5 are suitable for the design of duty cycles for battery performance evaluation within HP-BEV applications. Subsequently these methods yield two suitable duty cycles, one of which (HP-MSC) was selected for further testing. The new HP duty cycles provide a more representative test profile compared to traditional battery test standards. The resulting methodology including database generation and cycle design were published in the Journal of Energy Storage [1].

For HP-BEVs, the ability to more accurately predict the performance requirements for the battery system within this emerging and strategically important BEV sector will further support a range of engineering functions, such as the ability to optimise the energy capacity and power capability of a battery pack and to select and design the most appropriate thermal management strategy. This, in turn, may reduce system costs whilst concurrently increasing energy and power density of the resulting pack. Since its conception, the new HP duty cycle has facilitated further research regarding the evaluation of cell cooling strategies [3,7], and for the validation of a 1D electrochemical-thermal model of the Xalt 53Ah pouch cell [125]. On a wider impact, the devised methodologies are not limited to automotive use cases but are transferrable to all applications, where LIB performance and degradation are a concern. Therefore, the first two research tasks address the knowledge gap of a systematic approach to create duty cycles specifically for LIB performance and degradation testing.

Based on the derivation of the HP-MS, Chapter 6 addressed “**Research Task 3:** Devise an experiment to conduct LIB performance and degradation testing to investigate differences between HP-BEV applications and standard testing procedures.” This relates to the test definition step within Figure 8-1. It describes the experimental procedures for characterisation, performance and degradation testing. The selection and parameterisation of the characterisation tests that provide a detailed description of cell behaviour follows the best practices as discussed within the literature review in Chapter 2. The performance and degradation tests are designed to benchmark the HP-BEV use case against standard testing procedures.

The results of the experimental work and their analysis are presented within Chapter 7 and fulfil “**Research Task 4:** Analyse the experimental results and determine any use-case specific behaviour between HP-BEV applications and standard testing procedures.” The completion of research tasks 3 and 4 narrow the knowledge gap pertaining to LIB performance and degradation testing within HP-BEV applications. The results provide a direct comparison for battery cell thermal performance, and degradation behaviour between the HP and a standard test case. The results highlight the necessity for the proposed framework for performance testing, as indicated through the -symbol in column 4 within Table 8-1. From the experimental results obtained within this work, it is inconclusive whether this framework needs to be extended to degradation testing for this particular use case, as indicated through the -symbol in column 4 within Table 8-1. Considering the existing body of literature, however, the implementation of the framework for degradation testing would be expected to be beneficial. This assertion needs to be tested in further studies and could be achieved through continued testing until EOL is reached for both test groups. With regard to the degradation study, this work offers a hypothesis, based on

existing research, for the atypical degradation process observed. The testing methodology, results, and explanation for the likely degradation process from this experimental work have been published in the Journal of Energy Storage [2].

These findings impact the wider scientific community in a number of ways. The increase in cell temperature surface gradients for HP applications compared to standard testing procedures, and potential impact on degradation, require more capable thermal management strategies. Secondly, the atypical OCV, capacity and degradation progression pose additional challenges for the SOH and SOC estimation algorithms in a BMS. The changes observed within this study are not detectable without EIS and  $dQ/dV$  measurements, which are both time consuming and the implementation of which is not always feasible for commercialised vehicles due to the time-scales and equipment involved.

## 8.2 Future direction and further work

Both, the development and implementation of the proposed framework provide opportunities for additional research and further work.

Pertaining to the data collection phase, within this thesis the database of HP-BEV duty cycles is obtained through simulation and modelling. As such, the representation of the simulated duty cycles compared to real world driving scenarios is limited by the fidelity of the models that comprise the HP-BEV, AI driver, and racing circuits. The inclusion of additional validated component models or real-world battery data would improve the fidelity of the database. Within this study only one type of vehicle and driver were considered. An expansion of the database through additional driver and vehicle models, would allow the database to be split into several classes. From this database, a larger number of duty cycles can be constructed to represent a wider variety of HP use cases.

It was shown that the duty cycle construction methodologies that constitute part of the framework could be used to produce representative profiles for HP-BEV applications. Although in principle, these methodologies are transferrable to other use cases, their usefulness for these applications should be validated.

The battery cell characterisation and degradation testing has shown that the proposed framework is required within the context of performance testing. For degradation testing, the usefulness of the framework, based on experimental data acquired within this thesis, is

inconclusive. The continuation of the degradation study until the EOL of the batteries in both test groups would resolve this unknown.

Regarding the presented hypothesis explaining the atypical aging behaviour, a post mortem study should be conducted to validate the explanation of electrode cracking, or to provide an alternative rationale for the observed changes. A repetition of the study without active cooling would provide additional information regarding the thermal performance of the cell, and quantification of a safe HP-operation capacity. As this study only investigates one specific cell, this work should be extended to additional LIB chemistries and formats to investigate the transferability of the results on those factors.

The proposed framework has only been implemented for HP-BEVs. The usefulness of this framework to other automotive use cases or industrial applications should be investigated.

## 9 References

- [1] Q. Kellner, E. Hosseinzadeh, G. Chouchelamane, W.D. Widanage, J. Marco, Battery cycle life test development for high-performance electric vehicle applications, *J. Energy Storage*. 15 (2018) 228–244. doi:10.1016/j.est.2017.11.019.
- [2] Q. Kellner, D. Worwood, A. Barai, W.D. Widanage, J. Marco, Duty-cycle characterisation of large-format automotive lithium ion pouch cells for high performance vehicle applications, *J. Energy Storage*. 19 (2018) 170–184. doi:10.1016/j.est.2018.07.018.
- [3] D. Worwood, Q. Kellner, M. Wojtala, W.D. Widanage, R. McGlen, D. Greenwood, J. Marco, A new approach to the internal thermal management of cylindrical battery cells for automotive applications, *J. Power Sources*. 346 (2017) 151–166. doi:10.1016/j.jpowsour.2017.02.023.
- [4] Q. Kellner, W. Dhammika Widanage, J. Marco, Battery power requirements in high-performance electric vehicles, in: 2016 IEEE Transp. Electrification Conf. Expo, IEEE, Dearborn, MI, USA, MI, USA, MI, USA, 2016: pp. 1–6. doi:10.1109/ITEC.2016.7520194.
- [5] Q. Kellner, D. Worwood, W.D. Widanage, J. Marco, Electrical and Thermal Behavior of Pouch-Format Lithium Ion Battery Cells under High-Performance and Standard Automotive Duty-Cycles, in: 2017 IEEE Veh. Power Propuls. Conf., IEEE, 2017: pp. 1–5. doi:10.1109/VPPC.2017.8330865.
- [6] D. Worwood, E. Hosseinzadeh, Q. Kellner, J. Marco, D. Greenwood, W. McGlen, R., W. Dhammika, A. Barai, P.A. (Paul A.. Jennings, Thermal analysis of a lithium-ion pouch cell under aggressive automotive duty cycles with minimal cooling, *IET Hybrid Electr. Veh. Conf.* (2016) 2–3. <http://www.scopus.com/inward/record.url?eid=2-s2.0-85034654912&partnerID=MN8TOARS>.
- [7] D. Worwood, Q. Kellner, E. Hosseinzadeh, D. Mullen, D. Greenwood, J. Marco, R. McGlen, K. Lynn, Thermal Analysis of Fin Cooling Large Format Automotive Lithium-Ion Pouch Cells, in: 2017 IEEE Veh. Power Propuls. Conf., IEEE, 2017: pp. 1–6. doi:10.1109/VPPC.2017.8330874.
- [8] M. Kampa, E. Castanas, Human health effects of air pollution, *Environ. Pollut.* 151 (2008) 362–367. doi:10.1016/j.envpol.2007.06.012.
- [9] European Environment Agency, Greenhouse gas emissions from transport, 2015. doi:IND-111-en.



- 
- [10] IPCC, Summary for Policy Makers, in: *Clim. Chang. 2014 Impacts, Adapt. Vulnerability. Contrib. Work. Gr. II to Fifth Assess. Rep. Intergov. Panel Clim. Chang.*, 2014: pp. 1–32. doi:10.1016/j.renene.2009.11.012.
- [11] European Parliament, Council of the European Union, Regulation (EC) no. 443/2009, *Off. J. Eur. Union*. 140 (2009) 1–15. doi:10.1524/zkri.2009.1105.
- [12] UK Department of Transport, *The Road to Zero*, 2018. [https://assets.publishing.service.gov.uk/government/uploads/system/uploads/attachment\\_data/file/723501/road-to-zero.PDF](https://assets.publishing.service.gov.uk/government/uploads/system/uploads/attachment_data/file/723501/road-to-zero.PDF).
- [13] S. Campanari, G. Manzolini, F. Garcia de la Iglesia, Energy analysis of electric vehicles using batteries or fuel cells through well-to-wheel driving cycle simulations, *J. Power Sources*. 186 (2009) 464–477. doi:10.1016/j.jpowsour.2008.09.115.
- [14] C.D. Anderson, J. Anderson, *Electric and Hybrid Cars: A History*, McFarland & Co Inc, 2004.
- [15] B. Walsh, *The History of the Electric Car*, TIME Mag. (2007).
- [16] D. Neil, *The 50 Worst Cars of All Time*, TIME Mag. (2007).
- [17] T. Magnusson, C. Berggren, Entering an era of ferment - radical vs incrementalist strategies in automotive power train development, *Technol. Anal. Strateg. Manag.* 23 (2011) 313–330. doi:10.1080/09537325.2011.550398.
- [18] K. Palmer, J.E. Tate, Z. Wadud, J. Nellthorp, Total cost of ownership and market share for hybrid and electric vehicles in the UK, US and Japan, *Appl. Energy*. 209 (2018) 108–119. doi:10.1016/j.apenergy.2017.10.089.
- [19] T. Franke, I. Neumann, F. Bühler, P. Cocron, J.F. Krems, Experiencing Range in an Electric Vehicle: Understanding Psychological Barriers, *Appl. Psychol.* 61 (2012) 368–391. doi:10.1111/j.1464-0597.2011.00474.x.
- [20] O. Egbue, S. Long, Barriers to widespread adoption of electric vehicles: An analysis of consumer attitudes and perceptions, (2012). doi:10.1016/j.enpol.2012.06.009.
- [21] D. Deng, Li-ion batteries: Basics, progress, and challenges, *Energy Sci. Eng.* 3 (2015) 385–418. doi:10.1002/ese3.95.
- [22] B. Nykvist, M. Nilsson, Rapidly falling costs of battery packs for electric vehicles, *Nat. Clim. Chang.* 5 (2015) 329–332. doi:10.1038/nclimate2564.

- 
- [23] W. Sierzchula, S. Bakker, K. Maat, B. Van Wee, The competitive environment of electric vehicles: An analysis of prototype and production models, *Environ. Innov. Soc. Transitions*. 2 (2012) 49–65. doi:10.1016/j.eist.2012.01.004.
- [24] Aston Martin, Rapide E: Secrets of first all-electric Aston Martin revealed, (n.d.). <https://www.astonmartin.com/en/live/news/2018/09/12/rapide-e-secrets-of-first-all-electric-aston-martin-revealed> (accessed November 27, 2018).
- [25] FIA, Rules & Regulations, [Www.Fiaformulae.Com](http://www.fiaformulae.com). (2015).
- [26] Jaguar I-PACE eTROPHY Electric Racing Series | Jaguar, (n.d.). <https://www.jaguar.co.uk/electrification/i-pace-e-trophy/index.html> (accessed November 26, 2018).
- [27] J. Groot, M. Swierczynski, A.I. Stan, S.K. Kær, On the complex ageing characteristics of high-power LiFePO<sub>4</sub>/graphite battery cells cycled with high charge and discharge currents, *J. Power Sources*. 286 (2015) 475–487. doi:10.1016/j.jpowsour.2015.04.001.
- [28] Y. Zhang, C.Y. Wang, X. Tang, Cycling degradation of an automotive LiFePO<sub>4</sub> lithium-ion battery, *J. Power Sources*. 196 (2011) 1513–1520. doi:10.1016/j.jpowsour.2010.08.070.
- [29] X. Han, M. Ouyang, L. Lu, J. Li, Y. Zheng, Z. Li, A comparative study of commercial lithium ion battery cycle life in electrical vehicle: Aging mechanism identification, *J. Power Sources*. 251 (2014) 38–54. doi:10.1016/j.jpowsour.2013.11.029.
- [30] Y. Zhang, C.-Y. Wang, Cycle-Life Characterization of Automotive Lithium-Ion Batteries with LiNiO<sub>2</sub> Cathode, *J. Electrochem. Soc.* 156 (2009) A527. doi:10.1149/1.3126385.
- [31] M. Safari, C. Delacourt, Aging of a Commercial Graphite/LiFePO<sub>4</sub> Cell, *J. Electrochem. Soc.* 158 (2011) A1123. doi:10.1149/1.3614529.
- [32] A. Barré, F. Suard, M. Gérard, M. Montaru, D. Riu, Statistical analysis for understanding and predicting battery degradations in real-life electric vehicle use, *J. Power Sources*. 245 (2014) 846–856. doi:10.1016/j.jpowsour.2013.07.052.
- [33] N. Omar, P. Van den Bossche, G. Mulder, M. Daowd, J.M. Timmermans, J. Van Mierlo, S. Pauwels, Assessment of performance of lithium iron phosphate oxide, nickel manganese cobalt oxide and nickel cobalt aluminum oxide based cells for using in plug-in battery electric vehicle applications, in: 2011 IEEE Veh. Power Propuls. Conf., IEEE, 2011: pp. 1–7. doi:10.1109/VPPC.2011.6043017.

- 
- [34] International Electrotechnical Commission, International Electrochemical Commission, International Standard IEC 62660-1 - Secondary lithium-ion cells for the propulsion of electric road vehicles – Part 1: Performance testing, (2010).
  - [35] BSI Standards Publication (2012), BS ISO 12405-2:2012 Electrically propelled road vehicles — Test specification for lithium-ion traction battery packs and systems, BSI Stand. Publ. 2014 (2012).  
<https://extranet.cranfield.ac.uk/Download/,DanaInfo=bsol.bsigroup.com,SSL+SubscriptionPdfDocument?materialNumber=000000000030215328>.
  - [36] Idaho National Laboratory, U . S . Department of Energy Vehicle Technologies Program Battery Test Manual For Electric Vehicles, U.S. Dep. Energy. (2015) 16–18.
  - [37] M. Dubarry, V. Svoboda, R. Hwu, B.Y. Liaw, Capacity and power fading mechanism identification from a commercial cell evaluation, *J. Power Sources*. 165 (2007) 566–572. doi:10.1016/j.jpowsour.2006.10.046.
  - [38] M. Dubarry, B.Y. Liaw, Identify capacity fading mechanism in a commercial LiFePO<sub>4</sub> cell, *J. Power Sources*. 194 (2009) 541–549. doi:10.1016/j.jpowsour.2009.05.036.
  - [39] Z. Asus, E.-H. Aglzim, D. Chrenko, Z.-H.C. Daud, L. Le Moyne, Dynamic Modeling and Driving Cycle Prediction for a Racing Series Hybrid Car, *IEEE J. Emerg. Sel. Top. Power Electron*. 2 (2014) 541–551. doi:10.1109/JESTPE.2014.2307079.
  - [40] Z. Asus, D. Chrenko, E.H. Aglzim, A. Kebairi, A. Keromnes, L. Le-Moyne, Model and control strategy simulation of a racing series hybrid car, 2014 IEEE Veh. Power Propuls. Conf. VPPC 2014. (2015). doi:10.1109/VPPC.2014.7007100.
  - [41] A. Devie, E. Vinot, S. Pelissier, P. Venet, Real-world battery duty profile of a neighbourhood electric vehicle, *Transp. Res. Part C Emerg. Technol*. 25 (2012) 122–133. doi:10.1016/j.trc.2012.05.003.
  - [42] B.Y. Liaw, M. Dubarry, From driving cycle analysis to understanding battery performance in real-life electric hybrid vehicle operation, *J. Power Sources*. 174 (2007) 76–88. doi:10.1016/j.jpowsour.2007.06.010.
  - [43] Idaho National Laboratory, Plugged In: How Americans Charge Their Electric Vehicles, (2015) 1–24. <https://avt.inl.gov/sites/default/files/pdf/arra/SummaryReport.pdf>.
  - [44] Jaguar Land Rover Automotive PLC, Company Information, 2014.

- 
- [45] Delta Motorsport, Delta Motorsport, (n.d.).
- [46] G. Sarre, P. Blanchard, M. Broussely, Aging of lithium-ion batteries, *J. Power Sources*. 127 (2004) 65–71. doi:10.1016/j.jpowsour.2003.09.008.
- [47] J. Vetter, P. Novák, M.R. Wagner, C. Veit, K.-C. Möller, J.O. Besenhard, M. Winter, M. Wohlfahrt-Mehrens, C. Vogler, A. Hammouche, Ageing Mechanisms in lithium-ion batteries, *J. Power Sources*. 147 (2005) 269–281. doi:10.1016/j.jpowsour.2005.01.006.
- [48] J. Neubauer, A. Brooker, E. Wood, Sensitivity of battery electric vehicle economics to drive patterns, vehicle range, and charge strategies, *J. Power Sources*. 209 (2012) 269–277. doi:10.1016/j.jpowsour.2012.02.107.
- [49] J.M. Hooper, J. Marco, G.H. Chouchelamane, J.S. Chevalier, D. Williams, Multi-axis vibration durability testing of lithium ion 18650 NCA cylindrical cells, *J. Energy Storage*. 15 (2018) 103–123. doi:10.1016/j.est.2017.11.006.
- [50] M.S.D. Darma, M. Lang, K. Kleiner, L. Mereacre, V. Liebau, F. Fauth, T. Bergfeldt, H. Ehrenberg, The influence of cycling temperature and cycling rate on the phase specific degradation of a positive electrode in lithium ion batteries: A post mortem analysis, *J. Power Sources*. 327 (2016) 714–725. doi:10.1016/j.jpowsour.2016.07.115.
- [51] J. de Hoog, J.M. Timmermans, D. Ioan-Stroe, M. Swierczynski, J. Jaguemont, S. Goutam, N. Omar, J. Van Mierlo, P. Van Den Bossche, Combined cycling and calendar capacity fade modeling of a Nickel-Manganese-Cobalt Oxide Cell with real-life profile validation, *Appl. Energy*. 200 (2017) 47–61. doi:10.1016/j.apenergy.2017.05.018.
- [52] I. Bloom, B.. Cole, J.. Sohn, S.. Jones, E.. Polzin, V.. Battaglia, G.. Henriksen, C. Motloch, R. Richardson, T. Unkelhaeuser, D. Ingersoll, H.. Case, An accelerated calendar and cycle life study of Li-ion cells, *J. Power Sources*. 101 (2001) 238–247. doi:10.1016/S0378-7753(01)00783-2.
- [53] M. Kassem, J. Bernard, R. Revel, S. Pélissier, F. Duclaud, C. Delacourt, Calendar aging of a graphite/LiFePO<sub>4</sub> cell, *J. Power Sources*. 208 (2012) 296–305. doi:10.1016/j.jpowsour.2012.02.068.
- [54] S. Käbitz, J.B. Gerschler, M. Ecker, Y. Yurdagel, B. Emmermacher, D. André, T. Mitsch, D.U. Sauer, Cycle and calendar life study of a graphite|LiNi<sub>1/3</sub>Mn<sub>1/3</sub>Co<sub>1/3</sub>O<sub>2</sub> Li-ion high energy system. Part A: Full cell characterization, *J. Power Sources*. 239 (2013) 572–583. doi:10.1016/j.jpowsour.2013.03.045.

- 
- [55] M. Ecker, N. Nieto, S. Käbitz, J. Schmalstieg, H. Blanke, A. Warnecke, D.U. Sauer, Calendar and cycle life study of Li(NiMnCo)O<sub>2</sub>-based 18650 lithium-ion batteries, *J. Power Sources*. 248 (2014) 839–851. doi:10.1016/j.jpowsour.2013.09.143.
- [56] R. B. Wright, C. G. Motloch, Calendar-Life Studies of Advanced Technology Development Program Gen 1 Lithium Ion Batteries, Doe. (2001).
- [57] F.-S. Li, Y.-S. Wu, J. Chou, M. Winter, N.-L. Wu, A Mechanically Robust and Highly Ion-Conductive Polymer-Blend Coating for High-Power and Long-Life Lithium-Ion Battery Anodes, *Adv. Mater.* 27 (2015) 130–137. doi:10.1002/adma.201403880.
- [58] G. Zubi, R. Dufo-López, M. Carvalho, G. Pasaoglu, The lithium-ion battery: State of the art and future perspectives, *Renew. Sustain. Energy Rev.* 89 (2018) 292–308. doi:10.1016/j.rser.2018.03.002.
- [59] S.S. Zhang, A review on the separators of liquid electrolyte Li-ion batteries, *J. Power Sources*. 164 (2007) 351–364. doi:10.1016/j.jpowsour.2006.10.065.
- [60] P. Arora, Z. Zhang, Battery separators, *Chem. Rev.* 104 (2004) 4419–4462. doi:10.1021/cr020738u.
- [61] M.R. Palacín, Recent advances in rechargeable battery materials: a chemist's perspective., *Chem. Soc. Rev.* 38 (2009) 2565–2575. doi:10.1039/b820555h.
- [62] L.J. Fu, H. Liu, C. Li, Y.P. Wu, E. Rahm, R. Holze, H.Q. Wu, Surface modifications of electrode materials for lithium ion batteries, *Solid State Sci.* 8 (2006) 113–128. doi:10.1016/j.solidstatesciences.2005.10.019.
- [63] J. Miller, Propulsion Systems for Hybrid Vehicles, 2004.
- [64] D. Pletcher, A first course in electrode processes, 2nd Editio, RSC Publishing, 2009.
- [65] D. Linden, T.B. Reddy, Handbook of Batteries, 3rd ed., McGraw-Hill, 2002.
- [66] C.D. Rahn, C.-Y. Wang, Battery Systems Engineering, John Wiley & Sons Ltd, Oxford, UK, 2013. doi:10.1002/9781118517048.
- [67] S. Goriparti, E. Miele, F. De Angelis, E. Di Fabrizio, R. Proietti Zaccaria, C. Capiglia, Review on recent progress of nanostructured anode materials for Li-ion batteries, *J. Power Sources*. 257 (2014) 421–443. doi:10.1016/j.jpowsour.2013.11.103.
- [68] N. Nitta, F. Wu, J.T. Lee, G. Yushin, Li-ion battery materials: Present and future, *Mater. Today*.

- 18 (2015) 252–264. doi:10.1016/j.mattod.2014.10.040.
- [69] K. Brandt, Historical development of secondary lithium batteries, *Solid State Ionics*. 69 (1994) 173–183. doi:10.1016/0167-2738(94)90408-1.
- [70] T. Ohzuku, Formation of Lithium-Graphite Intercalation Compounds in Nonaqueous Electrolytes and Their Application as a Negative Electrode for a Lithium Ion (Shuttlecock) Cell, *J. Electrochem. Soc.* 140 (1993) 2490. doi:10.1149/1.2220849.
- [71] M. Winter, J.O. Besenhard, M.E. Spahr, P. Novák, Insertion electrode materials for rechargeable lithium batteries, *Adv. Mater.* 10 (1998) 725–763. doi:10.1002/(SICI)1521-4095(199807)10:10<725::AID-ADMA725>3.0.CO;2-Z.
- [72] K. Young, C. Wang, L.Y. Wang, K. Strunz, *Electric Vehicle Integration into Modern Power Networks*, 2013. doi:10.1007/978-1-4614-0134-6.
- [73] G.-N. Zhu, Y.-G. Wang, Y.-Y. Xia, Ti-based compounds as anode materials for Li-ion batteries, *Energy Environ. Sci.* 5 (2012) 6652. doi:10.1039/c2ee03410g.
- [74] K. Ariyoshi, R. Yamato, T. Ohzuku, Zero-strain insertion mechanism of  $\text{Li}[\text{Li}_{1/3}\text{Ti}_{5/3}]\text{O}_4$  for advanced lithium-ion (shuttlecock) batteries, *Electrochim. Acta.* 51 (2005) 1125–1129. doi:10.1016/j.electacta.2005.05.053.
- [75] B. Key, R. Bhattacharyya, M. Morcrette, V. Seznec, J. Tarascon, C.P. Grey, Real-Time NMR Investigations of Structural Changes in Silicon Electrodes for Lithium-Ion Batteries, *Society*. 131 (2009) 9239–9249. doi:10.1021/ja8086278.
- [76] Y.P. Wu, E. Rahm, R. Holze, Carbon anode materials for lithium ion batteries, *J. Power Sources*. 114 (2003) 228–236. doi:10.1016/S0378-7753(02)00596-7.
- [77] M. Broussely, P. Biensan, F. Bonhomme, P. Blanchard, S. Herreyre, K. Nechev, R.J. Staniewicz, Main aging mechanisms in Li ion batteries, *J. Power Sources*. 146 (2005) 90–96. doi:10.1016/j.jpowsour.2005.03.172.
- [78] P. Arora, Capacity Fade Mechanisms and Side Reactions in Lithium-Ion Batteries, *J. Electrochem. Soc.* 145 (1998) 3647. doi:10.1149/1.1838857.
- [79] M.M. Doeff, J.B. Goodenough, K. Naoi, K.R. Bullock, *Batteries for Sustainability*, Springer, New York, 2013. doi:10.1007/978-1-4614-5791-6.

- [80] E. Peled, The Electrochemical Behavior of Alkali and Alkaline Earth Metals in Nonaqueous Battery Systems—The Solid Electrolyte Interphase Model, *J. Electrochem. Soc.* 126 (1979) 2047. doi:10.1149/1.2128859.
- [81] K. Teshima, H. Inagaki, S. Tanaka, K. Yubuta, M. Hozumi, K. Kohama, T. Shishido, S. Oishi, Growth of Well-Developed  $\text{Li}_4\text{Ti}_5\text{O}_{12}$  Crystals by the Cooling of a Sodium Chloride Flux, *Cryst. Growth Des.* 11 (2011) 4401–4405. doi:10.1021/cg200578r.
- [82] A. Manthiram, Materials challenges and opportunities of lithium ion batteries, *J. Phys. Chem. Lett.* 2 (2011) 176–184. doi:10.1021/jz1015422.
- [83] M. Wagemaker, F.M. Mulder, Properties and promises of nanosized insertion materials for lithium ion batteries, *Acc. Chem. Res.* 46 (2013) 1206–1215. doi:10.1021/ar2001793.
- [84] W. Lu, I. Belharouak, J. Liu, K. Amine, Thermal properties of  $\text{Li}_4/3\text{Ti}_5/3\text{O}_4/\text{LiMn}_2\text{O}_4$  cell, 174 (2007) 673–677. doi:10.1016/j.jpowsour.2007.06.199.
- [85] I. Belharouak, Y. Sun, W. Lu, K. Amine, On the Safety of the  $\text{Li}_4\text{Ti}_5\text{O}_{12}/\text{LiMn}_2\text{O}_4$  Lithium-Ion Battery, *J. Electrochem. Soc.* 154 (2007) 1083–1087. doi:10.1149/1.2783770.
- [86] J.W. Fergus, Recent developments in cathode materials for lithium ion batteries, *J. Power Sources.* 195 (2010) 939–954. doi:10.1016/j.jpowsour.2009.08.089.
- [87] D. Andre, S.-J. Kim, P. Lamp, S.F. Lux, F. Maglia, O. Paschos, B. Stiaszny, Future generations of cathode materials: an automotive industry perspective, *J. Mater. Chem. A.* 3 (2015) 6709–6732. doi:10.1039/C5TA00361J.
- [88] Z. Chen, Z. Lu, J.R. Dahn, Staging Phase Transitions in  $\text{Li}_{\text{sub } x}\text{CoO}_{\text{sub } 2}$ , *J. Electrochem. Soc.* 149 (2002) A1604. doi:10.1149/1.1519850.
- [89] S.B. Chikkannanavar, D.M. Bernardi, L. Liu, A review of blended cathode materials for use in Li-ion batteries, *J. Power Sources.* 248 (2014) 91–100. doi:10.1016/j.jpowsour.2013.09.052.
- [90] G. Mulder, N. Omar, S. Pauwels, M. Meeus, F. Leemans, B. Verbrugge, W. De Nijs, P. Van Den Bossche, D. Six, J. Van Mierlo, Comparison of commercial battery cells in relation to material properties, *Electrochim. Acta.* 87 (2013) 473–488. doi:10.1016/j.electacta.2012.09.042.
- [91] A. Thaler, D. Watzenig, *Automotive Battery Technology*, Springer, Graz, 2014.
- [92] XALT Energy, Williams Advanced Engineering Announces XALT Energy Partnership, (2014). <https://www.xaltenergy.com/2014/09/11/xalt-energy-partners-with-williams-advanced->

- engineering2/ (accessed May 14, 2018).
- [93] S.K. Martha, O. Haik, E. Zinigrad, I. Exnar, T. Drezen, J.H. Miners, D. Aurbach, On the Thermal Stability of Olivine Cathode Materials for Lithium-Ion Batteries, *J. Electrochem. Soc.* 158 (2011) A1115. doi:10.1149/1.3622849.
  - [94] Rimac Automobili, Rimac Concept\_One Tech Specs, (2018). [http://www.rimac-automobili.com/en/supercars/concept\\_one/](http://www.rimac-automobili.com/en/supercars/concept_one/) (accessed July 20, 2018).
  - [95] M.A. Danzer, V. Liebau, F. Maglia, Aging of lithium-ion batteries for electric vehicles, in: *Adv. Batter. Technol. Electr. Veh.*, Elsevier, 2015: pp. 359–387. doi:10.1016/B978-1-78242-377-5.00014-5.
  - [96] A. Barré, B. Deguilhem, S. Grolleau, M. Gérard, F. Suard, D. Riu, A review on lithium-ion battery ageing mechanisms and estimations for automotive applications, *J. Power Sources.* 241 (2013) 680–689. doi:10.1016/j.jpowsour.2013.05.040 Review.
  - [97] A.M. Andersson, K. Edström, Chemical Composition and Morphology of the Elevated Temperature SEI on Graphite, *J. Electrochem. Soc.* 148 (2001) A1100. doi:10.1149/1.1397771.
  - [98] R. Kostecki, F. McLarnon, Microprobe study of the effect of Li intercalation on the structure of graphite, *J. Power Sources.* 119–121 (2003) 550–554. doi:10.1016/S0378-7753(03)00287-8.
  - [99] T. Waldmann, M. Wilka, M. Kasper, M. Fleischhammer, M. Wohlfahrt-Mehrens, Temperature dependent ageing mechanisms in Lithium-ion batteries - A Post-Mortem study, *J. Power Sources.* 262 (2014) 129–135. doi:10.1016/j.jpowsour.2014.03.112.
  - [100] T.D. Tran, J.H. Feikert, R.W. Pekala, K. Kinoshita, Rate effect on lithium-ion graphite electrode performance, *J. Appl. Electrochem.* 26 (1996) 1161–1167. doi:10.1007/BF00243741.
  - [101] N. Gunawardhana, N. Dimov, M. Sasidharan, G.J. Park, H. Nakamura, M. Yoshio, Suppression of lithium deposition at sub-zero temperatures on graphite by surface modification, *Electrochem. Commun.* 13 (2011) 1116–1118. doi:10.1016/j.elecom.2011.07.014.
  - [102] K. Zaghib, F. Brochu, A. Guerfi, K. Kinoshita, Effect of particle size on lithium intercalation rates in natural graphite, *J. Power Sources.* 103 (2001) 140–146. doi:10.1016/S0378-7753(01)00853-9.
  - [103] K. Zaghib, X. Song, A. Guerfi, R. Kostecki, K. Kinoshita, Effect of particle morphology on lithium intercalation rates in natural graphite, *J. Power Sources.* 124 (2003) 505–512. doi:10.1016/S0378-7753(03)00801-2.



- 
- [104] S.S. Zhang, The effect of the charging protocol on the cycle life of a Li-ion battery, *J. Power Sources*. 161 (2006) 1385–1391. doi:10.1016/j.jpowsour.2006.06.040.
- [105] L.E. Downie, L.J. Krause, J.C. Burns, L.D. Jensen, V.L. Chevrier, J.R. Dahn, In Situ Detection of Lithium Plating on Graphite Electrodes by Electrochemical Calorimetry, *J. Electrochem. Soc.* 160 (2013) A588–A594. doi:10.1149/2.049304jes.
- [106] Y. Liu, J.S. Xue, T. Zheng, J.R. Dahn, Mechanism of lithium insertion in hard carbons prepared by pyrolysis of epoxy resins, *Carbon N. Y.* 34 (1996) 193–200. doi:10.1016/0008-6223(96)00177-7.
- [107] T. Liu, A. Garsuch, F. Chesneau, B.L. Lucht, Surface phenomena of high energy Li(Ni<sub>1/3</sub>Co<sub>1/3</sub>Mn<sub>1/3</sub>)O<sub>2</sub>/graphite cells at high temperature and high cutoff voltages, *J. Power Sources*. 269 (2014) 920–926. doi:10.1016/j.jpowsour.2014.07.051.
- [108] G. Cherkashinin, K. Nikolowski, H. Ehrenberg, S. Jacke, L. Dimesso, W. Jaegermann, The stability of the SEI layer, surface composition and the oxidation state of transition metals at the electrolyte–cathode interface impacted by the electrochemical cycling: X-ray photoelectron spectroscopy investigation, *Phys. Chem. Chem. Phys.* 14 (2012) 12321. doi:10.1039/c2cp41134b.
- [109] J.B. Goodenough, Y. Kim, Challenges for rechargeable Li batteries, *Chem. Mater.* 22 (2010) 587–603. doi:10.1021/cm901452z.
- [110] M. Wohlfahrt-Mehrens, C. Vogler, J. Garche, Aging mechanisms of lithium cathode materials, *J. Power Sources*. 127 (2004) 58–64. doi:10.1016/j.jpowsour.2003.09.034.
- [111] D. Wang, X. Wu, Z. Wang, L. Chen, Cracking causing cyclic instability of LiFePO<sub>4</sub>cathode material, *J. Power Sources*. 140 (2005) 125–128. doi:10.1016/j.jpowsour.2004.06.059.
- [112] G.M. Ehrlich, *Lithium-Ion Batteries*, 2002. doi:10.1016/0378-7753(86)80059-3.
- [113] H.L. Zhang, S.H. Liu, F. Li, S. Bai, C. Liu, J. Tan, H.M. Cheng, Electrochemical performance of pyrolytic carbon-coated natural graphite spheres, *Carbon N. Y.* 44 (2006) 2212–2218. doi:10.1016/j.carbon.2006.02.037.
- [114] J.O. Besenhard, M. Winter, J. Yang, W. Biberacher, Filming mechanism of lithium-carbon anodes in organic and inorganic electrolytes, *J. Power Sources*. 54 (1995) 228–231. doi:10.1016/0378-7753(94)02073-C.
- [115] D. Aurbach, Review of selected electrode–solution interactions which determine the

- performance of Li and Li ion batteries, *J. Power Sources*. 89 (2000) 206–218. doi:10.1016/S0378-7753(00)00431-6.
- [116] K. Uddin, S. Perera, W. Widanage, L. Somerville, J. Marco, Characterising Lithium-Ion Battery Degradation through the Identification and Tracking of Electrochemical Battery Model Parameters, *Batteries*. 2 (2016) 13. doi:10.3390/batteries2020013.
- [117] X. Zhang, B. Winget, M. Doeff, J.W. Evans, T.M. Devine, Corrosion of Aluminum Current Collectors in Lithium-Ion Batteries with Electrolytes Containing LiPF<sub>6</sub>, *J. Electrochem. Soc.* 152 (2005) B448. doi:10.1149/1.2041867.
- [118] S.T. Myung, Y. Hitoshi, Y.K. Sun, Electrochemical behavior and passivation of current collectors in lithium-ion batteries, *J. Mater. Chem.* 21 (2011) 9891–9911. doi:10.1039/c0jm04353b.
- [119] L. Bodenes, R. Naturel, H. Martinez, R. Dedryvère, M. Menetrier, L. Croguennec, J.P. Pérès, C. Tessier, F. Fischer, Lithium secondary batteries working at very high temperature: Capacity fade and understanding of aging mechanisms, *J. Power Sources*. 236 (2013) 265–275. doi:10.1016/j.jpowsour.2013.02.067.
- [120] M. Lang, M.S.D. Darma, K. Kleiner, L. Riekehr, L. Mereacre, M. Ávila Pérez, V. Liebau, H. Ehrenberg, Post mortem analysis of fatigue mechanisms in LiNi<sub>0.8</sub>Co<sub>0.15</sub>Al<sub>0.05</sub>O<sub>2</sub> – LiNi<sub>0.5</sub>Co<sub>0.2</sub>Mn<sub>0.3</sub>O<sub>2</sub> – LiMn<sub>2</sub>O<sub>4</sub>/graphite lithium ion batteries, *J. Power Sources*. 326 (2016) 397–409. doi:10.1016/j.jpowsour.2016.07.010.
- [121] M. Fleckenstein, O. Bohlen, M.A. Roscher, B. Bäker, Current density and state of charge inhomogeneities in Li-ion battery cells with LiFePO<sub>4</sub> as cathode material due to temperature gradients, *J. Power Sources*. 196 (2011) 4769–4778. doi:10.1016/j.jpowsour.2011.01.043.
- [122] T.M. Bandhauer, S. Garimella, T.F. Fuller, A Critical Review of Thermal Issues in Lithium-Ion Batteries, *J. Electrochem. Soc.* 158 (2011) R1. doi:10.1149/1.3515880.
- [123] E. Sarasketa-Zabala, F. Aguesse, I. Villarreal, L.M. Rodriguez-Martinez, C.M. López, P. Kubiak, Understanding lithium inventory loss and sudden performance fade in cylindrical cells during cycling with deep-discharge steps, *J. Phys. Chem. C*. 119 (2015) 896–906. doi:10.1021/jp510071d.
- [124] K.-W. Nam, W.-S. Yoon, H. Shin, K.Y. Chung, S. Choi, X.-Q. Yang, In situ X-ray diffraction studies of mixed LiMn<sub>2</sub>O<sub>4</sub>–LiNi<sub>1/3</sub>Co<sub>1/3</sub>Mn<sub>1/3</sub>O<sub>2</sub> composite cathode in Li-ion cells during charge–discharge cycling, *J. Power Sources*. 192 (2009) 652–659. doi:10.1016/j.jpowsour.2009.02.088.

- 
- [125] E. Hosseinzadeh, R. Genieser, D. Worwood, A. Barai, J. Marco, P. Jennings, A systematic approach for electrochemical-thermal modelling of a large format lithium-ion battery for electric vehicle application, *J. Power Sources*. 382 (2018) 77–94. doi:10.1016/j.jpowsour.2018.02.027.
- [126] G.-N. Zhu, H.-J. Liu, J.-H. Zhuang, C.-X. Wang, Y.-G. Wang, Y.-Y. Xia, Carbon-coated nano-sized  $\text{Li}_4\text{Ti}_5\text{O}_{12}$  nanoporous micro-sphere as anode material for high-rate lithium-ion batteries, *Energy Environ. Sci.* 4 (2011) 4016. doi:10.1039/c1ee01680f.
- [127] E. Sarasketa-Zabala, I. Gandiaga, E. Martinez-Laserna, L.M. Rodriguez-Martinez, I. Villarreal, Cycle ageing analysis of a  $\text{LiFePO}_4$ /graphite cell with dynamic model validations: Towards realistic lifetime predictions, *J. Power Sources*. 275 (2015) 573–587. doi:10.1016/j.jpowsour.2014.10.153.
- [128] C. Pastor-Fernández, T. Bruen, W.D. Widanage, M.A. Gama-Valdez, J. Marco, A Study of Cell-to-Cell Interactions and Degradation in Parallel Strings: Implications for the Battery Management System, *J. Power Sources*. 329 (2016) 574–585. doi:10.1016/j.jpowsour.2016.07.121.
- [129] M.E.V. Team, A Guide to Understanding Battery Specifications, *Current*. (2008) 1–3. doi:10.3390/en7084895.
- [130] M. Kassem, J. Bernard, R. Revel, S. Pélissier, F. Duclaud, C. Delacourt, Erratum to “Calendar aging of a graphite/ $\text{LiFePO}_4$  cell” [Power 208 296–305], *J. Power Sources*. 217 (2012) 574. doi:10.1016/j.jpowsour.2012.06.069.
- [131] A.J. Smith, J.R. Dahn, Delta Differential Capacity Analysis, *J. Electrochem. Soc.* 159 (2012) A290–A293. doi:10.1149/2.076203jes.
- [132] M. Dubarry, C. Truchot, B.Y. Liaw, Synthesize battery degradation modes via a diagnostic and prognostic model, *J. Power Sources*. 219 (2012) 204–216. doi:10.1016/j.jpowsour.2012.07.016.
- [133] M. Dubarry, V. Svoboda, R. Hwu, B. Yann Liaw, Incremental Capacity Analysis and Close-to-Equilibrium OCV Measurements to Quantify Capacity Fade in Commercial Rechargeable Lithium Batteries, *Electrochem. Solid-State Lett.* 9 (2006) A454. doi:10.1149/1.2221767.
- [134] C. Pastor-Fernández, K. Uddin, G.H. Chouchelamane, W.D. Widanage, J. Marco, A Comparison between Electrochemical Impedance Spectroscopy and Incremental Capacity-Differential Voltage as Li-ion Diagnostic Techniques to Identify and Quantify the Effects of Degradation

- Modes within Battery Management Systems, *J. Power Sources*. 360 (2017) 301–318. doi:10.1016/j.jpowsour.2017.03.042.
- [135] D. Allart, M. Montaru, H. Gualous, Model of Lithium Intercalation into Graphite by Potentiometric Analysis with Equilibrium and Entropy Change Curves of Graphite Electrode, *J. Electrochem. Soc.* 165 (2018) A380–A387. doi:10.1149/2.1251802jes.
- [136] A. Barai, Improvement of Consistency , Accuracy and Interpretation of Characterisation Test Techniques for Li-ion Battery cells for Automotive Application By Anup Barai A thesis submitted in partial fulfilment of the requirements for the degree of Doctor of Philoso, 2015.
- [137] G. Mulder, N. Omar, S. Pauwels, F. Leemans, B. Verbrugge, W. De Nijs, P. Van Den Bossche, D. Six, J. Van Mierlo, Enhanced test methods to characterise automotive battery cells, *J. Power Sources*. 196 (2011) 10079–10087. doi:10.1016/j.jpowsour.2011.07.072.
- [138] A. Rahmoun, H. Biechl, Modelling of Li-ion batteries using equivalent circuit diagrams, *Prz. Elektrotechniczny*. 2 (2012) 152–156. <http://red.pe.org.pl/articles/2012/7b/40.pdf>.
- [139] L. Zhang, H. Peng, Z. Ning, Z. Mu, C. Sun, Comparative Research on RC Equivalent Circuit Models for Lithium-Ion Batteries of Electric Vehicles, *Appl. Sci.* 7 (2017) 1002. doi:10.3390/app7101002.
- [140] M. Ecker, J.B. Gerschler, J. Vogel, S. K??bitz, F. Hust, P. Dechent, D.U. Sauer, Development of a lifetime prediction model for lithium-ion batteries based on extended accelerated aging test data, *J. Power Sources*. 215 (2012) 248–257. doi:10.1016/j.jpowsour.2012.05.012.
- [141] W.D. Widanage, A. Barai, G.H. Chouchelamane, K. Uddin, A. McGordon, J. Marco, P. Jennings, Design and use of multisine signals for Li-ion battery equivalent circuit modelling. Part 1: Signal design, *J. Power Sources*. 324 (2016) 70–78. doi:10.1016/j.jpowsour.2016.05.015.
- [142] W.D. Widanage, A. Barai, G.H. Chouchelamane, K. Uddin, A. McGordon, J. Marco, P. Jennings, Design and use of multisine signals for Li-ion battery equivalent circuit modelling. Part 2: Model estimation, *J. Power Sources*. 324 (2016) 61–69. doi:10.1016/j.jpowsour.2016.05.014.
- [143] R. Pintelon, J. Schoukens, G. Vandersteen, K. Barb , Estimation of nonparametric noise and FRF models for multivariable systems—Part I: Theory, *Mech. Syst. Signal Process.* 24 (2010) 573–595. doi:10.1016/j.ymssp.2009.08.009.
- [144] T. Momma, M. Matsunaga, D. Mukoyama, T. Osaka, Ac impedance analysis of lithium ion battery under temperature control, *J. Power Sources*. 216 (2012) 304–307. doi:10.1016/j.jpowsour.2012.05.095.

- 
- [145] A. Barai, G.H. Chouchelamane, Y. Guo, A. McGordon, P. Jennings, A study on the impact of lithium-ion cell relaxation on electrochemical impedance spectroscopy, *J. Power Sources*. 280 (2015) 74–80. doi:10.1016/j.jpowsour.2015.01.097.
- [146] F. Fasmin, R. Srinivasan, Review—Nonlinear Electrochemical Impedance Spectroscopy, *J. Electrochem. Soc.* 164 (2017) H443–H455. doi:10.1149/2.0391707jes.
- [147] A. Barai, K. Uddin, W.D. Widanage, A. McGordon, P. Jennings, A study of the influence of measurement timescale on internal resistance characterisation methodologies for lithium-ion cells, *Sci. Rep.* 8 (2018) 1–13. doi:10.1038/s41598-017-18424-5.
- [148] V.A. Sethuraman, L.J. Hardwick, V. Srinivasan, R. Kostecki, Surface structural disordering in graphite upon lithium intercalation/deintercalation, *J. Power Sources*. 195 (2010) 3655–3660. doi:10.1016/j.jpowsour.2009.12.034.
- [149] K. Uddin, A.D. Moore, A. Barai, J. Marco, The effects of high frequency current ripple on electric vehicle battery performance, *Appl. Energy*. 178 (2016) 142–154. doi:10.1016/j.apenergy.2016.06.033.
- [150] G. Davies, Characterization of batteries using ultrasound: applications for battery management and structural determination, (2018).
- [151] A.G. Hsieh, S. Bhadra, B.J. Hertzberg, P.J. Gjeltema, A. Goy, J.W. Fleischer, D.A. Steingart, Electrochemical-acoustic time of flight: In operando correlation of physical dynamics with battery charge and health, *Energy Environ. Sci.* 8 (2015) 1569–1577. doi:10.1039/c5ee00111k.
- [152] J.B. Robinson, M. Maier, G. Alster, T. Compton, D.J.L. Brett, P.R. Shearing, Spatially resolved ultrasound diagnostics of Li-ion battery electrodes, *Phys. Chem. Chem. Phys.* 21 (2019) 6354–6361. doi:10.1039/c8cp07098a.
- [153] L. Gold, T. Bach, W. Virsik, A. Schmitt, J. Müller, T.E.M. Staab, G. Sextl, Probing lithium-ion batteries' state-of-charge using ultrasonic transmission – Concept and laboratory testing, *J. Power Sources*. 343 (2017) 536–544. doi:10.1016/j.jpowsour.2017.01.090.
- [154] D. Wong, B. Shrestha, D.A. Wetz, J.M. Heinzel, Impact of high rate discharge on the aging of lithium nickel cobalt aluminum oxide batteries, *J. Power Sources*. 280 (2015) 363–372. doi:10.1016/j.jpowsour.2015.01.110.
- [155] J. Cannarella, C.B. Arnold, Ion transport restriction in mechanically strained separator membranes, *J. Power Sources*. 226 (2013) 149–155. doi:10.1016/j.jpowsour.2012.10.093.

- 
- [156] J.M. Hooper, J. Marco, G.H. Chouchelamane, C. Lyness, Vibration durability testing of nickel manganese cobalt oxide (NMC) lithium-ion 18,650 battery cells, *Energies*. 9 (2016) 1–27. doi:10.3390/en9010052.
  - [157] N. Omar, Y. Firouz, H. Gualous, J. Salminen, T. Kallio, J.M. Timmermans, T. Coosemans, P. Van den Bossche, J. Van Mierlo, 9 - Aging and degradation of lithium-ion batteries, Elsevier Ltd., 2015. doi:10.1016/B978-1-78242-090-3.00009-2.
  - [158] K. Amine, C.H. Chen, J. Liu, M. Hammond, A. Jansen, D. Dees, I. Bloom, D. Vissers, G. Henriksen, Factors responsible for impedance rise in high power lithium ion batteries, *J. Power Sources*. 97–98 (2001) 684–687. doi:10.1016/S0378-7753(01)00701-7.
  - [159] N. Takami, H. Inagaki, Y. Tatebayashi, H. Saruwatari, K. Honda, S. Egusa, High-power and long-life lithium-ion batteries using lithium titanium oxide anode for automotive and stationary power applications, *J. Power Sources*. 244 (2013) 469–475. doi:10.1016/j.jpowsour.2012.11.055.
  - [160] Q. Zhang, R.E. White, Calendar life study of Li-ion pouch cells, *J. Power Sources*. 173 (2007) 990–997. doi:10.1016/j.jpowsour.2007.08.044.
  - [161] Q. Zhang, R.E. White, Calendar life study of Li-ion pouch cells Part 2: Simulation, *J. Power Sources*. 179 (2008) 785–792. doi:10.1016/j.jpowsour.2007.12.022.
  - [162] K. Smith, M. Earleywine, E. Wood, J. Neubauer, A. Pesaran, Comparison of Plug-In Hybrid Electric Vehicle Battery Life Across Geographies and Drive Cycles, (2012). doi:10.4271/2012-01-0666.
  - [163] K.L. Gering, S. V. Sazhin, D.K. Jamison, C.J. Michelbacher, B.Y. Liaw, M. Dubarry, M. Cugnet, Investigation of path dependence in commercial lithium-ion cells chosen for plug-in hybrid vehicle duty cycle protocols, *J. Power Sources*. 196 (2011) 3395–3403. doi:10.1016/j.jpowsour.2010.05.058.
  - [164] Y. Zheng, Y.B. He, K. Qian, B. Li, X. Wang, J. Li, S.W. Chiang, C. Miao, F. Kang, J. Zhang, Deterioration of lithium iron phosphate/graphite power batteries under high-rate discharge cycling, *Electrochim. Acta*. 176 (2015) 270–279. doi:10.1016/j.electacta.2015.06.096.
  - [165] X. Han, M. Ouyang, L. Lu, J. Li, A comparative study of commercial lithium ion battery cycle life in electric vehicle: Capacity loss estimation, *J. Power Sources*. 268 (2014) 658–669. doi:10.1016/j.jpowsour.2014.06.111.
  - [166] K. Jalkanen, J. Karppinen, L. Skogström, T. Laurila, M. Nisula, K. Vuorilehto, Cycle aging of

- commercial NMC / graphite pouch cells at different temperatures, *Appl. Energy*. 154 (2015) 160–172. doi:10.1016/j.apenergy.2015.04.110.
- [167] S. Chacko, Y.M. Chung, Thermal modelling of Li-ion polymer battery for electric vehicle drive cycles, *J. Power Sources*. 213 (2012) 296–303. doi:10.1016/j.jpowsour.2012.04.015.
- [168] L.H. Saw, K. Somasundaram, Y. Ye, A.A.O. Tay, Electro-thermal analysis of Lithium Iron Phosphate battery for electric vehicles, *J. Power Sources*. 249 (2014) 231–238. doi:10.1016/j.jpowsour.2013.10.052.
- [169] J. Groot, State-of-health estimation of Li-ion batteries: cycle life test methods, PhD, CHALMERS Univ. Technol. (2012) 138. <http://komar.bitcheese.net/files/JensGroot.pdf>.
- [170] Z. Ma, J. Jiang, W. Shi, W. Zhang, C.C. Mi, Investigation of path dependence in commercial lithium-ion cells for pure electric bus applications: Aging mechanism identification, *J. Power Sources*. 274 (2015) 29–40. doi:10.1016/j.jpowsour.2014.10.006.
- [171] A. Friesen, C. Schultz, G. Brunklaus, U. Rodehorst, A. Wilken, J. Haetge, M. Winter, F. Schappacher, Long Term Aging of Automotive Type Lithium-Ion Cells, *ECS Trans*. 69 (2015) 89–99. doi:10.1149/06918.0089ecst.
- [172] E.C. Castillo, Standards for electric vehicle batteries and associated testing procedures, Elsevier Ltd., 2015. doi:10.1016/B978-1-78242-377-5.00018-2.
- [173] S. Barcellona, S. Grillo, L. Piegari, A simple battery model for EV range prediction: Theory and experimental validation, 2016 Int. Conf. Electr. Syst. Aircraft, Railw. Sh. Propuls. Road Veh. Int. Transp. Electrification. Conf. ESARS-ITEC 2016. (2016). doi:10.1109/ESARS-ITEC.2016.7841441.
- [174] A. Tourani, P. White, P. Ivey, Analysis of electric and thermal behaviour of lithium-ion cells in realistic driving cycles, *J. Power Sources*. 268 (2014) 301–314. doi:10.1016/j.jpowsour.2014.06.010.
- [175] M. André, The ARTEMIS European driving cycles for measuring car pollutant emissions, *Sci. Total Environ*. 334–335 (2004) 73–84. doi:10.1016/j.scitotenv.2004.04.070.
- [176] M. André, R. Joumard, R. Vidon, P. Tassel, P. Perret, Real-world European driving cycles, for measuring pollutant emissions from high- and low-powered cars, *Atmos. Environ*. 40 (2006) 5944–5953. doi:10.1016/j.atmosenv.2005.12.057.
- [177] Environmental Protection Agency, Federal Test Procedure Review Project : Preliminary Technical Report May 1993, 1993.

- 
- [178] H.Y. Tong, W.T. Hung, C.S. Cheung, Development of a driving cycle for Hong Kong, *Atmos. Environ.* 33 (1999) 2323–2335. doi:10.1016/S1352-2310(99)00074-6.
  - [179] W.T. Hung, H.Y. Tong, C.P. Lee, K. Ha, L.Y. Pao, Development of a practical driving cycle construction methodology: A case study in Hong Kong, *Transp. Res. Part D Transp. Environ.* 12 (2007) 115–128. doi:10.1016/j.trd.2007.01.002.
  - [180] J. Lin, D.A. Niemeier, Regional driving characteristics, regional driving cycles, *Transp. Res. Part D Transp. Environ.* 8 (2003) 361–381. doi:10.1016/S1361-9209(03)00022-1.
  - [181] E. Tzirakis, K. Pitsas, F. Zannikos, S. Stournas, Vehicle Emissions and Driving Cycles : Comparison of the Athens Driving Cycle ( Adc ) With Ece-15 and European Driving Cycle ( Edc ), *Glob. NEST J.* 8 (2006) 282–290. [http://www.gnest.org/Journal/Vol8\\_No3/282-290\\_TZIRAKIS\\_376\\_8-3.pdf](http://www.gnest.org/Journal/Vol8_No3/282-290_TZIRAKIS_376_8-3.pdf).
  - [182] J.H. Kent, G.H. Allen, G. Rule, A driving cycle for Sydney, *Transp. Res.* 12 (1978) 147–152. doi:10.1016/0041-1647(78)90117-X.
  - [183] W.T. Hung, K.M. Tam, C.P. Lee, L.Y. Chan, C.S. Cheung, Comparison of driving characteristics in cities of Pearl River Delta, China, *Atmos. Environ.* 39 (2005) 615–625. doi:10.1016/j.atmosenv.2004.10.019.
  - [184] S.H. Ho, Y.D. Wong, V.W.C. Chang, Developing Singapore Driving Cycle for passenger cars to estimate fuel consumption and vehicular emissions, *Atmos. Environ.* 97 (2014) 353–362. doi:10.1016/j.atmosenv.2014.08.042.
  - [185] J.H. Tsai, H.L. Chiang, Y.C. Hsu, B.J. Peng, R.F. Hung, Development of a local real world driving cycle for motorcycles for emission factor measurements, *Atmos. Environ.* 39 (2005) 6631–6641. doi:10.1016/j.atmosenv.2005.07.040.
  - [186] E. Ericsson, Independent driving pattern factors and their influence on fuel-use and exhaust emission factors, *Transp. Res. Part D Transp. Environ.* 6 (2001) 325–345. doi:10.1016/S1361-9209(01)00003-7.
  - [187] K. Brundell-Freij, E. Ericsson, Influence of street characteristics, driver category and car performance on urban driving patterns, *Transp. Res. Part D Transp. Environ.* 10 (2005) 213–229. doi:10.1016/j.trd.2005.01.001.
  - [188] J. Lin, D.A. Niemeier, An exploratory analysis comparing a stochastic driving cycle to California’s regulatory cycle, *Atmos. Environ.* 36 (2002) 5759–5770. doi:10.1016/S1352-2310(02)00695-7.



- 
- [189] S. Shahidinejad, E. Bibeau, S. Filizadeh, Statistical development of a duty cycle for plug-in vehicles in a North American urban setting using fleet information, *IEEE Trans. Veh. Technol.* 59 (2010) 3710–3719. doi:10.1109/TVT.2010.2061243.
  - [190] J. Liu, X. Wang, A. Khattak, Customizing driving cycles to support vehicle purchase and use decisions: Fuel economy estimation for alternative fuel vehicle users, *Transp. Res. Part C Emerg. Technol.* 67 (2016) 280–298. doi:10.1016/j.trc.2016.02.016.
  - [191] S.H. Kamble, T. V. Mathew, G.K. Sharma, Development of real-world driving cycle: Case study of Pune, India, *Transp. Res. Part D Transp. Environ.* 14 (2009) 132–140. doi:10.1016/j.trd.2008.11.008.
  - [192] J. Lin, D.A. Niemeier, Estimating Regional Air Quality Vehicle Emission Inventories: Constructing Robust Driving Cycles, *Transp. Sci.* 37 (2003) 330–346. doi:10.1287/trsc.37.3.330.16045.
  - [193] J. Groot, Statistic method for extraction of synthetic load cycles for cycle life tests of HEV Li-ion batteries, in: 24th Int. Batter. Hybrid Fuel Cell Electr. Veh. Symp. Exhib. 2009, EVS 24, 2009: pp. 1336–1343.  
[http://www.engineeringvillage.com/blog/document.url?mid=cpx\\_6e3d6013b19e8ecf1M666c2061377553&database=cpx%5Cnhttps://www.engineeringvillage.com/blog/document.url?mid=cpx\\_6e3d6013b19e8ecf1M666c2061377553&database=cpx](http://www.engineeringvillage.com/blog/document.url?mid=cpx_6e3d6013b19e8ecf1M666c2061377553&database=cpx%5Cnhttps://www.engineeringvillage.com/blog/document.url?mid=cpx_6e3d6013b19e8ecf1M666c2061377553&database=cpx).
  - [194] A. Esteves-Booth, T. Muneer, H. Kirby, J. Kubie, J. Hunter, The measurement of vehicular driving cycle within the city of Edinburgh, *Transp. Res. Part D Transp. Environ.* 6 (2001) 209–220. doi:10.1016/S1361-9209(00)00024-9.
  - [195] A. Croft, R. Davidson, *Mathematics for Engineers*, 3rd Editio, Pearson Education Limited, Essex, England, 2008.
  - [196] S.J. An, J. Li, Z. Du, C. Daniel, D.L. Wood, Fast formation cycling for lithium ion batteries, *J. Power Sources.* 342 (2017) 846–852. doi:10.1016/j.jpowsour.2017.01.011.
  - [197] E.O. Brigham, *The Fast Fourier Transform and Its Applications*, 1988. doi:10.1109/TE.1969.4320436.
  - [198] J. Schoukens, R. Pintelon, Y. Rolain, *Generation and Analysis of Excitation Signals*, 2012.
  - [199] R. Pintelon, J. Schoukens, *System Identification: A Frequency Domain Approach*, Institute of Electrical and Electronics Engineers, 2001.

- 
- [200] J. Schoukens, T. Dobrowiecki, Design of broadband excitation signals with a user imposed power spectrum and amplitude distribution, in: IMTC/98 Conf. Proceedings. IEEE Instrum. Meas. Technol. Conf. Where Instrum. Is Going (Cat. No.98CH36222), IEEE, 1998: pp. 1002–1005. doi:10.1109/IMTC.1998.676874.
  - [201] K. Sundaravadivelu, G. Shantharam, P. Prabakaran, N. Raghavendra, Analysis of vehicle dynamics using co-simulation of AVL-CRUISE and CarMaker in ETAS RT environment, 2014 Int. Conf. Adv. Electr. Eng. ICAEE 2014. (2014) 1–4. doi:10.1109/ICAEE.2014.6838554.
  - [202] V. Ivanov, D. Savitski, K. Augsburg, P. Barber, B. Knauder, J. Zehetner, Wheel slip control for all-wheel drive electric vehicle with compensation of road disturbances, J. Terramechanics. 61 (2015) 1–10. doi:10.1016/j.jterra.2015.06.005.
  - [203] S.A. Oleksowicz, K.J. Burnham, A. Southgate, C. McCoy, G. Waite, G. Hardwick, C. Harrington, R. McMurran, Regenerative braking strategies, vehicle safety and stability control systems: Critical use-case proposals, Veh. Syst. Dyn. 51 (2013) 684–699. doi:10.1080/00423114.2013.767462.
  - [204] IPG Automotive GmbH, IPG CarMaker User's Guide (v4.5.5), (2014).
  - [205] IPG Automotive GmbH, IPG Automotive, IPGDriver User Manual 6.4, (2014) 1–153.
  - [206] IPG Automotive GmbH, CarMaker Reference Manual V. 5.1, (2014).
  - [207] Tesla Model S P85D specs, Fastest Laps. (2014). <http://fastestlaps.com/models/tesla-model-s-p85d> (accessed July 20, 2018).
  - [208] Jaguar Land Rover, I-PACE FIRST EDITION, (2018). <https://www.jaguar.co.uk/jaguar-range-i-pace/specifications/index.html> (accessed July 20, 2018).
  - [209] G. Kacher, Nio EP9 (2017) review, Car Mag. (2017). <https://www.carmagazine.co.uk/car-reviews/nio/nio-ep9-2017-review/> (accessed July 20, 2018).
  - [210] J.M. GITLIN, 670 horsepower and 0-60 in 2.2 seconds: The Volkswagen I.D. R Pikes Peak, ArsTechnika. (2018). <https://arstechnica.com/cars/2018/04/670-horsepower-and-0-60-in-2-25-seconds-the-volkswagen-i-d-r-pikes-peak/> (accessed July 20, 2018).
  - [211] FIA, FIA Formula E Championship Technical Regulations; Règlement Technique du Championnat de Formule E de la FIA, 2017.
  - [212] Robert Bosch GmbH, Bosch Automotive Handbook, 7th ed., SAE, Plochingen, 2007.

- 
- [213] X. Yuan, J. Wang, K. Colombage, Torque distribution strategy for a front and rear wheel driven electric vehicle, 6th IET Int. Conf. Power Electron. Mach. Drives (PEMD 2012). 2 (2012) C32–C32. doi:10.1049/cp.2012.0316.
  - [214] M.A. Hannan, M.S.H. Lipu, A. Hussain, A. Mohamed, A review of lithium-ion battery state of charge estimation and management system in electric vehicle applications: Challenges and recommendations, *Renew. Sustain. Energy Rev.* 78 (2017) 834–854. doi:10.1016/j.rser.2017.05.001.
  - [215] M. Eshani, Y. Gao, S. Gay, A. Emadi, *Modern electric, hybrid electric and fuel cell vehicles* 2nd. Edition, 2010. doi:10.1201/9781420037739.
  - [216] S.C. Smith, *How Safety Has Killed Great Racetrack Design*, Car Driv. (2012).
  - [217] Rad am Ring - Nordschleife, (n.d.). <https://www.gpsies.com/map.do?fileId=gbgylnhrowrmhkhg> (accessed July 24, 2018).
  - [218] A. Moukadem, D.O. Abdeslam, A. Dieterlen, *Time-Frequency Domain for Segmentation and Classification of Non-Stationary Signals: the Stockwell Transform Applied on Bio-Signals and Electric Signals*, John Wiley & Sons, Incorporated, 2014. <https://ebookcentral.proquest.com/lib/warw/detail.action?docID=1650849>.
  - [219] J.M. Zaccardi, F. Le Berr, Analysis and choice of representative drive cycles for light duty vehicles - Case study for electric vehicles, *Proc. Inst. Mech. Eng. Part D J. Automob. Eng.* 227 (2013) 605–616. doi:10.1177/0954407012454964.
  - [220] M. Dubarry, C. Truchot, M. Cugnet, B.Y. Liaw, K. Gering, S. Sazhin, D. Jamison, C. Michelbacher, Evaluation of commercial lithium-ion cells based on composite positive electrode for plug-in hybrid electric vehicle applications. Part I: Initial characterizations, *J. Power Sources.* 196 (2011) 10328–10335. doi:10.1016/j.jpowsour.2011.08.077.
  - [221] A. Fröberg, L. Nielsen, Efficient drive cycle simulation, *IEEE Trans. Veh. Technol.* 57 (2008) 1442–1453. doi:10.1109/TVT.2007.907310.
  - [222] A.I. Antoniou, J. Komyathy, J. Bench, A. Emadi, Modeling and simulation of various hybrid-electric configurations of the high-mobility multipurpose wheeled vehicle (HMMWV), *IEEE Trans. Veh. Technol.* 56 (2007) 459–465. doi:10.1109/TVT.2007.891490.
  - [223] H. Lan, S. Wen, Y.Y. Hong, D.C. Yu, L. Zhang, Optimal sizing of hybrid PV/diesel/battery in ship power system, *Appl. Energy.* 158 (2015) 26–34. doi:10.1016/j.apenergy.2015.08.031.

- 
- [224] T.Q. Dinh, J. Marco, H. Niu, D. Greenwood, L. Harper, D. Corrochano, A Novel Method for Idle-Stop-Start Control of Micro Hybrid Construction Equipment—Part A: Fundamental Concepts and Design, *Energies*. 10 (2017) 962. doi:10.3390/en10070962.
- [225] T. Dinh, J. Marco, H. Niu, D. Greenwood, L. Harper, D. Corrochano, A Novel Method for Idle-Stop-Start Control of Micro Hybrid Construction Equipment—Part B: A Real-Time Comparative Study, *Energies*. 10 (2017) 1250. doi:10.3390/en10091250.
- [226] L. Lu, X. Han, J. Li, J. Hua, M. Ouyang, A review on the key issues for lithium-ion battery management in electric vehicles, *J. Power Sources*. 226 (2013) 272–288. doi:10.1016/j.jpowsour.2012.10.060.
- [227] W. Waag, S. Käbitz, D.U. Sauer, Experimental investigation of the lithium-ion battery impedance characteristic at various conditions and aging states and its influence on the application, *Appl. Energy*. 102 (2013) 885–897. doi:10.1016/j.apenergy.2012.09.030.
- [228] B. Stiaszny, J.C. Ziegler, E.E. Krauß, M. Zhang, J.P. Schmidt, E. Ivers-Tiffée, Electrochemical characterization and post-mortem analysis of aged LiMn 2O4-NMC/graphite lithium ion batteries part II: Calendar aging, *J. Power Sources*. 258 (2014) 61–75. doi:10.1016/j.jpowsour.2014.02.019.
- [229] A. Jossen, Fundamentals of battery dynamics, *J. Power Sources*. 154 (2006) 530–538. doi:10.1016/j.jpowsour.2005.10.041.
- [230] B. Stiaszny, J.C. Ziegler, E.E. Krauß, J.P. Schmidt, E. Ivers-Tiffée, Electrochemical characterization and post-mortem analysis of aged LiMn 2O4-Li(Ni0.5Mn0.3Co 0.2)O2/graphite lithium ion batteries. Part I: Cycle aging, *J. Power Sources*. 251 (2014) 439–450. doi:10.1016/j.jpowsour.2013.11.080.
- [231] D. Andre, M. Meiler, K. Steiner, C. Wimmer, T. Soczka-Guth, D.U. Sauer, Characterization of high-power lithium-ion batteries by electrochemical impedance spectroscopy. I. Experimental investigation, *J. Power Sources*. 196 (2011) 5334–5341. doi:10.1016/j.jpowsour.2010.12.102.
- [232] T. Grandjean, A. Barai, E. Hosseinzadeh, Y. Guo, A. McGordon, J. Marco, Large format lithium ion pouch cell full thermal characterisation for improved electric vehicle thermal management, *J. Power Sources*. 359 (2017) 215–225. doi:10.1016/j.jpowsour.2017.05.016.
- [233] Y. Troxler, B. Wu, M. Marinescu, V. Yufit, Y. Patel, A.J. Marquis, N.P. Brandon, G.J. Offer, The effect of thermal gradients on the performance of lithium-ion batteries, *J. Power Sources*. 247 (2014) 1018–1025. doi:10.1016/j.jpowsour.2013.06.084.

- 
- [234] I.A. Hunt, Y. Zhao, Y. Patel, J. Offer, Surface Cooling Causes Accelerated Degradation Compared to Tab Cooling for Lithium-Ion Pouch Cells, *J. Electrochem. Soc.* 163 (2016) A1846–A1852. doi:10.1149/2.0361609jes.
- [235] J. Christensen, Modeling Diffusion-Induced Stress in Li-Ion Cells with Porous Electrodes, *J. Electrochem. Soc.* 157 (2010) A366. doi:10.1149/1.3269995.
- [236] A. Barai, Y. Guo, A. McGordon, P. Jennings, A Study of the Effects of External Pressure on the Electrical Performance of a Lithium-ion Pouch Cell, *Int. Conf. Connect. Veh. Expo.* (2013) 295–299. doi:10.1109/ICCVE.2013.155.
- [237] R. Jung, M. Metzger, F. Maglia, C. Stinner, H.A. Gasteiger, Oxygen Release and Its Effect on the Cycling Stability of  $\text{LiNi}_x\text{Mn}_y\text{Co}_z\text{O}_2$  (NMC) Cathode Materials for Li-Ion Batteries, *J. Electrochem. Soc.* 164 (2017) A1361–A1377. doi:10.1149/2.0021707jes.
- [238] M. Dubarry, C. Truchot, B.Y. Liaw, Cell degradation in commercial  $\text{LiFePO}_4$  cells with high-power and high-energy designs, *J. Power Sources.* 258 (2014) 408–419. doi:10.1016/j.jpowsour.2014.02.052.
- [239] R. Genieser, S. Ferrari, M. Loveridge, S.D. Beattie, R. Beanland, H. Amari, G. West, R. Bhagat, Lithium ion batteries (NMC/graphite) cycling at 80 degrees C: Different electrolytes and related degradation mechanism (vol 373, pg 172, 2017), *J. Power Sources.* 382 (2018) 198. doi:10.1016/j.jpowsour.2018.02.044.